Topics in Current Chemistry 315

Kari Rissanen *Editor*

Advanced X-Ray Crystallography

Springer

315

Topics in Current Chemistry

Topics in Current Chemistry

Recently Published and Forthcoming Volumes

Advanced X-Ray Crystallography
Volume Editor: Kari Rissanen
Vol. 315, 2012

Pyrethroids: From Chrysanthemum to Modern Industrial Insecticide
Volume Editors: Noritada Matsuo, Tatsuya Mori
Vol. 314, 2012

Unimolecular and Supramolecular Electronics II
Volume Editor: Robert M. Metzger
Vol. 313, 2012

Unimolecular and Supramolecular Electronics I
Volume Editor: Robert M. Metzger
Vol. 312, 2012

Bismuth-Mediated Organic Reactions
Volume Editor: Thierry Ollevier
Vol. 311, 2012

Peptide-Based Materials
Volume Editor: Timothy Deming
Vol. 310, 2012

Alkaloid Synthesis
Volume Editor: Hans-Joachim Knölker
Vol. 309, 2012

Fluorous Chemistry
Volume Editor: István T. Horváth
Vol. 308, 2012

Multiscale Molecular Methods in Applied Chemistry
Volume Editors: Barbara Kirchner, Jadran Vrabec
Vol. 307, 2012

Solid State NMR
Volume Editor: Jerry C. C. Chan
Vol. 306, 2012

Prion Proteins
Volume Editor: Jörg Tatzelt
Vol. 305, 2011

Microfluidics: Technologies and Applications
Volume Editor: Bingcheng Lin
Vol. 304, 2011

Photocatalysis
Volume Editor: Carlo Alberto Bignozzi
Vol. 303, 2011

Computational Mechanisms of Au and Pt Catalyzed Reactions
Volume Editors: Elena Soriano, José Marco-Contelles
Vol. 302, 2011

Reactivity Tuning in Oligosaccharide Assembly
Volume Editors: Bert Fraser-Reid, J. Cristóbal López
Vol. 301, 2011

Luminescence Applied in Sensor Science
Volume Editors: Luca Prodi, Marco Montalti, Nelsi Zaccheroni
Vol. 300, 2011

Chemistry of Opioids
Volume Editor: Hiroshi Nagase
Vol. 299, 2011

Electronic and Magnetic Properties of Chiral Molecules and Supramolecular Architectures
Volume Editors: Ron Naaman, David N. Beratan, David H. Waldeck
Vol. 298, 2011

Natural Products via Enzymatic Reactions
Volume Editor: Jörn Piel
Vol. 297, 2010

Nucleic Acid Transfection
Volume Editors: Wolfgang Bielke, Christoph Erbacher
Vol. 296, 2010

Advanced X-Ray Crystallography

Volume Editor: Kari Rissanen

With Contributions by

A. Gavezzotti · K.D.M. Harris · P. Macchi · M.I. McMahon · P. Naumov

Editor
Prof. Dr. Kari Rissanen
Department of Chemistry
University of Jyväskylä
Nanoscience Center
PO Box 35
JYU
Finland
kari.t.rissanen@jyu.fi

ISSN 0340-1022 e-ISSN 1436-5049
ISBN 978-3-642-27406-0 e-ISBN 978-3-642-27407-7
DOI 10.1007/978-3-642-27407-7
Springer Heidelberg Dordrecht London New York

Library of Congress Control Number: 2011944825

Volume Editor

Prof. Dr. Kari Rissanen

Department of Chemistry
University of Jyväskylä
Nanoscience Center
PO Box 35
JYU
Finland
kari.t.rissanen@jyu.fi

Editorial Board

Topics in Current Chemistry Also Available Electronically

Topics in Current Chemistry is included in Springer's eBook package *Chemistry and Materials Science*. If a library does not opt for the whole package the book series may be bought on a subscription basis. Also, all back volumes are available electronically.

For all customers with a print standing order we offer free access to the electronic volumes of the series published in the current year.

If you do not have access, you can still view the table of contents of each volume and the abstract of each article by going to the SpringerLink homepage, clicking on "Chemistry and Materials Science," under Subject Collection, then "Book Series," under Content Type and finally by selecting *Topics in Current Chemistry*.

You will find information about the

– Editorial Board
– Aims and Scope
– Instructions for Authors
– Sample Contribution

at springer.com using the search function by typing in *Topics in Current Chemistry*.

Color figures are published in full color in the electronic version on SpringerLink.

Aims and Scope

The series *Topics in Current Chemistry* presents critical reviews of the present and future trends in modern chemical research. The scope includes all areas of chemical science, including the interfaces with related disciplines such as biology, medicine, and materials science.

The objective of each thematic volume is to give the non-specialist reader, whether at the university or in industry, a comprehensive overview of an area where new insights of interest to a larger scientific audience are emerging.

Thus each review within the volume critically surveys one aspect of that topic and places it within the context of the volume as a whole. The most significant developments of the last 5–10 years are presented, using selected examples to illustrate the principles discussed. A description of the laboratory procedures involved is often useful to the reader. The coverage is not exhaustive in data, but rather conceptual, concentrating on the methodological thinking that will allow the non-specialist reader to understand the information presented.

Discussion of possible future research directions in the area is welcome.

Review articles for the individual volumes are invited by the volume editors.

In references *Topics in Current Chemistry* is abbreviated *Top Curr Chem* and is cited as a journal.

Impact Factor 2010: 2.067; Section "Chemistry, Multidisciplinary": Rank 44 of 144

Preface

X-ray crystallography is at present the most powerful tool for detailed structural analysis of both single crystalline and micro-crystalline materials. The recent advances in the radiation sources (e.g. micro-focus X-ray tubes), detector technology (CCD, at present also CMOS technology) and most notably in computer programs and CPU power have greatly eased up the routine and non-routine structural analysis, allowing a nearly "black-box" structure solution and refinement. While only a few decades ago a single crystal X-ray diffraction study of a crystalline solid was considered a very tedious and time-consuming task that could be performed only by well-educated and experienced crystallographers, now that is not true anymore. Certainly, in those days X-ray crystallography was not generally accepted as a routine analytical tool for structural analysis, except for well-diffracting small molecule crystals. Meanwhile, the above mentioned advances have had a major impact on the speed and ease of X-ray diffraction analysis. Modern CCD and CMOS area detectors mounted on high-speed diffractometers allow very fast and accurate data collection and processing, so that several, even very large, data sets can be collected and processed in a day. Fast computers also speed up the structure solution and refinement, so that even very complicated solid state structural problems can be tackled within a reasonable time.

This volume does not try to cover the developments of the "classical" crystallography; instead, it intends to put forward those areas which have advanced most during the last two decades, have brought more visibility to these techniques and thus they have broadened the classical views of the crystallography. The volume opens with a comprehensive account on the development of computational crystallography by Professor Angelo Gavezzotti (Milan, Italy) in the contribution "Computational Studies of Crystal Structure and Bonding". The second chapter "Cryo-Crystallography: Diffraction at Low Temperature and More", by Dr. Piero Macchi (Bern, Switzerland), introduces the readers to crystallography at low temperatures. Chapter three titled "High Pressure Crystallography" which offers a similar treatise on crystallography under high pressures, where interesting crystallographic events occur, was written by Professor Malcolm McMahon (Edinburgh,

Scotland, UK). Maybe the youngest branch of crystallography, combining photochemistry and X-ray diffraction, *viz*. photocrystallography, is introduced by Professor Panče Naumov (Osaka, Japan) with the chapter "Chemical X-Ray Photodiffraction: Principles, Examples, and Perspectives". This concise five chapter volume is closed by an in-depth treatise of the recent advances in the field of X-ray powder diffraction by Professor Kenneth Harris (Cardiff, Wales, UK) titled "Powder Diffraction Crystallography of Molecular Solids".

On the whole, the contributors to this volume have provided personal accounts on the "new frontier" areas in contemporary crystallography. As editor, I have been truly privileged to have the opportunity to work with my very distinguished colleagues, who have been in the forefront of their research areas for many years. Thanks to their meticulous dedication I am very much convinced that this volume will be a valuable and widening reading experience for researchers and students willing to learn more about the "new frontiers" in crystallography.

Jyväskylä, November 2011 Kari Rissanen

Contents

Top Curr Chem (2012) 315: 1–32
DOI: 10.1007/128_2011_131

Published online: 20 April 2011

Computational Studies of Crystal Structure and Bonding

Angelo Gavezzotti

Abstract The analysis, prediction, and control of crystal structures are frontier topics in present-day research in view of their importance for materials science, pharmaceutical sciences, and many other chemical processes. Computational crystallography is nowadays a branch of the chemical and physicals sciences dealing with the study of inner structure, intermolecular bonding, and cohesive energies in crystals. This chapter, mainly focused on organic compounds, first reviews the current methods for X-ray diffraction data treatment, and the new tools available both for quantitative statistical analysis of geometries of intermolecular contacts using crystallographic databases and for the comparison of crystal structures to detect similarities or differences. Quantum chemical methods for the evaluation of intermolecular energies are then reviewed in detail: atoms-in-molecules and other density-based methods, ab initio MO theory, perturbation theory methods, dispersion-supplemented DFT, semiempirical methods and, finally, entirely empirical atom–atom force fields. The superiority of analyses based on energy over analyses based on geometry is highlighted, with caveats on improvised definitions of some intermolecular chemical bonds that are in fact no more than fluxional approach preferences. A perspective is also given on the present status of computational methods for the prediction of crystal structures: in spite of great steps forward, some fundamental obstacles related to the kinetic–thermodynamic dilemma persist. Molecular dynamics and Monte Carlo methods for the simulation of crystal structures and of phase transitions are reviewed. These methods are still at a very speculative stage, but hold promise for substantial future developments.

Keywords Crystallographic computing · Intermolecular energies · Organic crystals

A. Gavezzotti
Dipartimento di Chimica Strutturale, Università di Milano, 20133 Milano, Italy
e-mail: angelo.gavezzotti@unimi.it

Contents

1 Data Processing for X-Ray Diffraction

About a century ago, a consortium of genial physicists joined their intellectual power in realizing that periodically symmetric arrays of electron-containing objects, like atoms in crystals, would have interobject spacings of the same order of magnitude as the wavelength of the newly discovered Roentgen radiation, whose nature was at first so mysterious that it was provisionally given the spooky name of "X-rays". As we all know, the name stuck. The same intellectual power was then redirected to the application of the well known concepts of diffraction to an experiment in which X-rays were shined onto crystalline material [1]. The path from a collection of diffraction fringes (actually black spots on a gray background) to the shape and size of the diffracting objects is paved in Fourier algebra, and it soon became evident that computing – dull, heavy, recursive computing – was indispensable. People below the age of 30 will now find it difficult to understand that computing in those days did not involve electronic computers.

The next step in the newborn discipline called X-ray crystallography was the solution of a problem which, in perspective, looks now like minor detail: finding a way of unraveling the diffraction-*phase* information among what looked like just a set of diffraction *intensities*. Intensities alone provide at most a set of interobject vectors, not the absolute positions of the diffracting objects. One clearly needs phases (the relative timings of the diffracted waves) to reconstruct properly a diffracting object. After some struggle using astute but scarcely effective methods,

the phase problem was eventually solved by a strain of human ingenuity called "direct methods" [2, 3]. These require little more information than just the chemical composition of the molecule forming the crystal – even a reasonable approximation will do – and the space-group symmetry.

When properly diffracting single crystals are available, technical problems of crystal structure solution and refinement by computer are today completely solved and the software is stored in standard packages that are used thousands of times all year round [4, 5]; they sometimes come along with data-collection instruments with nicely composed commercial advertisements. In considering these tools, it may be worth mentioning that one single paper published in *Acta Crystallographica* with the recommended quotation for one such package [6] has – just by itself – increased the impact factor of that journal (normally in the 2.0–2.5 range) to an impressive 49.9 (indeed impressive, for better or for worse). There are of course still some tough nuts to crack, like solving structures on data from very small or recalcitrant crystals, or for complicated blends of chiral entities [7].

Quite often, no single crystals can be obtained for a given substance, and only powder samples are available. Ten years ago the chances of obtaining a definite structural determination from such samples were still very low, but things are quickly changing [8].

The International Union of Crystallography supports an electronic newsletter[1] with news and updates on crystallographic computing. Treatises and primers in X-ray diffraction data handling are available [9–11] (in order of decreasing length and detail). For small- or medium-size molecules, in ordinary routine application the overall solar time from the moment a crystal is handed over to the crystallographer to the moment a structural picture becomes available is presently of the order of a few hours. Computer demands in protein crystallography are of course one order of magnitude larger, parallel to the orders of magnitude of the larger number of diffracted intensities.[2]

There is no good science without good double-checking. Computational and practical X-ray crystallography has benefited – indeed its very existence has been made possible – by the availability of an enormously effective tool for checking and improving crystal data treatment: Anthony Spek's structure validation package, *PLATON* [12]. Thanks to this implement, X-ray crystallography appears as the first (and so far only) discipline that has been able to spot, unequivocally and quantitatively, a scientific fraud [13].

Nowadays computers are so absurdly fast that the phase problem can be solved by recursive computation: the newly proposed charge-flipping algorithm [14] performs in absence of *any* information on the target crystal structure; not even the molecular composition or the crystal symmetry is needed. The procedure starts with

[1] http://www.iucr.org/resources/commissions/crystallographic-computing/newsletters.

[2] See for the latest example, http//nobelprize.org/nobel_prizes/chemistry/laureates/2009/, for a 25-year long struggle for the determination of the structure of the ribosome, involving heavy computational effort.

random phases; structure factors are calculated, an electron density is calculated point by point, and the sign of low-density points is reversed. Atomic pseudo-positions are read off the peaks of the electron density, new structure factors are calculated, and the cycle is repeated until the correct solution is found, as judged by a lowering of the total integral electron density, by the conventional crystallographic R-factor, or by other statistical indicators. Apparently the charge-reversal (flipping) perturbation allows a wider and quicker sampling of the phase space domain. With raw structure factors, a typical number of cycles is 10^6–10^5; with normalized structure factors, the number may decrease to 10^3. In the latter case, however, the ab initio character of the method is partially lost because the stoichiometry must be known. But actually no one questions whether the method requires hundreds or hundreds of thousands of structure factor calculations, one of which might have taken a couple of months for a flesh-and-blood scientist 70 years ago, the best part of a night on a mainframe in the 1980s, or even a few minutes on a personal computer 15 years ago.

There are nonzero chances that the charge flipping algorithm may make direct methods obsolete. Performing as it is, the algorithm is obscure in its fundamentals. No equations, formulas, or proofs are proposed or derived. In the authors' own words [14]: "*we admit our own lack of understanding of it beyond the level of intuition*." This is a patent case in which the human brain is almost made superfluous by fast computing. Indeed, this facet of scientific activity has few precedents.

X-ray diffractometers are highly or even completely automated, to the point that all a human operator has to do is glue a crystal over a loop of wire and push the sample through the slot of a machine about the size of an IR spectrometer; one can even let a robot do the recursive job when many samples are available [15]. Diffraction data processing is as standardized as can be. As a result, X-ray crystallography has been pronounced a dead discipline and even large and well supported Universities are closing their crystallography departments, preserving at most an X-ray diffraction service unit attended by technicians, sometimes but not always supervised by a full-time scientist. Along this direction, teaching of crystallography and preservation of its higher-level aspects are declining, and there is an ever increasing dearth of trained X-ray crystallographers. It is no coincidence that the crystal structure of ribose could appear in the literature [7] only through the expertise of two of the best crystallographers around, both close to or well above 70. A case in point is the controversy over the discovery of a new polymorph of aspirin – no less. Further clarification [16] required an exercise in highly refined X-ray crystallography of which very few scientists, if any, will probably be capable in 20 years' time.

Fortunately, these adverse rumors are far from spelling the end of crystallography as a whole; on the contrary, if correctly interpreted, they just record a growth with a change of identity. With changing times, the business of crystallography shifts from crystal structure solution to the study of crystal structure in general, in aspects related to a wide variety of chemical issues like materials, magnetism, conductivity, pigments, or pharmaceutical formulation, and even mesophases down to semi-crystalline or amorphous states. Modern crystallography is the study of the

inner structure and properties of solid matter by experimental and computational techniques, and this remains one of the most vital aspects of modern research.

2 Crystallographic Databases

The large amount of presently available diffraction data is stored in electronic databases. For organic and organometallic compounds the data, with cell parameters, space-group symmetry, and atomic nuclear positions, are stored in the Cambridge Structural Database (CSD) [17], of a size of about 500,000 structures and quickly expanding. The data are accessible to academic users for a rather modest fee, of the order of 10^4 euro, or for more substantial fees, one order of magnitude larger, for profit companies. The Cambridge Crystallographic Data Center (CCDC) is now a large organization based in a multi-storey, fancy building. The CCDC also provides a very efficient and flexible amount of software for data analysis.[3] A parallel task is carried out for proteins by the Protein Databank [18] (already running into the tens of thousands of structures) and for inorganic compounds by the Inorganic Database [19] (132,000 entries of crystal structures of the elements, and of binary to quintenary compounds). The structural knowledge stored in such facilities has enormously helped and is still helping the advancement of crystallography and of chemical sciences in general.

Chemists invariably associate the identification and position of an atom with the position of its nucleus. But X-rays are diffracted by electrons, and the direct result of the diffraction experiment is an electron-density map, so that the positions of nuclei must be inferred as the centroids of local electron clouds. The error thus introduced is negligible for all atoms except hydrogen, because in any X–H bond the electron cloud is shifted towards the X nucleus and X–H separations are unreliable (i.e., too short). Neutron diffraction directly yields nuclear positions, but is more expensive as can be understood by noting that an X-ray source is about the size of a microwave oven while neutron sources, particle accelerators, are the size of a large building. X-ray positions for hydrogen nuclei can be renormalized to geometries determined by neutron diffraction. This renormalization is straightforward [20] and is imperative in all theoretical studies, which obviously require realistic, accurate nuclear positions.

The first use of the CSD was the determination of average intramolecular bond lengths. These are now coded for all types of chemical bond [21], and such reference values are so well established that any bond length determination at variance with them is presumably wrong. Intramolecular geometry is hardly a frontier topic any more.

[3] http://www.ccdc.cam.ac.uk/products.

3 Crystal Structure Analysis with Geometrical Descriptors

In the following sections of this chapter we discuss a particular brand of computational crystallography, a frontier scientific topic defined as *the use of X-ray crystallographic data to study chemical bonding in crystals and in general*. In order to restrain the contribution to a reasonable size, the discussion is restricted to organic compounds. We begin with methods that are built on geometrical data alone and do not involve a calculation of intermolecular energies.

3.1 "The Shorter, the Stronger"

When one knows the position of all nuclei in the asymmetric part of the unit cell, and the symmetry operations of the space group, even a small laptop computer can produce a vivid picture of the entire crystal. Sections or slabs of those structures are often displayed as "packing diagrams" in structural papers. Such diagrams must however be considered *cum grano salis*, for at least two reasons: (1) they convey a picture of a perfect infinite crystal, while a real crystal invariably includes defects (misplaced molecules) and dislocations; moreover, even the best crystalline specimen is made of a collection of domains in different orientations; and (2) they cannot portray collective thermal librations (lattice vibrations or phonons as they are called) and give an illusory impression of absolute molecular freezing. Lattice vibrations are of paramount importance in materials science, but are unfortunately much less easy to visualize on paper than average nuclear positions. Even discussions of crystal bonding cannot dispense with thermal motion.

In a cluster of molecules representing a short-range-ordered morsel of a crystal structure one identifies atom–atom "contacts" as significantly short separations between atomic nuclear positions. Intuitively, these short separations are appropriated by the ordinary chemist as the signature of some sort of chemical bonding. A brief consideration of the current literature shows that most if not all of the structural papers concerning crystals of organic and organometallic compounds are interspersed with declarations of putative "structure defining" intermolecular "bonds", sorted out on subjective or flexible criteria when not on plain prejudice; one sees what one wants to see. This temptation is hard to resist, in view of decades if not almost a century of a "the shorter, the stronger" view of a chemical bond, drawn from intramolecular bonding theories. In intermolecular systems, however, this assumption is often fallacious; apparently it does not hold even for strong hydrogen bonds [22]. We examine in the next section a robust criterion to assess the statistical significance of a distribution of atom–atom contacts, answering the question as to whether the distribution is random or biased somehow to a certain value. The discussion of chemical (as opposed to statistical) significance is deferred to a later section in this chapter.

3.2 Atom–Atom Contact Distribution Functions [23]

Consider a three-atom system A–B...C where A–B denotes an intramolecular chemical bond in one molecule, and C is an atom in a surrounding molecule in a crystal. Consider a collection of N intermolecular interatomic distances B...C for a given pair of atomic species, comprised between the limiting values $R_{\min}$ and $R_{\max}$, limits that for contacts in crystals of organic molecules are typically 1 and 10 Å. Let V be the total volume of the spherical shell of radius $R_{\max} - R_{\min}$. Single intermolecular interatomic distances r_k belong to distance bins having the volume ΔV_i of the spherical shell between R_i and $R_i + \Delta R$. When N_i is the number of contacts in the i-th distance bin, the bin volumes and the normalized one-dimensional contact distribution function $F(R_i)$ are given by

$$\Delta V(R_i) = 4/3\pi\left[(R_i + \Delta R)^3 - R_i^3\right] \quad F(R_i) = (N_i/\Delta V_i)/P_{\text{norm}}.$$

Simple counting of contacts in each bin is ambiguous; normalization over space volume is crucial for the significance of the function. The normalization factor is the total number of data points in the sample divided by the total volume, $P_{\text{norm}} = N/V$, or the density function for a random distribution of the data over the sample space. Thus, $F(R_i) = 1$ corresponds to a bin with random distribution, and $F(R_i) > 1$ indicates a statistical excess frequency of contacts in the corresponding bin. The distance distribution function has the same algebraic form as a radial distribution function (RDF), but not the exact physical meaning of an RDF because the statistical sample is a heterogeneous collection of different chemical systems, rather than a homogeneous set of particles within a single chemical system (e.g., a liquid). Care must be paid not to attach improper statistical thermodynamic meanings to findings derived from CSD surveys. The original reference [23] also presents a consistent method for the evaluation of two-dimensional (B...C distance vs A–B...C angles) contact density functions along the same conceptual lines. Distributions of intermolecular contacts can be displayed in pictorial ways using the CSD software IsoStar.[4]

Some typical CDFs are now discussed. The data stem from a sample of 48,312 organic crystal structures extracted from the CSD, each diagram being built on sets of 50,000–200,000 distance data. These very high numbers are indispensable: small-population statistics is the most underhand enemy of the physical and social sciences.

The CDFs for hydrogen bonding (Fig. 1) show very high and sharp peaks, clearly corresponding to a real bonding effect. The relative peak heights already indicate a hierarchy of bond strengths, in descending order: carboxylic acids, amides, N–H...N, and alcohols. The graph also clearly shows that O–H...O bonds are

[4] http://www.ccdc.cam.ac.uk/products/csd_system/isostar/.

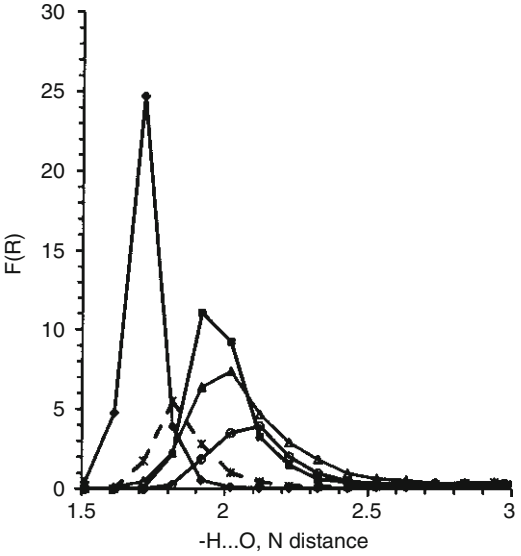

Fig. 1 The contact density function for the hydrogen bond: *full lines*, in descending order of peak height: O–H. . .O carboxylic acids, N–H. . .O amide, N–H. . .O non-amide oxygen, N–H. . .N. The *dotted line* is for O–H. . .O in alcohols

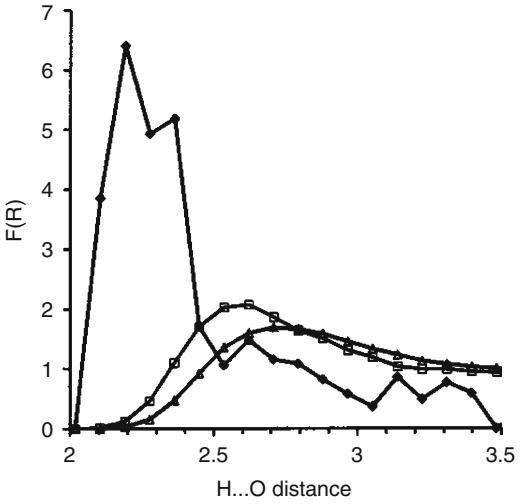

Fig. 2 Same as Fig. 1 but for the C–H. . .O contact. In descending order of peak height: acetylenic CH (*wavy line* because of too few data), aromatic CH, aliphatic CH. Note the large difference between ordinate scales in this figure and in Fig. 1

shorter than N–H. . .O bonds, but bond length and bond strength do not always correlate.

Figure 2 shows the same plot for the C–H. . .O approach. Peak heights are much smaller, and, as will be seen shortly, approach a limit below which the classification as a true bond becomes problematic. In fact, many other CDFs show peaks; indeed, nearly all the CDFs for atoms protruding from molecular cores (except hydrogens) show broad peaks of height 1.5–2.5. In a typical example, all halogen–halogen

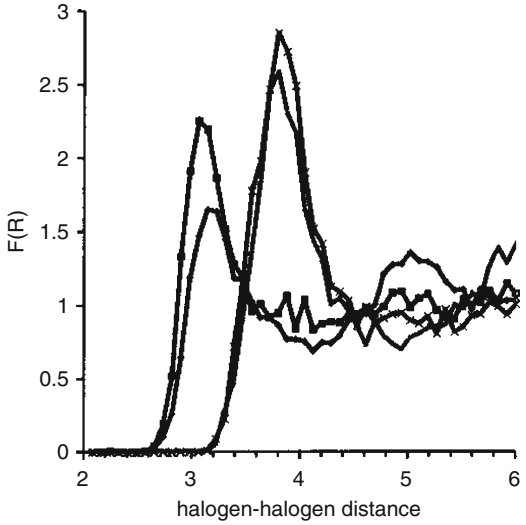

Fig. 3 Contact distribution functions for halogen–halogen contacts. *Left*: aromatic (*taller*) and aliphatic F. . .F; *right*: aromatic (*taller*) and aliphatic Cl. . .Cl

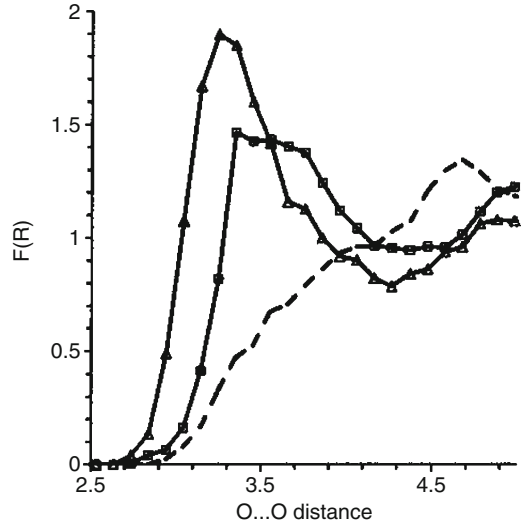

Fig. 4 Contact density functions for oxygen–oxygen contacts: *triangles*, nitro oxygen, *squares*, carbonyl oxygen. The *dotted line* is for ether oxygen (no peak)

CDFs show distinct peaks (Fig. 3); carbonyl C=O. . .O=C or nitro N=O. . .O=N oxygen–oxygen CDFs show prominent peaks (Fig. 4, while ether O. . .O CDFs do not. Contact densities seem more dictated by an unknown admixture of steric and electronic effects, and the identification of bonds on the basis of distance is unsafe (see the example of oxygen; is there an oxygen–oxygen intermolecular bond?) In general, geometry is but a poor substitute for physics; forthcoming sections in this chapter will show that many short atom–atom contacts in crystals correspond to neutral or even to slightly repulsive interactions.

3.3 Molecular Chains, Concatenation

The very idea of an intermolecular chemical bond, in conjunction with crystal periodicity, leads to the concept of chain formation. One is never too careful, however, because crystal structures are by definition periodic in space and, vice versa, the concept of chain can surreptitiously sneak in without the need of a real chemical bond. Once again, there is a dichotomy between geometrical appearance – a ribbon of molecules close to each other – and objective physics, or the presence of an effective electronic interaction between the partners in the supposed periodic structure. The basic question is, how and when is one allowed to trace a chemical bond, and thus legitimately to draw a chain structure? The answer – or at least what in this author's opinion is the only objective and physically sound answer – must come from quantitative evaluation of the involved contact energies, as discussed in the next paragraphs.

Concatenation and interpenetration are fascinating phenomena that involve the mutual intertwining of molecular chains in crystal structures. Such phenomena are less frequent in purely organic crystals, but can be commonplace and complex to a bewildering degree in organometallic crystal structures, where also the classification of chemical bonds is made easier by the presence of unequivocal liaison to the metal centers. The topological properties of these interpenetrating chains can be analyzed using the algorithms encoded in the TOPOS computer program package: one can thus see [24] astonishing many-fold interpenetration of several chain and even layer structures.

3.4 Comparing Crystal Structures

The comparison of different crystal structures and/or the quantification of similarity or of diversity are far from trivial tasks. Information on the degree of similarity of crystal packings may be important in discovering really new materials, in avoiding duplication of work, in distinguishing between real and false polymorphic structures, in helping the selection procedure in crystal structure prediction, etc. The task can be performed using only geometrical information on collections of interatomic distances and angles, as in the XPac procedure [25], or using a quantitative comparison of powder diffraction patterns (for a review see [26]). An even safer method involves a comparison of selected intermolecular energies (see Sect. 4).

4 Crystal Structure Analysis by Quantum Chemistry

We now proceed to discuss intermolecular bonding on the basis of intermolecular energies. Several approaches are reviewed in turn.

4.1 Electron Density Integrals and Atoms-in-Molecules Methods

Present-day diffraction facilities provide easy access to very low-temperature data collection and hence to an accurate determination of electron densities in crystals. Application of standard theorems of classical physics then provides an evaluation of the Coulombic interaction energies in crystal lattices [27]. These calculations are parameter-less and hence are as accurate as the electron density is. Moreover, for highly polar compounds, typically aminoacid zwitterions and the like, a fortunate coincidence cancels out all other attractive and repulsive contributions, and the Coulombic term almost coincides with the total interaction energy.

In a different approach, Bader's AIM theory is applied to the topological analysis of these electron densities, examples being the crystals of N_2O_4 [28], of hexachlorobenzene [29], or of aminoacids [30]. In AIM theory, the presence of a bond critical point – a multidimensional saddle point located between two nuclei in the electron density hypersurface – is the signature of a chemical bond. The value of the electron density at the bond critical point broadly correlates with the strength of the bond. Strong signatures are obtained for intramolecular covalent bonds and also for intra- or intermolecular hydrogen bonds, where the theory is beautifully unequivocal. For the rest of intermolecular contacts, for those lesser interactions that go under the (improper, as we shall see) name of van der Waals interactions, the signal-to-noise ratio seems less reassuring [31] and AIM weak bonds seem to be proliferating somewhat beyond control. Bond energies, or anyway interaction energies between intermolecular fragments, are not easily derived, and the information provided by AIM analyses of weak nonbonded interactions must still be regarded with some caution. At the moment there is no sign that AIM concepts may actually take over in the way of thinking of the average chemist; ideally, that information should be coupled and correlated to reliable interaction energy calculations by ab initio quantum chemical methods. Such a reunification of bonding languages has not yet been carried out, however, and AIM and quantum chemistry partisans still speak their own separate languages, often in sharp contrast [31]. To the family of traditional chemists, a disturbing facet of AIM is that it also predicts bond paths between ions of the same sign or between hydrogen atoms bound 1,4 in *cis*-HC=C–C=CH moieties, like biphenyl [32]. This obviously does not help the above-mentioned reunification with more traditional views. A possible way forward is the statistical coupling between ab initio calculated interaction energies and the topological descriptors generated by AIM, as exemplified in a study of Watson-Crick C:G base pairs [33].

4.2 Ab Initio Quantum Chemical Methods

Quantum chemistry was once confined to very small molecules, mainly because computing times and disk space allocation rise very sharply with the number of

electrons. Besides, the use of molecular orbital calculations in intermolecular problems was severely limited by the Hartree–Fock approach, with its inadequate treatment of electron correlation. Both problems are nowadays less critical, if not completely solved: benchmark ab initio calculations of top quality including dispersion effects can be carried out for intermolecular dimers of chemical significance, like aromatic ring-stacking or hydrogen-bonding [34–36], or DNA base pairs [37] or other biomolecular binding motifs [38, 39]. Nowadays, systems with about 30–50 second-row atoms are tractable [34]. The dimerization energies thus obtained are reliable beyond doubt, and much more reliable than the scarce and uncertain experimental values. This is a case in which theoretical chemistry is ahead of experimental chemistry. These calculations still require highly sophisticated computer resources, but computing times are quickly decreasing. Moreover, this benchmarking provides a safe way to the parameterization of much more cost-efficient semiempirical methods.

In typical organic crystals, molecular pairs are easily sorted out and ab initio methods that work for gas-phase dimers can be applied to the analysis of molecular dimers in the crystal coordination sphere. The entire lattice energy can then be approximated as a sum of pairwise molecule-molecule interactions; examples are crystals of benzene [40], alloxan [41], and of more complex aziridine molecules [42]. This obviously neglects cooperative and, in general, many-body effects, which seem less important in hard closed-shell systems. The positive side of this approach is that molecular coordination spheres in crystals can be dissected and bonding factors can be better analyzed, as examples in the next few sections will show.

The proper way of dealing with periodic systems, like crystals, is to periodicize the orbital representation of the system. Thanks to a periodic exponential prefactor, an atomic orbital becomes a periodic multicenter entity and the Roothaan equations for the molecular orbital procedure are solved over this periodic basis. Apart from an exponential rise in mathematical complexity and in computing times, the conceptual basis of the method is not difficult to grasp [43]. Software for performing such calculations is quite easily available to academic scientists (see, e.g., CASTEP at www.castep.org; CRYSTAL at www.crystal.unito.it; WIEN2k at www.wien2k.at).

There is, of course, a range of accuracy, inversely proportional to human and computational cost. To summarize, quantum chemical methods for intermolecular energy calculations are, in descending order of complexity and cost (each of these methods can be applied in a nonperiodic or a periodic-orbital approach):

– Full ab initio electron-correlation methods, from MP2 to CCSD(T) (the acronyms refer to increasing complexity in the treatment of correlation, with increasing computational cost); include polarization and dispersion contributions and apply to any molecular system. Accuracy depends on the size of the basis set, but so-called complete set limit calculations can nowadays be carried out.
– High-quality, large basis set Hartree–Fock calculations; may be reliable for highly polar molecular systems (typically, amino acids) where Coulombic energies play the major role [44].

- Density functional theory (DFT) methods; they share the same shortcoming of Hartree–Fock in that the mono-electronic character and the inadequacy of density functional formulations prevent the description of polarization/dispersion effects. Adoption of such methods requires a careful choice of the proper density functional [45].
- Corrected DFT methods: the standard DFT calculation is supplemented by an empirical atom–atom term that reproduces correlation effects. They perform well because the missing effect in pure DFT is exactly pinpointed and circumscribed. Examples are a comparison of calculated lattice energies with experimental thermochemical data [46], including periodic orbital treatment, or the accurate reproduction of organic crystal structures without distortion [47].

If well advanced for compounds made of the ordinary atoms of organic chemistry, ab initio techniques are less prone to application in the organometallic field, obviously due to the more complicated electronic structure of metals (the same difficulty appears with bromine and even more with iodine). In such cases it is customary to consider only valence orbitals and to replace the inner electrons of the heavy atoms by an effective pseudopotential, usually also represented by a Gaussian expansion. The number of integrals to be computed is enormously reduced, one super-Gaussian replacing tens or hundreds of core atomic-orbital Gaussians. Interaction energies for anion–pyridine–silver complexes have been calculated in such a way [48].

In nearly all cases the interaction energy is calculated as the difference between the total energy of the aggregate and the sum of the energies of the separate fragments. A major problem in this procedure is basis-set superposition error (BSSE), a spurious stabilization that arises because each separate fragment in the supramolecular aggregate also unduly avails itself, so to speak, of the basis-set orbitals belonging to other fragments. BSSE is routinely taken care of by the counterpoise method, which consists in evaluating the spurious excess stabilization by using as reference a separate calculation of the energy of each fragment including the "ghost" orbitals of the partner, but without the corresponding nuclei. After some initial doubts, there is now general consensus that this is the proper thing to do, although the price is a more than doubling of the computational load.

4.3 Perturbation Theory Methods

A fruitful approach to the problem of intermolecular interaction is perturbation theory. The wavefunctions of the two separate interacting molecules are perturbed when the overlap is nonzero, and standard treatment [49] yields separate contributions to the interaction energy, namely the Coulombic, polarization, dispersion, and repulsion terms. Basis-set superposition is no longer a problem because these energies are calculated directly from the perturbed wavefunction and not by difference between dimers and monomers. The separation into intuitive contributions is a special bonus, because these terms can be correlated with intuitive molecular

structure features: for example, Coulombic terms are large when the approach involves highly polar moieties, dispersion terms are larger when the approach involves polarizable π-clouds, and so on.

At present, however, such methods are limited in scope for crystalline systems because, for the most advanced version of the theory, a single benzene dimer is already at the upper limit of resources [50].

4.4 Semiempirical Methods: The PIXEL Density Sums Approach

PIXEL is a hybrid scheme for the calculation of intermolecular interaction energies, based on a quantum chemical determination of the molecular electron density, in the form of a raster of discrete elements, "pixels." The Coulombic interaction energy between two densities is evaluated by numerical integration on pixel–pixel pairs, and is parameter-less. Polarization energy results from the field of all surrounding pixels on any pixel of the polarized density; its semiempirical nature results from dependence on a scheme for distribution of polarizabilities over single pixels, and from damping of short-distance terms. Dispersion energy is a sum of pairwise pixel–pixel London-type interactions, and depends on a few screening parameters as well as local polarizability and ionization potentials. Repulsion energy is a semiempirical function of the overlap integral between approaching densities (Pauli repulsion), corrected by a contribution from electronegativity differences. The main parameters are one damping factor for polarization and one for dispersion, and two empirical constants for the dependence of repulsion from overlap and electronegativities. We like to call the framework of this conception the Coulomb–London–Pauli (CLP) force model, as opposed to the hardly justifiable name of "van der Waals" interaction.

The basic equations, as recently slightly updated from further experience [51], are now briefly reviewed. Consider a molecule (A) and let ρ_k be the electron density in an elementary volume V_k centered at point (k), with charge $q_k = \rho_k V_k$. For a medium-size organic molecule, with typical steps of 0.08 Å, one has some 10^6 pixels, too many for practical use; the distribution is then contracted into $n \times n \times n$ super-pixels. Each pixel is then formally assigned to the nearest atom. The same is done for a second molecule (B), and the Coulombic interaction energy $E_{\mathrm{Coul,AB}}$ is calculated by a summation over pixel–pixel, pixel–nuclei, and nuclei–nuclei terms.

Let ε_i be the total electric field exerted by surrounding molecules at pixel i, α_i the polarizability at pixel i, and μ_i the dipole induced at pixel i by that field. The linear polarization energy is $E_{\mathrm{Pol},i} = -1/2\ \mu_i\ \varepsilon_i = -1/2\ \alpha_i\ \varepsilon_i{}^2$. The local pixel polarizability is approximated as $\alpha_i = (q_i/Z_{\mathrm{atom}})\ \alpha_{\mathrm{atom}}$, where Z_{atom} and α_{atom} are the atomic charge and polarizability of the atom to whose basin the pixel belongs (from standard repertories). The polarization energy at pixel i is then damped as

$$E_{\mathrm{Pol},i} = -1/2\alpha_i[\varepsilon_i d_i]^2$$

$$d_i = \exp -(\varepsilon_i/(\varepsilon_{\max} - \varepsilon_i))$$

The expression holds for $\varepsilon < \varepsilon_{max}$ while $E_{Pol,i} = 0$ for $\varepsilon > \varepsilon_{max}$. ε_{max}, the limiting field, is an adjustable empirical parameter in the formulation. The total polarization energy at a molecule is the sum of polarization energies at each of its electron density pixels, $E_{Pol} = \Sigma\, E_{Pol,i}$.

Dispersion energies are calculated as a sum of pixel–pixel terms in a damped London-type expression:

$$E_{Disp,AB} = (-3/4)\left\{\Sigma_{i,A}\Sigma_{j,B}E_{OS}\,\alpha_i\alpha_j \Big/ \left[(4\pi\varepsilon^{\circ})^2 (R_{ij})^6\right]\right\} f(R),$$

$$f(R) = \exp\left[-(D/R_{ij} - 1)^2\right] \quad (\text{for } R_{ij} < D, \text{damping function}),$$

where D is an adjustable empirical parameter. E_{OS} (the London "oscillator strength") is estimated from the ionization potential of the atom to whose basin the pixel belongs.

For the repulsion energy, the total charge density overlap integral between molecules A and B, S_{AB}, is calculated and is subdivided into contributions from pairs of atomic species m and n, S_{mn}. Then

$$E_{Rep,mn} = (K_1 - K_2\,\Delta\chi_{mn})S_{mn},$$

where $\Delta\chi_{mn}$ is the corresponding difference in Pauling electronegativity. K_1 and K_2 are positive disposable parameters. The total repulsion energy is the sum over all m–n pairs.

The total intermolecular Pixel interaction energy is

$$E_{Tot} = E_{Coul} + E_{Pol} + E_{Disp} + E_{Rep}.$$

The empirical parameters in the Pixel formulation were optimized by reproducing experimental heats of sublimation for organic crystals and interaction energies between molecular dimers in comparison with ab initio calculations, and by semi-quantitative agreement between Pixel partitioned energies and intermolecular perturbation theory (IMPT) partitioned energies. Universal values for the parameters are available, but very minor adjustments can be made to fit any desired thermochemical or structural property of the particular system under investigation. Since each term of the PIXEL energy reproduces an actual physical effect, these adjustments may be guided by an analysis of the electronic properties of the system under consideration.

The PIXEL code and documentation (OPiX package) can be downloaded at the author's site: http://users.unimi.it/gavezzot. Computing times on an ordinary PC are of the order of a few seconds for a molecular dimer, to a few minutes for a complete crystal structure. PIXEL has been repeatedly shown to give results of accuracy comparable to ab initio MO methods [51]. For an example, Fig. 5 [52] shows a comparison between MP2, PIXEL, uncorrected and corrected periodic-orbital

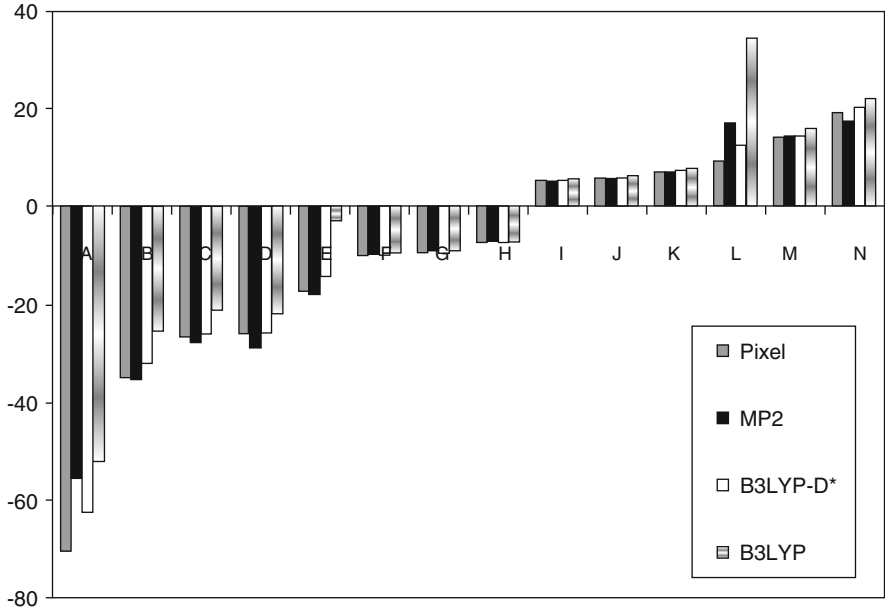

Fig. 5 *Bar diagram* showing the molecule–molecule energies in each pair of the coordination shell of the crystal of nitroguanidine (CSD refcode NTRGUA03). *A* to *N* label dimers in order of decreasing stabilization energy. The four methods give essentially identical results except for the two dispersion-dominated, flat parallel dimers *E* and *L* where uncorrected DFT fails

DFT for the pair energies in the coordination shell of the nitroguanidine crystal. The picture is instructive because the molecular pairs where uncorrected DFT gives the worst errors (pairs E and L) are dispersion-dominated stacked pairs. Not only are total energies nearly identical in DFT/D and PIXEL, but also the dispersion contributions are nearly identical, lending mutual support to the evaluation of the sum of Coulombic-polarization and repulsion terms in the two methods, as well as further validation to the PIXEL parameterization.

4.5 Empirical Methods: Atom–Atom Force Fields

Atom–atom force field methods are at the low-accuracy extreme of the range of computational tools. As the name implies, interaction centers in such procedures are the atomic nuclear positions, used as reckoning points to calculate intermolecular distances and hence intermolecular energies that on these distances depend. Functional forms are quite simple, being of a $C\,R^{-n}$ form with R an atom–atom distance among different molecules, n being an integer in the 4–6 range for dispersion, and usually 12 for modeling a quickly decaying interatomic repulsion. The Cs are totally empirical parameters calibrated using some kind of experimental

data, like sublimation enthalpies for crystals, or high-quality quantum chemical calculations [53]. The good side of such formulations is that the energy terms are very inexpensive computationally, and that first derivatives can be taken very easily when forces are required. In fact the atom–atom scheme is well suited, or is almost the only choice, in large-scale evolutionary simulation (see Sect. 6).

A term in $q\, q'\, R^{-1}$ with q, q' being atomic net point charges located at atomic nuclei is supposed to take care of Coulombic interaction. Actually – aside from the unrealistic placing of negative charges at atomic nuclei – it is intrinsically impossible to describe correctly a short-range Coulombic interaction using such a localized model, especially for moderately or strongly polar groups. This is demonstrated by comparison with presently available methods for the more accurate estimation of these separate terms: for example (see Fig. 6) modeling hydrogen bonds with point charges results in a gross underestimation of the Coulombic energy. If charges are turned up to reproduce the correct Coulombic energy, the result is a large overestimation of the long-range lattice terms. This imbalance between short-range and long-range terms is due to the neglect of penetration energy, the contribution from the diffuse parts of the electron density that reside in between the interacting moieties, obviously absent in a point-charge representation. Figure 7 shows that real and approximate atom–atom Coulombic energies differ even in sign in the crucial interaction region between π-systems.

Atom–atom point-charge schemes are expert systems that work on careful parameterization, witness the good performance in reproducing heats of sublimation (Fig. 8), where the calculation of one lattice energy takes a small fraction of a second. The atom–atom method cannot, however, be reconciled with the actual physics of the interaction.

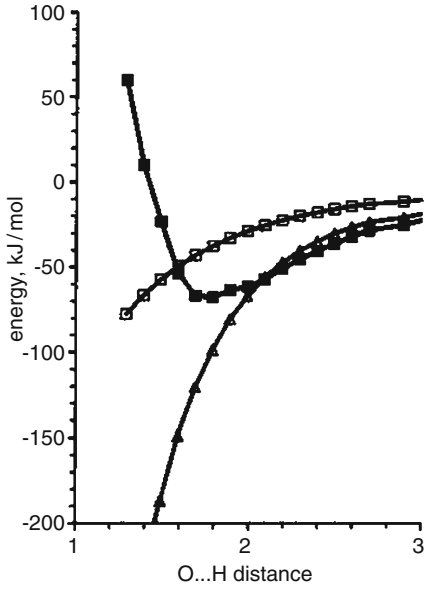

Fig. 6 The energy profile for a cyclic double hydrogen bond in acetic acid. *Filled squares*: total energy, *open squares*: atom–atom Coulombic energy, *triangles*: correct Coulombic energy. The result is insensitive to the choice of atomic point charges according to common schemes (e.g., Mulliken, ESP, etc.)

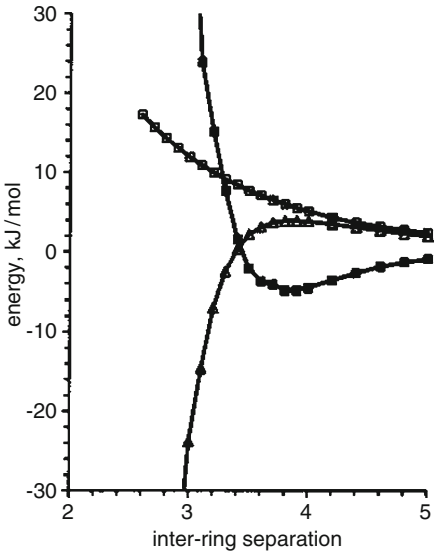

Fig. 7 The benzene stacked dimer: *filled squares*, total energy; *open squares*, atom–atom Coulombic energy; *triangles*, correct Coulombic energy. The ever increasing trend of the atom–atom energy is obviously insensitive to the choice of point charges

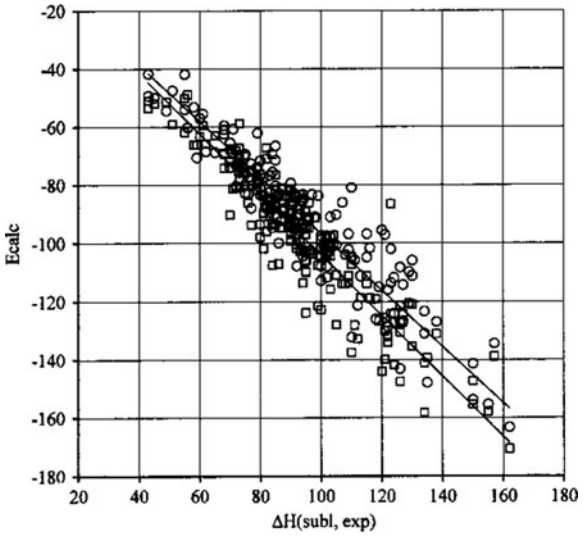

Fig. 8 Calculated lattice energies and experimental heats of sublimation. *Squares*: atom–atom, *circles*: PIXEL results. kJ mol^{-1} units

4.6 Chemical Bonds Versus "Approach Preferences" in Crystals

The last sections have shown that the strength of chemical interactions can nowadays be evaluated rather easily and reliably, but is it possible, convenient, necessary, or indispensable to define a chemical bond in a general conceptual way,

encompassing all cases of atomic linkage, from a gas-phase water molecule to a complex organometallic crystal? We assume here that chemical bonding is but one effect of the electron distribution in the system and that there is no fundamental distinction between intramolecular and intermolecular bonds.

Often, a chemical bond is unanimously recognized, but strange as it may seem, there is no definition of a chemical bond that may go unique and unchallenged throughout the chemical world. Are we chemists dwelling on an evanescent definition of the backbone concept of our science? In the current structural literature some atomic pairs in crystals are a priori treated as chemical bonds, apparently without the need of a definition, or of restrictions and conditions. Of particular concern is the tendency to designate as a chemical bond any proximity of atom pairs on subjective choice, under the assumption that the strength of a chemical bond can be a continuum down to almost zero. Along with an oxymoron, one sees a logical flaw and the danger of fostering more confusion than understanding.

The following is a tentative description of a chemical bond in terms of a few basic principles:

1. A chemical bond is a localized phenomenon that brings about a stable linkage between two atomic nuclei. A chemical bond must result from the interaction between the electron distributions in the basins close to the two involved atomic nuclei. The identification of the bond must not be sensitive to changes of the chemical environment (e.g., by induction effects).
2. A chemical bond produces proximity of the two involved atomic nuclei, whose separation must be less than the sum of commonly accepted random-contact radii (if there is arguing about the exact value of the contact radii then the connection is not a chemical bond). This is a necessary but not sufficient condition. Especially in the intermolecular case, proximity between two nuclei does not always imply a chemical bond.
3. A chemical bond is represented by a dissociation curve, as a function of separation between the two involved nuclei, with a well defined energy minimum at R° with depth E^{*}, the bond dissociation energy. Such a curve can be prepared by a quantum chemical calculation on model molecular systems designed so that the conditions set in points (1) and (2) are fulfilled. E^{*} must be much larger than 3RT and the effect of a small change in internuclear separation must be significantly higher than RT. The bond stretching vibration must be harmonic to a very good approximation at a significant distance from the minimum.

In organic condensed media, and especially in crystals, one sees quite often some recurring, close proximity of certain atom types. These phenomena are often called chemical bonds, but it is easily checked that they do not conform to some or all of the above requirements, mostly because the corresponding interaction energy curves are too shallow. These preferences should not be called chemical bonds because they are prone to shifting, alteration, or even sweeping out, upon minor changes in the environment. Consider a Boltzmann distribution of molecular configurations in the equilibrium liquid-state precursor, either a melt or a solution. Some configurations (e.g., those in which a positively charged CH fragment is close to a negatively

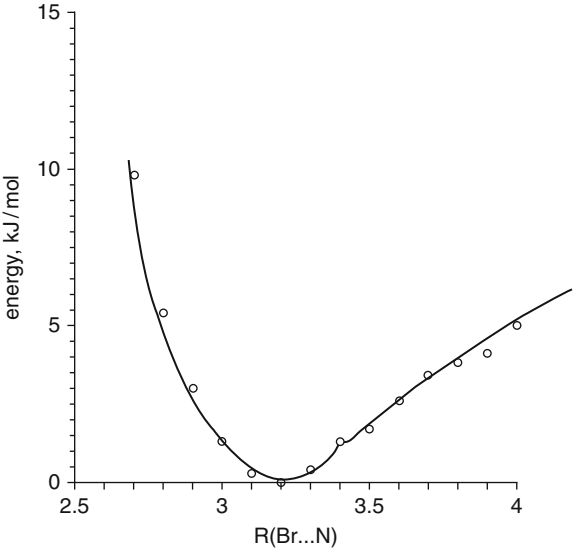

Fig. 9 The calculated energy profile (relative energies, MP2/6-31G** counterpoise corrected) for the direct approach of bromine and nitrogen in a bromobenzene–pyridine molecular dimer. The absolute well depth is 8.8 kJ mol^{-1}

charged oxygen region) are moderately more stabilizing, and hence slightly more frequent in a Boltzmann sense. This excess of residence of the implied *molecules* in such configurations in turn brings about a higher frequency of short atom–atom distances, a phenomenon that can hardly be assigned to the electron density basins of these atoms, but stems from the overall Coulomb–London–Pauli manifold of the entire electron distribution. Such differences in residence time often lead to the observed close proximities between atoms in the solid state. These contacts, however, result from a fluxional precrystallization stage, as opposed to the stability of a true chemical bond. Figure 9 shows, for example, that the Ph–Br. . .N(aromatic) confrontation between bromine and nitrogen occurs on a shallow energy profile, a few kJ mol^{-1} deep, where a stretch of 0.65 Å occurs at the energy cost of $2RT$. We propose the term "approach preference" to designate phenomena of this kind. The COOH. . .O=C connection is a chemical bond, while such connections as C–H. . .O, halogen. . .halogen, or halogen. . .nitrogen, C–H. . .π, and even π-stacking, etc., are approach preferences from diffuse electron clouds, and not chemical bonds. Forcing a diffuse and fluxional electronic event into the straightjacket of a stable and localized chemical bond may be misleading. A chemical electronic fact is surmised in place of a thermodynamic fluctuation. A matter of words? Perhaps, but careful definition is at the basis of the scientific enterprise and too broad a definition is no definition at all.

4.7 Perspective

Structural chemists have nowadays at their disposal a wide range of reliable methods for the quantitative estimation of intermolecular interaction energies.

The more theoretically versed may walk the intricate paths of ab initio theory with its many facets of choice of basis sets and of electron correlation treatments, with corresponding high demands in computing times. Semiempirical methods like PIXEL may offer a valid alternative, giving reliable results for a fraction of the computational effort. Anybody can afford intermolecular energy calculations with empirical potentials that run on standard personal computers in a matter of seconds, not to mention the fact that many of these force fields are embedded in user-friendly computer packages that any undergraduate can handle (the problem, if any, is that such packages may be *too* user-friendly, actually escaping user's control). As a result of massive progress in theoretical methods and computer resources, there is no longer an excuse for qualitative, subjective, geometry-based analyses of intermolecular interaction. Also, at least for crystals made of hard closed-shell molecules, the concept of atom–atom interactions (intermolecular bonds) can advantageously be abandoned, in favor of the consideration of the interaction between full molecular electron densities. Models in which atoms in molecules vanish into a continuum of electron density seem the most promising at the moment. No sensible journal should accept structural papers with the appendage of "structure-defining atom–atom interactions" or "weak bonds," or with a designation of structural motifs like chains or layers, without an indication of the relative interaction energies. Quantitative evaluation [54] has shown that molecular pair interaction energies may sometimes be overall destabilizing, especially in crystals of strongly polar compounds, and that many molecular pairs are held together by dispersion potentials that were once considered weak, but are in fact stronger than many conventional hydrogen bonds. Old ipse dixits like "all that is near is attractive," or "hydrogen bonds are always leaders in a crystal structure," have lost much of their generality. More than ever, qualitative is only poor quantitative and energy numbers now give a Copernican view of crystal packing.

5 Crystal Structure Prediction and Control

Theoretical chemistry, as we have seen, provides quantitative estimates of cohesive energies, given the structure of the involved systems. A further more demanding task is the prediction of structures based on energies. The most fundamental question is: what is the most likely solid-state (crystal) structure for a given compound when only the molecular structure, or even only the molecular connectivity, is known. A predictive answer is understandably extremely useful in designing new materials with desirable properties, or in polymorph screening of pharmaceutical compounds. Current methods for this task involve three main steps: (1) generation of candidate, reasonably stable crystal structures from the molecular formula, (2) accurate evaluation of cohesive energies for such structures, and (3) ranking these structures in order of likelihood of appearance, usually assuming that this order parallels the order of relative stabilizing energies. The procedure seems logical and hence straightforward,

but alas it is not, due to a number of intervening obstacles, some of which are discussed below.

The survey of possible structures may easily run into tens of thousands, especially when the generating molecule has flexible torsional degrees of freedom that add complexity to the landscape of crystal degrees of freedom, cell parameters, and space group. Then, it is by now firmly established that energy differences between polymorphic crystal structures are extremely small, sometimes almost vanishing, posing a severe accuracy problem to any computational scheme, especially so considering that for such large number of candidates, only approximate methods are affordable. The balance between intra- and intermolecular energy calculations may be problematic when, for example, atom–atom formulations must be used. A common approximation is to run the intermolecular search only for a small number of most likely conformations, as determined by a separate search of the gas-phase energy landscape: this obviously neglects the direct interplay between intra- and intermolecular terms in the global optimization of the energy of the system.

The most serious obstacle to consistent crystal structure prediction seems however the fact that kinetics of crystallization has an unknown, but certainly relevant, influence, even more relevant because the energy differences between polymorphs are relatively small. Yields of different polymorphs have been shown to depend as expected on solvent and temperature, but even on hardly traceable contingencies such as impurities, heterogeneous nucleation centers, heat and mass flow, stirring, and seeding. In presence of kinetically favored, metastable structures, when prediction is checked against experiment a "correct" prediction may actually be wrong in a thermodynamic sense, or a "wrong" prediction may actually be correct in pointing out the presence of an unknown more stable crystal phase. This point is particularly crucial, also because no crystal structure prediction method to date is able to take into account the effect of temperature, all calculations being carried out on potential energies alone, and of course, in the real world, stability is also a function of temperature (kinetic energy). In parallel, the neglect of the temperature dependence implies the assumption that enthalpy is equal to free energy, or that $T\Delta S = 0$, either because $T = 0$ or because entropy differences among polymorphs vanish. Thus the ultimate validation of a crystal structure prediction should involve an infinite sampling of the crystal energy landscape *and* an infinitely extensive screening of experimental forms in all conditions of solvent and temperature. The product of these two infinities makes robust structure prediction and control impossible. Success or failure must depend on computational effort but also (to the simulator's frustration) on a certain amount of unpredictable side effects – in one word, chance.

This much said, one may come to terms with reality by considering that in many cases a given compound reproducibly gives rise to only one crystal structure, and that in many cases an accurate energy evaluation recipe will predict that structure as the most stable one, thus verifying all the temperature-dependent assumptions. Although no sensible author would risk presenting a numerical estimate of percentage of such cases, over the last few years the theoretical chemistry community has had a glimpse of a statistical assessment through a series of blindfold tests organized by the Cambridge Crystallographic Data Center. Participants in the test

are given the connectivity formulae of a few compounds and are given a few months to produce a list of predicted crystal structures ranked in order of likelihood of appearance. The crystal structures are separately determined by X-ray diffraction and are secreted until all predictions are submitted. Predictions are considered successful if the experimental structure falls within the first three of the predicted ones. The results are instructive and, when carefully analyzed, confirm the above premises.

In the first test [55] candidate molecules were small and rigid (Fig. 10) and crystals were confined to belong in one of the most common space groups for organic compounds. Computational methods were mostly restricted to simple atom–atom formulations, i.e., quite unsuitable for an accurate task, or to more accurate distributed multipole methods. A relatively high number of hits were obtained, but were not distributed according to the accuracy of the procedure: the software written by the present author scored one of the most accurate hits even though prescriptions were not followed by the users who actually employed a hybridized, uncalibrated force field; the energy ranking depended on fractions of a kJ mol^{-1}. It was later disclosed that the corresponding compound possesses a second, more stable polymorph that had not been detected in any of the predictions.

The relative enthusiasm spurred by the results of the first test were quenched by those of the second test, when very few hits were recorded in spite of massive updating and presumed amelioration of the procedures on the basis of the previous experience. Things proceeded in ups and downs in the third test, but in the fourth one a participant group scored an impressive four hits out of four targets [56]. The apparently decisive factor was the adoption of an algorithm for exhaustive structure search, together with an ab initio DFT dispersion-corrected procedure for both intra- and intermolecular energies, at the price of an equivalent of several hundred thousand CPU hours on massive parallel hardware. In the latest test (Price et al. 2010, personal communication), the same group scored four hits out of six targets, missing what was thought the most difficult one, a giant molecule with at least six torsional degrees of freedom (Fig. 11). Unexpectedly, however, two other groups working with much less ambitious computational means were successful with this most elusive prey, but missed the much easier targets. One participant (B.P. van Eijck) has a constant record of one or two hits in each trial using mostly highly

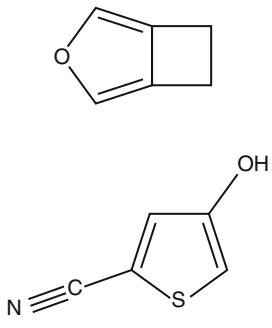

Fig. 10 Two molecules proposed as targets for crystal structure prediction in the first blindfold test

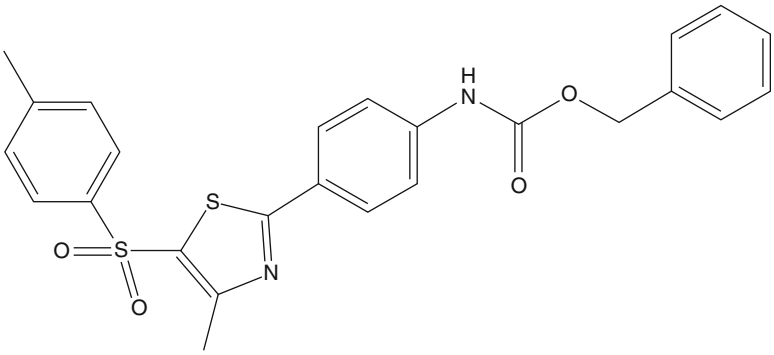

Fig. 11 The "giant" flexible molecule proposed as one of the six targets in the last crystal structure prediction blindfold test

refined atom–atom force fields, and working as a retired person on a PC at home, still scored two hits and one very near miss in the latest test.

There is no doubt that a giant step forward has been made in crystal structure prediction by coupling sound theoretical means with massive computer power, but the inherent uncertainties related to randomness and to handling of temperature remain – see above; improvement in force fields and in computational procedures, as results demonstrate, are very welcome but are neither indispensable nor sufficient. And there is no hope that this barrier may fall in the future, as it stems from first principles. The next step forward is the inclusion of kinetic energies and temperature in the model. This is already possible, although with great limitations, as described in Sect. 6.

6 Dynamic Simulation

6.1 Principles and Applicability

By "dynamic simulation" is meant here a computer procedure that may provide a view of the evolution of a chemical system at a molecular level; i.e., an algorithm that describes what happens when an ensemble of molecules is prepared in a given thermodynamic state, specified by position of – and forces on – all atoms or molecules at a given temperature and pressure. The system may stay at equilibrium in the provided state or may evolve by breaking some bonds or by changing its state of aggregation at a microscopic or macroscopic level. The discussion will be limited here to processes that are relevant to crystal chemistry, reaction-less processes where molecules may change position or conformation but not chemical connectivity: solid–liquid equilibria, crystal phase changes and polymorphism, glass transitions, or nucleation from solution and crystal growth. After a quick review of the basic principles, some examples and perspective will be given.

The computer simulation of dynamic evolution in a molecular system rests on a few, rather simple principles and basic procedures that can be summarized as follows [57]:

1. A simulation box is prepared with N polyatomic molecules of m atoms each, and $N \times m$ starting positional coordinates are assigned.
2. A potential energy field is postulated, and the starting total energy of the simulation box is computed, together with the corresponding forces at each atom (from the derivatives of the potential).

3a. Assuming an equipartition regime and thus neglecting quantization, classical equations of motion are solved for each atom, providing displacement vectors and velocities; new total energy and forces at a time $t' = t^{\circ} + \Delta t$ are computed after displacements; this is Molecular Dynamics (MD).

3b. Random changes in atomic positions are performed and the new configuration is accepted if the total energy decreases or increases by no more than the corresponding Boltzmann limit at a preset temperature; this is Monte Carlo (MC).

4. Temperature and pressure are calculated from standard formulas from statistical mechanics (equipartition kinetic energy and virial, respectively), and are regulated at preset values by computational thermostats and barostats.
5. Steps (3) and (4) are iterated and the trajectory in space of each atom is obtained, along with the energy trajectory, as a function of real time in MD or of some alias of real time (e.g., the number of steps) in MC.

Although MC does not have a proper time variable, the time equivalent of MC moves can be estimated, for example, by computing rotational correlation functions or molecular diffusion coefficients in well characterized liquids; these are time-dependent quantities also experimentally accessible, and the comparison between the number of MC moves and the corresponding experimental data provides the required time equivalents. An order of magnitude estimate with typical MC translational or rotational steps of 0.2 Å and 4° gives 1 or 2 ps per 10^6 translational or rotational MC moves, respectively.

Ideally, MD or MC gives a complete description of the equilibrium states of liquids and crystals, and a molecular-level picture of any chemical process occurring within the system, including phase transitions. The limitations are obvious. The calculation is heavy, with some 5,000 molecules at most, and times or time-equivalents of the order of at most milliseconds. Force fields are by necessity restricted to atom–atom empirical ones. One gets at best a blurred and very short glimpse of the simulated process. And yet, appropriately designed molecular simulation is, for example, the only access to molecular aspects of chemical evolution involved in crystal nucleation and growth.

The simulation of pure crystals at room temperature shows little, except a validation of the force field if the structure is not distorted in the run, and perhaps a picture of molecular average displacements that can be related to librational tensors. Phase changes are obviously more interesting. Generally speaking, the simulation of melting is easy because, as temperature increases and density decreases,

there are innumerable trajectories that lead from the anisotropic long-range periodic crystal structure to the isotropic liquid state, and even a short simulation can find one. The study of crystallization is, in contrast, very difficult because one has to wait for the simulation to find the unique (or at least, one among the very few) trajectory that leads from the isotropic state to a long-range ordered state. The intricacies of attempted simulation of crystallization, with its aspects of phase space sampling, of energy and entropy bottlenecks, as well as of mathematical obstacles to the derivation of appropriate order parameters, are well represented by the case of water [58], which is, at the same time, the structurally simplest and the physically most complicated molecule of all chemistry. The subject tends to be dealt with in physics journals rather than in the chemistry arena, and is well outside the scope of the present chapter. Suffice it to say, in a rough summarizing sentence, that for sizable organic molecules, the time- and size barriers prevent a complete reproduction of the actual proceedings: simulations cannot be long enough, nor can be applied to large enough systems. Probing studies (for simulation see [59]; for experiment see [60]), however, convincingly suggest that the first step in nucleation from solution is phase separation with the formation of liquid-like solute micelles.

Crystal phase transitions are a possible target with present day computational means, when the transition is a smooth one and does not involve melting of the mother phase and subsequent recrystallization into the daughter phase. For crystalline DL-norleucine, an MD simulation has provided a detailed picture of the mechanism of a solid–solid second-order transition between two polymorphic crystal forms, showing concerted molecular displacements involving entire bilayers [61].

6.2 Biased Methods, Ideas, Advantages and Shortcomings

There is little hope that improvement in computational resources, either in software or in hardware, may overcome the time and size barriers that seem today quite insurmountable in the short term. Something must be done to make progress. One possibility is biased methods, in which the computer is instructed to force the system along the desired process path, as described by some mathematical trace.

The idea of biasing the Monte Carlo or molecular dynamics procedures to avoid phase space "traps" or in general to expedite the sampling of more interesting regions of phase space has been applied in variants of the so-called free energy, umbrella-sampling methods, in which a reaction (or process) coordinate drives the system through phase space from a starting reference phase to the final state of interest. At each driving step, the leading coordinate is fixed while the surroundings of phase space are extensively sampled to obtain an estimate of the entropy contribution (hence the name of free energy methods). The procedure is in principle thermodynamically justifiable, although starting states must be chosen artificially, as, for example, ideal gases or idealized one-particle crystals. The calculations involve an increase of orders of magnitude in computational demand, as is always

the case when entropy is at stake: while enthalpy can be safely determined by averaging over rather restricted zones of phase space, the estimation of entropy requires an exhaustive sampling of the phase space available to the system (entropy *is* a measure of accessible phase space). It is not uncommon to have simulation runs that last several months on parallel processor arrays.

An example with a much simpler method will give an idea of how a dynamic simulation can be biased, with some epistemological annexes of simulation methods concerning crystals. Consider an isotropic liquid, in which all molecules are randomly oriented, and the corresponding crystal, in which molecules are somewhat equi-oriented. In order to keep the example as simple as possible, consider just translational symmetry or space group $P1$. When molecules are related by pure translation, once the appropriate reference system is chosen, any atom i in molecule k overlaps with the corresponding atom in another molecule m, and atomic coordinates are related as $\mathbf{x}_{ki} = \mathbf{x}_{mi}$. (The idea is easily extensible, for example for a perfect inversion center one would have $\mathbf{x}_{ki} = -\mathbf{x}_{mi}$.) Calling $D_{km,i}$ the distance between a pair of corresponding atoms when the symmetry relationship is not perfect, a practicable asymmetry index between the two molecules is

$$t_{km} = 1/N_{\text{atoms}} \sum_i D_{km,i}.$$

The overall asymmetry index for molecule k may be taken as the average of all the pairwise contacts to it, and the overall asymmetry index in a computational box as the average of all molecule–molecule indices:

$$S_k = 1/(N_{\text{mol}} - 1) \sum\nolimits_m t_{km},$$

$$S_{\text{all}} = 1/N_{\text{mol}} \sum\nolimits_k S_k.$$

If the computer is instructed to accept a Monte Carlo step only if it involves a favorable change in S_{all} (a decrease or a minor fluctuation within a preset tolerance), symmetrization is forced to occur, enhancing the presence of translation-related molecular pairs in the computational box. Although we all know that this is what does happen when *n*-hexane crystallizes from its liquid, there is no physical counterpart of the asymmetry index and the bias is purely artificial. The system drifts away from applicability of statistical mechanics, and a number of prescriptions related to Boltzmann statistics, to microscopic reversibility, etc., are violated. On the one hand, the above described procedure is no longer rigorous according to some formal laws, but may run overnight on an ordinary desktop PC; on the other hand, umbrella sampling methods are formally more rigorous but require enormously longer computing times and nonetheless accept unrealistic reference states and incorporate so many of the same approximations in what concerns the representation of molecular entities, the force fields, etc. A choice has to be made.

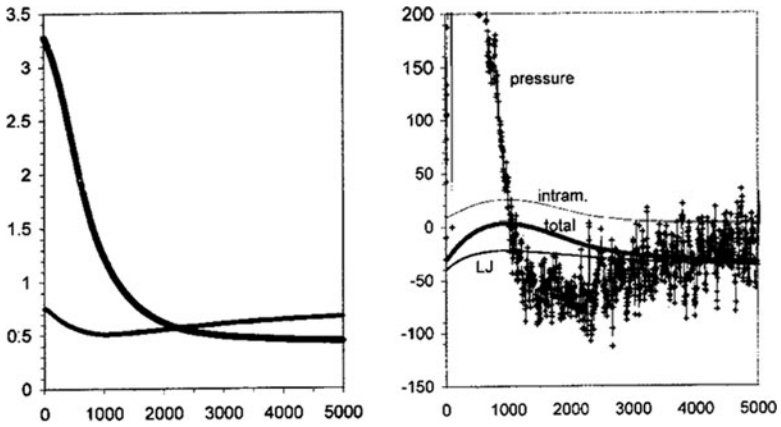

Fig. 12 Symmetrization run for *n*-hexane. *Left*: the evolution of the overall asymmetry index (*upper curve*) and of the overall density (*lower curve*). *Right*: the evolution of pressure (atm) and of intramolecular, intermolecular Lennard–Jones and total energy (kJ mol^{-1}). The abscissa shows the number of million MC moves, corresponding to a time of a few picoseconds

This forced symmetrization procedure has been applied [62] to simulate the transition of an *n*-hexane computational box from isotropic liquid to a semicrystalline phase. The result is that molecules become aligned as they are aligned in the real crystal structure, although the final, complete crystalline periodic symmetry cannot be reached; the time barrier is clearly still operating. The interesting result is not, however, the achieved linearization (this is just a confirmation that the algorithm has been properly programmed into the computer). The novel insight is contained in the evolution trajectory, depicted in Fig. 12, which shows that, as the asymmetry index decreases and molecules are brought into a parallel configuration, internal pressure goes up, and the system must overcome a barrier in which the internal energy rises and the density decreases. The result does not change on change of force fields, although detail of the tolerance imposed on the observance of the bias influences the height of the barriers. The simulation suggests that increasing symmetrization induces localized micro-expansions as molecules rearrange and find their way to the new configuration; for *n*-hexane, this process may involve a request of extra space as molecules uncoil from the partially *gauche* conformations in the liquid to the all-*trans* conformation in the solid.

6.3 What Is the Real Value of a Simulation?

The scope of evolutionary simulation is presently largely limited by the size and time problems. Its force fields are mostly expert systems and are far from a faithful reproduction of real physical effects – think of the wrong description of short-range Coulombic forces resulting from locating formal charges at atomic nuclei,

as discussed in former sections of this chapter. One may wonder, what is then the real value of such computational exercises?

To be sure, fundamental physical principles should be kept as a guideline of all simulations as much as possible; all detail of a simulation must be thoroughly described and carefully specified, in particular with respect to possible violations of such principles and their consequences. Old theories should not, however, be considered as gospel just because they have been around for a long time – especially classical nucleation theory, a construction based on macroscopic equilibrium quantities mostly without any atomic detail, or many aspects of formal statistical mechanics, hardly applicable to multiform real chemical systems in condensed phases. The force fields must at least be validated by comparison with some experimental data. Results must not be too dependent on small details in the overall formulation. Of particular concern is reproducibility: ideally, the simulation code should be deposited and made available to the community for independent verification (a request that is rarely met in publications, in part due to protection of intellectual property, but also because many codes are in-house packages undergoing continuing revision and updating, well known only to its authors and lacking a proper documentation). However, once these basic requirements are met, it should always be kept in mind that a simulation is not necessarily reality: the result is what *might* happen under the specified computational conditions, and not necessary what *does* happen. A properly validated simulation should not be used just to reproduce other experimental data: that would be at best a welcome, further validation, but not real research. The true value of a simulation is the production of new data or new insights, in the form of molecular trajectories, suggesting *possible* scenarios for chemical processes at the molecular level.

A related issue concerns the representation of the system. Undoubtedly, more accurate simulations can be (and are) conducted on the so-called Lennard–Jones fluid, an ensemble of hard- or soft-sphere pseudo-molecules, for which the connections to orthodox statistical mechanics are more strict. Although in this way one may correctly reproduce the phase diagram of, say, argon, this would hardly be considered as significant progress in chemistry. Computing resources are perhaps better used in attempting an approximate sketch of the evolution of real molecules than in super-accurate simulations on unrealistic systems, even at the price of entering a realm where statistical mechanics loses much of its formal strength.

In this perspective, "realistic" is not a proper adjective for a simulation: "informative" is probably more appropriate. For example, the simulation of the early stages of crystallization from the melt for *n*-hexane described above is properly validated (the force field correctly describes the density of the liquid as a function of temperature, the distribution of *gauche-trans* isomerism in the liquid, and the sublimation enthalpy of the crystal). It deals with a real molecule, including the torsional rearrangement of the chain. And yet, if a "realistic" simulation of the crystallization process of *n*-hexane is required, the computing time needed would be of the order of years, if at all possible. The simulation can, however, be considered informative, and hence useful, in that it provides a working hypothesis, a new insight that might stimulate further thought and perhaps even the planning of

an experimental scheme for its verification. And even if experiment were to disprove the hypothesis, some information would be gained anyway – that hexane molecules can uncoil and straighten at no expense of overall excess volume.

7 Summary and Conclusion

Computational crystallography has today a much broader scope and meaning than it had 20 years ago, when it was still mostly restricted to algorithms and software for X-ray data processing. The following is a brief summary of highlights.

The phase problem in crystallography is on its way to being solved by completely ex novo procedures like the charge flipping method. Fast computers sweep away the problem by carrying out hundreds of thousands of structure factor calculations in a few hours.

Structure analysis has shifted completely from intramolecular to intermolecular structure. Distributions of intermolecular distances can be statistically analyzed over hundreds of thousands of reliable data; these distributions should be properly normalized to be statistically significant. The chemical interpretation must, however, take into account the unavoidable fact that intermolecular separations are a combination of steric and electronic effects, and that "near to" does not always mean "bound to".

Chemical bonds should be kept distinct from the approach preferences that one often sees in organic crystals; the former involve permanent *stabilization* by electronic effects, the latter involve *fluxional* preferences that can be shifted and modulated by minor boundary conditions. Calculations of energy profiles provide an objective way of discriminating between the two concepts: in fact, theoretical chemistry has advanced to the point where the interaction energy over molecular dimers and even the complete lattice energies of organic crystals can be evaluated with great accuracy. These energies are available at modest cost both in human and material resources [63], so that there is no longer an excuse for qualitative reasoning on intermolecular cohesion, based only on geometrical parameters. The relative importance of cohesion factors in crystal can and should be given in energy numbers.

Crystal structure prediction by computer has made great steps forward in the last 10 years, with progress toward consistent success in blindfold tests. Fundamental uncertainties still remain, due to the unknown role of nucleation kinetics and to the neglect of temperature effects in the calculations. Success or failure still depends to some extent on hardly predictable factors and on the extent to which the experimental polymorph screening has been carried out. Presently, some of the best computational tools are not yet available to the general community of solid state scientists, being implemented in commercial, strictly copyrighted software.

The dynamic simulation of crystals at equilibrium is quite feasible [64] and gives information on molecular detail like the anisotropy of librations, or the frequency of molecular reorientations. Second-order phase transitions are also within scope,

being in fact extreme cases of continuous displacement or libration. Dynamic simulation of crystal formation, and in general of first-order transitions with discontinuous reconstructions, is still largely hampered by the timescale problem, with microsecond simulations against minutes or hours that nucleation and growth of a real crystal may take. In future perspective, there is little hope that things may change because of improvements in computer resources; progress must come by use of computational shortcuts to help overcome the timescale barrier. Resources are better spent in carrying out informative simulations on real systems and in nonequilibrium environments, rather than on systems rigorously adaptable to formal statistical mechanics, which deal mostly if not exclusively with idealized systems.

As a final remark it may be stated that the predictive simulation of crystal nucleation from a solvent, and of the consequent polymorph selectivity, is the grand challenge of computational crystallography in the next few decades.

References

1. von Laue M (1915) Concerning the detection of X-ray interferences, Nobel Lecture (see http//nobelprize.org/nobel_prizes/physics/laureates/1914/)
2. Sayre D (1952) Acta Cryst 5:60
3. Karle J, Hauptman H (1950) Acta Cryst 3:181
4. Altomare A, Burla MC, Camalli M, Cascarano G, Giacovazzo C, Guagliardi A, Moliterni AGG, Polidori G, Spagna R (1999) J Appl Cryst 32:115
5. Betteridge PW, Carruthers JR, Cooper RI, Prout K, Watkin DJ (2003) J Appl Cryst 36:1487
6. Sheldrick GM (2008) Acta Cryst A64:112
7. Sasak D, McCusker LB, Zandomeneghi G, Meier BH, Blaser D, Boese R, Schweizer WB, Gilmour R, Dunitz JD (2010) Angew Chem Int Ed 49:4503
8. Harris KDM, Cheung EY (2004) Chem Soc Rev 33:526
9. Dunitz JD (1995) X-ray analysis and the structure of organic molecules. Verlag Helevetica Chimica Acta, Basel
10. Glusker JP, Trueblood KN (1985) Crystal structure analysis, a primer. Oxford University Press, Oxford
11. Gavezzotti A (2007) Molecular aggregation. Oxford University Press, Oxford, Chapter 5
12. Spek AL (2009) Acta Cryst D65:148
13. Harrison WTA, Simpson J, Weil M (2010) Acta Cryst E66:e1
14. Oszlanyi G, Süto A (2008) Acta Cryst A64:123
15. Fuller AL, Scott-Hayward LAS, Li Y, Bühl M, Slawin AM, Woollins JD (2010) J Am Chem Soc 132:5799; a nice gadget not to be mistaken, as some seem inclined to do [Ball P (2010) Chemistry World 7(6):34] with the future of crystallography, a fully fledged science occupied with much more relevant tasks, as this very volume testifies
16. Bond AD, Boese R, Desiraju G (2007) Angew Chem Int Ed 46:618
17. Allen FH (2002) Acta Cryst B58:380
18. The Worldwide Protein Databank: Berman HM, Henrick K, Nakamura H (2003) Nat Struct Biol 10:980. http://www.wwpdb.org/
19. ICSD, Inorganic Crystal Structure Database: Belsky A, Hellenbrandt M, Karen VL, Luksch P (2002) Acta Cryst B58:364. http://www.fiz-karlsruhe.de/icsd.html
20. Gavezzotti A (2008) CrystEngComm 10:389
21. Orpen AG, Brammer L, Allen FH, Kennard O, Watson DG, Taylor R (1994) In: Bürgi H-B, Dunitz JD (eds) Structure correlation. VCH, Weinheim, Appendix A

22. D'Oria E, Novoa JJ (2004) CrystEngComm 6:367
23. Gavezzotti A (2010) J Appl Cryst 43:429
24. Baburin IA, Blatov VA, Carlucci L, Ciani G, Proserpio DM (2008) CrystEngComm 10:1822
25. Gelbrich T, Hursthouse MB (2005) CrystEngComm 7:324
26. deGelder R (2008) IUCr Commission on Crystallographic Computing Newsletter N.7 (see at: http://www.iucr.org/resources/commission/crystallographic_computing/newsletters/7)
27. Volkov A, Koritsanszky TS, Coppens P (2004) Chem Phys Lett 391:170
28. Tsirelson VG, Shishkina AV, Stash AI, Parsons S (2009) Acta Cryst B65:647
29. Leconte C, Espinosa E (2009) Angew Chem Int Ed 48:3838
30. Destro R, Soave R, Barzaghi M (2008) J Phys Chem B112:5163
31. Dunitz JD, Gavezzotti A (2005) Angew Chem Int Ed 44:1766
32. Matta CF, Hernandez-Trujillo J, Tang TH, Bader RFW (2003) Chem Eur J 9:1940
33. Xue C, Popelier PLA (2009) J Phys Chem 113:3245
34. Pitonak M, Hesselmann A (2010) J Chem Theory Comput 6:168
35. Kannemann FO, Becke AD (2010) J Chem Theory Comput 6:1081
36. Goerigk L, Grimme S (2010) J Chem Theory Comput 6:107
37. Jurecka P, Sponer J, Cerny J, Hobza P (2006) Phys Chem Chem Phys 8:1985
38. Riley KE, Pitonak M, Cerny J, Hobza P (2010) J Chem Theory Comput 6:66
39. Volkov A, King HF, Coppens P (2006) J Chem Theory Comput 2:81
40. Ringer AL, Sherrill CD (2008) Chem Eur J 14:2542
41. Dunitz JD, Schweizer WB (2007) CrystEngComm 9:266
42. Dyakonenko V, Maleev AV, Zbruyev AI, Chebanov VA, Desenko SM, Shishkin OV (2010) CrystEngComm 12:1816
43. Dovesi R, Civalleri B, Orlando R, Roetti C, Saunders VR (2005) Ab initio quantum simulation in solid state chemistry. In: Lipkowitz KB, Larter R, Cundari TR (eds) Reviews in computational chemistry, vol 21, chap 1. Wiley-VCH, Weinheim
44. Dalhus B, Görbitz CH (2004) J Mol Struct 675:47
45. Zhao Y, Truhlar DG (2005) J Chem Theory Comput 1:415
46. Civalleri B, Zicovich-Wilson CM, Valenzano L, Ugliengo P (2008) CrystEngComm 10:405
47. van de Streek J, Neumann MA (2010) Acta Cryst B66:544
48. Quiñonero D, Frontera A, Deyà PM (2008) ChemPhysChem 9:397
49. Stone AJ (1996) The theory of intermolecular forces. Clarendon, Oxford, Chapter 7
50. Podeszwa R, Szalewicz K (2005) Chem Phys Lett 412:488
51. Gavezzotti A (2008) Mol Phys 106:1473
52. Maschio L, Civalleri B, Ugliengo P, Gavezzotti A (2011) Manuscript in preparation
53. Sherrill CD, Sumpter BG, Sinnokrot MO, Marshall MS, Hohenstein EG, Walker RC, Gould IR (2009) J Comp Chem 30:2187
54. Gavezzotti A (2010) Acta Cryst B66:396
55. Lommerse JPM, Motherwell WDS, Ammon HL, Dunitz JD, Gavezzotti A, Hofmann DWM, Leusen FJJ, Mooij WTM, Price SL, Schweizer B, Schmidt MU, van Eijck BP, Verwer P, Williams DE (2000) Acta Cryst B56:697
56. Neumann MA, Leusen FJJ, Kendrick J (2008) Angew Chem Int Ed 47:2427
57. van Gunsteren WF, Berendsen HJC (1990) Angew Chem Int Ed 29:992
58. Brukhno AV, Anwar J, Davidchack R, Handel R (2008) J Phys Condens Matter 20:494243
59. Gavezzotti A (1999) Chem Eur J 5:567
60. Erdemir D, Lee AY, Myerson AS (2009) Acc Chem Res 42:621
61. Anwar J, Tuble SC, Kendrick J (2006) J Am Chem Soc 129:2542
62. Gavezzotti A (2011) CrystEngComm Advance Article DOI 10.1039/c1ce05106g
63. Gavezzotti A (2011) New J Chem Advance Article DOI 10.1039/c0nj00982b
64. Nemkevich A, Bürgi HB, Spackman MA, Corry B (2010) Phys Chem Chem Phys 12:14916

Top Curr Chem (2012) 315: 33–68
DOI: 10.1007/128_2011_207

Published online: 17 September 2011

Cryo-Crystallography: Diffraction at Low Temperature and More

Piero Macchi

Abstract This chapter comments on the motivations and the methods of crystallographic studies at low temperature. Cry-crystallography is a brunch of Crystallography, a science that is too often confused with a technique. On the other hand, the scientific background to study crystal phases at low temperature is here provided, together with a survey of many possible techniques that provide complementary or supplementary information. Several applications are discussed, in particular in relation with highly accurate studies like electron density determination or phase transition mechanisms.

Keywords Electron density · Low temperature · Phase transitions · X-ray diffraction

Contents

P. Macchi
Department of Chemistry and Biochemistry, University of Bern, Freistrasse 3, CH-3012, Bern, Switzerland
e-mail: piero.macchi@dcb.unibe.ch

1 What Is "Cryo-Crystallography"?

Low temperature crystallography is a discipline deeply entangled with the techniques of X-ray diffraction on cooled samples and very often *cryo-crystallography* and *low temperature diffraction* are used as synonymous. This reflects a more general problem of crystallography, a *science* often considered just at the level of a *technique*, a confusion that hopefully this book will contribute to remove.

Cryo-crystallography is much more than a technique, although it relies on sophisticated instrumentation and practices. Studying crystals at variable temperature opens new frontiers to the chemistry and physics of a substance in its solid state, crystal form. This extended knowledge can be used to obtain a more comprehensive picture of the phase diagram of a compound or more precise information on some properties of a material and an even more detailed image of a crystal structure down to subatomic level. Molecular chemists mainly appreciate the possibility to obtain more precise structures (which often just means easier to publish), whereas solid state chemists or physicists should be attracted by the additional opportunities offered by crystallographic investigations in a wider temperature range, as outlined above.

Cryo-crystallography clearly involves the study of materials at low temperature; however in general there is no obvious discontinuity between lowering and raising the temperature from ambient conditions, because much information becomes available after applying temperature gradients, no matter which sign. In some other cases, *low* temperature means making the image of a crystal structure more clear by reducing the thermal motion of atoms and molecules and therefore improving the Bragg diffraction from the crystal. However, *low* is ambiguous and it is definitely "material dependent," as we will see below. Another important point to clarify is that diffraction is not the only technique that could shed light on the behavior of a crystalline material as a function of the temperature. Other investigations could give complementary information, perhaps on a different size or time scale than diffraction.

In this chapter the author will focus on the theoretical aspects of crystals at low temperature, on the techniques to cool crystals, and on some illustrative examples of cryo-crystallographic studies.

2 Why Cryo-Crystallography? What Happens to Crystals at Low Temperature?

In a seminal review article, Larsen [1] described the state-of-the-art of the cryogenic techniques most commonly adopted for X-ray diffraction and lucidly showed the applications to all kind of crystallographic studies, stimulated by a variety of research interests. Already at that time, the availability of liquid nitrogen cryostats in many laboratories was highlighted, emphasizing the possibility to carry out many

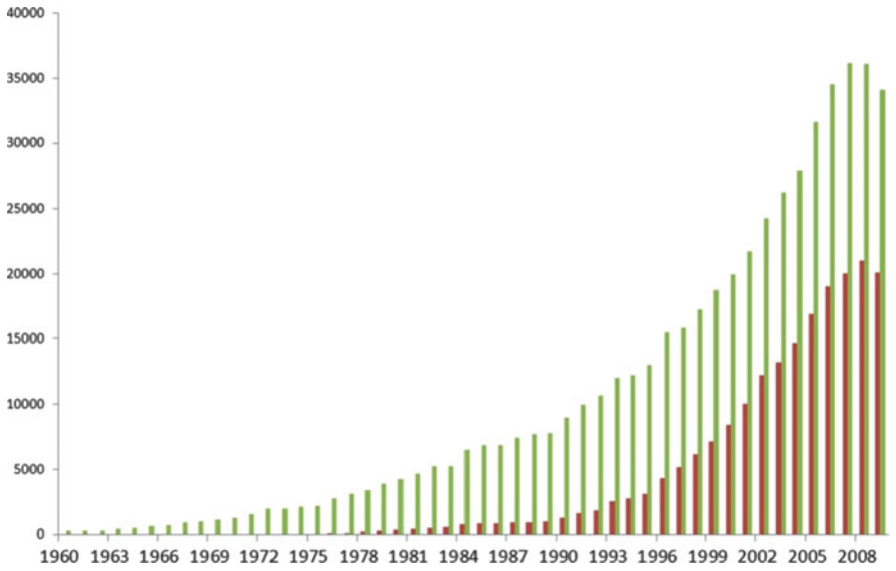

Fig. 1 The total number of crystal structures published since 1960 (*green bars*) and the number of those collected at temperature below 273 K (*red bars*). Data taken from the Cambridge Structural Database [2, 3] (the last bar is year 2009, but it is not complete)

experiments on single crystals or polycrystalline powders at low temperature, at variance from the past. This is of course even truer nowadays: a simple inspection of the database containing all the characterized organic/organometallic crystal structures [2, 3] shows how the percentage of experiments carried out below ambient temperature has increased over the years (Fig. 1) and it is now well above 50%, compared to 2% in 1960 and 15% in 1990. On the other hand, it is surprising that data collections below 80 K (that require more sophisticate and expensive techniques) are just 0.2% of the total number of experiments, with a decreasing trend. This tells us that many studies on crystals at low temperature are carried out just because easy and economic equipment is available in a laboratory, but without a genuine scientific interest in cryo-crystallographic studies. Were the scientific interests more pronounced, we would have witnessed a growth of experiments at very low temperature as well.

The change of the usual conditions for X-ray diffraction experiments may affect the interpretation of some results, especially by scientists outside crystallography. In fact, while one should appreciate the increased precision and accuracy of structures determined at low temperature, a drawback is that earlier benchmarks could be altered by sudden or progressive changes of experimental procedures. For example, theoretical chemists often use crystallographic tables reporting bonding distances or angles to test the quality of theoretical methods adopted for ab initio calculations. Most of those entries are given without any correction for thermal libration (see below), which means that they are significantly affected by atomic thermal motion (producing

inaccurate distances). As a consequence, the benchmark for theoreticians has changed somewhat, hopefully in the direction of higher accuracy, but earlier conclusions should be reconsidered, being based on different and less accurate observations. A side problem of low temperature "routine" crystal structure determination is that there is not a standard low temperature and experiments are carried out over a large range (90–173 K or even higher temperature) although using the same kind of liquid nitrogen devices. Structural correlation analysis [4] may also be significantly affected by the different temperatures of data collections because fragments retrieved from structures under largely different librational conditions certainly introduce systematic differences in the statistical analyses.

In his review, Larsen [1] focused on X-ray diffraction data at low temperature, mainly from a single crystal, and he outlined the following major advantages: (1) reducing the radiation damage; (2) improving the resolution; (3) decreasing systematic effects of the thermal motion. The fields of application were wide and basically covered all spectrums of crystallographic studies with X-ray diffraction: (1) structure determination of proteins; (2) structure determination of unstable small molecules; (3) phase transitions; (4) accurate electron density mapping.

Fifteen years later these fields are still central in crystallography and sample cooling is of equal importance for data quality. More applications can be envisaged and the great advantages offered by rapid data acquisitions may stimulate new and more sophisticated studies. However, data are often collected at low temperature without a clear scientific purpose, which is due to the insane attitude of contemporary scientists to use all possible guns in their hands to shoot the little mouse of a research target in order to impress reviewers and editors of a journal or panels of funding agencies. In this sense, the automatic checkup of crystal structure qualities provided by some software and recommended or even requested by many journals is one of the main causes, because high standards are suggested even when not requested. Data collections at room temperature are often adequate enough and efficiently provide the (little) information which is requested, like the structure of a molecule and its packing in the solid state.[1] A cryo-crystallographic study is necessary when the objective of a research study is more challenging and really requires exhaustive analyses of the physical-chemical behavior of a given crystal species.

In the following we will mainly analyze the thermodynamics of a perfect crystal at low temperature and the physics of diffraction at low temperature, in order to understand better the expectations from a cryo-crystallographic study, eventually discussed in Sect. 4.

[1] Sometimes an X-ray diffraction experiment is carried out only with the purpose of ascertaining the chemical composition of a given solid.

2.1 Crystals at Low Temperature

The definition of *crystal* is itself a developing concept, as demonstrated by the ongoing discussions [5, 6]. Most of the theoretical background proposed in this chapter is valid for a *perfect crystal*, i.e., an infinite mathematical object with an idealized crystal structure (*ideal crystal*) in thermodynamic equilibrium at a given pressure P and temperature T. In textbooks, only the gas phase thermodynamics is usually discussed in detail, whereas little attention is paid to the solid state. A full thermodynamic treatment of solids is beyond the scope of this chapter and the reader is referred to specific books on the subject, for example [7].

In chapter by Gavezzotti, the theoretical approaches to crystallography have been discussed and the reader has learnt methods to compute the potential energy of *ideal crystals* at various levels of approximation, with the purpose of estimating lattice energies [113]. It is important to stress that the crystal potential contains information on the nature of bonding in the molecular species and the type of intermolecular interactions, but calculations are typically carried out assuming no thermal energy, therefore in the hypothetical conditions of $T = 0$ K and neglecting the zero point motion. This means that lattice dynamics (hence entropic terms) are not explicitly considered. While this could be sufficient when searching the optimal structure of a molecular crystal or grossly estimating the relative stability of different polymorphs, from the experimental point of view one should not forget what are the consequences of dynamics and the effect of temperature. Einstein [8] first and Debye [9] later proposed approximated models to compute the free energy F of *perfect crystals* formed by N atoms, assumed to be harmonic oscillators:

$$F = \Phi_0 + E_{\text{vib}}(T) + TS(T), \tag{1}$$

where Φ_0 is the crystal potential (for example, computed as described in [113]), E_{vib} is the energy of the harmonic oscillators, and $S(T)$ is their entropic contribution. In Einstein approximation the oscillators are independent and no energy dispersion calculation is necessary. Debye's model, instead, assumes the crystal to be an isotropic elastic medium.

We will not discuss the theories of lattice dynamics [10] in detail, but we will just recall that atomic motion in crystals leads to characteristic equations that relate the frequencies ωs of waves traveling in the solid with vectors of correlated mass-weighted atomic displacements. Solutions to these Newton type equations give the three N dispersion relations for phonons, typically divided into 3 *acoustic* branches and 3N−3 *optic* branches (where N is the total number of atoms). Each dispersion relation describes an individual phonon along a given direction in wave vectors space. The three *acoustic* branches are associated with translations of the entire structure for a traveling wave of infinite wavelength; otherwise, they propagate in the crystal like acoustic waves. The *optic* modes are responsible for the atomic displacements about equilibrium positions, which are typically represented by a tensor **U** (with components $U_{ij} = \langle \Delta x_i \Delta x_j \rangle$) in relation to the unit cell

translational vectors. The **U** tensor affects the so-called Debye Waller factor $T(\mathbf{S})$, which is a kind of "damping factor" for the radiation scattered by an atom, as will be discussed in Sect. 2.2:

$$T(\mathbf{S}) = \exp\left(\frac{-8\pi^2\langle u_T^2\rangle \sin^2\vartheta}{\lambda^2}\right). \tag{2}$$

S is the scattering vector, u_T is the atomic displacement parameter in this simplified notation assumed to be isotropic, θ is the scattering angle, and λ the wavelength of the incident radiation. The atomic displacement depends on the temperature, and hence so does the Debye–Waller factor. If an atom is modeled by a classical oscillator, then the atomic displacement would change linearly with temperature:

$$\langle u_T\rangle = \frac{k_B T}{\bar{\omega}^2 m}. \tag{3}$$

m is the atomic reduced mass and k_B is the Boltzmann constant. However, in a quantum mechanical system, at low temperature the oscillator is temperature independent:

$$\langle u_T\rangle = \frac{\hbar}{2\bar{\omega}m}. \tag{4}$$

The typical behavior of an atomic displacement parameter is represented by the curve plotted in Fig. 2. This trend tells us that below the turn point ($\Theta_E/2$) atomic vibrations are not only smaller but also quite constant.

The important message from Einstein or Debye models is that vibrations of atoms in a crystal contribute to Entropy S and to Heat Capacity C; therefore they affect the thermodynamic equilibrium of a crystal by modifying both the Free energy F, which

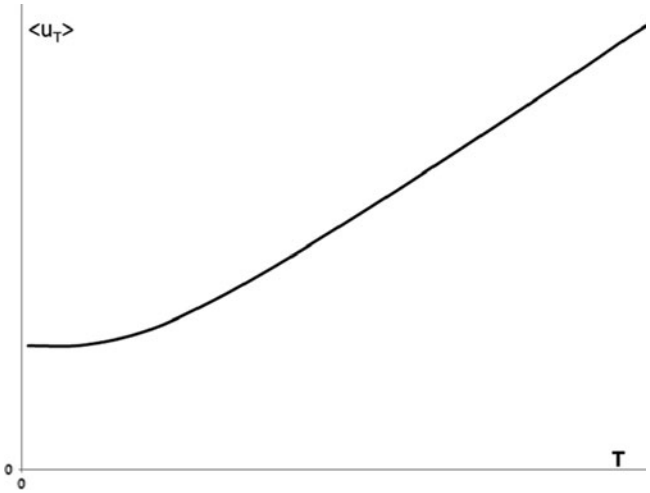

Fig. 2 The mean square displacement of a single harmonic oscillator as a function of temperature. Units are arbitrary because $\langle u_T\rangle$ and T values depend on the frequency of the oscillator and the mass of the particle. The plot shows that at low temperature the displacement is almost constant, whereas at high temperature it varies linearly with T. The change of regime occurs approximately at $\Theta_E/2$

determines the actual stability of a solid state phase at a given pressure, and temperature.

The *optic* modes can be further "decomposed" into *internal* and *external* when a molecular crystal is considered. Internal modes are associated with much higher energy (> 300 cm^{-1}), due to the intra-molecular chemical bonding beside some functional groups in a molecule which could be associated with large and independent librations (for example CX_3 groups, where X = H, Halogen, CH_3, etc.). External modes are instead associated with inter-molecular interactions and they are of much lower energy (< 300 cm^{-1}) and are therefore active even at low temperature. The atomic displacement of a molecular crystal, especially at low temperature, is mainly due to the external modes. This is well illustrated by comparing experimentally observed C_p and C_v of the crystal form of benzene against the calculated C_v from experimentally measured **u**s, after separating *internal* and *external* modes [11]. This calculation is possible assuming Debye and Einstein models for independent oscillators and gives the interesting result displayed in Fig. 3: up to $T = 100$ K the deviation is sufficiently small to conclude

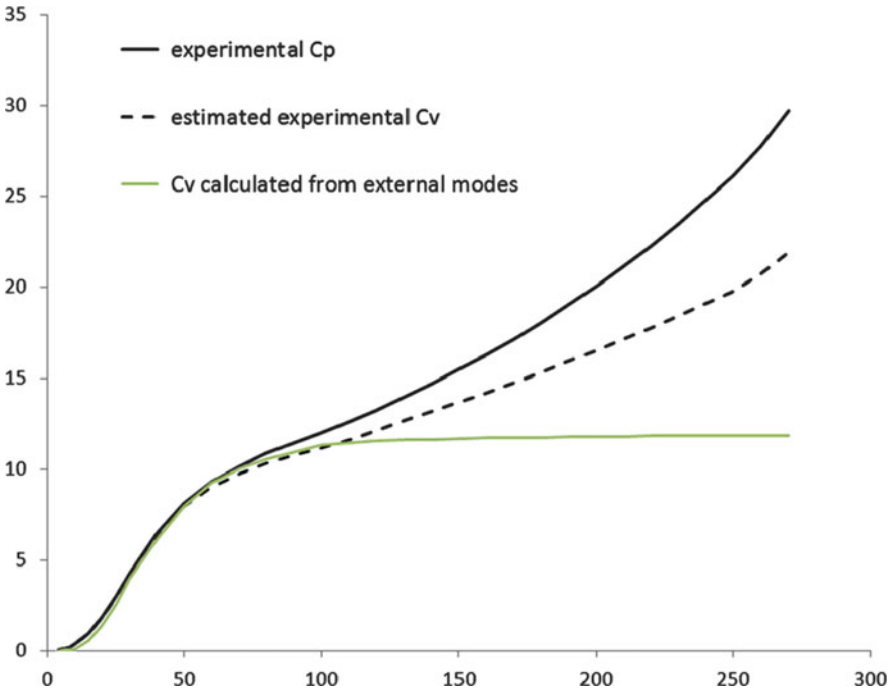

Fig. 3 Experimental heat capacities of benzene [11], C_v is obtained from observed C_p after subtracting the expansion work, computed using the experimentally determined bulk modulus. The C_v estimated from molecular translational and librational lattice modes (obtained from neutron diffraction ADP's) is also plotted. Note that these *external* modes well reproduce the observed C_v up to ca. 100 K. Above this temperature the *internal* modes are active and C_v exceeds the classical limit of 3 $k_B T$

that only *external* modes affect the heat capacity, but above that temperature this approximation does not hold any longer.

Because of the important distinction between internal and external modes, Bürgi proposed [12] for molecular crystals the so-called *molecular mean field model*, where each molecule is considered as a collection of independent oscillators in the average potential produced by other molecules in the crystal. The hypothesis that internal modes are less active than external ones leads to the *rigid body model*, where the atomic displacement parameters are assumed to be caused just by pure libration, pure translation, and coupled translation–libration of an isolated, rigid molecule [13]. In this respect, Hirshfeld [14] proposed a criterion to assess that atomic displacement tensors are meaningful when refined from X-ray or neutron diffraction data: two atoms covalently bonded to each other should have equal displacement along the bond direction within a given tolerance (that includes the effects of bending modes). This criterion is still applied when testing the quality of a structure determination and refinement for a molecular crystal, although weaker chemical bonds and unbalanced atomic masses in a bond produce breakdown of the Hirshfeld criterion, without implying incorrect structural refinement. This is, for example, the case in most of metal–ligand bonds of an organometallic molecule [15, 16].

So far, the models presented have assumed harmonic oscillators; however atoms in real crystals move in a substantially anharmonic potential. This has a number of implications for the properties of a material and a number of complications for the modeling, as the description of atomic displacement parameters becomes much more difficult [17, 18]. One of the first consequences of anharmonicity is the thermal expansion/contraction of the crystal lattice. In fact, a crystal composed of atoms moving in a purely harmonic potential would not expand or contract due to increased or decreased vibrations. In a harmonic potential, the force necessary to compress the crystal are equal in modulus to that necessary to expand it. However, the crystal potential is quite poorly harmonic, given that compression of atoms at distances smaller than their equilibrium position is energetically more expensive than expansion. The potential of a chemical bond has harmonic behavior only at the bottom of the energy potential well. Thus, anharmonic behavior is expected for all perfect crystals, but the nature of the species may play an important role. For example, covalent solids display harmonic behavior up to temperatures much higher than organic molecular crystals. In fact, weaker intermolecular interactions are associated with very flat and poorly harmonic potentials. Deviations from harmonicity are summarized by the Grüneisen parameter γ [19] through which one can explain the zero pressure equation of state of a material:

$$\gamma = \frac{V\beta}{k_T C_V} = \frac{V\beta}{k_S C_P} = \left(\frac{-d\ln\Theta_{E,D}}{d\ln V}\right). \tag{5}$$

Here V is the crystal volume, k_T and k_S are the isothermal and adiabatic *compressibility* (i.e., the contraction under pressure), β is the *expansivity* (expansion/contraction with temperature), C_p and C_v are heat capacities, and $\Theta_{E,D}$ are the Einstein or Debye Temperatures. Because β is only weakly temperature dependent,

from (5) one learns that the Grünesein parameter depends on the temperature, similar to heat capacity. Softer materials have larger γ and lower Debye Temperatures (Θ_D). For $T << \Theta_D$, heat capacity of dielectric materials increases with $(T/\Theta_D)^3$, whereas for $T >> \Theta_D$ the heat capacity becomes constant and larger (proportional to the number of oscillators; see also Fig. 3). As a consequence, in the "T^3 regime," the expansion of a crystal is much smaller. In addition, many lattice modes are not yet activated; thus atomic displacements are smaller and closer to their zero point limits. The reader will immediately appreciate that these two features play important roles for the study of crystals as they affect properties of the material (first of all the diffraction itself). Note that for metals, instead, the T^3 regime is only approximated because the electronic contribution to heat capacity ($\div T$) is not considered in the Debye (or Einstein) model.

The free energy of a phase is extremely important to explain phenomena like *phase transitions*, i.e., transformations of one solid state phase into another. Phase transitions are quite connected with *polymorphism*, i.e., the observation of two or more solid state phases of the same substance. On some occasions, in fact, kinetic effects allow observation of more than one polymorph at the same temperature and pressure conditions. Of course only one is thermodynamically stable, but transformation might be indefinitely slow, the most obvious example being transformation of diamond to graphite at ambient conditions. Along a given temperature range, it is possible that one solid state structure transforms into another at a given *critical* temperature (T_c). The same is true for pressure scans, of course (as will be discussed in [114]). Occurrence of a phase transition indicates that the free energy associated with a given structure has become lower than the other. In crystallography, there are a number of classifications of phase transitions that are sometimes dedicated to specific materials and are difficult to generalize. A unified description is not available, although a recent review article by Herbstein [20] has tried to rationalize different point of views and descriptors.

While cooling or warming crystals, phase transitions are not uncommon, but they are often overlooked. Many experiments can be useful to characterize a phase transition, as we will see in Sects 3 and 4. Diffraction, microscopy, spectroscopy, and calorimetry can all provide information on the structure, the energy, or the properties of a crystal. Their sudden change is the most obvious effect of a phase transformation and a matter of interesting study for scientists.

2.2 Low Temperature and X-Ray Diffraction from Ideal Crystals

The X-ray intensity diffracted from a single crystal and measured at the detector can be approximated as [21]

$$I_{\text{meas}}(\mathbf{S}_i) \approx I_0 v Q(\mathbf{S}_i) y \mathrm{A}(1+\alpha) + \sum_{m \neq i} p_m I_0 v Q(\mathbf{S}_m) + B, \tag{6}$$

where A is the transmission coefficient, y is the extinction coefficient [22], α is the correction for thermal diffuse scattering (TDS) [23], v is the sample volume, $\boldsymbol{B}$ is the *background*, and $p_m Q(\mathbf{S_m})$ is the contribution to the wave scattered along the direction $\mathbf{S_i}$ from all other vectors $\mathbf{S_m}$ through the so-called multiple scattering. The integrated reflectivity $Q(\mathbf{S})$ per volume of the crystal is

$$Q(\mathbf{S}_i) = \frac{a^2\lambda^3}{V^2}\frac{P}{\sin 2\theta}\left|F_{\text{Bragg}}(\mathbf{S}_i)\right|^2. \tag{7}$$

$a = e^2/mc^2$, λ is the wavelength, V is the cell volume, P is the polarization factor, and $\boldsymbol{F}$ is the structure factor. After applying several corrections, it is then possible to obtain the Bragg intensity.

The structure factor is the Fourier transform of the thermally averaged electron density:

$$F(\mathbf{S}_i) = \int_V \langle\rho(\mathbf{r})\rangle e^{2\pi i \mathbf{S}_i \mathbf{r}} \mathrm{d}\mathbf{r}. \tag{8}$$

Within an atomistic approximation, the structure factor can be expressed in terms of the atomic form factors, mean positions and mean-square displacements:

$$F(\mathbf{S}_i) = \sum_a f_a(\mathbf{S}) \exp(2\pi i \mathbf{S}_i \cdot \mathbf{r}_a) T_a(\mathbf{S}_i). \tag{9}$$

$T(\mathbf{S})$ is the Debye–Waller factor introduced in (2). The atomic form factors are typically calculated from the spherically averaged electron density of an atom in isolation [24], and therefore they do not contain any information on the polarization induced by the chemical bonding or by the interaction with electric field generated by other atoms or molecules in the crystal. This approximation is usually employed for routine crystal structure solutions and refinements, where the only variables of a least square refinement are the positions of the atoms and the parameters describing the atomic displacements. For more accurate studies, intended to determine with precision the electron density distribution, this procedure is not sufficient and the atomic form factors must be modeled more accurately, including angular and radial flexibility (Sect. 4.2).

As outlined above (6), there are many factors that affect the measured intensities, and therefore in a typical X-ray diffraction experiment there are many sources of systematic errors. The accuracy of the parameters obtained by X-ray crystal structure analysis depends on the measuring procedure, the strategy of the data-collection, the treatment of measured intensities to extract Bragg structure factors, the quality of the crystal sample, and its handling. It is important to recognize that cooling the sample cannot solve all inherent defects of a diffraction experiment, although it is true that it could enormously improve the quality of the data. First and most important, lower temperature reduces the atomic displacements, and consequently produces more Bragg scattering. Moreover, radiation damage of the crystals and dynamical disorder (if present) may be significantly reduced. Therefore, it is typical to read that *low temperature* improves the quality of the data, but the meaning of *low* depends on the material under study. One could use the Debye temperature as a kind of benchmark.

Table 1 Debye temperatures for some elemental solids and simple compounds. Data are obtained from thermal measurements at low temperature [25]

Solid	Θ_D (K)
Na	158
Si	640
Al	428
P	105
Ar	93
K	91
Fe	457
Cu	343
Cs	38
C (diamond)	2,230
KCl	235
NaCl	321
H_2O	218[a]
LiF	732

[a]From [26]

Crystals held together by strong forces between atoms and molecules will certainly have higher phonon frequencies (especially of external modes), and therefore higher Θ_D. In Table 1, we can see some known Debye temperatures obtained from experimental heat capacities measurement for some elements or simple compounds. We clearly see that Debye temperature can be quite low (such as for crystals of noble gases and alkali metals) or relatively higher (such as for transition metals and ionic solids). Very few data are available for most molecular crystals. The practical meaning of recommending $T < \Theta_D$ is that only translational and librational modes of an ideally rigid molecule in the crystal are actually activated. If the temperature is significantly lower than Θ_D ($T \sim 0.1\ \Theta_D$) then the Debye T^3 regime is valid. For most molecular crystals, in neutral electrostatic conditions and in the absence of strong intermolecular interactions like hydrogen bonding, the temperature should be well below 100 K. In reality it is enough to de-activate substantially the optic modes in order to maximize the benefits of low temperature as we will see in the following.

2.2.1 Resolution

As we saw in (9), the structure factors are affected by the temperature through the so-called Debye Waller factor $T(\mathbf{S})$. As temperature decreases, the diffracted intensity increases because $T(\mathbf{S})$ grows, especially for large diffraction angles. For a molecular crystal of an organic compound, the isotropic atomic displacement parameter can be reduced by a factor of 2–3 from room temperature down to 100 K (for example from 0.05 to 0.02 $Å^2$), corresponding to ca. 100 times larger intensity for a reflection at 0.5 Å resolution. The ratio could be even higher if the temperature is further reduced to 10 K, taking advantage of even smaller displacement parameters. A reflection at high diffraction angle is typically very weak because only core electrons contribute to the structure factor and, as discussed, Debye

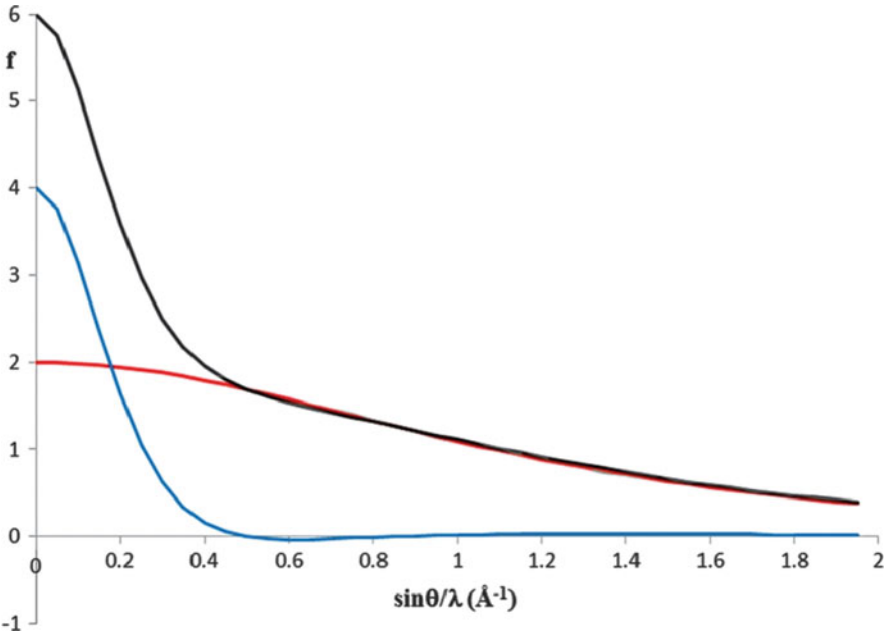

Fig. 4 The atomic form factor of a C atom (in $1s^2 2s^2 2p^2$ electronic configuration). Core electron scattering is in *blue*, Valence electron scattering is in *red* and total scattering in *black*

Waller factor implies a larger penalty to high scattering angles. Therefore, reducing the damping produced by $T(\mathbf{S})$ could bring the intensity of a high resolution reflection from hardly observable (at ambient temperature) to significant (at low temperature). For reflections at lower resolution the gain is smaller, but also less important because these reflections are inherently more intense (given the atomic form factors; see Fig. 4). It should be noted that for ionic crystals and minerals, the atomic displacements are already quite small at room temperature, and therefore the low temperature gain is not so large.

An additional advantage of the very low temperature is the smaller dependence of $\langle u^2 \rangle$ on the temperature. Thus, fluctuations of the temperature during an experiment are less troublesome. It should be taken into account that experiments without temperature control might easily experience ± 5 °C fluctuations (night/day variation, heating caused by other machines, etc.). This produces a fluctuation of 1–2% of the intensity for a reflection at 1.0 Å resolution and up to 10% for a reflection at 0.5 Å resolution (assuming it is measurable).

2.2.2 Thermal Diffuse Scattering

As seen in (6), the integrated intensities contain a contribution from Bragg diffraction as well as from diffuse scattering and background. TDS is caused by energy

exchange between the scattered radiation and the low-frequency lattice vibrational modes. The inelastic TDS has an opposite trend with respect to elastic scattering, which decreases as a function of θ. A proper estimation and correction of TDS is difficult and approximated algorithms are used in data correction procedures to extract pure Bragg intensities. The TDS depending on optic modes is typically included in the background, being substantially constant across the diffraction peak. The contribution from acoustic modes, instead, should be corrected separately with first- and second-order contributions [23] depending on the diffraction angle θ, the wavelength λ, the temperature, and the elastic constant of the crystal. Modes with frequency larger than 100 cm^{-1} are practically in the ground state at $T \approx 100$ K [27]; however, in molecular crystals librational modes may have smaller frequencies, suggesting that lower temperatures are necessary. TDS may significantly affect the correct estimation of atomic displacement parameters. At $T \approx 10$ K, instead, TDS is practically negligible up to the resolution normally obtained in an X-ray diffraction experiment.

2.2.3 Anharmonicity

The harmonic approximation assumes that forces between pairs of atoms are linearly proportional to their displacements. However, the potential is typically not harmonic and the **u** tensor should be replaced by a cumulant expression [17, 18], which significantly increases the number of parameters and may introduce additional correlation in a least squares refinement. At low temperature, anharmonic effects are typically negligible. Anyway, a good test to detect anharmonic motion is to check the thermal *expansivity* of the crystal by measuring accurate unit cell parameters at various temperatures. As outlined in Sect. 2.1, the equation of state is predicted from the Grüneisen parameter γ which basically accounts for the deviations of the atomic oscillators from the equilibrium positions expected from pure harmonic motion. Macchi and Sironi [28] for example showed the close relationship between anharmonic motion of some atoms and total strain of an organometallic molecular crystal. It is interesting that those atoms significantly modify their equilibrium position as a function of temperature (another indication of large anharmonicity).

A separate discussion of hydrogen atoms is merited, especially when involved in hydrogen bridges. The potential experienced by an H atom is highly anharmonic, especially when the hydrogen bonding is stronger. For this reason the atomic thermal parameters are usually very difficult to refine even from neutron diffraction experiments (the hydrogen scattering of X-rays being quite scarce). In general one can consider the thermal parameters of hydrogen as highly approximated anyway. Some procedures are known to calculate hydrogen displacement parameters from refined thermal motion of other atoms in the molecule, under rigid body assumption and including known high frequency stretching of X–H bonds (from infra-red spectroscopy or theoretical calculations [29]) or otherwise estimated from neutron diffraction works [30].

2.2.4 Radiation Damage and Crystal Instability

It may be that an important source of systematic errors can be corrected by monitoring standard intensities at regular intervals during data collection. Chemical damage of organic materials by X-rays and other forms of ionizing radiation is classified as *primary* or *secondary*. Primary damage is caused by interaction between the radiation beam and electrons of the compounds and it mainly depends on the radiation dose [31]. On the other hand, secondary damage, caused by the reactions of the resulting radiolytic products is typically reduced at low temperature [32, 33], though not completely removed. Another source of instability is the loss of solvated molecules that might occur even at temperatures well below the boiling point of this solvent (thus at temperatures at which the vapor tension of the solvent as pure liquid would be very small). De-solvation often damages the crystal, creating extended defect or fractures that severely affect the sample quality. Of course, by lowering the temperature all these phenomena can be reduced or even completely avoided for the entire duration of an experiment. Cooling the sample may not be the only way to solve the problem; in fact coating the sample properly, such as with a poly-fluorinated oil, or enclosing it in a closed capillary, may also be adopted. These alternatives allow temperature dependent investigation of the sample (even above room temperature).

Protective oil is a good alternative to glue for crystal mounting because of the large residual stress that epoxies can cause. Sensitive species must be handled with special care, because exposure to oxidative atmosphere or anyway to ambient temperature may produce irreversible damage. For this reason, mounting the sample in an inert atmosphere within glove boxes is sometimes necessary. If the sample must be kept at low temperature while under the microscope, special equipment is necessary as proposed by Stalke [34] or by Hope [35].

3 Cryo-Crystallographic Techniques

There are several techniques to cool crystal sample in order to carry out crystallographic studies and they depend on: (1) which investigation is carried out; (2) what is the target temperature; (3) how rapid shall be the experiment; (4) the available budget. In the following we will analyze these methods.

3.1 Single Crystal Diffraction

The diffraction from single crystals is certainly one of the most accurate techniques to obtain detailed information on the disposition of atoms in a solid. The crystals typically are very small ($\sim 10^{-3}$ mm^3), and they are selected and mounted in air on very small supports like glass fibers (or other amorphous and low absorbing

materials), centered on the goniometer of a diffractometer, and then exposed to the X-rays. Therefore, cooling a single crystal means removing a very small amount of heat from a very small sample (rotated in many positions during the experiment). The air medium around the crystal is often a problem. The humidity of the air, in fact, is enough to cause icing, whatever the method adopted to cool the sample.

The rapidity of currently available diffractometers equipped with area detectors allows employing the so-called open flow systems, where a cryogenic fluid (He or N_2) is flushed onto the sample without recycling. It is clear that these methods could be very expensive; however, liquid N_2 is typically available at low cost in many laboratories. The most commonly adopted systems use liquid nitrogen both to obtain an N_2 gas flow and to cool it to a temperature around the boiling point of nitrogen (77 K) [36]. The temperature is then adjusted by electric warming of the gas flow (in principle even above room temperature, guaranteeing uninterrupted data collection over a very wide temperature range). Earlier systems regulated the gas stream temperature by adjusting the evaporation of liquid nitrogen, a procedure that however required large amount of N_2 (especially to reach lower temperatures).

In the last decade, open flow systems working with helium have been introduced, despite the much higher costs of liquid or gaseous He. In experiments carried out at Synchrotron work stations, the measurements are very rapid. This makes less prohibitive the costs of experiments carried out with open flow He cryostats. Modern equipment for X-ray diffraction in laboratories (using rotating anode generators, multilayer optics, and area detectors) also allows rapid data collection. Therefore, open flow He systems are not so uncommon in university laboratories. Helium gas flow systems work using evaporation of the cryogenic medium [37, 38], consumption of which is proportional to the required temperature. These systems offer all the advantages of open flow systems, namely optical access to the sample, rapid or even flash cooling, low background of the gas stream. However, they also have some inherent defects: large consumption of the cryogen (that makes them inadequate for very long measurements), the necessity to have a warm outer stream to avoid turbulence and ice formation. Some problems could be created by a thermocouple in the gas stream, used to measure the flow temperature, because it could induce turbulence and break the laminar flow, which is particularly fragile for a He stream.

A different solution is a He gas stream refrigerated through conduction by a two-stage closed-cycle cooler, which works with compression/expansion cycles of He gas. The advantage of the two-stage cooler is the higher temperature stability, but the disadvantage is the base temperature ($>$10 K) and the temperature loss to reach the sample (ca. 15 K). The smaller amount of cryogen used with this system makes consumption very low, but the escaping attitude of low density He requires an open cup at the end of the nozzle to bring the flow onto the sample. The cup could be produced by a very light material (like beryllium) which is quite transparent to the X-rays. Proper windows for incoming and outgoing primary beams will decrease the scattering and therefore the background. An outer warm and dry stream is necessary to prevent icing formation.

The two-stage (or even three-stage) closed cycle systems were actually invented to cool the crystals directly through conduction, keeping the samples in closed

devices (like Be cups), evacuated to prevent icing. These systems are still quite common in laboratories and especially in large scale facilities. They offer excellent accuracy, the possibility to reach very low temperature without trouble, virtually no consumption of cryogenic medium, and long term stability, but they have some disadvantages when compared to open flow systems: (1) direct optic access is not possible (unless using the system proposed by Samson et al. [39]); (2) scattering from the rather thick cups must be considered and eliminated [40]; (3) rapid quenching of the sample is not possible. The two-stage devices are however extremely recommended for long measurements.

Most of the devices presented in this discussion could be used in both X-ray or neutron diffraction experiments, though taking into account that neutron diffraction measurements are typically longer and carried out on larger samples.

As has become clear, all devices may introduce some kind of error during data collection. Therefore proper corrections should be applied when analyzing the data. In particular, absorption of cups surrounding the crystal should be taken into account. Extra scattering is also present, but this is usually eliminated with proper masks (physical or digital) to avoid detection of spurious intensities. The scattering by the gas stream is usually a minor problem that increases the background in the same way as a glass fiber support. This is typically well accounted for from background determination of the image integrating software. Formation of ice, instead, would create more serious problems due to the increased and structure background produced and the absorption of incoming and diffracted beams.

Although this chapter is dealing with cryo-crystallography, as anticipated above, many studies of crystals over a large temperature range would be useful, and then one could also consider techniques to heat crystals, which are quite developed in large scale facilities and also available on the laboratory scale. Liquid nitrogen gas flow instruments are also typically able to reach temperatures above ambient (up to 500 K) and therefore are quite adequate for the study of organic crystals, taking into account that only a few species would remain solid (and crystalline) above those limits. For refractory materials, instead, more sophisticated heating is necessary, able to reach $T = 1{,}500$ K or more, using flame-heated inert gas [41, 42], electrically heated gas streams [43], or radiative heat transfer [44].

3.2 Powder Diffraction

Many kinds of high and low temperature chambers are available for diffraction of polycrystalline materials. In general, the equipment is based on similar technology as for single crystal diffraction techniques, although a great advantage is given by the reduced (or even null) movements of the sample holder. Therefore, low temperatures can be obtained by conduction in a much simpler way, using radiation transparent windows in the chamber to reduce absorption and background [45, 46]. High frequency induction and high vacuum are necessary to reach safely very high temperatures (for example above 2,000 K [47]).

3.3 Other Techniques

As mentioned above, cryo-crystallography is not just diffraction at low temperature and many other investigations could be carried out to obtain precious information on the chemical physics of a crystal. For example, differential scanning calorimetry (DSC) indicates the occurrence and the nature of a transformation, like a solid–solid phase transition. DSC instruments are quite common in many chemistry laboratories and low temperature attachments are easily installed. They work with cold nitrogen streams or otherwise removing the heat from the sample through conduction. DSC detects the heat of a transition, i.e., generated by the discontinuity in the enthalpy at the critical temperature; see Fig. 5. Some phase transformations are not associated with detectable heat of transition, but they show instead a discontinuity in the specific heat C_p. Modulated temperature DSC is a more recent technique [48, 49] that allows separation of reversible and irreversible heat exchange during the process. This could be useful to recognize processes controlled by thermodynamic equilibrium or by kinetic effects and the occurrence of hysteresis during phase transformations.

Another very useful technique for cryo-crystallographic studies is optical microscopy, in particular under polarized light. Cooling stages can be easily

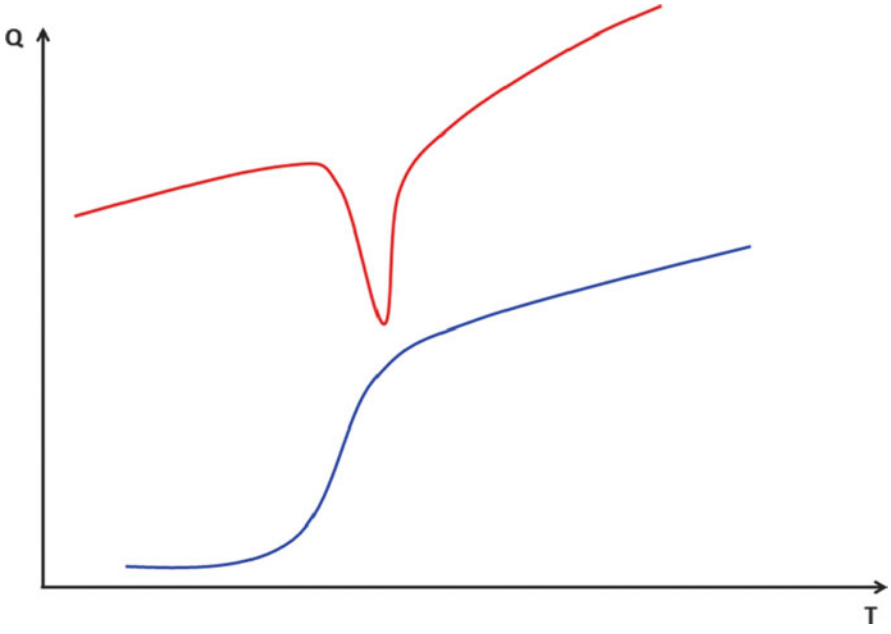

Fig. 5 The typical DSC diagram for solid state phase transition with latent heat (*red plot*) or without latent heat (*blue plot*). The scale is not the same; in general the curve for a second-order transition (*blue plot*) is associated with smaller changes of heat capacity (and therefore more difficult to detect)

attached on an optical microscope, allowing temperature ranges from 100 K up to very high temperatures. The hot/cold stage could be coupled with a calorimeter, allowing simultaneous heat capacity measurements. One very useful observation is the birefringence of the crystal that depends on the lattice symmetry and therefore can be sensitive to changes like structural phase transitions. The birefringence is easily observed using (partial) polarized light, cross polarizers, or otherwise a rotating polarizer (which gives the greatest amount of information) [50–53].

Computational chemistry is of course another technique to obtain theoretical information on *perfect crystals* at variable temperature. The background for this approach has been introduced in [113] and will not be further discussed here. It is important to stress that cryo-crystallography is not necessarily an experimental science, because predictions or explanations obtained from theoretical modeling are equally important in modern studies.

4 Cryo-Crystallographic Studies

Sometimes crystallographers consider that measuring a crystal at very low temperature is a kind of *panacea*, able to solve all defects of the sample, all kinds of experimental errors, and enhance the response indefinitely. Young students might be disappointed to learn that these miracles do not take place. A bad crystal sample remains as such even at 10 K, and sometimes it becomes even worse because the cooling process and the residual stress induced by a temperature gradient may produce further damage to the sample. Many other kinds of experimental problems and sources of error (for example absorption, extinctions, disorder, etc.) are not attenuated by the low temperature.

So, what can a scientist expect from a crystallographic study at low temperature? We give in the following a bunch of examples that cannot be fully comprehensive but should illustrate the potential of cryo-crystallography.

4.1 Crystal Structure Solution and Refinement

As anticipated, lower temperature increases the number of observations from an X-ray diffraction data collection (at constant radiation dose). This is however just one of the advantages that could improve a structure solution or a refinement. In fact, a reduced thermal motion usually implies a more reliable “standard” model, given that for smaller atomic displacements the harmonic approximation is more appropriate and less correlation is found between variables within a least squares refinement. This returns higher precision of the parameters calculated from those variables (for example bond distances, bond angles, etc.).

In X-ray diffraction experiments on small organic/organometallic molecules, it is less likely that low temperature will be really necessary to *solve* a crystal

structure, unless the species is unstable in air or under the X-rays. In this case, the low temperature could be one of the ways to reduce the damage (the easiest but not necessarily the best). Refinements of low temperature datasets are certainly easier because the increased resolution limit enables a larger observations/parameters ratio. However, if a crystal structure is severely affected by poor long range order (static disorder), a large part of the scattering which concentrates outside the Bragg position is often understood just as uninformative background noise. If diffuse scattering due to static disorder is large, any attempt to decrease the temperature with the purpose of obtaining more observable intensities would just be a desperate move and unlikely to succeed. On the contrary, one should provide thermal energy to increase long range order, for example through high temperature annealing.

The situation is different when the disorder is dynamical in nature, as it might occur when molecules have peripheral functional groups with enough flexibility to show large libration (in the gas phase and likely in the solid state as well). For example, substituted methyls are often associated with a relatively flat potential for rotation about the pseudo threefold axis. This implies very large displacements of the three carbon atoms. Sometime, the flat potential might display two or more minima and the dynamic disorder can somehow be "localized" with two or more competing conformations (see Fig. 6). By lowering the temperature the dynamic disorder can be significantly reduced or suppressed. In fact, one molecular conformation becomes favored over the other(s) either because the shape of the potential is itself modified or because the thermal energy is much reduced and less stable conformations become unavailable.

Other typical disorder conformations in the solid state are those of E-stilbenes or azobenzenes, where the two atoms of the central double bond are often involved in a complicated dynamic process (called *pedal motion*; see Fig. 6). Many crystallographic studies have been dedicated to analyze this kind of structural feature, including theoretical modeling of the dynamics; see, for example, Harada and Ogawa [54] and references therein. It is important to stress that this kind of dynamics severely affect the equilibrium positions of atoms refined from X-ray (or neutron) diffraction data, especially if the disorder cannot be satisfactorily modeled. As a consequence, geometrical parameters calculated from refined coordinates are typically quite incorrect (with severe underestimation of bond lengths). This is in general true when the thermal motion of a given molecule in a crystal is large. Therefore, a correction for libration, translation, and coupled translation/libration is necessary [13] to extract reliable bond distances from a set of refined coordinates. Unfortunately this correction is seldom applied and theoretical chemists often use uncorrected geometries as benchmark experimental results to test ab initio calculations.

For minerals and inorganic samples, low temperature is almost useless to improve structure solution and only marginally relevant to improve the refinement, unless dealing with host–guest materials like zeolites. In facts, for harder materials ambient temperature is already quite comparable and sometimes lower than the Debye temperature. Therefore, resolution is seldom a limitation for structure refinement of minerals at ambient temperature. On the contrary, for macromolecules and especially for proteins, the low temperature significantly increases the number of

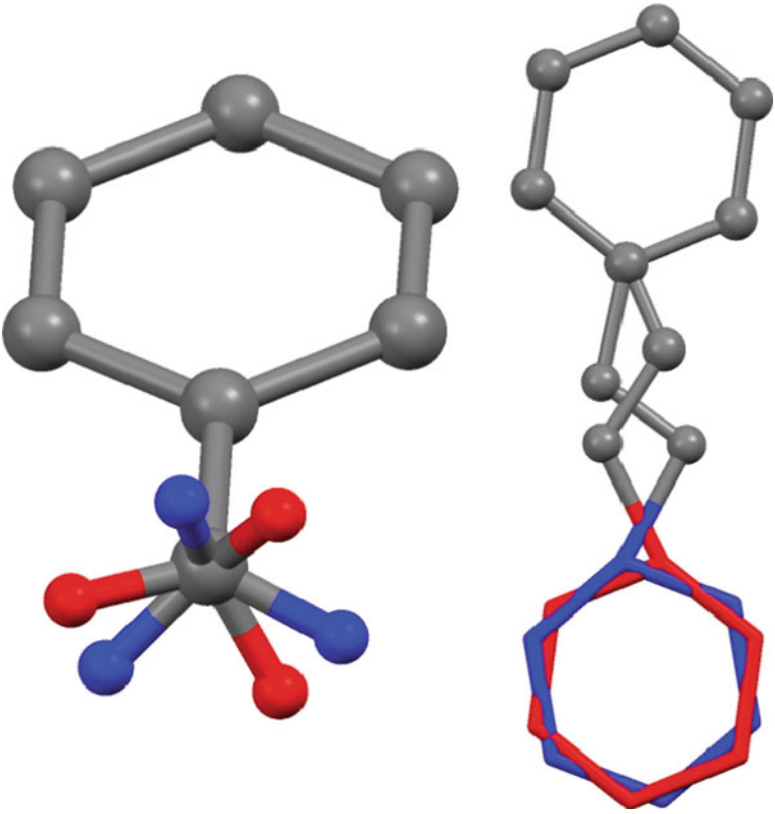

Fig. 6 The typical disorder of CX_3 peripheral groups about the pseudo threefold axis (*left*) and the typical pedal motion disorder about the central double bond in E-stilbene kind of molecules (*right*)

observations, especially because of the larger amplitudes of motions in these samples. In addition, proteins are often damaged by the incident radiation and cryo-protection is vital. As a consequence, the low temperature is a must for protein crystallographers [32], because it is relevant for the structure solution, not only for the refinement. However, cryo-crystallographic studies are not without disadvantages. For example, the crystal quality might be damaged by the cooling, in particular flash cooling. Moreover, some debate is open on the actual biological relevance of structures determined at 100 K, but intended to answer questions about phenomena occurring at 300 K [55].[2] In macromolecular crystallography, another debate is ongoing concerning the improvements when using helium as cryogenic agent [56] and therefore measuring the data at temperatures well below 80 K.

[2] More generally, one may ask whether a (macro)molecule frozen in the solid state can really be representative of the structure in solution, where the molecule is in fact active.

Interesting applications of low temperature single crystal diffraction have been presented in the field of metal organic frameworks (MOF) [57], porous materials based on metal *connectors* and organic *linkers*. Some large pore MOFs are able to host and exchange molecules like N_2, CO_2, noble gases, etc. The main problem is locating sites where the gas might be trapped, given the very weak interaction between the guest and the host framework. Therefore, diffraction on cooled species could reveal sites available to N_2 and Ar in channels of MOF-5, a structure with cubic array of $Zn_4O(CO_2)_6$ units connected by phenylene linkers [58].

Sometimes low temperature is claimed to be important to locate H atoms. This could be true in the case of organic species, where a reduced thermal motion of Hs may enhance electron density peaks in Fourier maps. These peaks compete against lone pair peaks of some atoms (especially O or N) and against peaks inside chemical bonds. At low temperature and using only low resolution data, the residuals due to lone pairs are smaller than residuals due to H atoms, yet missing in the structural model. In the case of organometallic molecules, expectations should instead be much lower, because the main source of residual peaks in a Fourier map are uncorrected absorption effects, which might overlap with potential sites for H atoms, especially those in the vicinity of a metal (like an agostic hydrogen, a hydride, etc.) [59].[3] Therefore, reducing the thermal motion of H may not be sufficient if careful absorption correction is not applied.

A problem affecting X-ray diffraction pattern of real crystals very close to ideality is *extinction* that is the manifest breakdown of the kinematic approximation. Within the mosaic crystals theory [60] we recognize a *primary extinction* (attenuation of the incident beam within a given crystal domain) and a *secondary extinction* (power loss due to the diffraction in the blocks traversed by the incident beam before it reaches the particular block under consideration). *Primary extinction* depends on the size of the domain and on the amplitude of the structure factors. The "critical thickness," beyond which extinction is negligible, inversely depends on λ. *Secondary extinction* depends on the degree of perfection of the crystal, hence on the misalignment of the domains (or mosaicity). The critical *mosaic spread*, above which the effect is negligible, depends on λ. Extinction may be severely anisotropic, especially if the crystal is under stress, which increases the mosaicity. As a matter of fact, an empirical way to decrease extinction is to stress the crystal by cooling and warming it, though the crystal may break during this procedure. For example, the mosaic spread of a crystal of KHC_2O_4 [61] studied at low temperature with three consecutive experiments was initially 3.3″ (first experiment with MoKα

[3] In [59] the authors reported the structure of a tri-osmium complex containing a hydride and clearly stated that a low temperature X-ray diffraction experiment would not be useful to locate the hydride if an accurate absorption correction is not carried out. Curiously, a few years before they had contacted Prof. A. Sironi and myself at the University of Milan proposing a low temperature data collection on that compound, with the purpose of locating the not so clearly visible hydride. As evident from [59], we were able to convince them on the real problems connected with the location of hydrogens close to heavy metals.

radiation at 125 K), 7.6″ (second experiment with AgKα radiation at 11 K), and 11.3″ (third experiment, AgKα at 11 K). The larger mosaicity implies that fewer reflections are significantly affected by extinction. As a matter of facts, an old technique used by macromolecular crystallographers was in fact shocking the crystal with rapid cooling in liquid nitrogen. The variation of extinction should be taken into account when repeating low temperature experiments on the same sample, sometimes producing scarce reproducibility of the data.

4.2 Accurate Electron Density

The possibility of probing the electronic structure of atoms by means of X-ray was recognized quite soon after the first diffraction experiments. In 1915, P. Debey wrote: "*It seems to me that experimental study of the scattered radiation, in particular from light atoms, should get more attention, since along this way it should be possible to determine the arrangement of the electrons in the atoms*" [62]. However, it was only in the mid-1960s that experimentally determined electron density maps could be obtained by combining X-ray and neutron diffraction techniques [63]. This breakthrough was certainly due to the improvements of the data measuring (using computer-controlled diffractometers and scintillator counters instead of photographic films), to the advent of neutron diffraction and the possibility to cool crystals, and to the significant improvement in data reduction and correction. Since then, methods of accurate determination of electron density have much improved together with models for mapping electron density from X-ray intensities [64]. We will now outline the advantages offered by low temperature measurements in this area, taking into account of course that for some materials cooling is absolutely mandatory, whereas for others it is not, although it could anyway be important to improve the quality of the data.

The mean thermal electron density in the unit cell can be computed by Fourier summation, over the reciprocal lattice vectors **S**, of the X-ray crystal structure factors:

$$\rho(\mathbf{r}) = 1/V \sum_{\mathbf{S}} \mathbf{F}(\mathbf{S}) \exp(-2\pi i \mathbf{S} \cdot \mathbf{r}_p). \tag{10}$$

Due to termination of the series, however, $\rho(\mathbf{r})$ is severely affected by ripples. In addition, especially in the case of non-centrosymmetric crystals, the phase of vector $\mathbf{F}(\mathbf{S})$ is not known with precision and this affects a correct reconstruction of the density. Therefore, Fourier summation cannot be used for precise and accurate mapping of electron density. On the other hand, a model is necessary to overcome these limitations and to produce a function that is sufficiently close to the real, quantum mechanical $\rho(\mathbf{r})$ in all regions of the crystal.

In the 1970s, among many other approaches, the method of multipolar expansion of atomic electron density was recognized as the most applicable and accurate.

Several formulations were proposed [65, 66], but the intuitive notation introduced by Hansen and Coppens [67] afterwards became the most popular. Within this method, the electron density of a crystal is expanded in atomic contributions. The expansion is better understood in terms of rigid *pseudoatoms*, i.e., atoms that behave structurally according to their electron charge distribution and rigidly follow the nuclear motion. A *pseudoatom* density is expanded according to its electronic structure, for simplicity reduced to the *core* and the *valence* electron densities (but in principle each atomic shell could be independently refined). Thus,

$$\rho(\mathbf{r}) = \sum_{\text{atoms}} \rho_i(\mathbf{r} - \mathbf{r}_i),$$

$$\rho_i(\mathbf{r}) = P_{i,\text{core}}\rho_{i,\text{core}}(\mathbf{r}) + P_{i,\text{valence}}\kappa_i^3\rho_{i,\text{valence}}(\kappa\mathbf{r}) + \sum_{l=0,l\,\text{max}}\left[\kappa_i'^3 R_l(\kappa'\mathbf{r})\sum_{m=0,l} P_{lm\pm}y_{lm\pm}(\mathbf{r}/r)\right] \tag{11}$$

The parameters $P_{lm\pm}$, P_{core}, and κ can be refined within a least square procedure, together with positional and thermal parameters of a normal refinement to obtain a crystal structure. In the Hansen and Coppens model, the valence shell is allowed to contract or expand and to assume an aspherical form [last term in (11)], as it is conceivable when the atomic density is deformed by the chemical bonding. This is possible by refining the κ and κ' radial scaling parameters and population coefficients $P_{lm\pm}$ of the multipolar expansion. Spherical harmonics functions $y_{lm\pm}$ are used to describe the deformation part. Several software packages [68–71] are available for multipolar refinement of the electron density and some of them [68, 70, 72] also compute properties from the refined multipolar coefficients.

As anticipated, the multipolar model is not the only technique available to refine electron density from a set of measured X-ray diffracted intensities. Alternative methods are possible, for example the direct refinement of reduced density matrix elements [73, 74] or even a wave function constrained to X-ray structure factor (XRCW) [75, 76]. Of course, in all these models an increasing amount of physical information is used from theoretical chemistry methods and of course one should carefully consider how "experimental" is the information obtained.

An X-ray atomic orbital (XAO) [77] method has also been adopted to refine electronic states directly. The method is applicable mainly to analyse the electron-density distribution in ionic solids of transition or rare earth metals, given that it is based on an atomic orbital assumption, neglecting molecular orbitals. The expansion coefficients of each atomic orbital are calculated with a perturbation theory and the coefficients of each orbital are refined to fit the observed structure factors keeping the orthonormal relationships among them. This model is somewhat similar to the valence orbital model (VOM), earlier introduced by Figgis et al. [78] to study transition metal complexes, within the Ligand field theory approach. The VOM could be applied in such complexes, within the assumption that the metal and the

ligands are linked by "low overlap" bonds between the atomic orbitals; therefore the electron density around metals or in the ligand shell can be treated as a perturbation of the atomic density. This assumption is also at heart for the determination of orbital coefficients from multipolar model as introduced by Coppens et al. [79].

All the above methods are somehow based on an orbital hypothesis. In fact, in the multipolar model, the core is typically frozen to the isolated atom orbital expansion, taken from Roothan Hartree Fock calculations (or similar [80]). Although the higher multipoles are not constrained to an orbital model, the radial functions are typically taken from best single ζ exponents used to describe the valence orbitals of a given atom [81]. Even tighter is the link to the orbital approach in XRCW, XAO, or VOM as described above. Obviously, an orbital assumption is not at all mandatory and other methods have been developed, for example those based on the Maximum Entropy Method (MEM) [82–86] where the constraints/restraints come from statistical considerations.

The role of low temperature in an experimental determination of electron density is multiple. The most important is certainly the reduction of thermal agitation of atoms, which makes the *pseudoatom* approach a more reliable approximation. As for normal structure refinements, smaller thermal motion means less correlation among parameters, hence higher reliability of the final model. Lower thermal motion also means that the harmonic approximation is more valid, as anticipated in Sect. 2.2. Although it is possible to go beyond the harmonic approximation, it should be considered that a model including, for example, a Grahm Charlier expansion [87] would be extremely costly because of the very large number of parameters. Mallinson et al. [88] could show that residuals due to anharmonic motion are somewhat similar to residuals of deformation density, especially when dealing with transition metals. This would of course create confusion between true electron density features and residuals due to atomic displacements exceeding the model, with obvious consequences for the interpretation of the results. It is important to warn that the physical significance of the refined Grahm Charlier parameters should be verified. In fact, it might easily occur that these coefficients are refined to nonsense values, implying, for example, negative nuclear probability at the equilibrium position (see the manual of the XD2006 package [68]).

Additional advantages of low temperature in electron density refinements are connected with the higher accuracy of the measured intensities, in particular at high resolution. It is important to stress that features of the bonding electron density are very likely not recorded at such resolution, which is typically dominated by core electron scattering (Fig. 4). However, the larger intensity at high angle can be very important to increase the precision of a refinement, including more reflections to refine atomic positions and thermal factors (apart for H atoms). As a matter of facts, a data/parameter ratio above 10 is often recommended; however in many cases the *effective* ratio is much smaller because variables introduced in (11) are mainly refined from low angle data [89]. Thus, if some parameters of a model (positions and thermal motion) could insist more on high angle observations, the correlation among variables would be significantly reduced.

Another reason why high angle reflections are better measured at low temperature is the decreased thermal diffuse scattering (see Sect. 2.2) which allows a more accurate integration of those intensities.

After listing all the benefits of low temperature on accurate electron density refinement, the reader might ask what temperature is really necessary. Of course, the lower the better; however some electron density studies at room temperature or even above have been reported. For example, Tanaka et al. have investigated electron density of lanthanide borides [90–92] at variable temperatures using XAO methods to determine the electronic configuration of the metal. Those studies addressed significant changes of the order and occupation of some electronic states (associated with 5d or 4f orbitals of Ce or Sm) as a function of temperature. Experiments of this kind are not so frequent and they would be quite impossible on molecular crystals. On the other hand, results of Tanaka et al. show that it would be interesting investigating temperature induced changes of electron density, even spanning the regime of high temperature.

We do not discuss here the very many applications of electron density studies which are summarized in many recent books on the subject [93–96].

4.3 Phase Transitions and Polymorphism

As introduced above, different forms of the same molecule can be observed in the solid state. The phenomenon is known as *polymorphism*, i.e., the concurrent presence of more crystal forms, only one of which is thermodynamically stable at a given pressure and temperature. However, more polymorphs can be observed simultaneously when kinetic conditions allow formation of metastable phases together with (or even in the absence of) the thermodynamically stable one. It might even occur that metastable phases are not recognized as such, simply because the most stable polymorph is (as yet) unknown. This might produce the extraordinary phenomenon of *disappearing polymorphs* [97].

At particular *critical* points (T_C, P_C) on the phase diagram of a substance, two phases can be found in thermodynamic equilibrium. Therefore, upon application of a pressure or a temperature gradient, a transformation occurs from one phase into the other. This is a *phase transition*, in many aspects similar to a transformation implying the change of aggregation state. However, the extent of the changes in a solid to solid transformation is much smaller. For example, latent heat or latent volumes associated with the transformations are quite small, sometimes even difficult to detect.

The number of cryo-crystallographic studies on phase transitions is quite large nowadays. It became common with the availability of single crystal diffractometers equipped with digital area detectors that allow very rapid data collections. They are optimal for repeated measurements at variable temperatures of the same crystal in a reasonable amount of time. Thus, the accurate and detailed structural information typically available from a single crystal X-ray diffraction experiment could be

associated with other useful information like, for example, heat capacity and heat exchange measurements (available from DSC experiments) or spectroscopic signals.

The nature and the mechanisms of phase transitions in solids are still matters of discussion among crystallographers, as nicely summarized in a recent review [20]. The reader is referred to textbooks for a comprehensive overview of this long term debate [98–100]. Here, we summarize the qualitative nature of the main changes that are possible in a solid to solid phase transition.

4.3.1 Symmetry

The symmetry of the crystal system could change during a phase transition, because of a transformation of the lattice into a super-lattice or sub-lattice, a change in the space group type, or both.[4] A change of symmetry (in $\mathbf{R}^3$ space) is a sufficient condition to assess occurrence of phase transformation, but it is not a necessary condition. It is not rare, however, to observe iso-symmetric phase transitions, i.e., transformations where the space group type and the lattice type remain unchanged, but two different structures are in equilibrium at the critical point. As a consequence the sole determination of the space group may not be sufficient to detect a phase transition, unless the thermal *expansivity* is calculated (which usually requires measures over a wide temperature range). A discontinuity of the cell volume [hence of the molar volume, $V(T)$] or a discontinuity of the *expansivity* [first derivative of $V(T)$] would reveal a phase transition. For the second-order type of transition (see below) it is necessary that a group–subgroup relationship is maintained between the space groups of the two phases [94, 95].

4.3.2 Molecular Structure

Changes of molecular structure as a function of temperature could reveal a phase transition. However, caution should be applied because molecular geometries can change together with crystal shrinking or expansion without implying formation of a new phase [101]. So what kind of structural changes are compatible with a phase transformation? If a crystallographic symmetry element appears/disappears through the phase transition, then the space group type would change and the phase transition is evident. Iso-symmetric phase transitions are instead caused by a

[4] It is important here to talk about *space group type*, not just *space group*. In fact, the *space group* is determined by the combination of lattice and symmetry operators. When crystallographers report a given *space group*, in reality they refer to a *space group type* (i.e., the coincidence of symmetry operations with those cataloged in the International Tables of crystallography, regardless the actual lattice dimensions). This distinction is particularly important when discussing phase diagrams and in particular it is fundamental to appreciate the exact meaning of *iso-symmetric* phase transition.

discontinuity of molecular or supramolecular geometries, for example a tautomerism, an intra-crystal oxidation/reduction, etc. It is important to note that sometimes it is not so easy to establish the discontinuous nature of the changes. For example, a proton shift within a strongly hydrogen bonded system might occur continuously [102] due to softer changes of the crystal potential, which come from the resonance between two (or more) electronic configurations. However, a discontinuity could also occur [103, 104] when the two electronic configurations of an HB system produce two separate minima on the potential energy surface. In this case, two distinct phases are recognized and a transition is established at (T_c, P_c).

4.3.3 Order of Transition

When the free energies F of the two crystal structures are identical, the system is at a critical point. The identity of F does not imply identical functions (otherwise the two phases would be indistinguishable). Therefore, at the critical point first derivatives of F might differ and therefore enthalpy, volume, and entropy of the two phases would be different. These transformations are first-order phase transitions, according to Ehrenfest [105]. A discontinuous enthalpy implies heat exchange at the transition temperature, which can easily be measured with DSC experiments. A discontinuous volume is evident under the microscope or, more precisely, with diffraction experiments on single crystals or powders. Some phase transitions are however characterized by continuous first derivatives of the free energy, whereas the second derivatives (specific heat, compressibility, or thermal expansivity, etc.) are discontinuous. These transformations are second-order transitions and are clearly softer.

To exemplify first- or second-order phase transitions, the behavior of $Co_2(CO)_6(As(C_6H_5)_3)_2$ [106] (**1**) (see Fig. 7) and $Ni(C_2H_8N_2)_3(NO_3)_2$ (**2**) [107] (see Fig. 8) are illustrated. In **1**, a transition occurs on cooling the crystals from ambient condition at ca. 210 K. The space group type (R-3) does not change, but the *c*

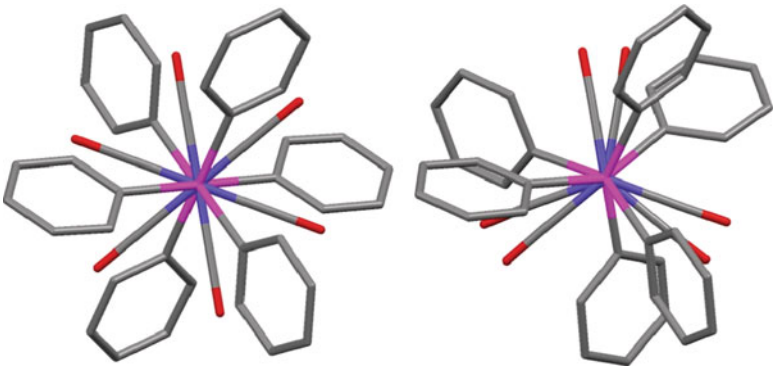

Fig. 7 The molecular transformations occurring in $Co_2(CO)_6(XPh_3)_2$ (X = P, As) from ambient conditions (*left*) to low temperature or high pressure (*right*). The conformational change occurs gradually and at (T_c, P_c) the two structures coincide

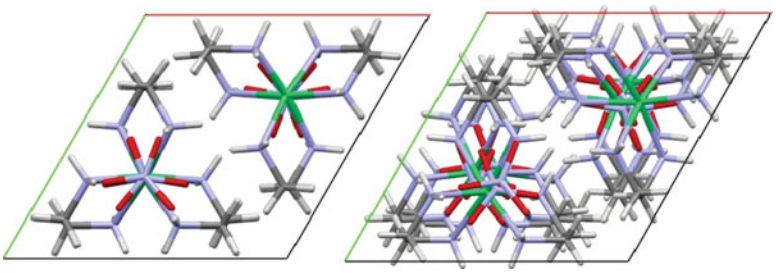

Fig. 8 The changes occurring to $[Ni(CH_2NH_2NH_2CH_2)_3][NO_3]_2$ from ambient conditions (*left*) to low temperature (*right*). The molecular geometry remains almost unchanged, but the molecule moves away from a crystallographic threefold axis producing a 3_1 helix. The phase change occurs abruptly and at (T_c, P_c) the two structures are different and in equilibrium

axis of the hexagonal lattice doubles below a critical temperature. At molecular level, the molecular symmetry is reduced from −3 to 3 and therefore the perfectly *staggered* conformation. Free rotation is now possible for the two $Co(CO)_3As(C_6H_5)_3$ moieties about the Co–Co axis. As temperature is lowered, the molecular conformation further changes, maintaining the threefold symmetry and without reaching the -6 m^2 of a perfectly *eclipsed* conformation. It is interesting that the group–subgroup relationship at the critical temperature is such that no low temperature phase is actually possible above T_c, because the two phases are simply identical. Therefore this is an example of second-order type phase transition, described in detail by Landau [99]. No discontinuity of molar volume, enthalpy, and entropy are expected, as in fact demonstrated by X-ray diffraction and DSC measurements. Sometime these transitions are called *continuous* to emphasize this soft nature, but one should remember that expansivity and specific heat are discontinuous. The high temperature phase could exist below T_c, but no hysteresis is observed. Notably the same kind of phase transition is observed for the isomorphic species $Co_2(CO)_6(P(C_6H_5)_3)_2$ (**3**) [108] and both **1** and **3** undergo similar transitions at high pressure.

$Ni(C_2H_8N_2)_3(NO_3)_2$ is quite different – the space group type and the lattice change at T_c (ca. 106 K). The transition show discontinuity of the cell volume and, as expected, there is a latent heat of transition. Notably at the critical temperature the two phases are structurally different and therefore they are in equilibrium at that temperature. A minor hysteresis is observed.

As mentioned above, sometimes two phases are recognized even though no space group type change is actually observed. Often these transformations are associated with competition between two different electronic configurations, or otherwise between two molecular conformations. The latter are, for example, order/disorder transitions caused by a group in a molecule subjected to weakly bounding potential surface, and therefore showing multiple minima. Below a critical temperature the higher energy conformer may be inaccessible. More interesting is instead the competition between different electronic configurations. This implies different bonding in a molecule (or supramolecular synthon). Notable examples are *spin crossover* materials, i.e., molecular compounds with the ability

to switch between a paramagnetic high spin state (HS) and a diamagnetic low-spin ground state (LS) [109]. This does not necessarily imply a change of crystal symmetry, but it clearly modifies the molecular geometry, hence the packing.

Phase transitions are not only characterized by atomic or molecular structural changes – they can also be characterized by significant modifications in the microstructure and domains and at a much larger size scale. One notable example has been recently reported by Glazer et al. [110] using linear birefringence measurements in $LiTaO_3$ and $LiTa_xNb_{1-x}O_3$ crystals at high temperature.

In this chapter combinations of low/high temperature and pressure have not been discussed. However it might be clear that this would offer even further possibilities to expand the knowledge on the phase diagram of a given species. At the same time, further accuracy could be obtained from high pressure experiments if atomic displacements are significantly reduced. Most of these applications can be exploited in the future with the continuous improvements of high pressure techniques and scientific research in this area (see [114] for more details).

4.4 Thermodynamics from Multi-Temperature Diffraction

As has become clear in previous sections, atomic thermal parameters refined from X-ray or neutron diffraction data contain information on the thermodynamics of a crystal, because they depend on the atom dynamics. However, as diffracted intensities (in kinematic approximation) provide magnitudes of structure factors, but not their phases, so atomic displacement parameters provide the mean amplitudes of atomic motion but not the "phase" of atomic displacement (i.e., the relative motion of atoms).[5] This means that vibrational frequencies are not directly available from a model where U_{ij} parameters are refined. However, Bürgi demonstrated [111] that such information is in fact available from sets of U_{ij}s refined on the same molecular crystals at different temperatures.

Using a rigid body approximation, i.e., assuming that molecules move in crystals without correlation between external (low frequency) and internal (high frequency) modes, Cruickshank demonstrated in 1956 how the atomic displacements (at just one temperature) could be used together with infra-red spectroscopy to obtain information on the entropy of crystalline naphthalene [112]. A partial rigid body approximation could also be applied to some functional groups in a molecule, having much lower rotational barriers (for example methyl, *tert*-butyl groups attached to some rigid aromatic skeleton).

Bürgi generalized the model, assuming a temperature independent high frequency term accounting for displacements due to the internal modes. By means of multi-

[5] This problem is sometimes referred to as the *second phase problem* in crystallography.

temperature experiments and refinement, the internal displacements can be separated from the external ones. In fact the atomic displacement parameters are expressed as

$$\Sigma^X(T) = \mathbf{AgV}\delta(T)\mathbf{V^T g^T A^T} + \varepsilon^X. \quad (12)$$

The matrices **g** and **A** transform the normal modes with frequencies v_i and eigenvectors **V** into atomic displacements Σ^X (T), ADPs are the 3 × 3 diagonal blocks of Σ^X, and ε^X is a temperature-independent term accounting for the high-frequency vibrations (internal modes).

The potentiality of multi-temperature studies has not been exploited much so far and only a few complete works have been reported in the literature; however it is likely that more applications could be proposed in the future.

5 Comments and Personal Perspectives

A typical paper on cryo-crystallographic applications is usually concluded by the author's encouragement to study more and more samples at lower and lower temperature. The message from this chapter is instead somewhat different and can be summarized as follows: (1) *use temperature critically and think carefully when it is necessary to measure structures or properties of crystals at lower temperature*; (2) *use all the additional information available when studying the sample at low temperature*; (3) *do not limit the temperature scans in the range below ambient conditions* (even when studying organic crystals).

Temperature offers an additional point of view on the structure of a material, and that's why it should be used with careful thinking and not randomly. In this respect, it is important to stress that what is the *ambient temperature* for the experimentalist may have no special meaning for the material under study. On the other hand, a given species may be of little interest at low temperature apart from the data quality improvement (this is especially true for compounds biological interest).

In this chapter we have emphasized that experiments on crystals at low temperature may provide information on the chemical bonding and on the thermodynamics of a system. A tight connection is evident between theoretical chemistry and cryo-crystallography.

Acknowledgements The author thanks the Swiss National Science Foundation for financial support (Project 200021_125313) and Professor Angelo Sironi (University of Milan, Italy) for continuous scientific inspiration.

References

1. Larsen FK (1995) Diffraction studies of crystals at low temperatures – crystallography below 77 K. Acta Crystallogr B 51:468–482
2. Cambridge Crystallographic Data Center (2010) Cambridge structural database. Cambridge Crystallographic Data Center, Cambridge

3. Allen FR (2002) Acta Crystallogr B 58:380–388
4. Bürgi H-B, Dunitz JD (eds) (1993) Structure correlation. VCH, Weinheim, Germany
5. Steurer W (2007) What is a crystal? Introductory remarks to an ongoing discussion. Z Kristallogr 222:308–309
6. Lifshitz R (2007) What is a crystal. Z Kristallogr 222:313–317
7. Wallace DC (1972) Thermodynamics of crystals. Wiley, New York
8. Einstein A (1907) The Planck theory of radiation and the theory of specific heat. Ann Phys 22:180–190
9. Debye P (1912) The theory of specific warmth. Ann Phys 39:789–839
10. Born M, Huang K (1954) Dynamical theory of crystal lattices. Clarendon Press, Oxford
11. Capelli SC, Förtsch M, Bürgi HB (2000) Dynamics of molecules in crystals from multi-temperature anisotropic displacement parameters. II. Application to benzene (C_6D_6) and urea [$OC(NH)_2$]. Acta Crystallogr A 56:413–424
12. Bürgi H-B (1995) Motion in crystals: the molecular mean field. Acta Crystallogr B 51:571–579
13. Shomaker V, Trueblood KN (1968) On the rigid-body motion of molecules in crystals. Acta Crystallogr B 24:63–76
14. Hirshfeld FL (1976) Can X-ray data distinguish bonding effects from vibrational smearing? Acta Crystallogr A 32:239–244
15. Smith GT, Mallinson PR, Frampton CS, Farrugia LJ, Peacock RD, Howard JAK (1997) Experimental determination of the electron density topology in a non-centrosymmetric transition metal complex: [$Ni(H_3L)$][NO_3][PF_6] [H_3L = N, N′,N″-tris(2-hydroxy-3-methylbutyl)-1,4,7-triazacyclononane]. J Am Chem Soc 119:5028–5034
16. Farrugia LJ, Frampton CS, Howard JAK, Mallinson PR, Peacock RD, Smith GT (2006) Experimental determination of the electron density topology in a non-centrosymmetric transition metal complex: [$Ni(H_3L)$][NO_3][PF_6] [H_3L = N, N′,N″-tris(2-hydroxy-3-methylbutyl)-1,4,7-triazacyclononane]: a reappraisal. Acta Crystallogr B 62:236–244
17. Johnson CK, Levy HA (1974) International tables for X-ray crystallography, vol IV. Kynoch Press, Birmingham, pp 311–336
18. Kendal MG, Stuart A (1958) The advanced theory of statistics. Griffin, London
19. Grüneisen E (1926) Geiger H, Scheel K (eds) Handbuch der Physik, vol 10. Springer, Berlin, pp 1–59
20. Herbstein FK (2006) On the mechanism of some first-order enantiotropic solid-state phase transitions: from Simon through Ubbelohde to Mnyukh. Acta Crystallogr B 62:341–383
21. Rees B (1977) Data-processing and structure-factor determination. Isr J Chem 16:154–158
22. Coppens P, Hamilton WC (1970) Anisotropic extinction corrections in the Zachariasen approximation. Acta Crystallogr A 26:71–83
23. Lucas BW (1969) On contribution of thermal diffuse X-ray scattering to integrated Bragg intensities of single crystals. Acta Crystallogr A 25:627–631
24. Coppens P, Su Z, Becker PJ (2003) Analysis of charge and spin densities, International Tables for Crystallography, vol C, 3rd edn. Kluwer Academic Publisher, Dordrecht, pp 713–734
25. American Institute of Physics (1972) Handbooks, 3rd edn. McGraw-Hill, New York
26. Leadbetter AJ (1965) Thermodynamic and vibrational properties of H_2O ice and D_2O ice. Proc R Soc London, Ser A 287:403–425
27. Coppens P, Vos A (1971) Electron density distribution in cyanuric acid. 2. Neutron diffraction study at liquid nitrogen temperature and comparison of X-ray and neutron diffraction results. Acta Crystallogr B 27:146–158
28. Macchi P, Sironi A (2004) Variable-temperature X-ray crystallographic studies: a complementary tool for charge-density investigation of soft (organometallic) bonds. Acta Crystallogr A 60:502–509
29. Munshi P, Madsen AØ, Spackman MA, Larsen S, Destro R (2008) Estimated H-atom anisotropic displacement parameters: a comparison between different methods and with neutron diffraction results. Acta Crystallogr A 64:465–475

30. Madsen AØ (2006) SHADE web server for estimation of hydrogen anisotropic displacement parameters. J Appl Crystallogr 39:757–758
31. Teng T-Y, Moffat K (2000) Primary radiation damage of protein crystals by an intense synchrotron X-ray beam. J Synchrotron Radiat 7:313–317
32. Hope H (1988) Cryocrystallography of biological macromolecules – a generally applicable method. Acta Crystallogr B 44:22–26
33. Hope H, Frolow F, Von Böhlen K, Makowski I, Kratky C, Halfon Y, Danz H, Webster P, Bartels KS, Wittmann HG, Yonath A (1989) Cryocrystallography of ribosomal particles. Acta Crystallogr B 45:190–199
34. Kottke T, Stalke D (1993) Crystal handling at low temperatures. J Appl Crystallogr 26:615–619
35. Parkin S, Hope H (1998) Macromolecular cryocrystallography: cooling, mounting, storage and transportation of crystals. J Appl Crystallogr 31:945–953
36. Cosier J, Glazer AM (1986) A nitrogen-gas-stream cryostat for general X-ray-diffraction studies. J Appl Crystallogr 19:105–107
37. Hardie MJ, Kirschbaum K, Martin A, Pinkerton AA (1998) An open-flow helium cryostat for single-crystal X-ray diffraction experiments. J Appl Crystallogr 31:815–817
38. Hanson BL, Martin A, Harp JM, Parrish DA, Bunick CG, Kirschbaum K, Pinkerton AA, Bunick GJ (1999) Use of an open-flow helium cryostat for macromolecular cryocrystallography. J Appl Crystallogr 32:814–820
39. Samson S, Goldish E, Dick CJ (1980) A novel low-temperature X-ray goniometer with closed-cycle cooling to about 18 K. J Appl Crystallogr 13:425–432
40. Darovsky A, Coppens P (1998) A device for low-temperature crystal reorientation in data collection with the oscillation method. J Appl Crystallogr 31:296–298
41. Peterson RC (1992) A flam-heated gas-flow furnace for single crystal X-ray diffraction. J Appl Crystallogr 25:545–548
42. Lindley PF (2004) Mounting and setting of specimens for X-ray crystallographic studies, International Tables for Crystallography Vol. C: Mathematical, physical and chemical tables, 3rd edn. Kluwer Academic Publishers, Dordrecht, pp 162–170
43. Tsukimura K, Sato-Sorensen Y, Ghose Y (1989) A gas flow furnace for X-ray crystallography. J Appl Crystallogr 22:401–405
44. Swanson DK, Prewitt CT (1986) A new radiative single crystal diffractometer microfurnace incorporating MgO as a high temperature cement and internal temperature calibrant. J Appl Crystallogr 19:1–6
45. Sayetat F, Prat A (2001) A new X-ray powder diffractometer working in the 87 $\pm$ 1000 K range for phase-transition analyses. J Appl Crystallogr 34:311–317
46. Arzi E, Sándor E (1983) A variable temperature sample container for low temperature neutron powder diffraction. J Appl Crystallogr 16:449–452
47. Debrenne PP, Laugier J, Chaudet M (1970) Diffractometre de rayons X à haute temperature (2500 C) sous vide pousse (10–8 Torr). J Appl Crystallogr 3:493–496
48. Reading M, Hahn BK, Crowe BS (1993) Method and apparatus for modulated differential analysis. US Patent 5 224 775
49. Kamasa P, Merzlyakov M, Pyda M, Pak J, Schick C, Wunderlich B (2002) Multi-frequency heat capacities measured with different types of TMDSC. Thermochimica Acta 392–393:195–207
50. Hartshorne NH, Stuart A (1970) Crystals and the polarizing microscope, 4th edn. Edward Arnold, London
51. Glazer AM, Lewis JG, Kaminsky W (1996) An automatic optical imaging system for birefringent media. Proc R Soc London Ser A 452:2751–2765
52. Pajdzik LA, Glazer AM (2006) Three-dimensional birefringence imaging with amicroscope tilting-stage. I. Uniaxial crystals. J Appl Crystallogr 39:326–337
53. Pajdzik LA, Glazer AM (2006) Three-dimensional birefringence imaging with a microscope tilting stage. II. Biaxial crystals. J Appl Crystallogr 39:856–870

54. Harada J, Ogawa K (2001) Invisible but common motion in organic crystals: a pedal motion in stilbenes and azobenzenes. J Am Chem Soc 123:10884–10888
55. Juers DH, Matthews BW (2004) Cryo-cooling in macromolecular crystallography: advantages, disadvantages and optimization. Q Rev Biophys 37:105–119
56. Teng T-Y, Moffat K (2002) Radiation damage of protein crystals at cryogenic temperatures between 40 K and 150 K. J Synchrotron Radiat 9:198–201
57. Yaghi OM, Li GM, Li HL (1995) Selective binding and removal of guests in a microporous metal-organic framework. Nature 378:703–706
58. Rowsell JLC, Spencer EC, Eckert J, Howard JAK, Yaghi OM (2004) Gas adsorption sites in a large-pore metal-organic framework. Science 309:1350–1354
59. Aime S, Diana E, Gobetto R, Milanesio M, Valls E, Viterbo D (2002) Structural and spectroscopic study of the dihydrogen bond in an imine triosmium complex. Organometallics 21:50–57
60. Zachariasen WH (1945) Theory of X-ray diffraction in crystals. Wiley, New York
61. Macchi P, Iversen BB, Sironi A, Chackoumakos BC, Larsen FK (2000) Interanionic O-H–-O interactions: the charge density point of view. Angew Chem 39:2719–2722
62. Debey P (1915) X-ray dispersal. Ann Phys 48:809–823
63. Coppens P (1067) Comparative X-ray and neutron diffraction study of bonding effects in s-triazine. Science 158:1577–1579
64. Coppens P (1997) X-ray charge densities and chemical bonding. Oxford University Press, New York
65. Stewart RF, Bentlety J, Goodman B (1975) Generalized X-ray scattering factors in diatomic molecules. J Chem Phys 63:3786–3793
66. Kurki-Suonio K (1977) Charge density deformation models. Isr J Chem 16:115
67. Hansen NK, Coppens P (1978) Electron population analysis of accurate diffraction data. 6. Testing aspherical atom refinements on small-molecule data sets. Acta Crystallogr A 34:909–921
68. Volkov A, Macchi P, Farrugia LJ, Gatti C, Mallinson P, Richter T, Koritsanszky T (2006) XD2006 – a computer program package for multipole refinement, topological analysis of charge densities and evaluation of intermolecular energies from experimental and theoretical structure factors. University of Buffalo, USA
69. Hansen NK, MOLLY (1978) A Computer Program for Multipole Charge-Density Refinement. Univ. Henri Poincare, Nancy I, France. See [67]
70. Stewart RF, Spackman MA, Flensburg C (2000) VALRAY – user's manual, 2.1 ed. Carnegie Mellon University, Pittsburgh, PA, USA, and University of Copenhagen, Denmark
71. Petricek V, Dusek M, Palatinus L (2006) JANA2006, Structure Determination Software Programs, Institute of Physics, Praha
72. Ghermani NE, Bouhmaida N, Lecomte C (1992) ELECTROS: Computer program to calculate electroststic properties from high resolution X-ray diffraction. Universite´ de Nancy I, France
73. Becker P, Gillet J-M, Cortona P, Ragot S (2001) Complementary aspects of charge and momentum densities for the study of the chemical bond. Theor Chem Acc 105:284–291
74. Clinton WL, Frishberg C, Massa LJ, Oldfield PA (1973) Methods for obtaining an electron-density matrix from X-ray diffraction data. Int J Quantum Chem Symp 7:505–514
75. Jayatilaka D, Grimwood DJ (2001) Wavefunctions derived from experiment. I. Motivation and theory. Acta Crystallogr A 57:76–86
76. Jayatilaka D, Grimwood DJ (2004) Electron localization functions obtained from X-ray constrained Hartree-Fock wavefunctions for molecular crystals of ammonia, urea and alloxan. Acta Crystallogr A 60:111–119
77. Tanaka K, Makita R, Funahashi S, Komori T, Win Z (2008) X-ray atomic orbital analysis. I. Quantum mechanical and crystallographic framework of the method. Acta Crystallogr B 64:437–449
78. Figgis BN, Reynolds PA, Williams GA (1980) Spin-density and bonding in the $CoCl_4^{2-}$ ion in Cs_3CoCl_5. 2. Valence electron-distribution in the $CoCl_4^{2-}$ ion. J Chem Soc, Dalton Trans 2339–2347

79. Holladay A, Leung PC, Coppens P (1983) Generalized relations between d-orbital occupancies of transition-metal atoms and electron-density multipole population parameters from X-ray diffraction data. Acta Crystallogr A 39:377–387
80. Clementi E, Roetti C (1974) Tables of Roothaan-Hartree-Fock wavefunctions, special issue in atomic data and nuclear data table. Academic Press, New York
81. Clementi E, Raimondi DL (1963) Atomic screening constants from SCF functions. J Chem Phys 38:2686–2689
82. Collins DM (1982) Electron density images from imperfect data by iterative entropy maximization. Nature 298:49–51
83. Jaynes ET (1968) Prior probabilities. IEEE Trans Syst Sci Cybern SSC-4:227–240
84. Roversi P, Irwin JJ, Bricogne G (1998) Accurate charge-density studies as an extension of Bayesian crystal structure determination. Acta Crystallogr A 54:971–996
85. Palatinus L, van Smaalen S (2005) The prior-derived F constraints in the maximum-entropy method. Acta Crystallogr A 61:363–372
86. van Smaalen S, Netzel J (2009) The maximum entropy method in accurate charge-density studies. Physica Scripta 79:048304
87. Johnson CK (1969) Addition of higher cumulants to the crystallographic structure-factor equation: a generalized treatment for thermal-motion effects. Acta Crystallogr A 25:187–194
88. Mallinson PR, Koritsanszky T, Elkaim E, Li N, Coppens P (1988) The Gram-Charlier and multipole expansions in accurate X-ray diffraction studies: can they be distinguished? Acta Crystallogr A 44:336–343
89. Roversi P, Barzaghi M, Merati F, Destro R (1996) Charge density in crystalline citrinin from X-ray diffraction at 19 K. Can J Chem 74:1145–1161
90. Makita R, Tanaka K, Onuki Y (2008) 5d and 4f electron configuration of CeB_6 at 340 and 535 K. Acta Crystallogr B 64:534–549
91. Tanaka K, Onuki Y (2002) Observation of 4f electron transfer from Ce to B_6 in the Kondo crystal CeB_6 and its mechanism by multi-temperature X-ray diffraction. Acta Crystallogr B 58:423–436
92. Funahashi S, Tanaka K, Iga F (2010) X-ray atomic orbital analysis of 4f and 5d electron configuration of SmB_6 at 100, 165, 230, 298 K. Acta Crystallogr B 66:292–306
93. Coppens P (1997) X-ray charge densities and chemical bonding. IUCr texts on crystallography 4. International Union of Crystallography, Oxford University Press, Oxford
94. Bader RFW (1990) Atoms in molecules: a quantum theory. International series of monographs on chemistry 22. Oxford Science Publications, Oxford
95. Matta CF, Boyd RJ (eds) (2007) The quantum theory of atoms in molecules: from solid state to DNA and drug design. Wiley-VCH, Weinheim
96. Gatti C, Macchi P (eds) (2011) Modern charge density analysis, Springer
97. Dunitz JD, Bernstein J (1995) Disappearing polymorphs. Acc Chem Res 28:193–200
98. Mnyukh Yu (2001) Fundamentals of solid state phase transitions, ferromagnetism and ferroelectricity, First Books New York
99. Landau LD, Lifshitz EM (1958) Statistical physics. Pergamon, Oxford
100. Toledano J-C, Toledano P (1997) The Landau theory of phase transitions: application to structural, incommensurate, magnetic, and liquid crystal systems. World Scientific Pub. Co Inc., Singapore
101. Threlfall TL, Gelbrich T (2007) The crystal structure of methyl paraben at 118 K does not represent a new polymorph. Cryst Growth Des 7:2297
102. Morrison CA, Siddick MM, Camp PJ, Wilson CC (2005) Toward understanding mobile proton behavior from first principles calculation: the short hydrogen bond in crystalline urea-phosphoric acid. J Am Chem Soc 127:4042–4048
103. Casati N, Macchi P, Sironi A (2009) Hydrogen migration in oxalic acid di-hydrate at high pressure? Chem Commun 2679–2681
104. Macchi P, Casati N, Marshall WG, Sironi A (2010) The α and β forms of oxalic acid di-hydrate at high pressure: a theoretical simulation and a neutron diffraction study. CrystEngComm 12:2596–2603

105. Ehrenfest P (1933) Phase changes in the ordinary and extended sense classified according to the corresponding singularities of the thermodynamic potential. Proc Acad Sci Amsterdam 36:153–157
106. Macchi P, Garlaschelli L, Martinengo S, Sironi A (1998) Characterization of the solid-solid phase transition of $Co_2(CO)_6(AsPh_3)_2$. Inorg Chem 37:6263–6268
107. Farrugia LJ, Macchi P, Sironi A (2003) Reversible displacive phase transition in $[Ni(en)_3]^{2+}(NO_3^-)_2$: a potential temperature calibrant for area-detector diffractometers. J Appl Crystallogr 36:141–145
108. Casati N, Macchi P, Sironi A (2005) Staggered to eclipsed conformational rearrangement of $[Co_2(CO)_6(PPh_3)_2]$ in the solid state: an X-ray diffraction study at high pressure and low temperature. Angew Chem 44:7736–7739
109. Gütlich P, Garcia Y, Goodwin HA (2000) Spin crossover phenomena in Fe(II) complexes. Chem Soc Rev 29:419–427
110. Glazer AM, Zhang N, Bartasyte A, Keeble DS, Huband S, Thomas PA (2010) Observation of unusual temperature-dependent stripes in $LiTaO_3$ and $LiTa_xNb_{1-x}O_3$ crystals with near-zero birefringence. J Appl Crystallogr 43:1305–1313
111. Bürgi H-B, Capelli SC (2000) Dynamics of molecules in crystals from multi-temperature anisotropic displacement parameters. I. Theory. Acta Crystallogr A 56:403–412
112. Cruickshank DWJ (1956) The entropy of crystalline naphthalene. Acta Crystallogr 9:1010–1011
113. Gavezzotti A (2011) Computational studies of crystal structure and bonding. Top Curr Chem, DOI: 10.1007/128_2011_131
114. McMahon MI (2011) High-pressure crystallography. Top Curr Chem, DOI: 10.1007/128_2011_132

Top Curr Chem (2012) 315: 69–110
DOI: 10.1007/128_2011_132

Published online: 13 May 2011

High-Pressure Crystallography

Malcolm I. McMahon

Abstract The ability of pressure to change inter-atomic distances strongly leads to a wide range of pressure-induced phenomena at high pressures: for example metallisation, amorphisation, superconductivity and polymerisation. Key to understanding these phenomena is the determination of the crystal structure using x-ray or neutron diffraction. The tools necessary to compress matter above 1 million atmospheres (1 Megabar or 100 GPa) were established by the mid 1970s, but it is only since the early 1990s that we have been able to determine the detailed crystal structures of materials at such pressures. In this chapter I briefly review the history of high-pressure crystallography, and describe the techniques used to obtain and study materials at high pressure. Recent crystallographic studies of elements are then used to illustrate what is now possible using modern detectors and synchrotron sources. Finally, I speculate as to what crystallographic studies might become possible over the next decade.

Keywords Crystallography · High-Pressure · X-ray Diffraction · Neutron Diffraction

Contents

M.I. McMahon
SUPA, Centre for Science at Extreme Conditions, School of Physics and Astronomy, The University of Edinburgh, Edinburgh EH9 3JZ, UK
e-mail: mim@ph.ed.ac.uk

1 Introduction

Pressure is a sadly underused thermodynamic variable in the study of chemical systems, despite the effects of pressure being very much more dramatic than those of temperature. The ability of pressure to change inter-atomic distances strongly leads to even the simplest chemical systems undergoing a variety of pressure-induced structural and electronic phase transitions that can change insulating solids into superconducting metals [1–3], gases into exotic coloured crystals with unusual inter-molecular bonding [4] and alkali metals into transparent insulators [5].

Key to understanding the effects of compression on materials is the determination of the crystal structure. Crystallography at high pressure stretches back to the late 1950s and early 1960s, but has undergone a revolution in the last 20 years as the result of both breakthroughs in high-pressure techniques and the development of new X-ray and neutron sources. In this chapter, I will briefly review the history of high-pressure crystallography, describe the experimental methods used to study materials at high pressures, and then illustrate the effects of high pressure on a number of different elemental systems.

2 A Brief History of High-Pressure Crystallography

Before reviewing the history of high-pressure crystallography, it is perhaps first necessary to define what is meant by "crystallography". The Oxford English Dictionary describes it as "*That branch of physical science which treats of the structure of crystals, and their systematic classification*". By "structure" I will mean the determination of the fractional coordinates of atoms, and their displacement parameters, in a crystalline material. At high pressures, this typically involves the measurement of the intensities of Bragg reflections using X-ray or neutron diffraction, followed by structural solution and/or least-squares refinement.

The history of high-pressure science is described extremely well in two books by R.M. Hazen, and the reader is directed to these for an excellent introduction to the field [6, 7]. While much high-pressure science was conducted prior to the 1950s, most notably by P.W. Bridgeman [8], who received the 1946 Nobel Prize in physics for "*the invention of an apparatus to produce extremely high pressures, and for the discoveries he made therewith in the field of high pressure physics*" [9], it was the

advent in the late 1950s of pressure cells utilising single-crystal diamonds to compress samples that heralded the dawn of high-pressure crystallography. Initial designs of the pressure cell used the diamonds in a piston-cylinder arrangement, with a small cylindrical sample chamber being drilled through the diamond [10, 11]. But the invention of the diamond anvil cell (DAC) in 1958 by Jamieson et al. and Weir et al. [12, 13] was *the* key turning point in high-pressure crystallography. The first diffraction studies were performed almost immediately afterwards by Jamieson, Weir and colleagues, who determined the structure-types of the high-pressure phases of elements by matching observed X-ray diffraction patterns with those obtained from other materials at ambient pressure [14–17]. The small Merrill-Bassett DAC, developed in 1974, allowed DACs to be used on commercial diffractometers [18], and was used extremely successfully by researchers at the Geophysical Laboratory at the Carnegie Institution of Washington to explore the structures of complex minerals at high pressure, and to pioneer high-pressure single-crystal diffraction techniques. Much of the work conducted at this time is described in the seminal book by R.M. Hazen and L.W. Finger [19]. The DAC celebrated its 50th anniversary in 2009 and, to mark this, W.B. Bassett, an early pioneer of high-pressure mineralogy, has recently reviewed its history [20].

The greatly increased X-ray flux available from synchrotron light sources in the 1970s enabled high-pressure diffraction studies to be pushed to ever higher pressures: 1 Mbar (100 GPa) in 1976 [21], 200 GPa in 1984 [22], 300 GPa in 1989 [23] and 400 GPa in 1990 [24] or 2010 [25]. However, such studies typically used energy-dispersive X-ray powder-diffraction methods in order to utilise the extreme intensity of the polychromatic synchrotron X-ray beam, and it was not possible to determine accurate Bragg peak intensities and therefore structure factors. As a result, while equations of state of known materials could be followed to very high pressures [26], diffraction information on many high-pressure phases remained at the level of structure type (cubic, tetragonal, "β-tin") or "distortions" thereof. (See, for example, many of the phase diagrams reproduced in [27].)

A major transformation in the power of high-pressure powder diffraction came about through, first, the pioneering application of image-plate detectors for angle-dispersive X-ray diffraction (ADXRD) in Japan in the late 1980s [28], and then, in the early 1990s, the development of advanced ADXRD techniques using DACs and an image-plate detector at the SRS synchrotron in the UK [29, 30]. In a short period of two or three years, it became possible to perform crystallography to extreme pressures comparable in resolution and quality to ambient-pressure studies. The use of a sensitive two-dimensional (2D) image-plate detector, and short-wavelength monochromatic X-rays, allowed Rietveld refinement of high-pressure powder-diffraction data for the first time [30, 31]. The replacement of the restricted-aperture pressure cells used for energy-dispersive studies by cells with wide conical apertures, as developed for single-crystal applications, allowed full 2D Debye-Scherrer (DS) diffraction patterns to be collected, giving data with the high resolution of ADXRD techniques coupled with high signal-to-background and unmatched sensitivity to weak diffraction features [30, 32]. Two things became immediately apparent from the use of these new techniques: (1) many of the structural descriptions

reported previously in many materials were incorrect [27], and (2) the true structural behaviour of even simple elemental and binary systems at high pressures was often extremely complex, and far more interesting than believed previously [33].

The development of ADXRD techniques was perfectly timed with regards to the construction and commissioning of third generation synchrotron sources in the mid-1990s. Such sources – the ESRF in Europe, the APS in the US and SPring-8 in Japan – were *ideally* suited to the new high-pressure ADXRD studies, by providing extremely high-intensity, high-energy, microfocused, monochromatic X-ray beams [34]. As a result, the new synchrotrons allowed high-pressure diffraction to be pushed both to ever higher pressures and to more weakly-scattering systems [35, 36]. ADXRD techniques are now utilised routinely on high-pressure beamlines around the world [37], and have been used by many different researchers to study a wide range of materials such as the alkali metals [38–42], silicon [43], scandium [44], phosphorus [45, 46], titanium [47], gold [48], vanadium [49], calcium [50], iodine [51], oxygen [35, 52, 53] and nitrogen [54, 55]. In addition, a large number of more complex materials of geological or technological interest have also been studied, and ADXRD methods have been combined with laser heating to enable structural studies to be carried out at extremes of pressure and temperature [56–59].

Simultaneously with the developments in powder-diffraction techniques at synchrotrons, high-quality single-crystal studies continued to be made on X-ray laboratory sources during this period (see for example [60–63] and references therein). And the availability of chemical crystallography beamlines on a number of different synchrotrons around the world [64–66] was being exploited by researchers in order to perform high-pressure single-crystal studies using these machines, enabling ever more complex systems to be studied, including proteins and other systems of biological and biochemical interest [67–69].

While the availability and intensity of X-ray sources, and the ease of compressing suitably-small samples in DACs, has meant that X-ray diffraction techniques have dominated high-pressure crystallography since the 1970s, powder and single-crystal studies have continued to be conducted at neutron sources around the world, exploiting the power of neutrons to probe H/D-containing materials [70, 71], magnetism [72, 73] and phonons [74], or to make high real-space resolution studies of thermal motion [75].

Unfortunately, although such studies generally gave very high quality diffraction data, and structural information that was, in many cases, superior to that obtainable by X-ray methods, they were limited to much lower pressures, constrained by both the relative weakness of neutron sources, and the large samples (tens of cubic millimetres) therefore needed to obtain useable diffraction data. However, the 1990s saw a revolution in experimental methods that has greatly increased the scope of high-pressure neutron diffraction. The advent of the compact Paris–Edinburgh (P-E) press, first developed at the ISIS pulsed neutron (spallation) source in 1992 [76], enabled neutron powder-diffraction structural studies to be pushed routinely to above 25 GPa [77] while, more recently, full single-crystal data collection with sufficient, and sufficiently-accurately measured, intensities for full structure refinement has been extended to above 10 GPa [78].

The principal breakthrough of the P-E press was the ability to compress a sufficient volume of powder (or size of single crystal) in a pressure cell and press small enough to mount in situ on a neutron beamline. P-E presses have opened high-pressure neutron diffraction to a much wider range of users, and have become a standard experimental facility at several neutron sources. As a result, they have been used to study a wide range of materials, both crystalline and amorphous [79–83]. The presses have also been widely used at synchrotron sources for studies of non-crystalline materials and liquids, for example [84–86].

As said, the advent of ADXRD techniques revealed that many of the previously-reported structures observed at high pressure were incorrect, with the true structures being very much more complex than previously believed; see for example [33]. Indeed, the complexity being observed was such that the inherent limitations of the powder-diffraction method – particularly the 1-dimensional nature of the data – were now the limiting factor in determining crystal structures at high pressure. High-pressure single-crystal techniques therefore began to be developed at synchrotrons, with the specific aim of studying phases that existed beyond strongly first-order phase transitions. The use of these techniques led to the almost immediate discovery of a host of incommensurate crystal structures in a wide variety of elements, as reviewed in [87]. The solution to these very complex structures could almost certainly not have been determined from powder data alone.

Full single-crystal structure refinement has been extended to pressures above 50 GPa [88] at the second-generation HASYLAB synchrotron, and then to above 100 GPa at third-generation synchrotrons such as Diamond and the ESRF. These latter developments were helped greatly by the uniquely-low melting temperature of Na metal at 100 GPa [89], which allowed the growth of high-quality single crystals directly from the melt at these extreme pressures [90]. Since the initial work at Diamond, structure refinements of Na from full single-crystal data have been extended to almost 150 GPa at the ESRF [91, 92]. The use of single-crystal techniques is becoming increasingly popular at synchrotron sources, with a growing number of crystallographic studies in recent years, for example [93–99].

So, where does high-pressure crystallography stand as we enter the second decade of the twenty-first century? Using the DAC, it is possible to compress materials to 400 GPa [25], and to solve and refine their crystal structures using ADXRD methods to almost 300 GPa [44]. Using the more recently developed single-crystal techniques, the pressure at which it is possible to solve and refine complex crystal structures has already reached 150 GPa [92], and is likely to go much higher in due course. Both powder and single-crystal studies can be performed at both high [97, 100] and low temperatures [101]. Using neutrons, it is possible to perform highly-detailed crystallographic studies using powder techniques to well above 20 GPa [102], and single-crystal studies to 10 GPa [78]. And data can be collected routinely at both high and low temperatures. Researchers are thus able to cover an extremely wide range of pressures and temperatures, opening the way to studies of a wide range of pressure-induced phenomena. Further advances in the future will widen this range still further, and these are discussed in Sect. 5. Before describing these, and giving examples of the kind of studies

that are possible at present in Sect. 4, the next section reviews high-pressure crystallographic methods.

3 Experimental Methods

3.1 Pressure Cells

3.1.1 Diamond-Anvil Cell

While a great deal of high-pressure science was conducted prior to the invention of the DAC in 1958, very few diffraction studies were performed prior to this date [6, 7]. Those that were conducted mostly involved the use of either Be cylinders [103], or a diamond in a piston-cylinder arrangement where the diamond, with a small hole drilled through it, acted as the cylinder [11]. The invention of the DAC, in which the sample is compressed between two opposing single-crystal diamond anvils, opened the door to X-ray diffraction science. In initial studies, a powdered sample was compressed directly between the two anvils. However, the subsequent introduction of the gasketed DAC in 1962 [104] in which a thin sheet of metal is placed between the diamonds, with a small hole to contain the sample, greatly increased the scope of the DAC. It enabled higher pressures to be reached by providing support to the tip (culet) of the diamonds, and also enabled liquids and gases to be loaded and compressed, and therefore the use of a hydrostatic fluid to achieve more hydrostatic pressures and hence better quality diffraction patterns. It also allowed single-crystals to be loaded and studied. The use and history of the DAC has been extensively reviewed by others, and the reader is referred to these excellent reviews for detailed further information [19, 20, 61, 63, 105–111].

The basics of the DAC are shown in Fig. 1. A detailed description of how to align a DAC, and the details of its loading, have been described by Miletich et al. [63], and the reader is directed to this excellent description if they wish more details. The diamond anvils are flawless gem-quality stones of typically 0.25 carats, with a culet size of 50–800 μm: the smaller the culet, the higher the achievable pressure (but the smaller the sample). For pressures above 100 GPa, where the tip of the diamond undergoes significant distortion, so-called bevelled diamonds are used [112]. The anvils are mounted on anvil seats, made of a hard material such as Be or BN, both of which are X-ray transparent, or tungsten carbide. The metallic gasket between the anvils is initially 200–250 μm thick, but is preindented to a thickness of 5–50 μm before the sample chamber is drilled by electrical spark erosion or laser drilling. The diameter of the sample chamber hole is typically one-third of the diameter of the culets.

The sample is loaded into the gasket hole, and surrounded by a pressure transmitting fluid – which might be an alcohol:water mixture (which provides a quasi-hydrostatic medium to ~10–16 GPa) or a crystalline gas such as Ar, Ne or He (loaded either at high pressures or cryogenically as a liquid) which is

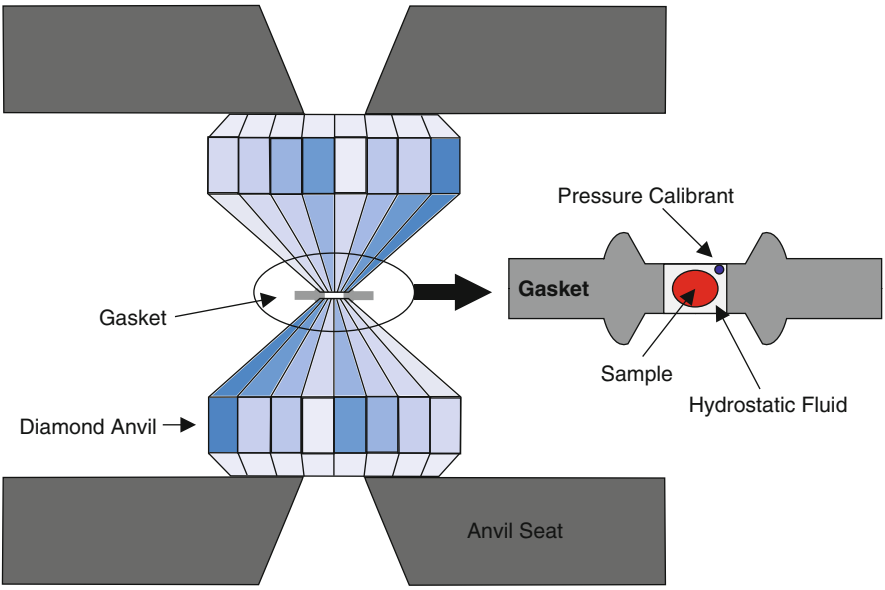

Fig. 1 Schematic diagram of a diamond anvil cell (DAC). The sample, pressure calibrant and hydrostatic fluid are loaded into the gasket hole, which is then compressed between the culets of the two diamond anvils

quasi-hydrostatic to 50 GPa or so [113–116]. Along with the sample, it is also necessary to include a pressure calibrant with the sample. This might be a small (5 μm diameter) piece of ruby or other fluorescing material, the fluorescence wavelength of which is known to change with pressure, or a calibrant (Au, Cu, Ta) whose equation of state has been calibrated previously (see Sect. 3.2).

For crystallographic studies, the typical diffraction geometry is that in which the incident X-ray beam enters the sample through one anvil, and the diffracted X-rays exit through the other. This is the so-called *transmission* geometry. In order to ensure that the maximum amount of powder-diffraction data are accessible, the opening angle in the anvil seat on the exit side of the pressure cell should be as large as possible. Anvil seats with conical apertures with a full opening angle of 70° are now used routinely (see Sect. 3.3).

For single-crystal studies, it is important that the opening angle in the anvil seat on the incident-beam side of the DAC is also as large as possible. Even so, during a single-crystal study, only a limited fraction of all single-crystal reflections are typically accessible, because the particular orientation of the sample crystal requires the incident or diffracted beam, or both, to be outside the DAC apertures. In particular, all reflections with scattering vectors along or close to the axis of the pressure cell are not accessible [63, 111]. This restriction on accessible reflections can have serious consequences for the refinement of certain crystallographic parameters, and can be overcome by using a DAC with a *transverse* diffraction geometry [117], in which diffraction takes place

in approximately the plane of the (typically X-ray transparent) gasket. Using such cells, the volume of reciprocal space accessible in single-crystal studies is increased considerably. A DAC that allows data to be collected in both transverse and transmission geometries has also been designed [118]. However, while they offer increased access to reciprocal space, the complex X-ray attenuation corrections that need to be used on data collected in DACs with the transverse geometry means that they are not as well suited to crystallography as those using the transmission geometry.

DAC technology continues to develop. Recently, the development of Boehler–Almax anvil seats [119] means that DACs no longer need to use X-ray transparent beryllium or BN seats in order to have the widest possible angular apertures. Single-crystal data can thus be collected to high angles without any contaminating diffraction lines from the anvil seats themselves [68]. The Boehler–Almax seats also enable cells with full conical apertures to be used at pressures to 150 GPa [120]. A still more recent development has been to use transparent anvils made from sintered nanocrystalline diamond [121–123]. Such anvils do away with the effects of the intense Bragg reflections from the anvils (although these are replaced by powder-diffraction lines). These sintered anvils are also tougher than single-crystal diamond anvils, and their lower thermal conductivity is advantageous for laser-heating studies [124].

3.1.2 Cells for Neutron Diffraction

The large sample sizes required for neutron-diffraction studies means that the diamond anvil cells so widely used for X-ray studies cannot be used routinely for neutron diffraction studies – although attempts have been made to use DACs with extremely large anvils [125]. However, the low neutron-absorption of many materials means that pressure cells constructed from Al alloys and other strong materials can be used. Pressure cells for neutron diffraction typically fall into three different categories: (1) cells utilising high-pressure gas to compress the sample, (2) those using a piston-cylinder arrangement and (3) cells with opposed anvils. The gas cell design of Paureau and Vettier [126] is capable of compressing several cubic centimetres of sample in a perfectly hydrostatic environment to 1 GPa by using He gas as a pressure transmitting medium. Such cells have been used extensively at the Institut Laue-Langevin (ILL) reactor source in Grenoble and at the IPNS neutron source at Argonne National Laboratory, and have produced extremely high quality crystallographic data on a wide range of different materials. In piston–cylinder designs [127, 128], the cells use a liquid pressure medium, and pressures of 2 GPa are achievable with both powder and single-crystal samples. The cells are typically pressurised off-line using a press, and then clamped to maintain the sample pressure. These cells have also been designed to be inserted into cryostats, extending studies to temperatures of 4 K and below.

The widest range of pressures has been achieved with opposed-anvil designs. Cells for single-crystal diffraction studies have been based on the DAC and have

used either sapphires or large diamonds for the anvils. For example, by using very large diamonds, Glaskov et al. [125] were able to collect diffraction data from a single-crystal of D_2 to 40 GPa, although the diffraction information was limited to the d-spacings of one or two strong peaks, because of the very small sample size for neutron diffraction. A similar diamond anvil cell was also used by Goncharenko and Loubeyre to study single-crystals of D_2 to 38 GPa at temperatures down to 1.2 K [129]. An opposed-anvil cell with moissonite anvils has been developed by Zhao et al. for use up to 20 GPa at the LANSCE neutron source [130, 131]. In order to increase sample size, opposed-anvil cells for neutron diffraction have used anvils in which the sample volume is increased by hollowing out the centre of the anvil, or using toroidal anvils in which toroidal grooves are cut into the anvils around the sample volume [132, 133], or a combination of the two. This latter design has been applied particularly successfully in both the Paris–Edinburgh [76] and other [131] presses.

A diagrammatic plan of the Paris–Edinburgh press is shown in Fig. 2. The press can use a variety of anvil designs, with the toroidal anvils of Khvostantsev [132]

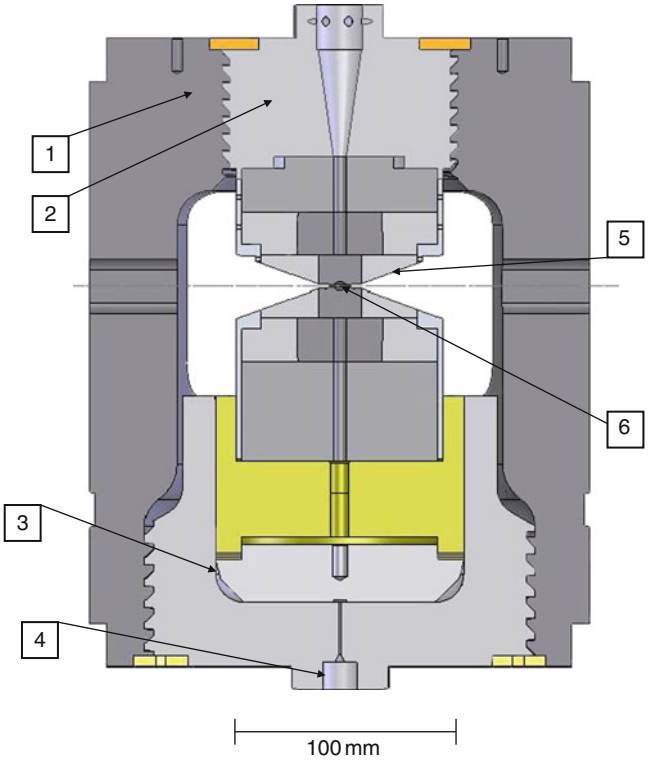

Fig. 2 A schematic diagram of the VX3 model of the Paris-Edinburgh (P-E) press. Key: (1) Hardened steel main frame; (2) Breech; (3) Piston; (4) Hydraulic fluid inlet; (5) Tungsten carbide toroidal-profile anvils with 2° bevel angle; (6) Sample chamber. Note the scale

being particularly popular. The sample volume is very much larger than that compressible in a diamond anvil cell: the PE cell can compress 100 mm^3 to 10 GPa and 35 mm^3 to 30 GPa [76, 77]. And the open, opposed-anvil geometry facilitates working with samples loaded as liquids or condensed gases, like ammonia and methane [269–271]. Samples can also be contained in encapsulated gaskets [134, 135], which allow fluids to be compressed to higher pressures and thus makes it possible to use pressure-transmitting liquids or high-pressure gases [136]. A two-column, VX version of the cell, has been specifically designed for single-crystal diffraction studies [137]. This cell has recently been used to collect and refine full single-crystal data sets to 10 GPa for the first time, at both reactor and spallation neutron sources [78]. Despite the 70 kg mass of the cell, it could also be cooled to temperatures as low as 35 K using a closed-cycle refrigerator and a structural study has been carried out at 7 GPa and 35 K [78]. A smaller, 10 kg, version of the cell was successfully cooled to 10 K at 13 GPa (see section 3.3.4 below).

3.2 Pressure Calibration

Knowledge of the sample pressure is essential in all high-pressure experiments. It is vital for determinations of equations of state, for comparisons with other experimental studies and for comparisons with theoretical calculations. Unfortunately, one cannot determine the sample pressure directly from the applied force on the anvils and their cross-sectional area, as losses due to friction and elastic deformation cannot be accurately accounted for. While an absolute pressure scale can be obtained from the volume and compressibility, by integration of the bulk modulus [109], the most commonly-employed methods to determine pressures in crystallographic experiments are to use a luminescent pressure sensor, or the known equation of state of a calibrant placed into the sample chamber with the sample. W.B. Holzapfel has recently reviewed both fluorescence and calibrant data with the aim of realising a practical pressure scale to 300 GPa [138].

3.2.1 Laser-Induced Fluorescence

The optical access to the sample chamber in a DAC means that it is possible both to excite fluorescence in a material and to measure its wavelength. If the wavelength of the fluorescence is pressure dependent, and this pressure dependence is known, a measurement of the fluorescence wavelength can give a quick and simple determination of the pressure. The most commonly used fluorescence sensor is ruby (Cr-doped Al_2O_3), which fluoresces strongly when illuminated with a laser to give two strong R-line peaks at 692.86 and 694.25 nm [139–142]. The wavelength shift of these two R-lines was initially calibrated to 19.5 GPa against the calculated equation of state (EoS) of NaCl [141], and then to 180 GPa against the known EoS of a number of metals [22, 143, 144]. An example of a ruby R-line fluorescence spectrum obtained from a DAC containing Pr metal at 21.9 GPa [145] is shown in

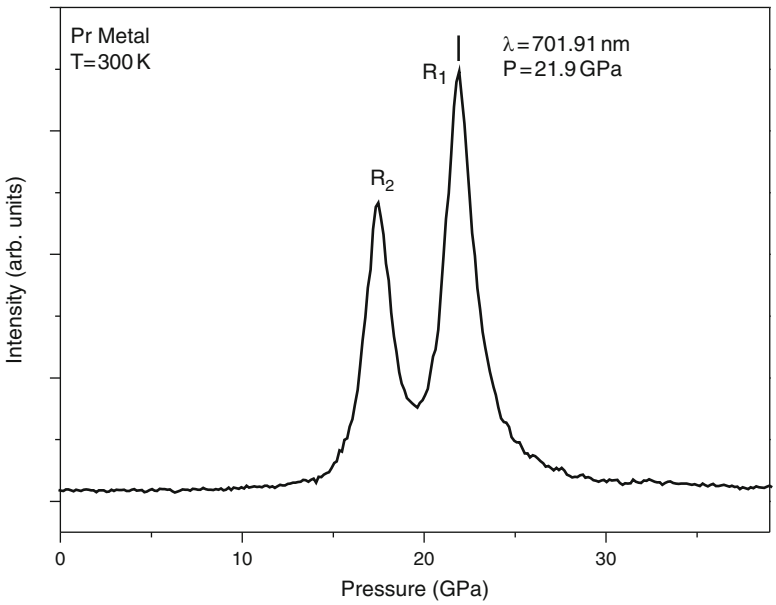

Fig. 3 Ruby R-line spectrum at 21.9 GPa and 300 K, as measured from a pressure cell containing Pr metal [145]. The total wavelength shift at this pressure is some 8 nm

Fig. 3. When subjected to non-hydrostatic pressure, the width of the R-lines increases [113, 139], and this has been used to determine the hydrostatic limits of a number of pressure transmitting fluids. An extensive review of ruby at high pressures has recently been written by K. Syassen [142].

One drawback of using the ruby-fluorescence method is that the wavelengths of the R-lines are strongly temperature dependent, and the fluorescence peaks both broaden and weaken in intensity at elevated temperatures [140]. There has thus been a search for alternative fluorescent sensors that do not have these problems. Amongst the most popular of these has been the use of rare earth doped fluorescent sensors, in particular Sm^{2+}:SrB_4O_7 [146–148]. This sensor has a single, sharp fluorescence peak at 685.4 nm, the wavelength of which is almost temperature independent. This material has been calibrated to 124 GPa [148], and is becoming increasingly popular for high-temperatures studies. Very recently, both diamond [149] and cubic-BN [150] have been proposed as further calibrants.

3.2.2 Equations of State

While fluorescent techniques enable the sample pressure to be determined quickly and easily, the precision of the technique is limited. Higher precision might be obtained from a determination of the lattice parameters of a calibrant included with the sample, and the pressure determined from that material's known equation of

state (EoS). This technique has the added advantage of enabling the pressure to be determined from the diffraction measurement itself, rather than making a separate optical measurement. However, the technique does have the drawback that the sample pressure can only be determined *after* the diffraction measurement, rather than the sample pressure being adjusted to a required value *before* the data collection.

The calibrant included with the sample should have a number of desired qualities. It should have high symmetry and a small unit cell (to reduce the number of diffraction peaks that might overlap those from the sample); its volume should be strongly pressure dependent in order to maximise pressure sensitivity; it should not react with the sample or the pressure transmitting fluid; and it should be strongly scattering so that little of the calibrant is needed. Popular materials include NaCl [151], quartz [152] and a number of cubic elemental metals such as Pt, Au, Cu and Ta [153, 154]. The latter materials are most widely used for ultrahigh-pressure studies.

3.3 Diffraction Techniques

There are four principal methods of determining crystal structures at high pressures employing powders or single-crystals, using X-rays or neutrons. Here I will give a brief review of the relevant diffraction techniques and analysis methods used with each technique, focusing on recent developments.

3.3.1 X-Ray Powder Diffraction

While this has long been the most popular method to study crystal structures, it was not until the introduction of ADXRD on synchrotron sources in the 1990s that it became routine to determine atomic position parameters using this technique at high pressure. While such studies have been performed principally at synchrotron sources, laboratory-based studies have also been performed; see for example [155–158].

The use of powder samples greatly simplifies sample loading. In addition, since many pressure-induced phase transitions are strongly first order (the Si-I to Si-II phase transition at 11.4 GPa has a volume change $\Delta V/V_{\text{trans}}$ of 20.4% [159]), samples which are initially loaded as single crystals do not typically remain single crystals as the pressure is increased. As described in Sect. 2, prior to 1990 high-pressure powder-diffraction studies were typically conducted using energy-dispersive diffraction (EDX) techniques at synchrotron sources in which a polychromatic incident beam was diffracted at a fixed angle (defined by tightly-collimating slits) into an energy-resolving detector (see for example, [160]). Although the extremely high intensity of the "white" synchrotron beam meant that this technique could be used to pressures in excess of 300 GPa [23], the relatively poor energy resolution of the detector, and the very tight collimation of both the incident and diffracted beams, meant that the diffraction patterns have

broad peaks, and the powder averaging of the sample (the number of diffracting crystallites) was poor. Combined with the many wavelength-dependent corrections that need to be applied to the data (for example, sample and pressure cell absorption, scattering power, detector efficiency), these limitations meant that accurate intensities were not measurable. "Structure" determination thus remained at the level of lattice type or structure type, e.g. tetragonal, "β-tin" or "distortions" thereof. The term "distorted" typically meant that additional reflections were observed, but were not interpretable.

The advent of angle-dispersive techniques with full conical-aperture DACs revolutionised powder diffraction [30]. The technique uses monochromatic radiation, and a highly-sensitive image-plate detector to collect the 2D Debye-Scherrer (D-S) pattern [28, 29]; see Fig. 4a. This is then integrated azimuthally to provide a standard 1D diffraction profile (Fig. 4b) which has high resolution, and, because of the averaging around the D-S rings, both accurate peak intensities and an extremely high signal-to-noise [30, 161, 162]. The image-plate techniques were first utilised with DACs designed for energy-dispersive studies – which required only narrow slot-apertures in the pressure cell body in order to provide access and egress for the X-ray beam [28]. But such cells enabled only a small portion of the D-S pattern to be collected, and integrated azimuthally. Developments at the SRS synchrotron in the UK made three significant improvements on the original methods [29, 30]. Firstly, the introduction of DACs with full conical apertures allowed the full two-dimensional D-S pattern to be collected, leading to greatly improved signal-to-noise. These DACs, which were originally designed for single-crystal diffraction studies, used Be seats for the diamond anvils. Although such seats are inherently weaker than the tungsten carbide used for slot-aperture seats, the use of specially hardened Be allowed these cells, which had full conical apertures of $4\theta = 80°$, to be used to pressures above 25 GPa [163], eventually reaching 75 GPa or more.

Second, shielding, collimation and alignment methods were developed to the extent that all non-sample scattering was removed from the data. This enabled extremely weak sample reflections to be uncovered, which revealed the unexpected structural complexity that had previously been masked by the lower-quality energy-dispersive data. Thirdly, the first GUI interactive software for integrating full two-dimensional images was developed [30, 162].

The resulting increase in data quality is illustrated in Fig. 5, which shows a comparison of ADX and EDX data from the same sample of InSb. The quality achieved was such that more sophisticated techniques could be applied, such as the use of anomalous scattering to distinguish similarly-scattering elements, like In (Z = 49) and Sb (Z = 51) [164, 165]. And the combination of the high-resolution 2D data and the GUI software made it possible to distinguish mixed phases simply from the difference in appearance of the diffraction rings [164, 245].

The 1D diffraction profiles are also ideally suited to profile refinement, as illustrated in Figs. 9 and 13 in Sect. 4, from which atomic coordinates can be obtained using standard Rietveld methods.

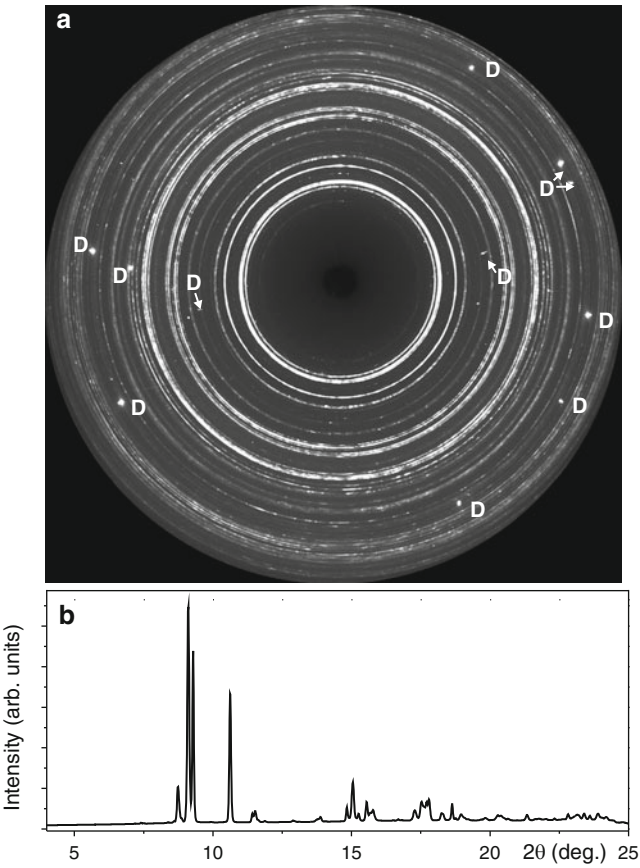

Fig. 4 (**a**) 2D diffraction pattern collected from a polycrystalline sample of orthorhombic Pr-VII at a pressure of 19 GPa [145]. The data were collected in a 2 s exposure on beamline ID09 at the ESRF synchrotron, during which the diamond anvil pressure cell was oscillated ±9° to improve the powder averaging. This large oscillation angle resulted in the appearance of a number of Bragg reflections (marked with a D) from the anvils of the pressure cell. (**b**) The resulting 1D diffraction profile, after azimuthal integration of the 2D pattern using Fit2D [161]. The diamond reflections were omitted from the integration

The ability to collect the full 2D diffraction profiles had an additional, but unexpected, benefit. In studies of the III–V semiconductor InSb, it became immediately clear that samples which were very good powders when loaded, giving smooth D-S rings, could sometimes recrystallise at high pressure, giving very "spotty" diffraction patterns [164]. However, the later discovery that this phenomenon was relatively widespread led to more systematic use of it to identify phases that might be grown as single-crystals at high pressure simply by compression at room temperature, rather than by growing crystals from the melt. The prospect thus opened up of single-crystal studies beyond the first-order phase transitions that had been thought to prohibit such studies. The exact "recipe" for growing a useful single

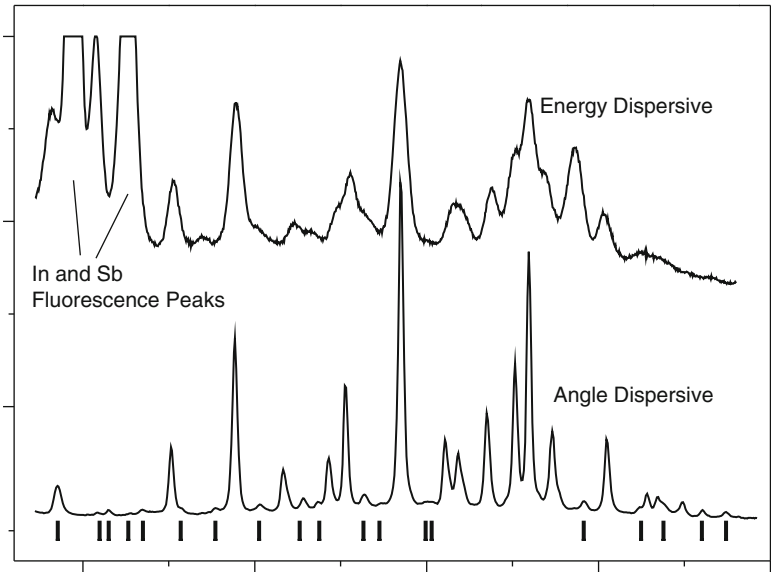

Fig. 5 Diffraction profiles collected from the same powdered sample of InSb at ~2 GPa, using (*top*) energy- and (*bottom*) angle-dispersive diffraction. The angle-dispersive data clearly have higher angular resolution, and are not contaminated by X-ray fluorescence peaks. The *tick marks* below the angle-dispersive data mark the positions of some of the weak superlattice reflections that were essential to determining the structure of the InSb-IV phase [165]

crystal by recrystallisation is different from sample to sample. For example, in Ba a single crystal of the high-pressure phase Ba-IV can be grown by increasing the pressure *very* slowly through the Ba-II to Ba-IV phase transition at 12 GPa [166]. And in Bi, a single crystal of Bi-III can be grown by first increasing the pressure on a quasi-single-crystal of Bi-I into the higher-pressure Bi-V at ~10 GPa, before slowly reducing the pressure through the Bi-V to Bi-III phase transition at ~8 GPa [167].

3.3.2 X-Ray Single-Crystal Diffraction

As described previously, the invention of the small, gasketed Merrill-Bassett DAC in 1974 meant that single-crystal studies could be performed on standard single-crystal diffractometers [18]. Such studies require as wide an access as possible to reciprocal space, and in the Merrill-Bassett DAC the diamond anvils thus sit on beryllium anvil seats, which are highly transparent to X-rays [18]. Optical access to the sample is via a small (~1 mm) axial hole in the Be seat. While such an arrangement provides greatly increased angular access on both incident and diffracted sides of the cell, the tensile strength of Be is quite low, limiting the pressures available with such cells to ~10 GPa. It was such Be-equipped cells that were

used for the initial development of angle-dispersive powder-diffraction methods [30, 31]. Improved designs of single-crystal DACs, incorporating a piston-cylinder arrangement and using harder Be seats, enabled pressures of 75 GPa to be reached.

While the Be-equipped cells provide wide angular access, the seats introduce complications. First, Be is toxic and care must be taken when working with the discs. Second, the seats introduce additional angle-dependent absorption that must be corrected for [168]. Third, the illumination of the Be seat nearest the detector by the straight-though X-ray beam results in an intense Be powder-diffraction pattern that is superimposed on the single-crystal diffraction pattern. While much of this scatter can be removed by a collimator fitted to a point detector, this is not possible when using a 2D area detector. Finally, the strength of the Be discs reduces markedly at high temperatures, limiting the scope of Be-equipped cells for combined high-pressure high-temperature studies.

The limited angular-access provided by even Merrill-Bassett DACs means that single-crystal data collection strategies need to be optimised in order to ensure that all possible reflections are measured. For point detectors, the best method is the so-called "fixed-phi" data collection strategy in which the azimuthal angle at which each reflection is measured is chosen so that the DAC's cylindrical axis is always in the diffraction plane [168]. This is therefore not the commonly-used bisecting geometry, and results in a greatly increased volume of reciprocal space being available, while simultaneously reducing the absorption of the pressure cell.

Since 1990, four significant advances in technology and techniques have resulted in single-crystal studies being extended to above 150 GPa. The first of these was the availability of affordable CCD detectors. While these have revolutionised crystallography in general, by greatly speeding up data collection times and giving better quality data, their use at high pressures has been particularly beneficial [169, 170]. Since high-pressure samples are necessarily small, and the backgrounds from the pressure cells are high, then the increase in signal-to-noise afforded by the use of such detectors is universal in high-pressure studies.

In the mid 1990s, chemical crystallography beamlines equipped with commercially-available CCD-equipped diffractometers started to appear as user facilities on synchrotron sources. These facilities offered a ~1,000-fold intensity increase over laboratory-based X-ray sources, and were thus perfectly suited to high-pressure studies [65, 66]. The ability of CCD-based methods to collect full single-crystal data sets *prior* to the determination of the UB orientation matrix meant that data collection times were decreased still further, as valuable synchrotron beamtime did not have to be expended on alignment and UB matrix determination. The ability to collect all of the accessible reciprocal space on the CCD detector also means (as it does with ambient pressure studies) that satellite peaks and other features are collected automatically. Given the large number of high-pressure studies that were later to show incommensurate phases, this ability has proved invaluable.

As discussed previously, the anvil seats on which the diamond anvils are mounted have traditionally been made of X-ray transparent beryllium (Fig. 6a), although other hard, low-Z materials have also been used, such as B_4C and BN. The disadvantage of all of these is the large background scatter that arises once the

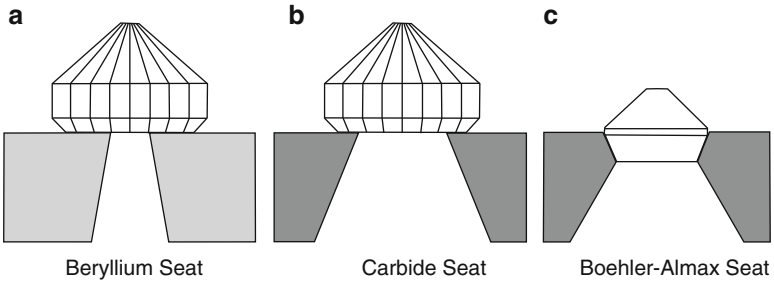

Fig. 6 Schematic diagrams of the different types of anvil seats used in diamond anvil cells. In seat (**a**), the anvil sits on X-ray transparent beryllium. The small hole in the seat is for optical access only, as X-rays can pass through the seat with little absorption. In seat (**b**), the anvil sits on X-ray opaque tungsten carbide. The aperture in the seat needs to be significantly larger than in (**a**) in order to allow the X-rays to enter or exit the pressure cell over a sufficient angular range. The size of the aperture results in greatly reduced support to the base of the anvil. In seat (**c**), the anvil has a double-conical shape and is recessed into the tungsten-carbide seat. This design allows a wide-angle aperture, while still strongly supporting the anvil. (Adapted from [171])

straight-though X-ray beam hits them. One can reduce the scatter by having as wide an optical aperture as possible, but the seats are then mechanically weak, limiting the upper pressure range of single-crystal studies (Fig. 6b). These problems have been solved completely by the use of so-called Boehler–Almax anvil seats [119], in which the anvil has a double-conical shape, and fits into a conical aperture in the seat (Fig. 6c). The result is a much stronger design in which wide-angle apertures can be obtained from a seat made only of tungsten carbide [68]. Using such seats, it is possible to utilise wide-angular openings to pressures above 150 GPa, giving high quality single-crystal data at such pressures [92]. While still higher pressures may require the angular aperture to be reduced, the limitations imposed by this might be overcome by the use of short-wavelength X-rays to "compress" reciprocal space.

These developments have all been used in the development of single-crystal crystallographic studies at third generation synchrotron sources such as the ESRF, APS and SPring-8. The high-energy radiation from such machines can be focussed to beams of only a few microns in diameter, meaning that single-crystal studies might be performed where the beam was smaller than the actual sample crystal. (This is in contrast to the "normal" way of collecting single-crystal data in which the entire crystal is bathed in an X-ray beam that is larger than the sample.) This has enabled single-crystal studies to be performed from samples within gasket holes only 15 μm in diameter, in which there is little, if any, diffraction pattern from the gasket itself [91, 92]. The beamlines at such synchrotrons also lend themselves to the use of large experimental apparatus, such as heating stages and cryostats. Single-crystal studies are now thus possible over a very wide range of pressures and temperatures. As a result, such studies are now limited only by the availability of suitable samples, not by the technical limits of collecting and analysing the data.

3.3.3 Neutron Powder Diffraction

As with X-ray diffraction studies, the simplicity of powder methods means that such studies have proved more popular than single-crystal neutron studies. Diffraction data have been collected using both angle- and energy-dispersive methods, typically at reactor and pulsed (spallation) neutron sources, respectively. However, the early high-pressure study of Bi by Brugger et al. [172] used a reactor source but with a mechanical chopper in order to utilise time-of-flight diffraction methods. While detailed crystallographic studies were conducted using neutron powder-diffraction methods prior to 1990, using both high-pressure gas [173, 174] and clamped piston-cylinder [175, 176] cells, the upper pressures were limited to some 1 GPa for gas cells, and 2–3 GPa for clamped cells.

The scattering of the neutrons from the pressure cell body and/or anvils can be greatly reduced, or removed completely, in energy-dispersive experiments performed on spallation neutron sources by collecting the diffraction data at 90° to the incident beam. With careful collimation of both incident and diffracted beams, only the sample is both illuminated by the incident beam and viewed by the detector. The P-E cell, when used on such a source, is mounted so that the incident beam is incident through one anvil, while the diffracted beam exits at 90° through the gasket (see Fig. 2). This enables very high quality diffraction data to be collected, free from contamination from the pressure cell components. The data can also be corrected accurately for pressure cell absorption and other systematic errors [177], with the result that accurate relative peak intensities can be collected to very high scattering vectors. At the ISIS facility, this ability has been used to make detailed studies of crystalline samples, for example ammonia and gas hydrates [102, 178–180], as well as both liquid water [181], and the various forms of amorphous ice that exist at high pressures and low temperatures [182, 183].

In angle-dispersive studies, using the high-pressure gas or piston-cylinder clamped cells, an intense background can arise from the cell body. However, the contaminant diffraction peaks are typically few in number, arising from Al or Al_2O_3, and those regions of the diffraction pattern are typically omitted from a Rietveld fit. The intensity of these peaks can be greatly reduced by increased collimation of the detectors. When P-E cells are employed on reactor sources, the use of highly-absorbing boron nitride anvils results in almost all of the scattering from the anvils being absorbed, giving high quality diffraction profiles, ideally suited to Rietveld refinement [184].

3.3.4 Neutron Single-Crystal Diffraction

As with neutron powder methods, both monochromatic and time-of-flight (Laue) techniques have been used for single-crystal neutron studies. Such studies are much less numerous, however, as a result of the difficulty of compressing suitably sized (>1 mm^3) single-crystal sample to the required pressure while maintaining the crystal quality. The piston cylinder cell design of McWhan and others [128] has been used at the ILL reactor source for a number of neutron structural studies to

~2 GPa [185, 186]. As the design of this cell has limited access for the incident and diffracted beams, data collection is limited to perhaps only one layer of reciprocal space (although a few reflections from other layers might be visible if the crystal is slightly tilted relative to the window in the cell body). The crystal must thus be mounted in the cell so as to have the reflections of interest accessible, and also aligned so that the reflections remain visible as the pressure is increased. Other (perhaps perpendicular) layers of reflections can be obtained using crystals with different orientations. Data collection using this cell does not require a four-circle diffractometer, and a lifting-counter diffractometer has been used successfully at the ILL [185, 186]. Although the pre-compressed Al_2O_3 cylinder within these cells produces an intense background, the effected regions of the diffraction pattern are omitted from the fit.

Prompted by the success of the DAC, opposed-anvil cells equipped with large, normally sapphire, anvils have been used in a number of high-resolution diffraction studies that have used classical four-circle diffractometers [187–189] to perform high quality studies to above 2 GPa. The quality of the data is excellent, particularly if collected using small area detectors which became available in the late 1980s [190], and the use of which is now widespread.

Using the VX variant of the P-E cell, specifically designed for single-crystal diffraction [137], Bull et al. have recently pushed high-resolution single-crystal structural studies above 10 GPa using time-of-flight techniques at the ISIS neutron source and crystals with volumes of several mm^3 [78]. Careful design of the anvil geometry was necessary in order to be able to correct for their considerable absorption [191]. One disadvantage of the standard P-E anvils is that they are either sintered WC or sintered diamond, both of which are optically opaque. It is therefore not possible to inspect visually the single crystal on compression, nor to be able to monitor the sample chamber in order to grow single crystals in situ from, say, the melt. Again, using the VX variant of the P-E press, Bull et al. have overcome this by using anvils which are large synthetic diamonds with a culet size of 3 mm [192]. This enabled them to monitor the growth of a single-crystal of ice-VI as it was grown from the melt at 1.3 GPa. The structure was subsequently studied at 1.3 GPa and 10 K. Very recently, the same authors have performed single-crystal studies on the D9 diffractometer at the ILL in full 4-circle geometry to 3 GPa, with the small pressure cell mounted on the chi-circle, and to 10 GPa with a larger pressure cell mounted on the omega circle and a lifting arm detector in normal-beam geometry. They have also made preliminary studies at ISIS to 17 GPa using Ar as a pressure transmitting medium.

Although the VX variant of the P-E press was designed specifically for single-crystal studies, and has wider angular apertures than the original design, large segments of reciprocal space are still obscured by the frame press. This has been overcome by the development of a rotation mechanism that allows the anvils to be rotated within the frame of the cell, while maintaining the load on the sample, to allow much greater access to reciprocal space for single-crystal studies [193].

The advantages of using polychromatic radiation from a reactor source, coupled with Laue diffraction methods, have been investigated by McIntyre et al. for high-pressure studies [194]. Using a 0.5-mm^3 crystal in a moissanite anvil pressure cell

(but at atmospheric pressure), a full data collection was taken in only 3 h, resulting in the collection of over 600 unique reflections.

3.3.5 Non-Ambient Temperature Studies

The close link between high-pressure crystallography and mineralogy has meant that high-pressure high-temperature (HP–HT) studies have long dominated over high-pressure low-temperature studies [195]. The overwhelming majority of these HP–HT studies have employed powder methods, as these avoid many of the problems that arise when having to rotate a pressure cell equipped with electrical leads and piping for water-cooling. However, almost all the methods employed for powder studies are applicable to HP–HT single-crystal methods.

For diamond anvil cells, heating comes in two distinctive forms, resistive and laser, with the former being more convenient although the upper temperature is considerably less than that obtainable with lasers. Both techniques were pioneered by W.A. Bassett and his coworkers [196, 197]. Two recent reviews [198, 199] provide an excellent introduction to HP–HT methods.

In resistive heating, the thermal conductivity of the cell body, diamonds and gasket are used to transfer heat from a resistive heater to the sample chamber. The heater can either be external to the pressure cell, and thus heat the whole cell body, or it can be internal, with its heating localised to the gasket and diamonds [196, 199–201]. External heaters of the appropriate size can be purchased commercially, and may need to be quite powerful in order to the heat the entire cell to 1,000 K. However, heating the entire cell body will undoubtedly lead to heating of the thrust mechanism of the cell, which may result in significant pressure loss on heating. This can be overcome by using a DAC that utilises a gas membrane to generate the thrust mechanism, allowing the gas pressure in the membrane to be adjusted on heating in order to maintain a constant pressure [202].

Internal resistive heating, where a miniature heater is placed inside the pressure cell, requires considerably less power than external heaters. A number of internal heater designs in which the heating element is either attached to the gasket [203], is part of the gasket [204], or is inside the sample chamber itself [205–207] have been described. Care must be taken to ensure that the heater is electrically insulated from the gasket and other metallic components. Resistively heated cells can attain temperatures as high as ~2,700 K [207], particularly if both internal and external heaters are employed.

As stated, HP–HT studies using single-crystal samples have proved much rarer than those utilising powder methods, because of the additional constraints that arise when collecting single-crystal data. The main difficulty was the softening of the beryllium seats at high temperatures, and the need to replace them with either more strongly-absorbing boron carbide [208] or tungsten carbide seats with reduced apertures. The recent advent of Boehler–Almax anvil seats has removed these constraints, allowing high quality single-crystal data to be collected at high temperatures and pressures [97, 100].

If one wants to attain temperatures higher than those attainable with resistive heating, then this can be achieved with laser heating, in which either ~1-μm or ~10-μm infrared radiation from Nd:YAG or CO_2 lasers, respectively, is focused onto the sample. The focus spots can be as small as ~10 μm across, with temperature gradients of many 100 s of K per micron. To ensure as uniformly heated spot as possible, the sample should be heated from both sides simultaneously, and the lasers defocused slightly, or passed through beam-shaping optics, to increase the size of the heated region, and to give more uniform heating. It is essential that the X-ray beam be centred precisely within the heated spot, thereby ensuring that the diffraction data are collected only from the heated region. Recent advances in laser technology have resulted in a move to fibre lasers, the small size of which adds a flexibility that is well suited to installation on synchrotron beamlines. Using two such lasers, Tateno et al. have recently obtained high quality diffraction data from iron at 377 GPa and 5,700 K, which corresponds to Earth inner-core conditions [209]. There is an extremely large number of papers describing laser-heating systems, and the reader is pointed to the review of Eremets [109] and the recent papers by Prakapenka et al. [210], Dubrovinsky et al. [211] and Goncharov et al. [212] for more details of the technique.

Resistive heating techniques have also been widely used in pressure cells suitable for neutron diffraction studies. However, additional problems are raised by the necessity of having to keep the larger-volume samples necessary for neutron-diffraction studies heated for the typically longer data collection times. Using an internal cylindrical furnace held within the gasket, the P-E press has been used for neutron diffraction studies to 10 GPa and 1,500 K [135, 213–216]. Neutron radiography was used to determine the temperature in the furnace with a precision of ±20 K. A P-E press, combined with a T-cup multi-anvil stage, has been developed for angle-dispersive X-ray power diffraction studies to 25 GPa and 2,000 K [217].

Low-temperature studies have typically been more popular in high-pressure neutron diffraction studies than in X-ray studies, perhaps because of the combined use of neutron scattering techniques and low temperatures to study magnetism. All of the various pressure cells used for neutron diffraction studies can be cooled with liquid-He cryostats or closed-cycle refrigerators. The P-E press has also been cooled more simply by direct liquid-N_2 cooling, with good temperature control then possible between 77 and 200 K. High-pressure low-temperature crystallographic studies using X-rays have proved somewhat rarer, although more studies are appearing as cryostats have begun to appear on some high-pressure synchrotron beamlines as standard sample environment equipment [218, 219].

4 Experimental Examples

The following four examples have been chosen to illustrate the variety of different crystal structures now being found in simple materials at high pressure, and the quality of diffraction information that was necessary to solve the crystal

structures. All are taken from our own studies, using X-ray powder and single-crystal diffraction.

4.1 Incommensurate Te

The high-pressure behaviour of tellurium exhibits many of the phenomena induced in materials by compression. It undergoes a pressure-induced semiconductor to metal transition [220]; it has numerous high-pressure phases with low-symmetry structures [221]; it becomes a superconductor with a T_c that is highly pressure dependent [222]; and it has an unusual melting curve [223]. These features have prompted a wide range of resistivity [220], diffraction [16, 221, 224–226], density [227], optical [228], superconductivity [222, 229] and theoretical [230] studies. But despite these, the actual atomic structures of the high-pressure phases have long remained unclear. In particular, the structures of Te-III, reported to be stable between ~7 and 10.6 GPa, and Te-IV, stable between 10.6 and 27 GPa, were unclear, with Te-III being reported as orthorhombic and Te-IV as rhombohedral [221]. However, more recent studies reported that Te-III and Te-IV were one and the same phase, and that this was monoclinic [231], although numerous weak diffraction peaks still remained unaccounted for.

An X-ray powder-diffraction pattern from Te-III at 8.5 GPa collected at the SRS synchrotron is shown in Fig. 7. The quality of the pattern is excellent, with sharp

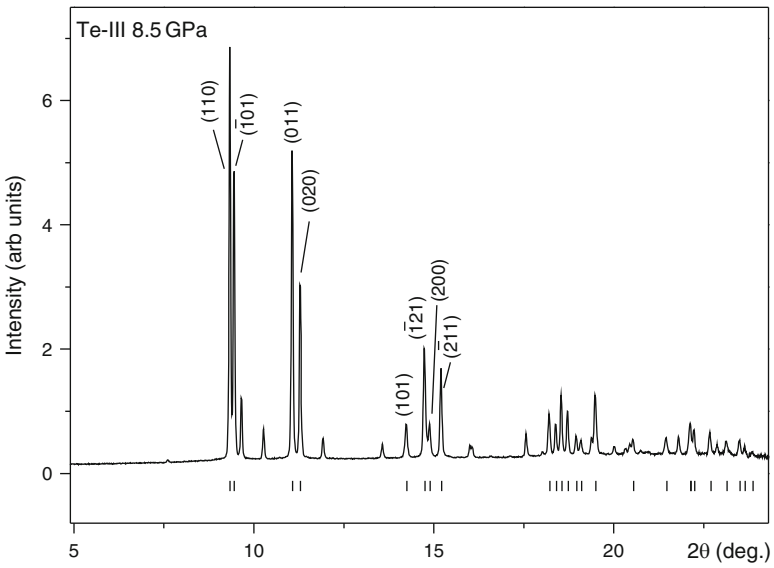

Fig. 7 Diffraction profile collected from Te-III at 8.5 GPa. The data were collected on beamline 9.1 at the SRS synchrotron, with an exposure time of 23 min. The *tick marks* beneath the profile identify those reflections that are explained by the body-centred monoclinic unit cell

diffraction peaks on a low, flat background. However, powder indexing methods were completely unable to index all the peaks in the pattern, despite numerous and lengthy attempts. However, when compressed further, it was noticed that some peaks reduced in intensity, while others coalesced into single peaks. Indexing of only the latter revealed that their positions were all accounted for by a very simple body-centred monoclinic unit cell with lattice parameters $a = 3.9189(3)$ Å, $b = 4.7334(4)$ Å, $c = 3.0617(2)$ Å, and $\beta = 113.525(6)$ at 8.5 GPa [232]. But this solution still left some 16 peaks unaccounted for, as illustrated in Fig. 7. Attempts to fit these reflections as either a different phase, or as superlattice of the monoclinic cell, were unsuccessful.

By 9 GPa, tellurium has passed through two phase transitions, and the atomic volume has been reduced to less than 80% of the ambient value [233]. Despite this, we attempted to load and pressurise a single-crystal of Te-I with the aim of obtaining a single-crystal of Te-III that we could use to obtain more structural information on the phase. After 29 attempts, we finally succeeded in obtaining a twinned single-crystal of Te-III, part of the diffraction pattern from which is shown in Fig. 8. From the d-spacings of the reflections it was immediately clear that the strongest Bragg peaks were those accounted for by the body-centred monoclinic cell, while the weaker satellite reflections were the same as those we were unable to account for in the powder data. Analysis of the positions of these satellite peaks revealed they were all located in the same relative position to the main Bragg peaks at $(h, k \pm q, l)$ with $q \sim 0.3$: Te-III is incommensurate [232]. It should be noted that a full single-crystal data set was not collected from the Te-III crystal, nor was it necessary. The single image in Fig. 8 was sufficient to determine the incommensurate nature of the phase.

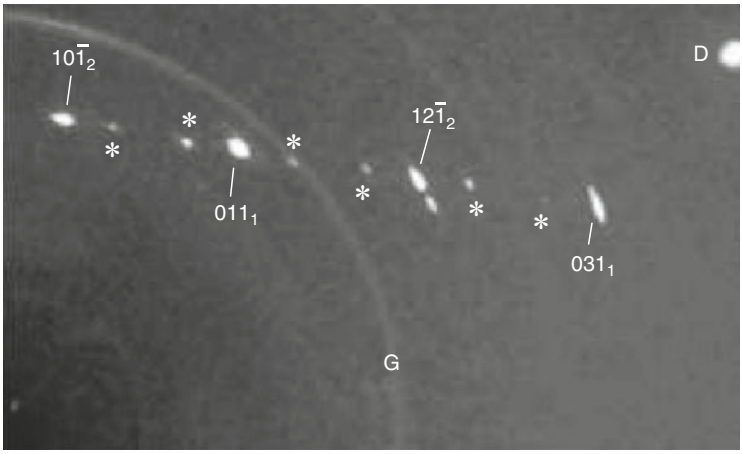

Fig. 8 Part of the 2D diffraction pattern obtained from a twinned single-crystal of Te-III at 7.4 GPa. The main body-centred monoclinic reflections from the two twin components are shown, indexed $(hkl)_1$ and $(hkl)_2$. The satellite reflections are marked with *asterisks*, and a powder line from the tungsten gasket is marked "G". "D" marks a reflection from one of the diamond anvils

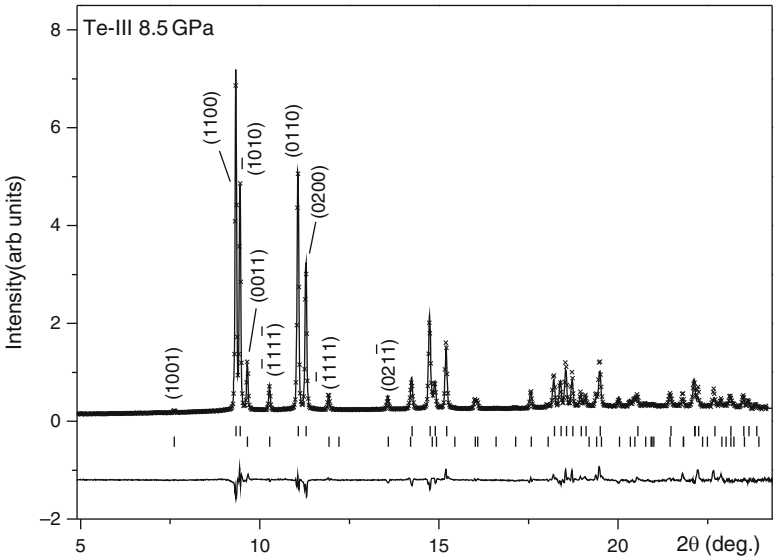

Fig. 9 Rietveld refinement of incommensurate Te-III at 8.5 GPa. The *upper* and *lower tick marks* below the profile mark the peak positions of the main and first order satellite reflections, respectively. The reflections shown in Fig. 8 are identified by their (*hklm*) indices, where the main reflections are indexed (*hkl*0)

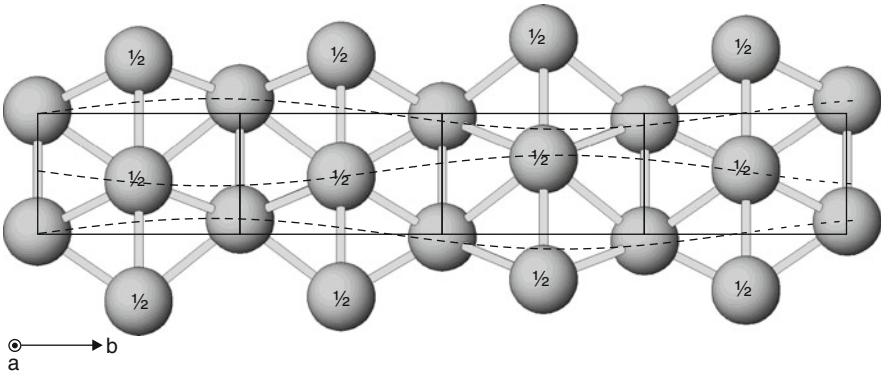

Fig. 10 Four unit cells of Te-III at 8.5 GPa, as viewed down the *a* axis. The six nearest-neighbour contact distances for each atom are shown, and those atoms at the body centres are labelled with "1/2". The modulation wave is indicated by the *dotted lines*

Once Te-III was identified as incommensurate, subsequent analysis was conducted on the previously-collected powder-diffraction data using the formalism of 4D superspace [234], and the JANA2000 software for structure refinement [235]. The Rietveld refinement of the incommensurate Te-III diffraction profile is shown in Fig. 9, and the modulated structure is shown in Fig. 10. Tellurium was only the second element found to have a modulated crystal structure at high-pressure, the

first, in iodine, having been discovered only 5 months before [51]. The incommensurate Te-III structure has since been found in selenium between 29 and ~80 GPa [236, 237], and in sulphur between 80 and 150 GPa [237, 238]. Sulphur was the first element shown to have an incommensurate form above 100 GPa.

4.2 Incommensurate Sc

Scandium, the first of the 3*d* transition metals, undergoes a phase transition from the ambient-pressure hexagonal-close-packed phase to a high-pressure superconducting form, Sc-II, at 21 GPa. The structure of this high-pressure phase has long been uncertain, despite the diffraction pattern from Sc-II being extremely simple (Fig. 11). Using energy-dispersive diffraction methods, the structure was initially reported as tetragonal [239–241], while a later study reported a large 24-atom body-centred cubic unit cell and a structure comprising icosahedral clusters [242]. However, our own data collected at the SRS synchrotron showed none of these structures to be correct (Fig. 11), although we were unable to determine the true structure. In 2005, Fujihisa et al. [243] solved Sc-II as having an incommensurate host–guest composite structure very similar to that we had reported previously in high-pressure Ba-IV, Sr-V, Bi-III and Sb-II [167, 244, 245]. This structure is shown in Fig. 12 and comprises an eight-atom tetragonal "host" structure that contains channels running along the *c*-axis. Contained within these channels are 1D

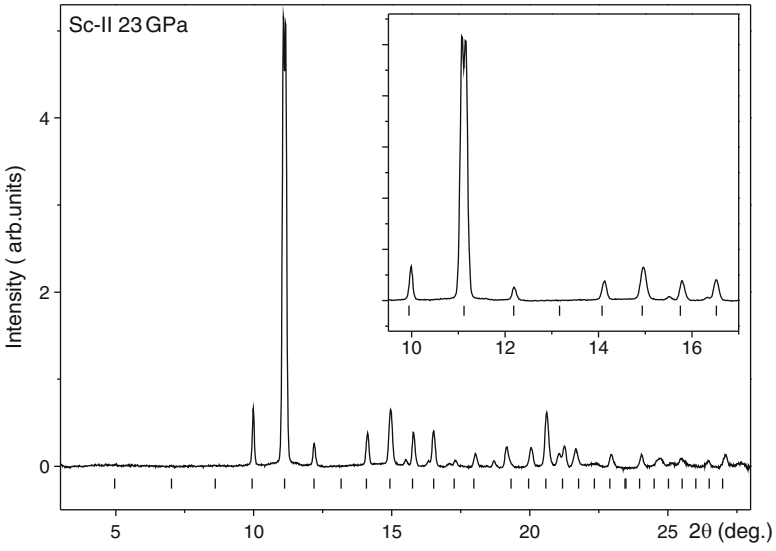

Fig. 11 Diffraction profile from Sc-II at 23 GPa obtained on beamline 9.5 at the SRS synchrotron using an exposure time of 25 min. The *tick marks* show the calculated peak positions for the best-fitting body-centred cubic cell [242]. The *inset* shows an enlarged view of the low-angle part of the profile, highlighting the doublet peak at $2\theta \sim 11.1^\circ$ which is not accounted for by the cubic unit cell

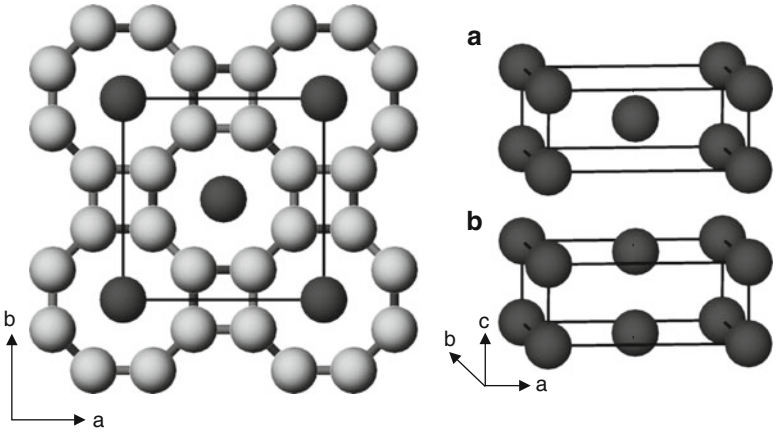

Fig. 12 The composite incommensurate structure of Sc-II, as viewed down the *c* axis. The eight-atom host framework is shown in *grey*, and the ID guest chains are shown in *black*. The *insets* show perspective views of (**a**) the body-centred guest structure of Fujihisa et al. and (**b**) the C-centred guest structure of McMahon et al. The crystallographic axes are labelled

chains of "guest" atoms that comprise the guest structure, the spacing of which is incommensurate with the host along *c*. In Sc-II the guest structure was reported to be body-centred tetragonal, as in Bi-III and Sb-II (Fig. 12a).

However, close analysis of the structural parameters of the host–guest structure reported by Fujihisa et al. [243] showed that at 23 GPa the distance between the guest atoms in the ID chains was only 2.285 Å, some 18% shorter than the average distance between the nearest-neighbour atoms in the host structure, and that this difference increased to 21% at 101 GPa, where the guest–guest spacing was only 1.957 Å. This behaviour was quite unlike all the other composite structures found to that time, where the guest–guest spacing differed from the host–host spacing by no more than 2%. This problem was noted by Fujihisa et al., who suggested that the short guest–guest spacing might arise from a difference in the electronic structure of the host and guest atoms. Analysis of our own Sc-II powder data revealed that an almost identical fit could be obtained by a host–guest structure comprising the same eight-atom host structure as Fujihisa et al., with $a = 7.5672(1)$ Å, $c = 3.4398(2)$ Å at 23 GPa, but with a C-face-centred tetragonal guest with $a = 7.5672(1)$ Å, and $c = 2.686(1)$ Å, and thus a guest–guest spacing of 2.686(1) Å [246]. A fit to the same data using the body-centred guest structure of Fujihsa et al. gave a guest–guest spacing of only 2.288(1) Å. Surprisingly, despite the two guest structures having very different unit cell parameters, and indeed very different symmetries, peak overlap between the host and guest reflections meant that both structures gave almost identical powder-diffraction patterns, although the C-face-centred solution gave a very slightly better overall fit to the data, and also explained a subtle asymmetry in a high-angle peak [246]; see inset to Fig. 13.

Because of the very different cell dimensions and symmetries of the two guest structures, they could be distinguished trivially using single-crystal data, as their

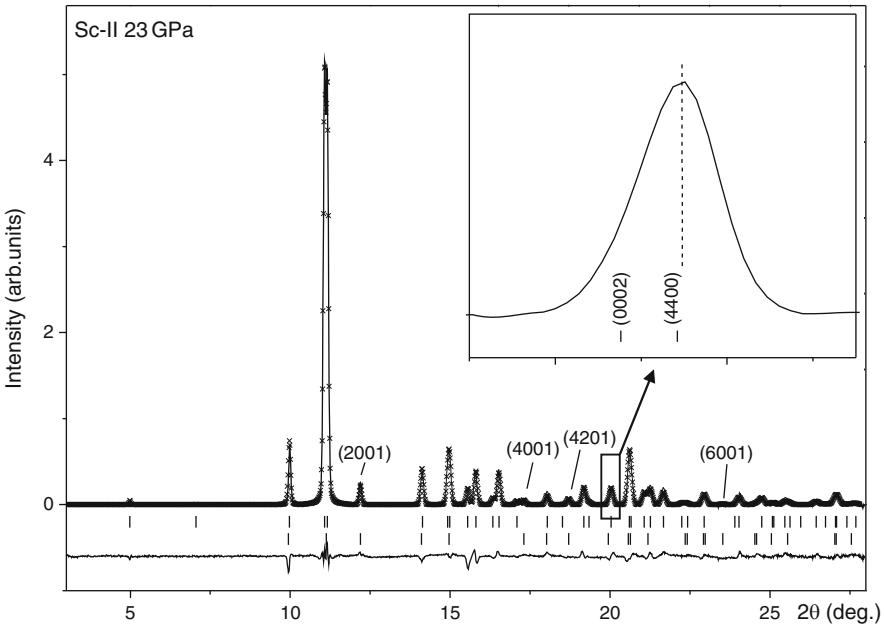

Fig. 13 Rietveld refinement of Sc-II at 23 GPa using the C-centred guest structure. Reflections are indexed using their *hklm* indices. The *upper tick marks* show the calculated peak positions for (*hkl*0) host reflections and (*hk*00) host/guest reflections, and *lower* ones mark (*hk*0*m*) guest-only reflections. The difference between the observed and calculated profiles is shown below the *tick marks*. The *inset* shows an enlarged view of the asymmetric peak at 17.5°, showing that it is accounted for by the (4400) and (0002) peaks. The *vertical dashed line* is a guide to the eye

diffraction patterns would be completely different, even though the diffraction peaks from the two phases have very similar d-spacings (Fig. 14). However, Sc is a hard metal, and preparing a small single crystal of Sc-I, and then compressing it to >20 GPa through the Sc-I to Sc-II transition such that the sample remained a single-crystal, seemed unfeasible. However, we noted that while the diffraction pattern from a small piece of Sc-I gave a perfect powder pattern, the diffraction rings from the same sample in the Sc-II phase were slightly "spotty", suggesting a degree of recrystallisation of the sample at the transition. We had seen this previously in InSb [164], and particularly in Ba [244], where the degree of recrystallisation was such that we were able to grow a single-crystal of the Ba-IV phase. Compressing a small piece of Sc in a helium pressure transmitting medium, rather than the mineral oil medium used in our initial study, revealed significant recrystallisation at the Sc-I to Sc-II transition, such that layer lines of reflections were clearly visible in the Sc-II diffraction patterns (Fig. 15). These had the very distinctive pattern of diffraction peaks from a host–guest structure, and analysis of those reflections from the guest component of the structure revealed them to be completely consistent with a C-face-centred, rather than a body-centred guest.

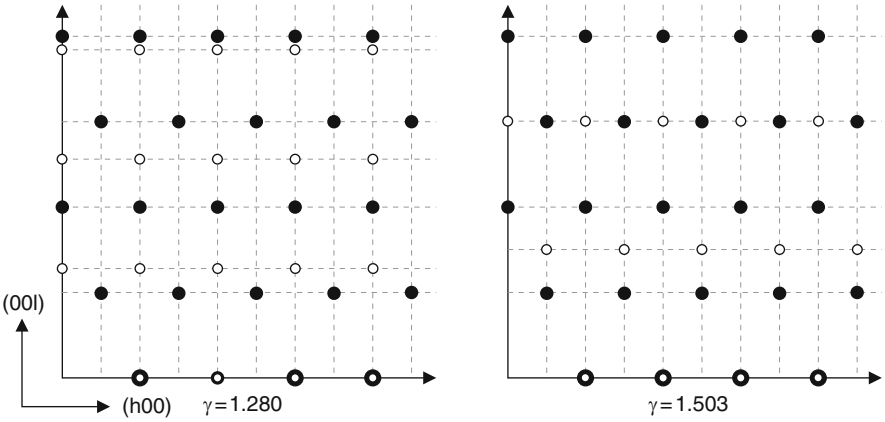

Fig. 14 The (*h*0*l*) reciprocal lattice planes of the composite structure of Sc-II, with (*left*) the C-centred guest structure of McMahon et al. and (*right*) the I-centred guest structure of Fujihisa et al. The host reflections are shown in *black*, and the guest reflections in *white*. The host and guest reflections are superimposed along (*h*00) in both structures

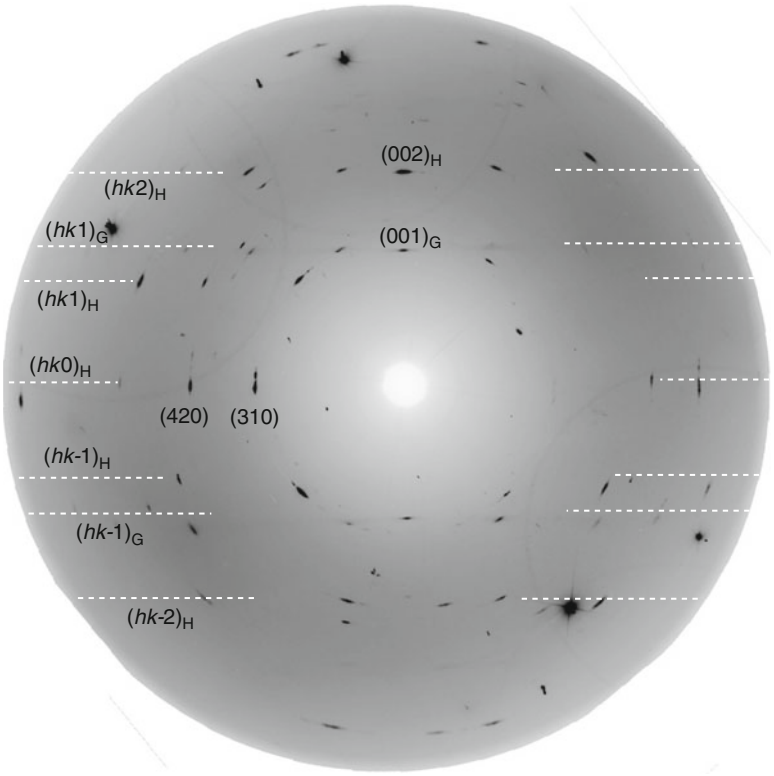

Fig. 15 2D diffraction pattern from a quasi-single-crystal of Sc-II at 48 GPa. The relative spacing of the layers of reflections from the host $(hkl)_H$ and guest $(hkl)_G$ structures (compare to Fig. 14), and the presence of the (001) guest reflection confirms the guest structure to be C-centred

This study revealed, once again, that despite the extremely high quality of powder data now obtainable at high pressures using angle-dispersive techniques at synchrotron sources, the unavoidable problems of peak overlap remains, and can be such that structural identification can remain ambiguous. The study also revealed, however, that recrystallisation can occur at phase transitions, even in hard metals, some 1,500 K below their melting temperatures, suggesting that single-crystal studies may be possible in other systems hitherto thought to be inaccessible to such techniques.

4.3 Single-Crystal Studies of Na Above 100 GPa

The group I metal sodium crystallises in the bcc structure at ambient conditions, and has a simple electronic structure that is well explained by the nearly-free electron model. Early predictions that sodium would undergo a metal–insulator transition at pressure close to 100 GPa [247] were followed by powder diffraction studies to above 100 GPa, which revealed a series of transitions to low-symmetry structures [39, 89, 248] similar to those seen previously in Li [38]. In addition, studies of the melting temperature found that, after reaching a maximum of ~1,000 K at 31 GPa, it reduced strongly, reaching ~300 K at 118 GPa. Such a low melting temperature above 100 GPa is unique to sodium, and enabled us to grow high quality single-crystals of the numerous complex crystal structures that exist in the vicinity of the melting minimum [90].

Within a ±2 GPa range about the minimum at 118 GPa, our diffraction studies revealed six different crystalline phases, four of which are unique to sodium [91]. The simplest of these is an orthorhombic structure with space group *Pnma* and eight atoms per unit cell (oP8-Na), which has since also been found in potassium above 54 GPa [100]. But the other four structures are extremely complex, with tetragonal, orthorhombic, monoclinic and triclinic symmetries, and with approximately 52, 120, 512 and 90 atoms, respectively, per unit cell [91]. Determining the lattice types and lattice parameters of these complex structures would not have been possible using powder methods. However, the availability of high quality single-crystals of each phase meant that we were able to obtain this information with confidence, although full solution of these four structures will require further experiments.

On further pressure increase at 300 K, the oP8 phase of Na transforms at 125 GPa to another form [120], accompanied by a marked decrease in optical reflectivity. A diffraction pattern from this phase is shown in Fig. 16, and contains characteristic lines of diffuse scattering. This, and the highly-distinctive spacing of the planes of Bragg reflections, reveal this phase to have an incommensurate host–guest composite structure, of the type found previously in Sc, and in a number of other elemental metals [87]. The host–guest structure of Na, as seen down the crystallographic *c*-axis, is shown in Fig. 17, and comprises a 16-atom body-centred tetragonal host framework, isostructural with that found previously in Rb and K [249, 250], but different to the 8-atom host structure found in Sc, Ba, Sr, Bi, Sb and As (compare Fig. 17 to Fig. 12). As in Sc, the host framework has channels along

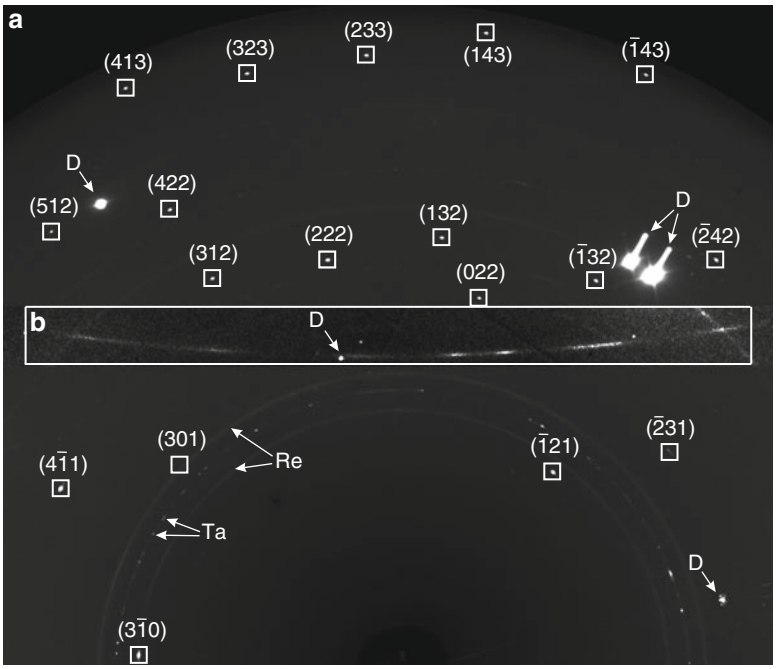

Fig. 16 A diffraction image from the tI19 phase of Na at 130 GPa, obtained using a ± 10° oscillation. Eighteen reflections from the host component of the structure are marked and indexed. The smooth powder-diffraction rings in the lower part of the image are from the rhenium gasket and the spotty ring is from the tantalum pressure marker. Those reflections marked with a "D" are from the diamond anvils. A section of the pattern, (**b**), has been replaced with a long-exposure non-oscillated diffraction image collected in the same orientation and with its contrast enhanced to reveal the first layer of very weak, elongated reflections from the guest component of the structure

the *c*-axis, contained within which are linear chains of atoms that make up the guest structure, which is primitive monoclinic, space group P2/m (Fig. 17) [120]. Closer examination of the Bragg reflections from the guest component of the structure reveals them to be clearly elongated in the *hk* plane, showing that the correlation length in this plane is less than that along the *c*-axis. From the increase in width at 147 GPa, the correlation length between the guest chains can be estimated as only 28(3) Å, or approximately six times the inter-chain spacing at this pressure [120]. This value is very similar to the correlation length of ~30 Å, or four times the interchain spacing, found previously in the host–guest composite phase Rb-IV at 16.2 GPa. However, while the interchain correlation length in Rb-IV was found to increase exponentially on pressure increase, reaching more that 500 Å at 16.8 GPa [251], the correlation length varies little with pressure in Na.

The host–guest phase of Na is stable at room temperature to 190 GPa, where it transforms to a transparent insulating form, with a hexagonal hP4 structure which calculations suggest contains distinct pockets of interstitial electron density [5]. The same hP4 structure is observed in K at lower pressures [252]. The experimental

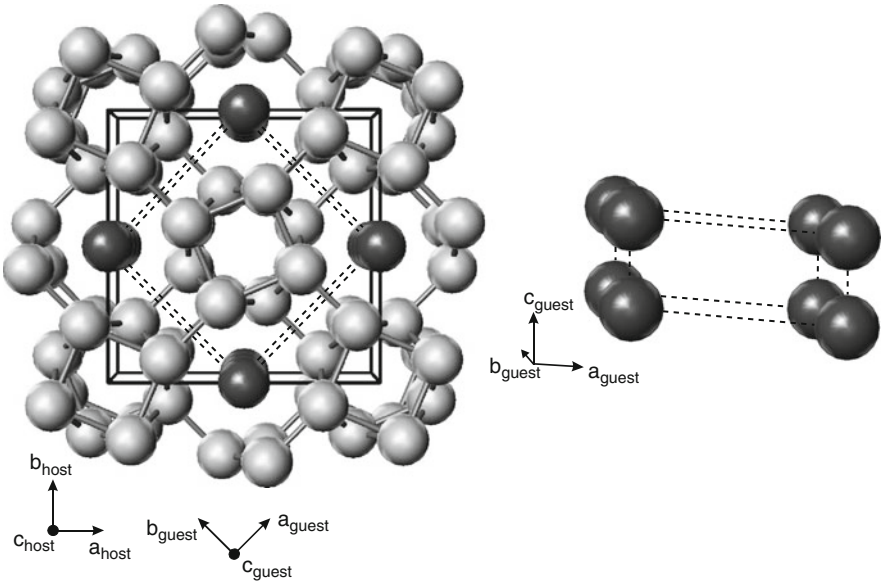

Fig. 17 The host–guest composite structure of the tI19 phase of Na shown in projection down the *c*-axis. The host atoms are shown in *light grey* and guest atoms in *dark grey*. The monoclinic guest component unit cell is outlined with *dashed lines*, and a separate perspective view of the guest structure is shown

confirmation of the e-density pockets in hP4-Na will require very high accuracy diffraction data to be collected to high diffraction angles. This represents a substantial experimental challenge for crystallographic studies, and remains slightly beyond current capabilities.

5 Twenty-First Century High-Pressure Crystallography

After the revolutions of the 1990s in both X-ray and neutron diffraction techniques, and the consolidation and exploitation of the last 10 years, what does the future hold for high-pressure crystallography? DACs are currently capable of obtaining pressures in excess of 400 GPa (4 Mbar) and there is a current international effort to extend this limit to 500 GPa (0.5 TPa) and beyond. Diamond anvil cells are now being equipped with large man-made single-crystal [253, 254] or nanocrystalline [121, 124] anvils, and recent advances in pulsed laser heating provide access to ever higher temperatures [255–257]. X-ray beams are becoming ever smaller, with nanoscale X-ray probes being employed to reduce stress gradients at multimegabar pressures, and to perform single-crystal diffraction studies of individual single grains of powder samples at ultrahigh pressures [258]. In further exploitation of the P-E press, we are developing anvils with transparent insets that will allow many of the benefits of diamond anvil cells (such optical access for spectroscopy, laser heating and monitoring in situ crystal growth) to be used with much larger samples.

As with previous eras in high-pressure science, new breakthroughs will arise through the development of new X-ray and neutron sources. The high-pressure SNAP beamline at the new spallation neutron source at Oak Ridge National Laboratory will offer intensities much greater than those currently available at the ISIS source, while new focusing technology will enable such beams to be focused from a diameter of 1 cm down to <100 μm. This will enable single-crystal studies to be carried out on 1 mm^3 samples to 50–100 GPa on a routine basis [259, 260]. At third generation synchrotrons, facility upgrades will enable X-ray beams to be focused routinely to spot sizes below 1 μm, allowing ever smaller samples to be studied to ever higher pressures.

However, perhaps the biggest changes will come from the new fourth generation light sources under development in the US [261], Europe [262] and Japan [263]. These laser-like X-ray sources will provide coherent radiation with peak brightnesses some 10^9 times higher than existing storage ring sources. The X-rays are also contained within ultra-short (100 fs) pulses, opening the way to a host of imaging, spectroscopy and dynamic pump-probe experiments; see for example [264]. The full possibilities of what such sources will provide for static high-pressure diffraction experiments is not yet clear. Indeed, it is not yet known whether the diamond anvils of a typical pressure cell will even survive being illuminated by such X-ray pulses.

One area where such sources will offer great advantages is in using dynamic compression techniques, where extremely intense laser beams with intensities of 10^{12} Wcm^{-2} are used to compress samples to extremely high densities over nanosecond timescales (for a recent description, see [265]). While little crystallography, in the sense of the determining of crystal structures, has been done to date using such techniques, this is changing, and recent experiments have recorded X-ray diffraction data to above 450 GPa [266]. In addition, advances in laser compression science at the National Ignition Facility (NIF) in the US now provide the possibility of compressing matter to multi-TPa pressures, such as those that exist at the centre of Jupiter, in the near future. This is ten times the pressures currently accessible to static compression techniques, and promises to reveal wholly new phases of matter. As always, determining the crystal structure at these conditions will be crucial, and predicting the structures of simple materials at these pressures has already produced some interesting results, including a six-coordinated cubic phase of lithium [267] and an incommensurate host-guest phase of aluminium [268]. Studying the crystallography of matter at such conditions is no longer beyond the realms of imagination, and promises many new discoveries over the coming decade.

Acknowledgements I would like to thank and acknowledge the numerous colleagues and collaborators who have contributed to the research and developments published by our group over the past 20 years that I have cited in this review. I would also like to thank facility staff at synchrotron and neutron sources for their assistance and support in the experiments and technical developments. This work was supported by grants from the Engineering and Physical Sciences Research Council and the Royal Society, and facilities and funding provided by SRS Daresbury Laboratory, ISIS, the European Synchrotron Radiation Facility, the Advanced Photon Source, the Institut Laue-Langevin, and Diamond Light Source.

References

1. Luo H, Desgreniers S, Vohra YK, Ruoff AL (1991) Phys Rev Lett 67(21):2998
2. Struzhkin V, Hemley RJ, Mao HK, Timofeev Y (1997) Nature 390(6658):382
3. Kometani S, Eremets MI, Shimizu K, Kobayashi M, Amaya K (1997) J Phys Soc Jpn 66 (9):2564
4. Lundegaard LF, Weck G, McMahon MI, Desgreniers S, Loubeyre P (2006) Nature 443 (7108):201. doi:10.1038/nature05174
5. Ma Y, Eremets M, Oganov AR, Xie Y, Trojan I, Medvedev S, Lyakhov AO, Valle M, Prakapenka V (2009) Nature 458(7235):182. doi:10.1038/nature07786
6. Hazen RM (1994) The new alchemists: breaking through the barriers of high pressure. Times Books, New York
7. Hazen RM (1999) The diamond makers. Cambridge University Press, Cambridge
8. Bridgman PW (1964) Collected experimental papers by P.W. Bridgman. Harvard University Press, Cambridge
9. Nobel Lectures (1964) Physics 1942–1962. Elsevier, Amsterdam
10. Lawson AW, Tang TY (1950) Rev Sci Instrum 21(9):815
11. Jamieson JC (1957) J Geol 65(3):334
12. Jamieson JC, Lawson AW, Nachtrieb ND (1959) Rev Sci Instrum 30(11):1016
13. Weir CE, Lippincott ER, Vanvalkenburg A, Bunting EN (1959) J Res Natl Bureau Stand Sect A Phys Chem 63(1):55
14. Jamieson JC, Lawson AW (1962) J Appl Phys 33(3):776
15. Jamieson JC (1963) Science 139(355):762
16. Jamieson JC, McWhan DB (1965) J Chem Phys 43(4):1149
17. Weir C, Block S, Piermarini G (1965) J Res Natl Bureau Stand Sect C Eng Instrum C 69(4):275
18. Merrill L, Bassett WA (1974) Rev Sci Instrum 45(2):290
19. Hazen RM, Finger LW (1982) Comparative crystal chemistry: temperature, pressure, composition and the variation of crystal structure. Wiley, London
20. Bassett WA (2009) High Press Res 29(2):CP5. doi:10.1080/08957950802597239
21. Mao HK, Bell PM (1976) Science 191(4229):851
22. Bell PM, Mao HK, Goettel K (1984) Science 226(4674):542
23. Mao HK, Hemley RJ, Chen LC, Shu JF, Finger LW, Wu Y (1989) Science 246(4930):649. doi:10.1126/science.246.4930.649
24. Ruoff AL, Xia H, Xia Q (1992) Rev Sci Instrum 63(10):4342. doi:10.1063/1.1143734
25. Akahama Y, Kawamura H (2010) J Phys Conf Ser 215:012195
26. Duclos SJ, Vohra YK, Ruoff AL (1990) Phys Rev B 41(17):12021
27. Young DA (1991) Phase diagrams of the elements. University of California Press, Berkeley
28. Shimomura O, Takemura K, Fujihisa H, Fujii Y, Ohishi Y, Kikegawa T, Amemiya Y, Matsushita T (1992) Rev Sci Instrum 63(1, part 2b):967. Fourth International Conference on Synchrotron Radiation Instrumentation, Chester, England, 15–19 Jul 1991
29. Nelmes RJ, Hatton PD, McMahon MI, Piltz RO, Crain J, Cernik RJ, Bushnell-Wye G (1992) Rev Sci Instrum 63(1, part 2b):1039. Fourth International Conference on Synchrotron Radiation Instrumentation, Chester, England, 15–19 Jul 1991
30. Nelmes RJ, McMahon MI (1994) J Synchrotron Radiat 1(Part 1):69
31. Nelmes RJ, McMahon MI, Hatton PD, Crain J, Piltz RO (1993) Phys Rev B 47(1):35
32. McMahon MI, Nelmes RJ (1993) Phys Rev B 47(13):8337
33. Nelmes RJ, McMahon MI (1998) In: High pressure in semiconductor physics I, semiconductors and semimetals, vol 54, pp 145–246
34. Hausermann D, Hanfland M (1996) High Press Res 14(4–6):223. Fourth workshop of the IUCr high pressure group on synchrotron and neutron sources, KEK, Japan, 22–24 Mar 1995
35. Akahama Y, Kawamura H, Hausermann D, Hanfland M, Shimomura O (1995) Phys Rev Lett 74(23):4690

36. Loubeyre P, LeToullec R, Hausermann D, Hanfland M, Hemley RJ, Mao HK, Finger LW (1996) Nature 383(6602):702
37. Paszkowicz W (2002) Nuclear Instrum Methods Phys Res B Beam Interact Mater Atoms 198 (3–4):142
38. Hanfland M, Syassen K, Christensen NE, Novikov DL (2000) Nature 408(6809):174
39. Hanfland M, Loa I, Syassen K (2002) Phys Rev B 65 (18). doi:10.1103/PhysRevB.65.184109
40. Schwarz U, Takemura K, Hanfland M, Syassen K (1998) Phys Rev Lett 81(13):2711
41. Schwarz U, Grzechnik A, Syassen K, Loa I, Hanfland M (1999) Phys Rev Lett 83(20): 4085
42. Takemura K, Christensen N, Novikov D, Syassen K, Schwarz U, Hanfland M (2000) Phys Rev B 61(21):14399
43. Hanfland M, Schwarz U, Syassen K, Takemura K (1999) Phys Rev Lett 82(6):1197
44. Akahama Y, Fujihisa H, Kawamura H (2005) Phys Rev Lett 94(19). doi:10.1103/PhysRev-Lett.94.195503
45. Akahama Y, Kawamura H, Carlson S, Le Bihan T, Hausermann D (2000) Phys Rev B 61 (5):3139
46. Fujihisa H, Akahama Y, Kawamura H, Ohishi Y, Gotoh Y, Yamawaki H, Sakashita M, Takeya S, Honda K (2007) Phys Rev Lett 98(17). doi:10.1103/PhysRevLett.98.175501
47. Akahama Y, Kawamura H, Le Bihan T (2001) Phys Rev Lett 87(27). doi:10.1103/PhysRev-Lett.87.275503
48. Dubrovinsky L, Dubrovinskaia N, Crichton WA, Mikhaylushkin AS, Simak SI, Abrikosov IA, de Almeida JS, Ahuja R, Luo W, Johansson B (2007) Phys Rev Lett 98(4):045503. doi:10.1103/PhysRevLett.98.045503
49. Ding Y, Ahuja R, Shu JF, Chow P, Luo W, Mao HK (2007) Phys Rev Lett 98(8):085502. doi:10.1103/PhysRevLett.98.085502
50. Mao WL, Wang L, Ding Y, Yang WG, Liu WJ, Kim DY, Luo W, Ahuja R, Meng Y, Sinogeikin S, Shu JF, Mao HK (2010) Proc Natl Acad Sci USA 107(22):9965. doi:10.1073/pnas.1005279107
51. Kenichi T, Kyoko S, Hiroshi F, Mitsuko O (2003) Nature 423(6943):971. doi:10.1038/nature01724
52. Fujihisa H, Akahama Y, Kawamura H, Ohishi Y, Shimomura O, Yamawaki H, Sakashita M, Gotoh Y, Takeya S, Honda K (2006) Phys Rev Lett 97(8). doi:10.1103/PhysRevLett.97.085503
53. Weck G, Loubeyre P, LeToullec R (2002) Phys Rev Lett 88(3). doi:10.1103/Phys-RevB.88.035504
54. Gregoryanz E, Goncharov AF, Sanloup C, Somayazulu M, Mao HK, Hemley RJ (2007) J Chem Phys 126(18). doi:10.1063/1.2723069
55. Eremets M, Gavriliuk A, Serebryanaya N, Trojan I, Dzivenko D, Boehler R, Mao H, Hemley R (2004) J Chem Phys 121(22):11296. doi:10.1063/1.1814074
56. Andrault D, Fiquet G, Kunz M, Visocekas F, Hausermann D (1997) Science 278(5339):831
57. Dubrovinsky L, Lazor P, Saxena S, Haggkvist P, Weber H, Le Bihan T, Hausermann D (1999) Phys Chem Miner 26(7):539
58. Lin J, Heinz D, Mao H, Hemley R, Devine J, Li J, Shen G (2003) Proc Natl Acad Sci USA 100(8):4405. doi:10.1073/pnas.252782399
59. Ma Y, Somayazulu M, Shen G, Mao H, Shu J, Hemley R (2004) Phys Earth Planet Interiors 143:455. doi:10.1016/j.pepi.2003.06.005. High Pressure Mineral Physics Seminars, Verbania, Italy, 26–31 Aug 2002
60. Angel RJ, Ross NL, Wood IG, Woods PA (1992) Phase Trans 39(1–4, Part B):13
61. Katrusiak A (2004) In: Katrusiak A, McMillan P (eds) High-pressure crystallography, NATO science series, series II: mathematics, physics and chemistry, vol 140, pp 57–68. NATO. Springer, Po Box 17, 3300 AA Dordrecht, Netherlands. NATO Advanced Research Workshop on High-Pressure Crystallography, Erice, Italy, 04–15 Jun 2003
62. Guionneau P, Le Pevelen D, Marchivie M, Pechev S, Gaultier J, Barrans Y, Chasseau D (2004) J Phys Condens Matter 16(14, Sp. Iss. SI), S1151. doi:10.1088/0953-8984/16/14/025.

International Conference on High Pressure Science and Technology, Bordeaux, France, 07–11 Jul 2003
63. Miletich R, Allan DR, Kuhs WF (2000) In: High-temperature and high-pressure crystal chemistry, reviews in mineralogy and geochemistry, vol 41. Mineralogical Soc America, 1015 Eighteenth St, NW, Suite 601, Washington, DC 20036–5274 USA, pp 445–519
64. Sowa H, Reithmayer K, Macavei J, Rieck W, Schulz H, Kupcik V (1990) J Appl Crystallogr 23(Part 5):397
65. Cernik RJ, Clegg W, Catlow CRA, Bushnell-Wye G, Flaherty JV, Greaves GN, Burrows I, Taylor DJ, Teat SJ, Hamichi M (1997) J Synchrotron Radiat 4(Part 5):279
66. Cernik RJ, Clegg W, Catlow CRA, Bushnell-Wye G, Flaherty JV, Greaves GN, Burrows I, Taylor DJ, Teat SJ, Hamichi M (2000) J Synchrotron Radiat 7(Part 1):40
67. Fourme R, Girard E, Kahn R, Ascone I, Mezouar M, Lin T, Johnson JE (2004) In: Katrusiak A, McMillan P (eds) High-pressure crystallography, NATO science series, series II: mathematics, physics and chemistry, vol 140, pp. 527–542. NATO Advanced Research Workshop on High-Pressure Crystallography, Erice, Italy, 04–15 Jun 2003
68. Moggach SA, Parsons S, Wood PA (2008) Crystallogr Rev 14(2):143. doi:10.1080/08893110802037945
69. Kurpiewska K, Lewinski K (2010) Cent Eur J Biol 5(5):531. doi:10.2478/s11535-010-0044-y
70. Lobban C, Finney JL, Kuhs WF (1998) Nature 391(6664):268
71. Nelmes RJ, McMahon MI, Hatton PD, Crain J, Piltz RO (1993) Phys Rev B 48(13):9949
72. Mirebeau I (2007) Comptes Rendus Physique 8(7–8):737. doi:10.1016/j.crhy.2007.09.020
73. Goncharenko IN (2005) Phys Rev Lett 94(20). doi:10.1103/PhysRevLett.94.205701
74. Klotz S, Besson JM, Braden M, Karch K, Pavone P, Strauch D, Marshall WG (1997) Phys Rev Lett 79(7):1313
75. McMahon MI, Piltz RO, Nelmes RJ (1990) Ferroelectrics 108:277. Seventh International Meeting on Ferroelectricity (IMF-7), Saarbrucken, Fed Rep Ger, 28 Aug–01 Sep 1989
76. Besson JM, Nelmes RJ, Hamel G, Loveday JS, Weill G, Hull S (1992) Physica B 180 (Part B):907. International Conference on Neutron Scattering (ICNS 91), Oxford, England, 27–30 Aug 1991
77. Klotz S, Besson JM, Hamel G, Nelmes RJ, Loveday JS, Marshall WG, Wilson RM (1995) Appl Phys Lett 66(14):1735
78. Bull CL, Guthrie M, Nelmes RJ, Loveday JS, Komatsu K, Hamidov H, Gutmann MJ (2009) High Press Res 29(4):780. doi:10.1080/08957950903414763
79. Besson JM, Pruzan P, Klotz S, Hamel G, Silvi B, Nelmes RJ, Loveday JS, Wilson RM, Hull S (1994) Phys Rev B 49(18):12540
80. vonDreele R (1995) High Press Res 14(1–3):13. International Seminar on Neutron Scattering at High Pressure, Dubna, Russia, 05–07 Oct 1994
81. Loveday JS, Nelmes RJ, Klotz S, Besson JM, Hamel G (2000) Phys Rev Lett 85(5):1024
82. Marshall WG, Nelmes RJ, Loveday JS, Klotz S, Besson JM, Hamel G, Parise JB (2000) Phys Rev B 61(17):11201
83. Klotz S, Strassle T, Nelmes RJ, Loveday JS, Hamel G, Rousse G, Canny B, Chervin J, Saitta A (2005) Phys Rev Lett 94(2). doi:10.1103/PhysRevLett.94.025506
84. Monaco G, Falconi S, Crichton WA, Mezouar M (2003) Phys Rev Lett 90(25). doi:10.1103/PhysRevLett.90.255701
85. Crichton WA, Mezouar M (2005) In: Chen J, Wang Y, Duffy TS, Shen G, Dobrzhinetskaya LF (eds) Advances in high-pressure technology for geophysical applications. Elsevier, Amsterdam, pp 353–369. doi:10.1016/B978-044451979-5.50019-3
86. Morard G, Sanloup C, Fiquet G, Mezouar M, Rey N, Poloni R, Beck P (2007) Earth Planet Sci Lett 263(1–2):128. doi:10.1016/j.epsl.2007.09.009
87. McMahon MI, Nelmes RJ (2006) Chem Soc Rev 35(10):943. doi:10.1039/b517777b
88. Friedrich A, Haussuehl E, Boehler R, Morgenroth W, Juarez-Arellano EA, Winkler B (2007) Am Miner 92(10):1640. doi:10.2138/am.2007.2549

89. Gregoryanz E, Degtyareva O, Somayazulu M, Hemley RJ, Mao HK (2005) Phys Rev Lett 94 (18). doi:10.1103/PhysRevLett.94.185502
90. McMahon MI, Gregoryanz E, Lundegaard LF, Loa I, Guillaume C, Nelmes RJ, Kleppe AK, Amboage M, Wilhelm H, Jephcoat AP (2007) Proc Natl Acad Sci USA 104(44):17297. doi:10.1073/pnas.0709309104
91. Gregoryanz E, Lundegaard LF, McMahon MI, Guillaume C, Nelmes RJ, Mezouar M (2008) Science 320(5879):1054. doi:10.1126/science.1155715
92. Lundegaard LF, Gregoryanz E, McMahon MI, Guillaume C, Loa I, Nelmes RJ (2009) Physical Review B 79(6) doi: 10.1103/PhysRevB.79.064105
93. Uemura E, Akahama Y, Kawamura H, Le Bihan T, Shobu T, Noda Y, Shimomura O (2002) J Phys Condens Matter 14(44):10423
94. Yamanaka T, Komatsu Y, Nomori H (2007) Phys Chem Miner 34(5):307. doi:10.1007/s00269-007-0149-7
95. Merlini M, Gemmi M, Hanfland M, Crichton WA (2009) Am Miner 94(5–6):704. doi:10.2138/am.2009.3072
96. Yamanaka T, Okada T, Nakamoto Y (2009) Phys Rev B 80(9). doi:10.1103/PhysRevB.80.094108
97. Datchi F, Giordano VM, Munsch P, Saitta AM (2009) Phys Rev Lett 103(18). doi:10.1103/PhysRevLett.103.185701
98. Weck G, Desgreniers S, Loubeyre P, Mezouar M (2009) Phys Rev Lett 102(25). doi:10.1103/PhysRevLett.102.255503
99. Somayazulu M, Dera P, Goncharov AF, Gramsch SA, Liermann P, Yang W, Liu Z, Mao HK, Hemley RJ (2010) Nat Chem 2(1):50. doi:10.1038/NCHEM.445
100. Lundegaard LF, Guillaume C, McMahon MI, Gregoryanz E, Merlini M (2009) Journal Of Chemical Physics 130:16 doi 10.1063/1.3118970
101. Sanloup C, Gregoryanz E, Degtyareva O, Hanfland M (2008) Phys Rev Lett 100(7). doi:10.1103/PhysRevLett.100.075701
102. Ninet S, Datchi F, Klotz S, Hamel G, Loveday JS, Nelmes RJ (2009) Phys Rev B 79(10). doi:10.1103/PhysRevB.79.100101
103. Lawson AW, Riley NA (1949) Rev Sci Instrum 20(11):763
104. Vanvalkenburg A (1962) Rev Sci Instrum 33(12):1462
105. Jayaraman A (1983) Rev Mod Phys 55(1):65
106. Jayaraman A (1984) Sci Am 250(4):54
107. Jayaraman A (1986) Rev Sci Instrum 57(6):1013
108. Ahsbahs H (1987) Prog Cryst Growth Charact Mater 14:263
109. Eremets MI (1996) High pressure experimental methods. Oxford University Press, Oxford
110. Holzapfel WB, Isaacs NI (1997) High-pressure techniques in chemistry and physics. Oxford University Press, Oxford
111. Katrusiak A (2008) Acta Crystallogr Sect A 64(Part 1):135. doi:10.1107/S0108767307061181
112. Mao HK, Bell PM (1978) Science 200(4346):1145
113. Piermarini GJ, Block S, Barnett JD (1973) J Appl Phys 44(12):5377
114. Eggert JH, Xu LW, Che RZ, Chen LC, Wang JF (1992) J Appl Phys 72(6):2453
115. Angel RJ, Bujak M, Zhao J, Gatta GD, Jacobsen SD (2007) J Appl Crystallogr 40(Part 1):26. doi:10.1107/S0021889806045523
116. Klotz S, Chervin JC, Munsch P, Le Marchand G (2009) J Phys D Appl Phys 42(7). doi:10.1088/0022-3727/42/7/075413
117. Schiferl D (1987) Rev Sci Instrum 58(7):1316
118. Malinowski M (1987) J Appl Crystallogr 20(Part 5):379
119. Boehler R, De Hantsetters K (2004) High Press Res 24(3):391. doi:10.1080/08957950412331323924
120. Lundegaard LF, Gregoryanz E, McMahon MI, Guillaume C, Loa I, Nelmes RJ (2009b) Phys Rev B 79(6). doi:10.1103/PhysRevB.79.064105

121. Irifune T, Kurio A, Sakamoto S, Inoue T, Sumiya H (2003) Nature 421(6923):599
122. Irifune T, Kurio A, Sakamoto S, Inoue T, Sumiya H (2003) Nature 421(6925):806. doi:10.1038/421806b
123. Nakamoto Y, Sumiya H, Matsuoka T, Shimizu K, Irifune T, Ohishi Y (2007) Jpn J Appl Phys Part 2 Lett Express Lett 46(25–28):L640. doi:10.1143/JJAP.46.L640
124. Ohfuji H, Okada T, Yagi T, Sumiya H, Irifune T (2010) J Phys Conf Ser 215(1):012192
125. Glazkov VP, Goncharenko IN, Irodova VA, Somenkov VA, Shilstein SS, Besedin SP, Makarenko IN, Stishov SM (1989) Zeitschrift fur Physikalische Chemie Neuefolge 163 (Part 2):509
126. Paureau J, Vettier C (1975) Rev Sci Instrum 46(11):1484
127. Mizuki J, Endoh Y (1981) J Phys Soc Jpn 50(3):914
128. McWhan DB (1984) Revue de Physique Appliquee 19(9):715
129. Goncharenko I, Loubeyre P (2005) Nature 435(7046):1206. doi:10.1038/nature03699
130. Ding Y, Xu J, Prewitt C, Hemley R, Mao H, Cowan J, Zhang J, Qian J, Vogel S, Lokshin K, Zhao Y (2005) Appl Phys Lett 86(5). doi:10.1063/1.1852075
131. Zhao Y, Zhang J, Xu H, Lokshin KA, He D, Qian J, Pantea C, Daemen LL, Vogel SC, Ding Y, Xu J (2010) Appl Phys A Mater Sci Process 99(3, Sp. Iss. SI):585. doi:10.1007/s00339-010-5640-1
132. Khvostantsev LG, Vereshchagin LF, Novikov AP (1977) High Temp High Press 9:637
133. Khvostantsev LG, Slesarev VN, Brazhkin V (2004) High Press Res 24(3):371. doi:10.1080/08957950412331298761
134. Marshall WG, Francis D (2002) J Appl Crystallogr 35(1):122
135. Le Godec Y, Strassle T, Hamel G, Nelmes RJ, Loveday JS, Marshall WG, Klotz S (2004) High Press Res 24(1):205. doi:10.1080/08957950410001661972. Meeting on matter under extreme conditions, Paris, France, 16 May 2003
136. Bocian A, Bull CL, Hamidov H, Loveday JS, Nelmes RJ, Kamenev KV (2010) Rev Sci Instrum 81(9):093904. doi:10.1063/1.3480555. URL:http://link.aip.org/link/?RSI/81/093904/1
137. Klotz S, Hamel G, Frelat J (2004) High Press Res 24(1):219. doi:10.1080/08957950410001661963. Meeting on Matter Under Extreme Conditions, Paris, France, 16 May 2003
138. Holzapfel WB (2005) High Press Res 25(2):87. doi:10.1080/09511920500147501
139. Forman RA, Block S, Barnett JD, Piermarini GJ (1972) Science 176(4032):284
140. Barnett JD, Block S, Piermarini GJ (1973) Rev Sci Instrum 44(1):1
141. Piermarini GJ, Block S, Barnett JD, Forman RA (1975) J Appl Phys 46(6):2774
142. Syassen K (2008) High Press Res 28(2):75. doi:10.1080/08957950802235640
143. Bell P, Xu J, Mao HK (1986) Shock waves in condensed matter. Plenum, New York, p 125130
144. Mao H, Xu J, Bell P (1986) J Geophys Res Solid Earth Planets 91(B5):4673
145. Evans SR, Loa I, Lundegaard LF, McMahon MI (2009) Phys Rev B 80(13). doi:10.1103/PhysRevB.80.134105
146. Lacam A, Chateau C (1989) J Appl Phys 66(1):366
147. Leger JM, Chateau C, Lacam A (1990) J Appl Phys 68(5):2351
148. Datchi F, LeToullec R, Loubeyre P (1997) J Appl Phys 81(8, Part 1):3333
149. Occelli F, Loubeyre P, LeToullec R (2003) Nat Mater 2(3):151
150. Goncharov AF, Sinogeikin S, Crowhurst JC, Ahart M, Lakshtanov D, Prakapenka V, Bass J, Beck P, Tkachev SN, Zaug JM, Fei Y (2007) High Press Res 27(4):409. doi:10.1080/08957950701659726
151. Birch F (1986) J Geophys Res Solid Earth Planets 91(B5):4949
152. Angel RJ, Allan DR, Milletich R, Finger LW (1997) J Appl Crystallogr 30(Part 4):461
153. Dewaele A, Loubeyre P, Mezouar M (2004) Phys Rev B 70(9). doi:10.1103/PhysRevB.70.094112
154. Hanfland M, Syassen K, Kohler J (2002) J Appl Phys 91(7):4143. doi:10.1063/1.1454200

155. Errandonea D, Martinez-Garcia D, Segura A, Haines J, Machado-Charry E, Canadell E, Chervin JC, Chevy A (2008) Phys Rev B 77(4). doi:10.1103/PhysRevB.77.045208
156. Dubrovinsky L, Dubrovinskaia N, Kantor I, Nestola F, Gatta D (2006) High Press Res 26 (2):137. doi:10.1080/08957950600765301. European Science Foundation Workshop on Novel Superhard Materials, Bayreuth, Germany, 16–20 Nov 2005
157. Haines J, Leger J, Gorelli F, Klug D, Tse J, Li Z (2001) Phys Rev B 64(13)
158. Delattre J, Badding J (1999) J Solid State Chem 144(1):16
159. Hu JZ, Merkle LD, Menoni CS, Spain IL (1986) Phys Rev B 34(7):4679
160. Baublitz MA, Arnold V, Ruoff AL (1981) Rev Sci Instrum 52(11):1616
161. Hammersley AP, Svensson SO, Hanfland M, Fitch AN, Hausermann D (1996) High Press Res 14(4–6):235. Fourth Workshop of the IUCr High Pressure Group on Synchrotron and Neutron Sources, Kek, Japan, 22–24 Mar 1995
162. Piltz RO, McMahon MI, Crain J, Hatton PD, Nelmes RJ, Cernik RJ, Bushnell-Wye G (1992) Rev Sci Instrum 63(1, Part 2A):700. Fourth International Conference on Synchrotron Radiation Instrumentation, Chester, England, 15–19 Jul 1991
163. McMahon MI, Nelmes RJ (1997) Phys Rev Lett 78(19):3697
164. Nelmes RJ, McMahon MI, Hatton PD, Crain J, Piltz RO (1993) Physical Review B 47(1):35–54
165. Nelmes RJ, McMahon MI (1995) Phys Rev Lett 74(1):106
166. Nelmes RJ, Allan DR, McMahon MI, Belmonte SA (1999) Phys Rev Lett 83(20):4081
167. McMahon MI, Degtyareva O, Nelmes RJ (2000) Phys Rev Lett 85(23):4896
168. Finger LW, King H (1978) Am Miner 63(3–4):337
169. Dawson A, Allan DR, Parsons S, Ruf M (2004) J Appl Crystallogr 37(Part 3):410. doi:10.1107/S0021889804007149
170. Allan DR, Clark SJ, Parsons S, Ruf M (2000) J Phys Condens Matter 12(39):L613
171. Moggach SA, Allan DR, Parsons S, Warren JE (2008) J Appl Crystallogr 41(Part 2):249. doi:10.1107/S0021889808000514
172. Brugger RM, Bennion RB, Worlton TG (1967) Phys Lett A 24(13):714. doi:10.1016/0375-9601(67)90230-7
173. Worlton T, Decker D, Jorgensen J, Kleb R (1986) Physica B & C 136(1–3):503. doi:10.1016/S0378-4363(86)80128-0. URL:http://www.sciencedirect.com/science/article/B6X43-4RWNMK2-4 J/2/f3dc3844dd2ac028370ed89a9f842c2b. Proceedings of the International Conference on Neutron Scattering
174. Jorgensen JE, Jorgensen JD, Batlogg B, Remeika JP, Axe JD (1986) Phys Rev B 33(7):4793
175. Kuhs WF, Finney JL, Vettier C, Bliss DV (1984) J Chem Phys 81(8):3612
176. Nelmes RJ, Wilding NB, Hatton PD, Caignaert V, Raveau B, McMahon MI, Piltz RO (1990) Physica C 166(3–4):329
177. Wilson RM, Loveday JS, Nelmes RJ, Klotz S, Marshall WG (1995) Nuclear Instrum Methods Phys Res Sect A Accelerators Spectrometers Detectors and Associated Equipment 354(1):145. Third Workshop on Neutron Scattering Data Analysis (WONSDA 94), Chilton, England, 13–15 Apr 1994
178. Loveday JS, Nelmes RJ (2008) Phys Chem Chem Phys 10(7):937. doi:10.1039/b704740a
179. Loveday JS, Nelmes RJ, Guthrie M, Belmonte SA, Allan DR, Klug D, Tse J, Handa Y (2001) Nature 410(6829):661
180. Loveday JS, Nelmes RJ, Marshall WG, Besson JM, Klotz S, Hamel G (1996) Phys Rev Lett 76(1):74
181. Strassle T, Saitta A, Le Godec Y, Hamel G, Klotz S, Loveday JS, Nelmes RJ (2006) Phys Rev Lett 96(6). doi:10.1103/PhysRevLett.96.067801
182. Klotz S, Hamel G, Loveday JS, Nelmes RJ, Guthrie M, Soper AK (2002) Phys Rev Lett 89(28). doi:10.1103/PhysRevLett.89.285502
183. Nelmes RJ, Loveday JS, Strassle T, Bull CL, Guthrie M, Hamel G, Klotz S (2006) Nat Phys 2(6):414. doi:10.1038/nphys313
184. Klotz S, Strassle T, Rousse G, Hamel G, Pomjakushin V (2005) Appl Phys Lett 86(3). doi:10.1063/1.1855419

185. Nelmes RJ, Tun Z, Kuhs WF (1987) Ferroelectrics 71(1–4):125
186. Nelmes RJ, McMahon MI, Piltz RO, Wright NG (1991) Ferroelectrics 124(1–4):355
187. Ahsbahs H (1984) Revue de Physique Appliquee 19(9):819
188. Kuhs WF, Ahsbahs H, Londono D, Finney JL (1989) Physica B 156:684
189. Kuhs WF, Bauer FC, Hausmann R, Ahsbahs H, Dorwarth R, Holzer K (1996) High Press Res 14(4–6):341. Fourth Workshop of the IUCr High Pressure Group on Synchrotron and Neutron Sources, Kek, Japan, 22–24 Mar 1995
190. Lehmann MS, Kuhs WF, McIntyre GJ, Wilkinson C, Allibon JR (1989) J Appl Crystallogr 22(Part 6):562
191. Bull CL, Guthrie M, Klotz S, Philippe J, Strassle T, Nelmes RJ, Loveday JS, Hamel G (2005) High Press Res 25(4):229. doi:10.1080/08957950500452893
192. Bull CL, Guthrie M, Nelmes RJ, Loveday JS, Hamidov H, Gutmann MJ (2009) High Press Res 29(4):644. doi:10.1080/08957950903415752. 47th Meeting of the European-High Pressure Research Group (EHPRG 47), Paris, France, 06–11 Sep 2009
193. Fang J, Bull CL, Hamidov H, Loveday JS, Gutmann MJ, Nelmes RJ, Kamenev KV (2010) Rev Sci Instrum 81(11):113901. doi:10.1063/1.3494606. URL:http://link.aip.org/link/?RSI/81/113901/1
194. McIntyre G, Melesi L, Guthrie M, Tulk C, Xu J, Parise JB (2005) J Phys Condens Matter 17(40, Sp. Iss. SI):S3017. doi:10.1088/0953-8984/17/40/004. International Workshop on Medium Pressure Advances for Neutron Scattering, Grenoble, France, 20–23 Oct 2004
195. Angel RJ, Downs RT, Finger LW (2000) In: High-temperature and high-pressure crystal chemistry, reviews in mineralogy and geochemistry, vol 41. Mineralogical Society of America, pp 559–596
196. Bassett WA, Takahashi T (1965) Am Miner 50(10):1576
197. Bassett WA (2001) Rev Sci Instrum 72(2):1270. Workshop on Advances in Laser Heated Diamond Cell Techniques, Chicago, IL, 25–27 May 2000
198. Fei YW, Wang YB (2000) In: High-temperature and high-pressure crystal chemistry, reviews in mineralogy and geochemistry, vol 41, pp 521–557
199. Dubrovinskaia N, Dubrovinsky L (2005) In: Chen J, Wang Y, Duffy TS, Shen G, Dobrzhinetskaya LF (eds) Advances in high-pressure technology for geophysical applications. Elsevier, Amsterdam, pp 487–501. doi:10.1016/B978-044451979-5.50027-2
200. Bassett WA, Shen AH, Bucknum M, Chou IM (1993) Rev Sci Instrum 64(8):2340. doi:10.1063/1.1143931
201. Dubrovinskaia N, Dubrovinsky L (2003) Rev Sci Instrum 74(7):3433. doi:10.1063/1.1578151
202. LeToullec R, Pinceaux JP, Loubeyre P (1988) High Press Res 1(1):77
203. LeToullec R, Datchi F, Loubeyre P, Rambert N, Sitaud B, Thevenin T (1996) In: High pressure science and technology, Proceedings of Joint 15th AIRAPT and 33rd EHPRG International Conference. World Scientific Publishing, Warsaw, p 5456
204. Miletich R, Cinato D, Johaenntgen S (2009) High Press Res 29(2):290. doi:10.1080/08957950902747403
205. Boehler R, Nicol M, Zha CS, Johnson ML (1986) Physica B & C 139(1–3):916
206. Saxena SK, Dubrovinsky LS (1998) Petrology 6(6):535
207. Zha CS, Bassett WA (2003) Rev Sci Instrum 74(3, Part 1):1255. doi:10.1063/1.1539895
208. Hazen RM, Finger LW (1981) Rev Sci Instrum 52(1):75
209. Tateno S, Hirose K, Ohishi Y, Tatsumi Y (2010) Science 330(6002):359. doi:10.1126/science.1194662
210. Prakapenka VB, Kubo A, Kuznetsov A, Laskin A, Shkurikhin O, Dera P, Rivers ML, Sutton SR (2008) High Press Res Int J 28(3):225
211. Dubrovinsky L, Glazyrin K, McCammon C, Narygina O, Greenberg E, Übelhack S, Chumakov AI, Pascarelli S, Prakapenka V, Bock J, Dubrovinskaia N (2009) J Synchrotron Radiat 16(6):737. doi:10.1107/S0909049509039065
212. Goncharov AF, Beck P, Struzhkin VV, Hemley RJ, Crowhurst JC (2008) J Phys Chem Solids 69(9):2217. doi:10.1016/j.jpcs.2008.03.037

213. Le Godec Y, Dove M, Redfern S, Tucker M, Marshall WG, Syfosse G, Besson JM (2001) High Press Res 21(5):263
214. Le Godec Y, Dove M, Francis D, Kohn S, Marshall WG, Pawley A, Price G, Redfern S, Rhodes N, Ross N, Schofield P, Schooneveld E, Syfosse G, Tucker M, Welch M (2001) Mineral Mag 65(6):737
215. Le Godec Y, Dove M, Redfern S, Tucker M, Marshall WG, Syfosse G, Klotz S (2003) High Press Res 23(3):281. doi:10.1080/0895795032000102496. 40th Meeting of the European High Pressure Research Group (EHPRG), Edinburgh, Scotland, 04–07 Sep 2002
216. Le Godec Y, Hamel G, Martinez-Garcia D, Hammouda T, Solozhenko V, Klotz S (2005) High Press Res 25(4):243. doi:10.1080/08957950500368982
217. Le Godec Y, Hamel G, Solozhenko VL, Martinez-Garcia D, Philippe J, Hammouda T, Mezouar M, Crichton WA, Morard G, Klotz S (2009) J Synchrotron Radiat 16(Part 4): 513. doi:10.1107/S0909049509012928
218. Degtyareva O, Magnitskaya MV, Kohanoff J, Profeta G, Scandolo S, Hanfland M, McMahon MI, Gregoryanz E (2007) Phys Rev Lett 99(15). doi:10.1103/PhysRevLett.99.155505
219. Ahart M, Somayazulu M, Cohen RE, Ganesh P, Dera P, Mao HK, Hemley RJ, Ren Y, Liermann P, Wu Z (2008) Nature 451(7178):545. doi:10.1038/nature06459
220. Bridgman PW (1952) Proc Am Acad Arts Sci 81:167
221. Parthasarathy G, Holzapfel WB (1988) Phys Rev B 37(14):8499
222. Akahama Y, Kobayashi M, Kawamura H (1992) Solid State Commun 84(8):803
223. Brazhkin VV, Voloshin RN, Popova SV, Umnov AG (1992) J Phys Condens Matter 4(6):1419
224. Aoki K, Shimomura O, Minomura S (1980) J Phys Soc Jpn 48(2):551
225. Yaoita K, Tsuji K, Katayama Y, Koyama N, Kikegawa T, Shimomura O (1993) J Non-Crystalline Solids 156(Part 1):157. Eighth International Conference on Liquid and Amorphous Metals, Vienna, Austria, 31 Aug–04 Sep 1992
226. Funamori N, Tsuji K (2002) Phys Rev B 65(1). doi:10.1103/PhysRevB.65.014105
227. Vaidya SN, Kennedy GC (1972) J Phys Chem Solids 33(7):1377
228. Hsueh HC, Lee CC, Wang CW, Crain J (2000) Phys Rev B 61(6):3851
229. Bundy FP, Dunn KJ (1980) Phys Rev Lett 44(24):1623
230. Mauri F, Zakharov O, de Gironcoli S, Louie SG, Cohen ML (1996) Phys Rev Lett 77(6):1151
231. Takumi M, Masamitsu T, Nagata K (2002) J Phys Condens Matter 14(44):10609
232. Hejny C, McMahon MI (2003) Phys Rev Lett 91(21). doi:10.1103/PhysRevLett.91.215502
233. Hejny C, McMahon MI (2004) Phys Rev B 70(18). doi:10.1103/PhysRevB.70.184109
234. Van Smallen S (1995) Crystallogr Rev 4(2):79
235. Petricek V, Dusek M (2000) The crystallographic computing system JANA2000. Institute of Physics, Praha, Czech Republic
236. McMahon MI, Hejny C, Loveday JS, Lundegaard LF, Hanfland M (2004) Phys Rev B 70(5). doi:10.1103/PhysRevB.70.054101
237. Degtyareva O, Gregoryanz E, Somayazulu M, Mao HK, Hemley RJ (2005) Phys Rev B 71(21). doi:10.1103/PhysRevB.71.214104
238. Hejny C, Lundegaard LF, Falconi S, McMahon MI, Hanfland M (2005) Phys Rev B 71(2). doi:10.1103/PhysRevB.71.020101
239. Vohra YK, Grosshans W, Holzapfel WB (1982) Phys Rev B 25(9):6019
240. Grosshans W, Vohra Y, Holzapfel WB (1982) J Magn Magn Mater 29(1–3):282
241. Akella J, Xu J, Smith GS (1986) Physica B & C 139(1–3):285
242. Zhao YC, Porsch F, Holzapfel WB (1996) Phys Rev B 54(14):9715
243. Fujihisa H, Akahama Y, Kawamura H, Gotoh Y, Yamawaki H, Sakashita M, Takeya S, Honda K (2005) Phys Rev B 72(13). doi:10.1103/PhysRevB.72.132103
244. Nelmes RJ, Allan DR, McMahon MI, Belmonte SA (1999) Physical Review Letters 83: 4081–4084
245. Bovornratanaraks T, Allan DR, Belmonte SA, McMahon MI, Nelmes RJ (2006) Phys Rev B 73(14). doi:10.1103/PhysRevB.73.144112

246. McMahon MI, Lundegaard LF, Hejny C, Falconi S, Nelmes RJ (2006) Phys Rev B 73(13). doi:10.1103/PhysRevB.73.134102
247. Siringo F, Pucci R, Angilella G (1997) High Press Res 15(4):255
248. Syassen K (2002) In: Hemley RJ, Chiarotti GL, Bernasconi M, Ulivi L (eds) High pressure phenomena. Proceedings of the International School of Physics. IOS Press, Amsterdam, p 266268
249. McMahon MI, Rekhi S, Nelmes RJ (2001) Phys Rev Lett 87(5). doi:10.1103/PhysRevLett. 87.055501
250. McMahon MI, Nelmes RJ, Schwarz U, Syassen K (2006) Phys Rev B 74(14). doi:10.1103/ PhysRevB.74.140102
251. McMahon MI, Nelmes RJ (2004) Phys Rev Lett 93(5). doi:10.1103/PhysRevLett.93.055501
252. Marques M, Ackland GJ, Lundegaard LF, Stinton G, Nelmes RJ, McMahon MI, Contreras-Garcia J (2009) Phys Rev Lett 103(11). doi:10.1103/PhysRevLett. 103.115501
253. Liang Q, Yan CS, Meng Y, Lai J, Krasnicki S, Mao HK, Hemley RJ (2009) Diam Relat Mater 18(5–8, Sp. Iss. SI):698. doi:10.1016/j.diamond.2008.12.002. 19th European Conference on Diamond, Diamond-Like Materials, Carbon Nanotubes, Nitrides and Silicon Carbide, Sitges, Spain, 07–11 Sep 2008
254. Zha CS, Krasnicki S, Meng YF, Yan CS, Lai J, Liang Q, Mao HK, Hemley RJ (2009) High Press Res 29(2):317. doi:10.1080/08957950902941048
255. Deemyad S, Sterer E, Barthel C, Rekhi S, Tempere J, Silvera IF (2005) Rev Sci Instrum 76(12). doi:10.1063/1.2140493
256. Rekhi S, Tempere J, Silvera IF (2003) Rev Sci Instrum 74(8):3820. doi:10.1063/1.1593790
257. Goncharov AF, Montoya JA, Subramanian N, Struzhkin VV, Kolesnikov A, Somayazulu M, Hemley RJ (2009) J Synchrotron Radiat 16(Part 6):769. doi:10.1107/S0909049509033433. Workshop on Advances in High-Pressure Science Using Synchrotron X-Rays, Upton, NY, 04 Oct 2008
258. Wang L, Ding Y, Yang W, Liu W, Cai Z, Kung J, Shu J, Hemley RJ, Mao WL, Mao HK (2010) Proc Natl Acad Sci USA 107(14):6140. doi:10.1073/pnas.1001141107
259. http://neutrons.ornl.gov/instruments/sns/snap/
260. Jenkins T, Hemley RJ, Mao HK, Parise JB, Tulk C (2005) Abs Papers Am Chem Soc 230:497. 230th National Meeting of the American Chemical Society, Washington, DC, 28 Aug–01 Sep 2005
261. http://lcls.slac.stanford.edu/
262. http://xfel.desy.de/
263. http://www-xfel.spring8.or.jp/
264. Altarelli M (2010) Magnetism and synchrotron radiation: new trends. Springer Proceedings in Physics. Springer, pp 407–419
265. Drake RP (2010) Physics Today 63(6):28
266. J.H. Eggert. Unpublished
267. Ma Y, Oganov AR, Xie Y (2008) Physical Review B. 78(1). Doi:10.1103/PhysRevB. 78.014102
268. Pickard CJ, Needs RJ (2010) Nat Mater 9(8):624
269. Klotz S, Gauthier M, Besson JM, Hamel G, Nelmes RJ, Loveday JS, Wilson RM, Marshall'WG (1995) Applied Physics Letters 67(9):1188–1190
270. Maynard HE, Loveday JS, Klotz S, Bull CL, Hansen TC (2009) High Pressure Research 29 (1):125–128
271. Maynard-Casely HE, Bull CL, Guthrie M, Loa I, McMahon MI, Gregoryanz E, Nelmes RJ, Loveday JS (2010) Journal Of Chemical Physics 133(6): doi 10.1063/1.3455889

Top Curr Chem (2012) 315: 111–132
DOI: 10.1007/128_2011_156

Published online: 20 May 2011

Chemical X-Ray Photodiffraction: Principles, Examples, and Perspectives

Panče Naumov

Abstract *X-ray photodiffraction* (in the chemical literature also referred to as *photocrystallography*), which is based on the combination of X-ray diffraction methods with samples excited by UV or visible light to solve fundamental photochemical or photophysical issues, has developed in the last couple of decades into a very promising technique for direct observation of photoinduced chemical species in the solid state. The capability of providing direct information on very small perturbations in atomic positions and thus on the minute changes in molecular geometry during (or as a consequence of) photoexcitation appears to be the most important asset of this emerging analytical technique. When combined with other physicochemical methods, X-ray photodiffraction can be a powerful tool for analysis of steady-state photoinduced structures as well as slow or very fast time-dependent phenomena. Despite being a very useful approach, however, due to a number of practical requirements that it places with regard to the system to be studied, at the present stage of developments the technique is not widely and indiscriminately applicable to any photoinduced process. In some particular chemical systems the inherent pitfalls could be practically overcome by practical or theoretical means. In this short chapter, the basic principles of X-ray photodiffraction are briefly summarized, and the prospects of its application to "physical" and "chemical" problems is illustrated with selected examples from recent literature. Some possible future developments and alternative approaches with this and related methods are also presented.

Keywords Chemical crystallography · Photocrystallography · Photodiffraction · Solid-state · Time-resolved methods

P. Naumov
Department of Material and Life Science, Graduate School of Engineering, Osaka University, 2-1 Yamada-oka, Suita, Osaka 565-0871, Japan
e-mail: npance@wakate.frc.eng.osaka-u.ac.jp

Contents

1 Introduction

1.1 X-Ray Based Methods for Structure Analysis

X-ray-based methods have remained the main tool for structure determination throughout the twentieth century. The increased use of X-ray diffraction (XRD) for crystal structure analysis or routine characterization of new materials was largely fostered by technical developments of the X-ray sources and detectors – the two essential components of any system for XRD analysis. The developments in this field from the times when photographic film had been utilized to record the diffraction pattern, to the advent of point detectors where the detector had to pick the orientation of each individual reflection, to the currently commonly available two-dimensional detectors which are able to record larger slices of the reciprocal space at a single exposure of the sample to the X-ray beam, have greatly decreased the time necessary for structure determination. Simultaneously, the brilliance of X-ray sources from the early X-ray tubes to third-generation synchrotron sources has increased by over 15 orders of magnitude, and strong, brilliant and monochromatic X-rays are now available for structure determination in continuous or in pulsed mode [1]. In addition to basic structural science, chemistry, physics, molecular biology, and, more recently, the interdisciplinary field of materials science have all greatly benefitted from development of the instrumentation and software for XRD structure analysis. From an incomprehensibly laborious and lengthy process, XRD structure determination of macromolecules, for instance, has become a feasible task, and in the case of structures of "small" molecular compound, it is nowadays a normal part of routine chemical characterization.

The convenience of using X-rays for structure determination stems from the nature of their interactions with matter: the wavelengths of radiation in the X-ray region of the electromagnetic spectrum are comparable to the sizes of atoms and interatomic distances that are to be analyzed. Although, in principle, interatomic distances can be determined by electron *microscopy*, unlike electron microscopic

methods, low-intensity X-rays are normally non-destructive to the sample and they also provide comparably better resolution. Moreover, while by using electron *spectroscopy* in the UV–visible region – nowadays routinely employed to study photoinduced and dynamic processes – one inevitably has to excite electrons, X-rays do not interfere with electron transitions; thus they can be employed to study electron excitations without interference with the observed phenomenon, which is one of the most important assets of the technique discussed in this chapter. From a practical viewpoint, X-rays are commonly available in either continuous mode (e.g., from an X-ray tube) or pulsed mode (e.g., when produced by laser-induced excitation of metals, or as synchrotron X-ray radiation obtained by slowing very fast electrons), and they can be conveniently manipulated and easily detected. In that respect, the Laue XRD method, which utilizes non-monochromatic X-rays and for which some of the most important obstacles that were relevant in the past have now been solved, holds great promise for further application to systems spanning from small molecules to macromolecules [2, 3]. More importantly, X-rays interact with matter at very short (attosecond) timescales, and are thus a convenient tool to probe a very wide range of processes which are slower than that time-limit. Due to these properties, X-rays are the principle component of a wider group of analytical methods for structural analysis of bulk materials and surfaces, that, in addition to XRD methods (methods of single crystal and powder diffraction), include techniques that are based on scattering (small-angle X-ray scattering, grazing-incidence X-ray scattering, and similar) and spectroscopy (X-ray absorption and emission spectroscopy), some of which are extensively elaborated on in the other chapters of this volume. Moreover, by using X-rays, both surface and bulk phenomena can be accessed, while the operating mode and conditions can be adapted so as to provide spatially and time-averaged (or time-resolved) information on structures of varying complexity. For instance, complex enzyme-catalyzed processes can be conveniently "frozen" by physicochemical means at a certain desired stage and directly studied [4]. While diffraction-based *steady-state* XRD techniques are usually employed to investigate spatially averaged bulk structure, imaging [5] or microscopic X-ray-based methods provide additional insights into the spatial non-homogeneities of the material that are related to multiple phases, defects, impurities, and similar imperfections of the structure. On the other hand, the more recently developed *time-resolved* X-ray-based methods (some of which are mentioned in the concluding section of this chapter), which are still rather demanding in respect of instrumentation, can be used to study the structural consequences of ultrafast photoinduced perturbations, while also analyzing the temporal profile of the related processes.

1.2 The Basic Principles

At the forefront of recent developments in the field of X-ray-based analytical methods is *X-ray photodiffraction*, usually referred to as *X-ray*

photocrystallography.[1] This evolving analytical technique is related to application of XRD diffraction methods to resolve photophysical or photochemical problems. In its most general definition, X-ray photodiffraction utilizes XRD on samples that are excited by light, aimed at studying the minor changes in their structure related to photoexcitation – either during the process, immediately after excitation, or after the system has relaxed to a ground state. In practice, a sample in single crystal or powder state is excited by UV or visible light, and diffraction data are collected before, during, and/or after excitation (Fig. 1). Depending on the process (reversible or irreversible) and the stability of the photoinduced species (unstable, metastable, or stable), the duration and the timing of the "excitation" beam (UV or visible light) and the "analytical" beam (X-rays) is adjusted so as to collect a sufficient amount of data which would provide meaningful information on the structure before and during/after photoexcitation. With ordinary experimental setups, typical times of data collection are on the order of hours, while with special experimental setups and in time-resolved mode they can be in the millisecond, microsecond, or picosecond range (currently, down to a resolution of several tens to several hundreds of picoseconds). When the timescale of the experiment is ultrafast, the excitation and analytical beams are pulsed and they are usually termed the "pump" and "probe."

In principle, X-ray photodiffraction can be used in *steady-state mode* (Figs. 2 and 3) or in *time-resolved mode* (Fig. 4) by application on either single crystals (Fig. 2) or microcrystals (Fig. 3). In the course of steady-state photodiffraction, the sample is excited ex situ (the species is created before actual structure analysis) or in situ (the species is being created simultaneously with data collection for structure determination) by using either a continuous-wave source or pulsed light source (or a combination of several sources, some of which can be used for creation and other for intentional decay of the desired species). The structural changes are probed by using X-rays from a laboratory or synchrotron source. For instance, in the simplest

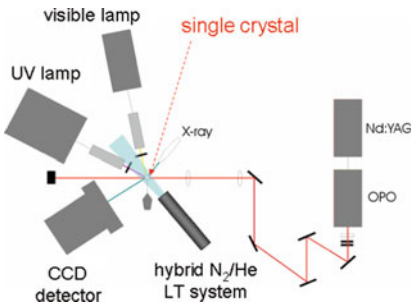

Fig. 1 Schematic of a setup for in situ steady-state X-ray photodiffraction using continuous wave and pulsed excitation sources

[1]Because the term "diffraction" describes the actual physical phenomenon, it is more general in meaning, and it is also frequently used by physicists and biologists, "X-ray photodiffraction" appears to be a more appropriate term than "photocrystallography" and thus it will be used throughout this article.

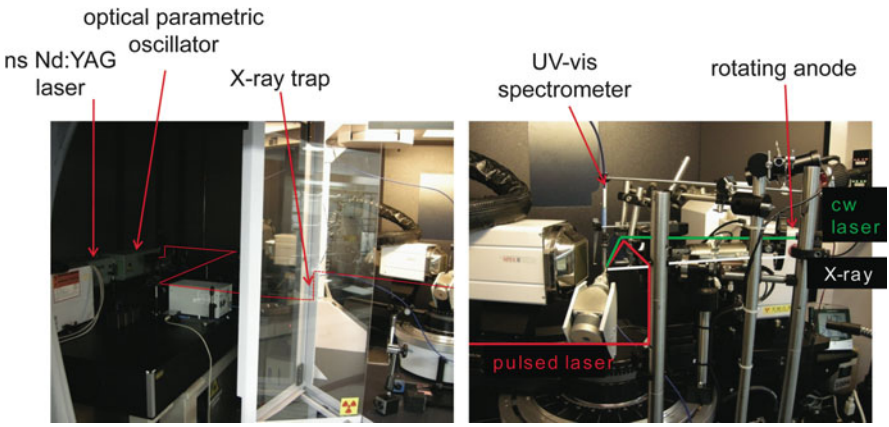

Fig. 2 Experimental setup for in situ single crystal X-ray photodiffraction at Osaka University

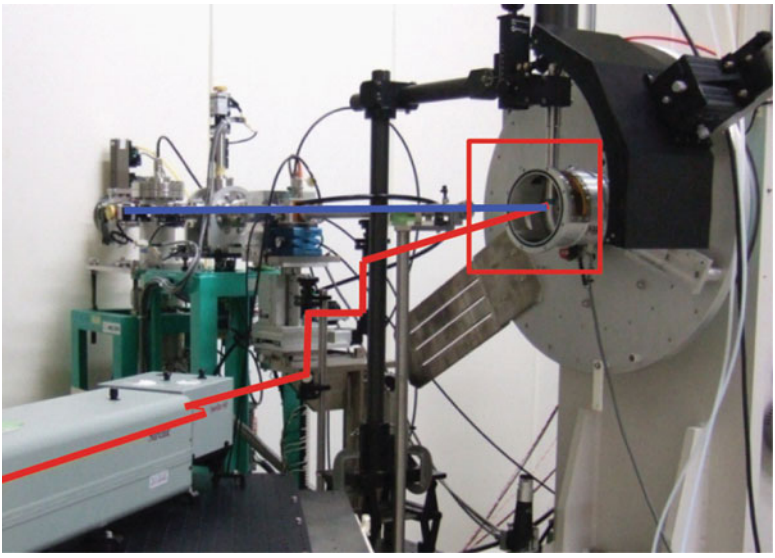

Fig. 3 Setup for in situ powder X-ray photodiffraction at beamline BL15XU, SPring-8, Harima, Japan (the custom diffractometer was built by M. Tanaka, Y. Katsuya, and the NIMS staff at SPring-8)

case of the most common steady-state single crystal X-ray photodiffraction, in order to accumulate sufficient photoinduced unstable, metastable, or stable product, the crystal is exposed to the appropriate excitation light. The unstable species is usually produced ex situ, and the sample is transferred to the diffractometer for data collection, or it can be produced in situ by irradiation directly on the goniometer (Figs. 1 and 2). The product is trapped at low temperature to extend its lifetime and

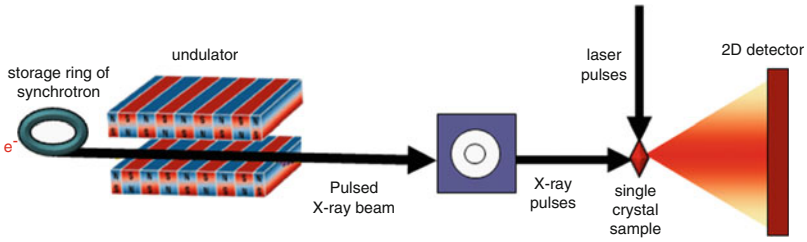

Fig. 4 Schematic representation of the principles of pump-probe time-resolved X-ray photodiffraction

to increase its concentration to a sufficient amount, and the structure of the partially reacted crystal is determined. The concentration of the species produced in such an experiment which is considered sufficient for a reliable structure determination depends on the particular case, and also relates to factors that include the magnitude of the expected structural change, the diffraction resolution/ability of the sample, and eventual deterioration of crystallinity during excitation. For organic crystals, as a very arbitrary value, approximate conversions of $>10\%$ are commonly considered sufficient to obtain a reliable structural signature, whereas yields down to 2–5% are also significant for metal–organic or inorganic samples. It should be noted, however, that the estimated values of conversion yields are inherently biased by the method of their measurement (in particular, they could largely depend on the details of the refinement procedure). As there is no method for straightforward and completely accurate detection of yield in single crystals, yields can occasionally be very different when they are obtained by different methods. Empirically, the best estimates are obtained when two or more (diffraction and spectroscopic) methods based on fundamentally different signals from the product species are used to estimate the photoyield.

In the absence of undesired phase transitions, in order to decrease decay of the product and thermal effects, which would otherwise cause additional smearing of electron density due to atomic oscillations, X-ray photodiffraction methods are usually performed at low temperatures or even under cryogenic conditions. Although in ordered crystals temperature effects on atomic positions can be determined precisely, in disordered crystals, and especially when occupancies of the two components are very different, when component structures have very similar conformations or in cases of multiply disordered structures, increased thermal motion adds up to burden structural complexity. Low temperatures also contribute to decreased heating effects, and they could also prevent decreased diffraction ability due to partial melting of the sample, desolvation, or undesired side reactions (e.g., diffusion-controlled recombination in the case of radical reactions). On rare occasions, however, application of low temperature may be unsuitable and counterproductive, for example, if the studied reactions/processes have qualitatively different product(s) as outcome at low temperature relative to room temperature, or when reactants or products undergo thermal phase transitions by cooling. Selective

and short-term excitation can be very useful in decreasing thermal effects or side reactions, while exciting selectively particular electronic transitions without significant side-effects. In practice, heating can be measured either directly or by using internal standards, such as peak positions of purposefully added compounds with known structure and heat capacity. Heating can also be estimated by relatively simple calculations, considering the power of incident excitation light, heat capacity of the sample, and other predetermined parameters.

The use of light for excitation of the sample in the X-ray photodiffraction method provides an important convenience to the experiment, because the excitation light can be easily created, it can be precisely energy-tuned and controlled (especially, by using pulsed tabletop nanosecond or femtosecond laser sources). Moreover, by using light, it is relatively simple to access the sample in the often rather space-demanding geometries of such experiments. More importantly, study of light-and-matter interaction holds very important application prospects that range from triggering or switching of photoactive molecular units coupled within electrical nanocircuits and controlling molecule-sized nanomachines, to understanding the functions of photooptical recording materials, light-coupled spintronics applications, and photoactivation (uncaging) of bioactive compounds and photoactive proteins.

1.3 Applications

The X-ray photodiffraction technique represents a very useful tool for *structure determination of short-lived, unstable or metastable species* while they are being created or after their creation [6]. It also provides the possibility to *study the reaction progress by real-time in situ monitoring of chemical reactions in solid state*. By using X-ray photodiffraction methods, *direct insight into the spatial atomic distribution can be obtained with precise information about the related structural parameters* (coordinates, distances, and angles). Thus, in principle, one can observe three-dimensional molecular and crystal structures as they change and evolve. It is important that such information is not readily available from the spectroscopic methods, although, by being commonly available with time-resolution down to the femtosecond scale, they can be exceedingly useful to complement and even to assess the accuracy of photodiffraction data. Indeed, photodiffraction experiments are regularly preceded by a time-resolved spectroscopic assessment of the particular phenomenon (for example, the photoyield and magnitude of effects that are expected), or the results are usually supported by other physicochemical evidence which often includes various spectroscopies and/or theoretical calculations.

X-ray photodiffraction methods are increasingly being utilized, and are now well established as an indispensible tool for direct structural study of photoexcited or photoreacted molecular species. Various aspects of this technique have been extensively reviewed by some of the leaders in this field, including Moffat [7–9],

Coppens [10–13], Cole [14–16], Ohashi [17, 18], and Raithby [19], and some aspects were also covered by a publication preceding this review [20]. The intentions with this short chapter were to summarize the basic principles of the technique, to provide a brief overview of the basic ideas behind this method, and – with systems ranging in size from simple metals and homonuclear molecules to highly complex systems such as protein crystals – to illustrate the diversity of applications which could be realized on similar systems in future. Along with the general theme of this review series, we provide in Sect. 2 of this chapter more details on systems which are of "chemical" interest. The results included there are by no means intended to be a collection of the most representative nor of the most important examples; they were simply selected so as to provide a diverse ensemble of chemical and physical cases of study aimed to illustrate the potentials of this technique in a manner comprehensible to a reader with a general chemical background. Some of the examples are from our laboratory, while other examples were selected from the works of some of the leading research groups in the field.

The X-ray photodiffraction method has already been successfully applied to study both chemical and physical processes. The chemical processes (chemical reactions) normally involve alteration of the bonding topology by breaking or creating chemical bonds and subsequent conformational changes. Reactions or processes such as electrocyclizations, cycloadditions, bond isomerizations, dimerizations, transfer of atoms or atomic groups, displacements or movements of molecules or their parts, polymerizations, and bond dissociations have been documented. The physical processes that were investigated include excitations and structure of excited states, evolution and structures of exciplexes, progression of phonons and shock waves, monitoring of lattice dynamics, laser-induced heating effects, photomagnetization, light-induced spin-crossover, charge transfer, photoinduced phase transitions, and similar processes. The size of the studied systems ranges between single atoms or diatomic molecules, to single molecules or ensembles of protein molecules.

1.4 Possible Pitfalls

Despite the unquestionable advantages that it bears for structure elucidation of photoinduced species, at the present state of development, the applicability of the X-ray photodiffraction technique is still limited to systems which must conform to a large number of requirements. Some of the highest hurdles on that road are: (1) often strong absorption of the excitation light by the photoinduced form (the product) in the solid state, (2) occasional decrease of the three-dimensional order of the crystal lattice during photoexcitation as a result of a large structural change (homogeneous process) and/or inability of the lattice to withstand the internal pressure created by the evolution of the photoinduced phase (heterogeneous process), (3) high thermal instability and difficulties with accumulation of sufficient (detectable) amount of the product, and (4) other practical problems which are

commonly encountered with the XRD method. In some particular cases, some of these difficulties can be practically overcome by careful planning of the experiments to maximize their performance based on preliminary information on the properties of the chemical system of interest obtained through scanning of the effect of various factors (temperature, excitation wavelength, irradiation time, etc.) on the reaction, the literature data on results obtained by using other methods, and even with a trial-and-error approach. On certain occasions, unwanted effects can be successfully removed by practical means (for example, by designing specific geometry, temperature regime, or a combination of excitation/deexcitation sources), and, in others, such effects can be accounted for by theoretical calculations.

As one of the major difficulties, the very different cross-sections for absorption by solid samples of electromagnetic radiation in the visible/ultraviolet region and in the X-ray region of the spectrum often result in different portions of the sample being excited and analyzed. In cases of products which absorb strongly in the UV–visible region, accumulation of the product can result in increased absorption of the excitation beam and localized excitation close to the exposed surface of the sample, an effect which has become well known from solution-state spectroscopy as the "filtering effect". Similarly to the approach employed in spectroscopy, selective, off-maximum excitation of the desired electronic transitions, which normally spread over large intervals of energies due to solid-state effects, or multiphoton instead of single-photon excitation could occasionally be employed to solve this problem, thus preventing significant reabsorption of the excitation light by the product. Although these approaches could, in principle, provide more uniform conversion, they depend critically on the presence of (real or virtual) energy levels, other than the main transitions, which should have sufficiently large cross-sections for light absorption. It should also be noted that, due to the imperfections of the excitation beams, long-term excitation with wavelengths that are close to the infrared region (low energy) could significantly excite thermal processes, so that, as a result, undesired thermal reactions may become competitive with the photoexcited transitions. In some difficult cases, reactions from the excited state and from the ground state lead to qualitatively identical (ground-state) product, which is easy to detect but is very difficult to establish its exact origin.

The decreased crystal quality (sometimes referred to as "increased mosaicisity") is caused by relaxation of the lattice from the strains and stresses that had built up as a result of either mechanical pressure from the laser pulses, or, more frequently, the large structural change that occurs during or after the chemical reaction. If the energy gained by the reaction progress outweighs the interaction energy between the molecules, the reaction can still proceed, but it usually does so at the expense of partial crystal disintegration. As a result, macroscopic changes of the crystal can also occur, that sometimes manifest as partial cracking, acquired opaqueness, evolution of visible defects, or slippage or distortion of parts of the crystal. The formation of crystalline domains can also readily be detected by aberrations from the discrete diffraction pattern which is characteristic for the regular translational order in a homogenous single crystal. As a result, some reflections may become smeared, distorted, stronger, weaker, or completely extinguished. Especially if the

reaction and the partial disintegration are operative simultaneously, the assignment of these effects in the diffraction pattern to one particular factor may be difficult without more quantitative assessment and consideration of the overall scattering power and the spatial distribution, shape, and/or intensity of the reflections. In some cases, although present, the disruption of the crystalline order may not be readily visually distinguishable from the effects in the diffraction pattern which occur as a result of the chemical transformation (e.g., increased disorder). The compatibility of a certain solid-state structure to the geometric perturbations required by some chemical reaction can also be assessed by trial steady-state experiments aimed at determining the maximum possible conversion of the reactant to the product without significant decrease in the crystal quality. In practice, the use of polarized light may be helpful to detect such intrinsic non-homogeneities. Yet other, more practical, approaches to overcome the decreased crystallinity problem are preparation of host–guest crystals or cocrystals with suitable secondary molecules, inclusion of the reactants in molecular containers, or using powder samples instead of single crystals.

2 Selected Examples of Application of the X-Ray Photodiffraction Method to Chemical Reactions and Physical Processes

2.1 Steady-State X-Ray Photodiffraction

If species which appear as products in the reaction have very different absorption spectra and color from the reactants in the visible region, progress of the reaction can be analyzed by electron (optical) spectroscopy. If color change can be reverted by exposure of the product to light or heat, the respective reactions are commonly termed *photochromic*. Such changes are usually related to significant changes in the molecular structure (for example, in the degree of electron delocalization) and they can be easily monitored by spectroscopic methods, which turns such systems into important and convenient targets for application of the X-ray photodiffraction method. Many (although not all) of the known organic photochromic systems are based on chemical reactions, such as electrocyclizations or transfer of chemical groups, and they provide the possibility to study these processes in detail. As a typical example, in the case of the widely studied photochromic anil (salicylideneaniline) compounds, the photoinduced enol–keto tautomeric equilibrium due to an intramolecular proton transfer is combined with subsequent *cis–trans* isomerization. X-ray photodiffraction was successfully applied to a number of anils to solve the dilemma of the identity of the product, which was identified as the *trans*-keto form [21]. Other proton transfer reactions, such as the nitro-assisted proton transfer in the nitrobenzylpyridines [22], have also been studied. The electrocyclization/ring-opening reactions comprise another important family of photochromic

systems. In a very recent example, we employed electronic effects to stabilize the product of a spiropyran molecule, which was then analyzed with steady-state ex situ X-ray photodiffraction [23]. The structure refinement showed that the two halves of the molecule undergo out-of-plane and in-plane shifts so that, as a result of the opening of the spiropyran heterocyclic system, the molecule bends slightly. Recently, we have also reported the observation of the electron transfer between free radical molecules in the solid state [24]. Around room temperature, crystalline 1,3,5-trithia-2,4,6-triazapentalenyl radical undergoes paramagnetic-to-diamagnetic phase transition between violet (high-temperature) and yellow (low-temperature) phases, accompanied by wide thermal hysteresis. Excitation by pulsed laser light of the low-temperature diamagnetic phase, in which the molecules are dimerized, causes an inter-dimer electron transfer and local instability within the stacks. The structure of the photoinduced phase was refined from the powder diffraction pattern of the biphasic mixture.

Photocyclization reactions which are not accompanied by drastic color changes characteristic for the photochromic systems have also been investigated by X-ray photodiffraction [25, 26] and neutron diffraction [27]. In 1998, Scheffer published two structures of partially reacted single crystals of salts that undergo Norrish type II (Yang) photocyclization following hydrogen abstraction [28]. In one of the crystals, 60% of the cyclobutanol salt was produced and directly observed. The prospects of the technique for studying similar systems were illustrated by the recent application by Garcia-Garibay and collaborators to the determination of the ring-extended intermediate during the photoreaction of α-santonin [29], one of the oldest antiparasitic drugs. The analysis of the partially reacted crystals helped to identify unequivocally the mechanism of this reaction.

The examples of ex situ steady-state X-ray photodiffraction utilized to follow the photodimerizations of olefin bonds in a single-crystal-to-single-crystal (or nearly so) manner are ubiquitous in the chemical literature.[2] The interest of solid-state chemists in this reaction dates back to the work of Cohen and Schmidt [30, 31], and it has become much of a "guinea pig" in organic solid-state photochemistry. In 1993, Enkelmann and collaborators published two seminal papers in the *Journal of the American Chemical Society* [32] and in *Angewandte Chemie* [33], where they presented a series of structures of α-*trans*-cinnamic acid crystals reacted to various extents. These reports laid the way for a plethora of later studies on the olefin photodimerization reaction. The convenience of the high conversion and the simple mechanism, combined with the relatively small structural perturbation that it requires, has turned this reaction into a very useful tool to probe intermolecular

[2]It may be argued whethere these examples, which have usually employed X-ray diffraction analysis of previously UV irradiated crystals, fall within the domain of the X-ray photodiffraction methods or solid state photochemistry, and whether the term 'X-ray photodiffraction' should be reserved only for time-dependent studies. Although that in the original publications many of these examples have not been labeled as such, because they involve application of XRD methods to study photochemical reactions, we believe that they should be considered as part of the X-ray photodiffraction method in its broadest definition.

interactions, as well as to explore the efficiency of utilization of purposefully tailored supramolecular architectures to control the reactivity. This has been well documented by a great number of reports of studied dimerizations [34] and polymerizations [35], only a small selection of which from the works of the most active researchers in this subject will be mentioned here [36–49] to illustrate the application of X-ray photodiffraction. For instance, the method can be used to determine the reasons behind unusual solid-state kinetics, as has been demonstrated by Techert and collaborators [50] on [4 + 4] photodimerization of β-9-anthracenecarboxylic acid. In combination with spectroscopy and theoretical calculations, analysis of this system unraveled an autocatalytic process. Based on the combined results, at least three possible product configurations were suggested. Recently, we employed the X-ray photodiffraction technique to study isomerization of the red mineral realgar to its yellow polymorph pararealgar [51, 52]. The intermediate phase in which half of the realgar molecule is retained in its envelope-type conformation, while the other half is transformed by effective switching of the positions of one sulfur and one arsenic atom, was observed. The stepwise analysis of the two stages of this reaction (dark and light) unraveled very complex kinetics, with the several reactions acting as a solid-state autocatalytic set with balanced thermodynamics [52].

Photolysis of organic molecules has been employed to access important reactive intermediates (e.g., radicals), either for studying their properties or in order to obtain information on the respective reaction mechanisms. A prerequisite for the analysis of photoinduced radicals is prevention of the recombination reactions, which can be achieved by physical (separation) or chemical (conversion to less reactive species) isolation of the reactive intermediates. As an example, we reported recently the creation of an amidyl radical during a solid-state rearrangement where a chlorine atom of an aromatic *N*-chloroamide is exchanged with an aromatic hydrogen atom [53]. It was found that, after homolysis of the nitrogen–chlorine bond, the detached chlorine atom and an aromatic hydrogen atom switch their positions within the slanted head-to-tail hydrogen-bonded columns of the amide.

Another thoroughly studied group of reactions are the photoinduced linkage isomerizations, which involve change of the coordination mode of small molecular ligands coordinated to metal atoms. Due to the relatively small change in the overall structure at sufficiently large changes in the positions of the non-hydrogen atoms that facilitates analysis of the intermediate states of the reaction, these systems are very suitable for X-ray photodiffraction analysis, because in many cases the lattice has the capacity to sustain the stress exerted by the transformation. Photo- and pressure-induced linkage isomerizations of Co(III) pentaammine nitro/nitrito complexes were studied extensively by Boldyreva and the collaborators [54–59]. This meticulous work has revealed important details on solid-state reactivity, especially, the effects on the structure of the perturbations that occur as a result of coordination switching, as well as their macroscopic consequences such as modified morphology and macroscopic appearance of the crystals. In an early powder diffraction study of photoirradiated samples, the group of Boldyreva has investigated the linkage nitro-nitrito isomerization of $[Co(NH_3)_5NO_2]Br_2$ to $[Co(NH_3)_5ONO]Br_2$ [59], which unraveled the structure of the photochemically produced nitrito isomer and showed

continuous lattice distortion of back (nitrito-to-nitro) isomerization. Some of the other representative examples studied more recently are linkage isomerization of sulfur dioxide complexes of ruthenium [60, 61], where the excited SO_2 molecule, which is coordinated through the sulfur atom, changes its coordination mode to bidentate, where it is coordinated through one sulfur and one oxygen atom. Similar reactions can also proceed with larger ligands [62].

X-ray photodiffraction provides a unique possibility to peek into the geometric changes that take place during molecular excitation, and to determine the accurate geometries of long-lived (metastable) excited states. One necessary condition for such an analysis is relatively long lifetime of the excited states, such as, for example, unusually long-lived states or spin-trapped triplets. A second prerequisite is that the structure of the excited state is sufficiently different from the ground-state structure, which facilitates the analysis at small population ratios of the excited species. One of the pioneering works in this direction was provided by structure analysis of the metastable excited state of sodium nitroprusside, $Na_2[Fe(CN)_5NO]\cdot 2H_2O$ by Coppens et al. [63]. Upon excitation of the anion, Fe–N bond stretches by 0.049(8) Å. More recently, more efforts have been focused on paddle-wheel diplatinum complexes with long-lived luminescent excited states. By employing in situ steady-state irradiation [64], for example, significant shortening of the Pt–Pt bond was observed in a diplatinum paddlewheel complex with a bridging diphosphine ligand (pop), $[Pt_2(H)_2(pop)_4]^{2-}$. By using steady-state X-ray diffraction in their equilibrium (photosteady) states the excited-state structures of similar anions $[Pt_2(pop)_4]^{4-}$ and $[Pt(pop)_2(popH)_2]^{2-}$, isolated from each other in the lattice by bulky quaternary ammonium cations, were analyzed [65]. The results confirmed that significant decrease of the central Pt–Pt and Pt–P distances occurs in the excited state. These experiments are important since they demonstrate the simplicity of the experimental setup which could be employed for such analysis. By the virtue of the steady-state X-ray photodiffraction, the group of Ohashi has analyzed the excited-state structure of gold(I) complex, $[AuCl(PPh_3)_2]\cdot CHCl_3$ [66]. It was demonstrated that due to excitation from an anti-bonding to a bonding molecular orbital, in the excited state there is significant contraction of the Au–P and Au–Cl bonds, which is expressed better at lower temperatures. By using a laboratory-scale setup, recently the excited state of oxovanadium(IV) cation in its acetylacetonato complex $VO(acac)_2$ was analyzed [67]. In the latter case, both bonds V=O and V–O expand by excitation, which appears as a result of photoexcited *d*–*d** transition.

Photoinduced spin-related phenomena are a particularly important field of the solid-state photophysics, because fast spin switching is a prospective basis for applications in the field of spintronics. An illustrative example is the production of the metastable state of the iron propyltetrazole (ptz) complex $[Fe(ptz)_6](BF_4)_2$ by laser light-induced excited spin-state trapping (LIESST) and the determination of the resulting structure by steady-state X-ray photodiffraction [68]. In another example, steady-state X-ray photodiffraction at cryogenic temperatures was successfully utilized to study photoinduced phase transition due to spin crossover in the tris(α-picolylamine)iron(II) complex [69]. The phase transition is accompanied by

a significant increase of the mean length of the Fe–N bonds from 2.011(2) to 2.197 (2) Å. The structure of the resulting photoinduced phase produced from the low-temperature phase resembles that of the high-temperature phase. The crystal structure of the metastable high-spin light induced (LIESST) state of $[Fe(phen)_2(NCS)_2]$ (phen=1,10-phenanthroline) was analyzed with steady-state X-ray photodiffraction by Guionneau et al. [70]. At 30 K, the lengths of the Fe–N bonds increase from 1.990, 2.007, and 1.953 Å in the low-spin phase to 2.177, 2.184, and 2.006 Å in the LIESST phase, respectively, and become closer to the respective values of the high-spin phase at 293 K (2.199, 2.213, and 2.057 Å). Recently, Iversen et al. [71] reported an interesting example of a photomagnetic hetero-bimetallic complex, where in the excited state, contrary to the LIESST phenomenon, the metal–ligand bonds shrink upon photoexcitation. This observation indicated occurrence of ligand-to-metal charge transfer or change of the inter-metal superexchange.

2.2 Time-Resolved X-Ray Photodiffraction

X-ray photodiffraction and structure science have experienced a tremendous development by the advent of *time-resolved diffraction*, which provides the great opportunity to monitor the course of photoinduced processes in real time. Nevertheless, by operating at ultrafast timescales, at which the fast solid-state phenomena proceed, this method is still technically demanding, particularly with respect to the inevitable use of pulsed X-rays and laser light as the probe and excitation beams. Nevertheless, with the earliest examples coming from macromolecular Laue crystallography, an increasing number of examples are now becoming available, most of which are related to reversible photoinduced ultrafast processes. The basic principles behind time-resolved X-ray photodiffraction, for instance, of its "stroboscopic" version, are analogous to time-resolved spectroscopy, but it employs ultrashort X-rays to probe the resulting structural changes. When applied to simple inorganic structures, where the number of independent structure parameters is small, the method can also be conveniently employed to observe laser-induced effects, such as laser-induced atomic shifts that precede larger structural changes (e.g., phase transitions). Selected examples of the application of this method include real-time observation of the progression of shock waves [72], observation of the lattice dynamics [73], and laser heating effects [74]. An elegant early example was provided by Sokolowski-Tinten and collaborators [75] who employed the technique to monitor strong and coherent lattice vibrations near to the Lindemann limit of lattice stability. Short X-ray pulses were produced by acting with an intense laser pulses on a metal and used to probe the change of scattering factors due to oscillations of one of the bismuth atoms away from its equilibrium position. The results are in good agreement with the frequencies obtained from terahertz spectroscopy. Other "physical" applications of the technique include observation of the melting of semiconductors at the femtosecond scale by Rousse and collaborators [76] and study of the structural changes that accompany

solid–solid phase transition of VO_2 at the femtosecond scale by Cavalleri and collaborators [77].

The method has also been applied to organic crystals, although the number of available examples is still rather limited. A remarkable example of a detailed study is the picosecond-scale observation of paraelectric-to-ferroelectric phase transition in the crystals of an organic charge transfer compound, the molecular complex of tetrathiafulvalene and chloranil, reported by Koshihara, Collet and their collaborators [78, 79]. Excitation by femtosecond laser pulses above the threshold triggers partial charge transfer between the alternating donor and acceptor molecules and results in reversible photoinduced phase transition. The phase change appears as lowering of the crystal symmetry caused by the change of intermolecular distances within the stacked columns. Techert and collaborators [80] have employed time-resolved X-ray diffraction to study the mechanism of bond cleavage and formation during [2 + 2] photocycloaddition reaction on α-styrylpyrylium trifluoromethanesulfonate. An extensive study of this system with picosecond time-resolution, supported by spectroscopic assessment, has provided a detailed insight into the mechanism of this important reaction. A sequence of processes, involving bond breaking and formation, phenyl group rearrangement, and anion rotation have been unraveled, and the kinetics of these processes was also deduced [80].

Ultrafast X-ray diffraction has been also employed recently to study the atomic structure and decay profile of excited molecules with long-lived excited states. These studies provide valuable information on the primary processes following photoexcitation. A time-resolved, stroboscopic experiment where the delay between pump and probe is systematically varied, provided direct atomic-scale evidence and the structure of the photoexcited state of the paddlewheel ion $[Pt_2(pop)_4]^{4-}$ [81]. Shortening of the central Pt–Pt bond and slight lengthening of the Pt–P bonds by excitation to the lowest excited triplet state were substantiated by density functional calculations and topological analysis of the charge density [82]. Intermolecular phenomena in electronically coupled systems, such as formation of excited-state complexes (exciplexes), were also observed by time-resolved X-ray photodiffraction, for example, in the case of a trimeric pyrazolate copper complex [83]. Techert and Zacchariase [84, 85] have employed picosecond-scale time-resolved powder X-ray photodiffraction to analyze intermolecular charge transfer in the excited state of solid 4-(diisopropylamino)benzonitrile. The result [85] showed "flattening" of the molecule by decrease of the torsional angle between the diisopropylamino group and the phenyl ring of 4°.

3 Summary and Future Outlook

Although technically still being at the development stages, X-ray photodiffraction is already being established as a very promising method for structure analysis of important photoinduced phenomena related to very fundamental physical and chemical processes that accompany the interaction of the matter with light.

The most important asset of the technique is definitely its capability to provide direct insight into atomic-scale changes that accompany the excitation, either during the time-span of the excited state or after deexcitation and related reactions. This first-hand information on the geometry of the reaction coordinate can be conveniently coupled with that on the energy diagram from other experimental techniques to arrive at complete description of the light-induced phenomena. Having said that, at the present stage, the method has certain limitations, mainly related to the requirements that it puts to the system of interest and to its technical realization. The low efficiency of the excitation represents one of the main burdens in obtaining a sufficiently strong signal of the photoconverted species. Moreover, the optimization of the experimental conditions which are necessary to obtain sufficiently high yields is still a time-consuming process; the result often depends on the particular system and is not universally applicable. In that respect, the utilization of crystal engineering [86, 87] to design crystal motifs which will comply with these requirements (for instance, by retardation of time-decay by modulation of the intermolecular interactions or trapping of the intermediates) might be one alternative approach. With several examples, the group of Coppens has recently demonstrated [88, 89] the usefulness of supramolecular chemistry in the course of "dilution" of the reactive species, although such an approach has its drawbacks, for example, such that are related to the (electronic) interaction of the medium and the photoactive species.

As some of the further developments in the field, development of techniques to probe ultrafast events in *irreversible* processes [90], the development of the experimental setups which will allow opportunities to study a larger number of "slow" processes (in the millisecond and microsecond range), and study of the ultrafast (sub-picosecond) processes are definitely some of the important directions for new developments in the future. Moreover, now, when the basic principles of the method have been developed, it seems natural that the applications should be focused on systems with actual practical interest, for example, systems that are important for alternative energy sources or application in electronics. X-ray free electron lasers that are nowadays becoming available are expected to shorten the timescales, an important direction for further development, both for physics as well as for structural biology [91]. These future applications will also require fast-determining detectors, which are currently a potential bottleneck in the process of further squeezing the timescale. While the importance of X-ray photodiffraction is being increasingly recognized, other X-ray-based methods to study processes in time-domain science, in solution as well as solid state, have simultaneously emerged, so that they now provide a platform to combine information with the results obtained with X-ray photodiffraction. As some of the recent representative examples, solution-state dynamics of small photoexcited molecules can be observed with X-ray scattering at picoseconds scale [92] and solvent reorganization around photoexcited species can be studied by X-ray absorption spectroscopy [93, 94]. The group of Lin Chen has greatly advanced time-resolved X-ray absorption techniques to study metal-to-ligand charge transfer excited states in copper(I) complexes. [95, 96] Time-resolved diffraction using neutrons or electrons for

studying phenomena such as those related to the dynamics of electron-phonon relaxation [97] in the femtosecond region is also on the rise, and will inevitably contribute in the future to deeper understanding of the most fundamental primary processes during interactions of the matter with light. Concomitantly with these experimental advances, the theoretical apparatus is being developed to substantiate and to complement the experimental advances of time-resolved diffraction [98]. These developments will definitely bring new and exciting insights into primary photochemical events in the near future.

References

1. Clegg W (2000) Synchrotron chemical crystallography. J Chem Soc Dalton Trans 3223–3232
2. Ren Z, Bourgeois D, Helliwell JR, Moffat K, Šrajer V, Stoddard BL (1999) Laue crystallography: coming of age. J Synchrotron Radiat 6:891–917
3. Šrajer V, T-y T, Ursby T, Pradervand C, Ren Z, Adachi S, Schildkamp W, Bourgeois D, Wulff M, Moffat K (1996) Photolysis of the carbon monoxide complex of myoglobin: nanosecond time-resolved crystallography. Science 274:1726–1729
4. Petsko GA, Ringe D (2000) Observation of unstable species in enzyme-catalyzed transformations using protein crystallography. Curr Opin Chem Biol 4:89–94
5. Neutze R, Wouts R, van der Spoel D, Weckert E, Hajdu J (2000) Potential for biomolecular imaging with femtosecond X-ray pulses. Nature 406:752–757
6. Schlichting I (2000) Crystallographic structure determination of unstable species. Acc Chem Res 33:532–538
7. Wulff M, Schotte F, Naylor G, Bourgeois D, Moffat K, Mourou G (1997) Time-resolved structures of macromolecules at the ESRF: single-pulse Laue diffraction, stroboscopic data collection and femtosecond flash photolysis. Nucl Instr Meth Phys Res A 398:69–84
8. Moffat K (1998) Time-resolved crystallography. Acta Cryst A 54:833–841
9. Moffat K (2001) Time-resolved biochemical crystallography: a mechanistic perspective. Chem Rev 101:1569–1581
10. Coppens P (2002) Time-resolved chemistry at atomic resolution. Faraday Discuss 122:1–11
11. Coppens P (2003) What can time-resolved diffraction tell us about transient species?: excited-state structure determination at atomic resolution. Chem Commun 1317–1320
12. Coppens P, Novozhilova I, Kovalevsky A (2002) Chem Rev 102:861–884
13. Coppens P, Benedict J, Messerschmidt M, Novozhilova I, Graber T, Chen Y-S, Vorontsov I, Scheins S, Zheng S-L (2010) Time-resolved synchrotron diffraction and theoretical studies of very short-lived photo-induced molecular species. Acta Crystallogr A 66:179–188
14. Cole JM, Raithby PR, Wulff M, Schotte F, Plech A, Teat SJ, Bushnell-Wye G (2002) Nanosecond time-resolved crystallography of photo-induced species: case study and instrument development for high-resolution excited-state single-crystal structure determination. Faraday Discuss 122:119–129
15. Cole JM (2004) Single-crystal X-ray diffraction studies of photo-induced molecular species. Chem Soc Rev 33:501–513
16. Cole JM (2008) X-Ray diffraction of photolytically induced molecular species in single crystals. In: Boeyens JCA, Ogilvie JF (eds) Models, mysteries, and magic of molecules. Springer, Heidelberg, pp 29–62
17. Ohashi Y (2008) Structural determination of unstable species. In: Boeyens JCA, Ogilvie JF (eds) Models, mysteries, and magic of molecules. Springer, Heidelberg, pp 109–135
18. Ohashi Y (1998) Real-time *in situ* observation of chemical reactions. Acta Crystallogr A 54:842–849

19. Raithby PR (2007) Small-molecule chemical crystallography – from three to four dimensions: a personal perspective. Crystallogr Rev 13:121–142
20. Naumov P (2010) Direct observation of dynamic solid-state processes with X-ray diffraction. In: Pignataro B (ed) Ideas in chemistry and molecular sciences. Advances in nanotechnology, materials and devices. Wiley-VCH, Weinheim, pp 207–224
21. Johmoto K, Sekine A, Uekusa H, Ohashi Y (2009) Elongated lifetime of unstable colored species by intermolecular hydrogen bonds formation in photochromic crystals. Bull Chem Soc Jpn 82:50–57
22. Naumov P, Sekine A, Uekusa H, Ohashi Y (2002) Structure of the photocolored 2-(2',4'-dinitrobenzyl)pyridine crystal: two-photon induced solid-state proton transfer with minor structural perturbation. J Am Chem Soc 124:8540–8541
23. Naumov P, Yu P, Sakurai K (2008) Electronic tera-order stabilization of photoinduced metastable species: structure of the photochromic product of spiropyran determined with *in situ* single crystal X-ray photodiffraction. J Phys Chem A 112:5810–5814
24. Naumov P, Hill JP, Sakurai K, Tanaka M, Ariga K (2007) Structural study of the thermally induced and photoinduced phase transitions of the 1,3,5-trithia-2,4,6-triazapentalenyl (TTTA) radical. J Phys Chem A 111:6449–6455
25. Hosomi H, Ohba S, Tanaka K, Toda F (2000) The first *in situ* observation of intramolecular rotation and cyclization of anilide by an X-ray study: partial single-crystal to single-crystal photocyclization of *N*-methyl-*N*-{(*E*)-methylmethacrolyl}anilide in inclusion crystals. J Am Chem Soc 122:1818–1819
26. Kodani T, Matsuda K, Yamada T, Kobatake S, Irie M (2000) Reversible diastereoselective photocyclization of a diarylethene in a single-crystalline phase. J Am Chem Soc 122: 9631–9637
27. Hosoya T, Uekusa H, Ohashi Y, Ohhara T, Kimura H, Noda Y (2003) Deuterium migration mechanism in chiral thiolactam formation by neutron diffraction analysis. Chem Lett 32: 742–743
28. Leibovitch M, Olovsson G, Scheffer JR, Trotter J (1998) An investigation of the Yang photocyclization reaction in the solid state: asymmetric induction studies and crystal structure-reactivity relationship. J Am Chem Soc 120:12755–12769
29. Natarajan A, Tsai CK, Khan SI, McCarren P, Houk KN, Garcia-Garibay MA (2007) The photorearrangement of α-santonin is a single-crystal-to-single-crystal reaction: a long kept secret in solid-state organic chemistry revealed. J Am Chem Soc 129:9846–9847
30. Schmidt GMJ (1971) Photodimerization in the solid state. Pure Appl Chem 27:647–678
31. Cohen MD (1975) The photochemistry of organic solids. Angew Chem Int Ed Engl 14: 386–393
32. Enkelmann V, Wegner G (1993) Single-crystal-to-single-crystal photodimerization of cinnamic acid. J Am Chem Soc 115:10390–10391
33. Novak K, Enkelmann V, Wegner G, Wagener KB (1993) Crystallographic study of a single crystal to single crystal photodimerization and its thermal reverse reaction. Angew Chem Int Ed Engl 32:1614–1616
34. MacGillivray LR, Papaefstathiou GS, Friscic T, Hamilton TD, Bucar D-K, Chu Q, Varshney DB, Georgiev IG (2008) Supramolecular control of reactivity in the solid state: from templates to ladderanes to metal-organic frameworks. Acc Chem Res 41:280–291
35. Hasegawa M (1983) Photopolymerization of diolefin crystals. Chem Rev 83:507–518
36. Tanaka K, Toda F, Mochizuki E, Yasui N, Kai Y, Miyahara I, Hirotsu K (1999) Enantioselective single-crystal-to-single-crystal photodimerization of coumarin and thiocoumarin in inclusion compounds with chiral host compounds. Angew Chem Int Ed Engl 38:3523–3525
37. Tanaka K, Mochizuki E, Yasui N, Kai Y, Miyahara I, Hirotsu K, Toda F (2000) Single-crystal-to-single-crystal enantioselective [2+2] photodimerization of coumarin, thiocoumarin and cyclohex-2-enone in the inclusion complexes with chiral host compounds. Tetrahedron 56:6853–6865
38. Balakrishna RB, Burjor C, Anand P, Ramamurthy V (2010) Thiourea as a template for photodimerization of azastilbenes. J Am Chem Soc 132:13434–13442
39. Yang S-Y, Naumov P, Fukuzumi S (2009) Topochemical limits for solid-state photoreactivity by fine tuning of the π-π interactions. J Am Chem Soc 131:7247–7249

40. Sharma CVK, Panneerselvam K, Shimoni L, Katz H, Carrell HL, Desiraju GR (1994) 3-(3',5'-Dinitrophenyl)-4-(2',5'-dimethoxyphenyl)cyclobutane-1,2-dicarboxylic acid: engineered topochemical synthesis and molecular and supramolecular properties. Chem Mater 6:1282–1292
41. Anthony A, Desiraju GR, Jetti RKR, Kuduva SS, Madhavi NNL, Nangia A, Thaimattam R, Thalladi VR (1998) Crystal engineering: some further strategies. Mater Res Bull 1:1–18
42. Kaftory M, Shteiman V, Lavy T, Scheffer JR, Yang J, Enkelmann V (2005) Discrimination in the solid state photodimerization of 1-methyl-5,6-diphenylpyrazin-2-one. Eur J Org Chem 847–853
43. Lavy T, Kaftory M (2007) Channels formation through photodimerization of guest molecules within solid inclusion compounds. CrystEngComm 9:123–127
44. Nagarathinam M, Peedikakkal AMP, Vittal JJ (2008) Stacking of double bonds for photochemical [2+2] cycloaddition reactions in the solid state. Chem Commun 5277–5288
45. Deng-Ke C, Thekku VS, Mark B, Gilad G, Jason BB, Menahem K (2010) Kinetics of solid state photodimerization of 1,4-dimethyl-2-pyridinone in its molecular compound. J Phys Chem A 114:7377–7381
46. Mir MH, Koh LL, Tan GK, Vittal JJ (2010) Single-crystal to single-crystal photochemical structural transformations of interpenetrated 3D coordination polymers by [2+2] cycloaddition reactions. Angew Chem Int Ed Engl 49:390–393
47. Davaasambuu J, Busse G, Techert S (2006) Aspects of the photodimerization mechanism of 2,4-dichlorocinnamic acid studied by kinetic photocrystallography. J Phys Chem A 110: 3261–3265
48. Fang G, Javier M-R, Zhigang P, Colan EH, Kenneth DMH (2008) Direct structural understanding of a topochemical solid state photopolymerization reaction. J Phys Chem C 112: 19793–19796
49. Turowska-Tyrk I (2001) Structural transformations in a crystal during the photochemical reaction of 2-benzyl-5-benzylidenecyclopentanone. Chem Eur J 7:3401–3405
50. Moré R, Busse G, Hallmann J, Paulmann C, Scholz M, Techert S (2010) Photodimerization of crystalline 9-anthracenecarboxylic acid: a nontopotactic autocatalytic transformation. J Phys Chem C 114:4142–4148
51. Naumov P, Makreski P, Jovanovski G (2007) Direct atomic scale observation of linkage isomerization of As_4S_4 clusters during the photoinduced transition of realgar to pararealgar. Inorg Chem 46:10624–10631
52. Naumov P, Makreski P, Gj P, Runčevski T, Jovanovski G (2010) Visualization of a discrete solid-state process with steady-state X-ray diffraction: observation of hopping of sulfur atoms in single crystals of realgar. J Am Chem Soc 132:11398–11401
53. Naumov P, Sakurai K, Tanaka M, Hara H (2007) Direct observation of aminyl radical intermediate during single-crystal to single-crystal photoinduced Orton rearrangement. J Phys Chem B 111:10373–10378
54. Boldyreva EV (2001) Structural aspects of intramolecular solid-state linkage isomerization in Co(III) pentaammine nitro/nitrito complexes. Russ J Coord Chem 27:1–28
55. Boldyreva EV, Sidelnikov AA, Chupakhin AP, Lyakhov NZ, Boldyrev VV (1984) Deformation and fragmentation of crystals of $[Co(NH_3)_5NO_2]X_2$ ($X = Cl^-$, Br^-, NO_3^-) during photochemical linkage isomerization. Proc Acad Sci USSR 277:893–896
56. Boldyreva EV, Sidel'nikov AA (1987) Effect of mechanical stresses on the photoisomerization in the crystals of Co(III) nitropentaammines. Proc Sib Dept Acad Sci USSR 5:139–145
57. Boldyreva EV, Podberezskaya NV, Virovets AV, Burleva LP, Dulepov VE (1993) X-ray powder diffraction study of linkage nitro-nitrito isomerization in $[Co(NH_3)_5NO_2]XY$ -> $[Co(NH_3)_5ONO]XY$ ($XY = 2Cl^-$, $2Br^-$, $2I^-$, $Cl^-(NO_3)^-$, $2(NO_3)^-$). J Struct Chem 34:128–138
58. Dulepov VE, Boldyreva EV (1994) A comparative study of the kinetics of solid state linkage isomerization $[Co(NH_3)_5ONO]XY \Leftrightarrow [Co(NH_3)_5NO_2]XY$ ($XY = Cl_2$, Br_2, I_2, $(NO_3)_2$, $Cl(NO_3)$). React Kin Catal Lett 53:289–296
59. Masciocchi N, Kolyshev A, Dulepov V, Boldyreva E, Sironi A (1994) Study of the linkage isomerization $[Co(NH_3)_5NO_2]Br_2 \Leftrightarrow [Co(NH_3)_5ONO]Br_2$ in the solid state by X-ray powder diffraction. Inorg Chem 33:2579–2585

60. Kovalevsky AY, Bagley KA, Cole JM, Coppens P (2002) The first photocrystallographic evidence for light-induced metastable linkage isomers of ruthenium sulfur dioxide complexes. J Am Chem Soc 124:9241–9248
61. Kovalevsky AY, Bagley KA, Cole JM, Coppens P (2003) Light-induced metastable linkage isomers of ruthenium sulfur dioxide complexes. Inorg Chem 42:140–147
62. Nakai H, Mizuno M, Nishioka T, Koga N, Shiomi K, Miyano Y, Irie M, Breedlove BK, Kinoshita I, Hayashi Y, Ozawa Y, Yonezawa T, Toriumi K, Isobe K (2006) Direct observation of photochromic dynamics in the crystalline state of an organorhodium dithionite complex. Angew Chem Int Ed 45:6473–6476
63. Presseprich MR, White MA, Vekhter Y, Coppens P (1994) Analysis of a metastable electronic excited state of sodium nitroprusside by X-ray crystallography. J Am Chem Soc 116: 5233–5238
64. Yasuda N, Kanazawa M, Uekusa H, Ohashi Y (2002) Excited-state structure of a platinum complex by X-ray analysis. Chem Lett 1132–1133
65. Yasuda N, Uekusa H, Ohashi Y (2004) X-Ray analysis of excited-state structures of the diplatinum complex anions in five crystals with different cations. Bull Chem Soc Jpn 77: 933–944
66. Hoshino M, Uekusa H, Ohashi Y (2006) X-Ray analysis of excited-state molecular structure of $[AuCl(PPh_3)_2]$. Bull Chem Soc Jpn 79:1362–1366
67. Hoshino M, Sekine A, Uekusa H, Ohashi J (2005) X-Ray analysis of bond elongation in VO $(acac)_2$ in the excited state. Chem Lett 34:1228–1229
68. Kusz J, Spiering H, Gütlich P (2000) X-Ray study of the light-induced metastable state of a spin-crossover compound. J Appl Crystallogr 33:201–205
69. Huby N, Guérin L, Collet E, Toupet L, Ameline J-C, Cailleau H, Roisnel T, Tayagaki T, Tanaka K (2004) Photoinduced spin transition probed by x-ray diffraction. Phys Rev B 69: 020101-1–0201010-4
70. Marchivie M, Guionneau P, Howard JAK, Chastnet G, Letard J-F, Goeta AE, Chasseau D (2001) Structural characterization of a photoinduced molecular switch. J Am Chem Soc 124:194–195
71. Svendsen H, Overgaard J, Chevallier M, Collet E, Iversen BB (2009) Angew Chem Int Ed 48:2780–2783
72. Lindenberg AM, Kang I, Johnson SL, Missalla T, Heimann PA, Chang Z, Larsson J, Bucksbaum PH, Kapteyn HC, Padmore HA, Lee RW, Wark JS, Falcone RW (2000) Time-resolved X-ray diffraction from coherent phonons during a laser-induced phase transition. Phys Rev Lett 84:111–114
73. Rose-Petruck C, Jimenez R, Guo T, Cavalleri A, Siders CW, Ráksi F, Squier JA, Walker BC, Wilson KR, Barty CPJ (1999) Picosecond-milliangstrom lattice dynamics measured by ultrafast X-ray diffraction. Nature 398:310–312
74. Rischel C, Rousse A, Uschmann I, Albouy P-A, Geindre J-P, Audebert P, Gauthier J-C, Förster E, Martin J-L, Antonetti A (1997) Femtosecond time-resolved X-ray diffraction from laser-heated organic films. Nature 390:490–492
75. Sokolowski-Tinten K, Blome C, Blums J, Cavalleri A, Dietrich C, Tarasevitch A, Uschmann I, Förster E, Kammler M, Horn-von-Hoegen M, von der Linde D (2003) Femtosecond X-ray measurement of coherent lattice vibrations near the Lindemann stability unit. Nature 422:287–289
76. Rousse A, Rischel C, Fourmaux S, Uschmann I, Sebban S, Grillon G, Balcou Ph, Förster E, Geindre JP, Audebert P, Gauthier JC, Hulin D (2001) Non-thermal melting in semiconductors measured at femtosecond resolution. Nature 410:65–68
77. Cavalleri A, Tóth Cs, Siders CW, Squier JA, Ráksi F, Forget P, Kieffer JC (2001) Femtosecond structural dynamics in VO_2 during an ultrafast solid-solid phase transition. Phys Rev Lett 87:237401-1–237401-4
78. Collet E, Lemée-Cailleau M-H, Buron-Le Cointe M, Cailleau H, Wulff M, Luty T, Koshihara S, Meyer M, Toupet L, Rabiller P, Techert S (2003) Laser-induced ferroelectric structural order in an organic charge-transfer crystal. Science 300:612–615

79. Guerin L, Collet E, Lemée-Cailleau M-H, Buron-Le Cointe M, Cailleau H, Plech A, Wulff M, Koshihara S, Luty T (2004) Probing photoinduced phase transition in a charge-transfer molecular crystal by 100 picosecond X-ray diffraction. Chem Phys 299:163–170
80. Hallmann J, Morgenroth W, Paulmann C, Davaasambuu J, Kong Q, Wulff M, Techert S (2009) Time-resolved X-ray diffraction of the photochromic α-styrylpyrylium trifluoromethanesulfonate crystal films reveals ultrafast structural switching. J Am Chem Soc 131: 15018–15025
81. Kim CD, Pillet S, Wu G, Fullagar WK, Coppens P (2002) Excited-state structure by time-resolved X-ray diffraction. Acta Cryst A 58:133–137
82. Novozhilova IV, Volkov AV, Coppens P (2003) Theoretical analysis of the triplet excited state of the $[Pt_2(H_2P_2O_5)_4]^{4-}$ ion and comparison with time-resolved X-ray and spectroscopic results. J Am Chem Soc 125:1079–1087
83. Vorontsov II, Kovalevsky AY, Chen Y-S, Graber T, Gembicky M, Novozhilova IV, Omary MA, Coppens P (2005) Shedding light on the structure of a photoinduced transient excimer by time-resolved diffraction. Phys Rev Lett 94:193003-1–193003-4
84. Busse G, Tschentscher T, Plech A, Wulff M, Frederichs B, Techert S (2002) Faraday Discuss 122:105–117
85. Techert S, Zachariasse KA (2004) Structure determination of the intramolecular charge transfer state in crystalline 4-(diisopropylamino)benzonitrile from picoseconds X-ray diffraction. J Am Chem Soc 126:5593–5600
86. Toda F (2002) Crystal engineering for molecular dynamics. CrystEngComm 4:215–222
87. Garcia-Garibay M (2003) Engineering carbene rearrangements in crystals: from molecular information to solid-state reactivity. Acc Chem Res 36:491–498
88. Coppens P, Zheng S-L, Gembicky M, Meeserschmidt M, Dominiak PM (2006) Supramolecular solids and time-resolved diffraction. CrystEngComm 8:735–741
89. Zheng S-L, Vande Velde CML, Messerschmidt M, Volkov A, Gembicky M, Coppens P (2008) Supramolecular solids as a medium for single-crystal-to-single-crystal *E/Z* photoisomerization: kinetic study of the photoreactions of two Zn-coordinated tiglic acid molecules. Chem Eur J 14:706–713
90. Poulin PR, Nelson KA (2006) Irreversible organic crystalline chemistry monitored in real time. Science 313:1756–1760
91. Neutze R, Huldt G, Hajdu J, van der Spoel D (2004) Potential impact of an X-ray free electron laser on structural biology. Rad Phys Chem 71:905–916
92. Neutze R, Wouts R, Techert S, Davidsson J, Kocsis M, Kirrander A, Schotte F, Wulff M (2001) Visualizing photochemical dynamics in solution through picoseconds X-ray scattering. Phys Rev Lett 87:195508-1–195508-4
93. Pham V-T, Gawelda W, Zaushitsyn Y, Kaiser M, Grolimund D, Johnson SL, Abela R, Bressler C, Chergui M (2007) Observation of the solvent shell reorganization around photoexcited atomic solutes by picoseconds X-ray absorption spectroscopy. J Am Chem Soc 129:1530–1531
94. Tomov IV, Rentzepis PM (2004) Ultrafast time-resolved transient structures of solids and liquids by means of extended X-ray absorption fine structure. ChemPhysChem 5:27–35
95. Chen LX, Jennings G, Liu T, Gosztola DJ, Hessler JP, Scaltrito DV, Meyer GJ (2002) Rapid excited-state structural reorganization captured by pulsed X-rays. J Am Chem Soc 124: 10861–10867
96. Chen LX, Shaw GB, Novozhilova I, Liu T, Jennings G, Attenkofer K, Meyer GJ, Coppens P (2003) MLCT state structure and dynamics of a copper(I) diimine complex characterized by pump-probe X-ray and laser spectroscopies and DFT calculations. J Am Chem Soc 125: 7022–7034
97. Harb M, Ernstorfer R, Dartigalongue T, Hebeisen CT, Jordan RE, Dwayne Miller RJ (2006) Carrier relaxation and lattice heating dynamics in silicon revealed by femtosecond electron diffraction. J Phys Chem B 110:25308–25313
98. Henriksen NE, Møller KB (2008) On the theory of time-resolved X-ray diffraction. J Phys Chem B 112:558–567

Top Curr Chem (2012) 315: 133–178
DOI: 10.1007/128_2011_251

Published online: 28 September 2011

Powder Diffraction Crystallography of Molecular Solids

Kenneth D.M. Harris

Abstract Many important crystalline solids cannot be prepared as single crystals of suitable size and quality for structural characterization by conventional single-crystal X-ray diffraction techniques and can instead be prepared only as microcrystalline powders. However, recent advances in techniques for determining crystal structures directly from *powder* X-ray diffraction data have created a unique opportunity for establishing structural properties of such materials. This chapter surveys the applications of powder X-ray diffraction across various aspects of structural and materials chemistry, focusing mainly on the opportunities that have emerged in recent years for carrying out complete crystal structure determination from powder X-ray diffraction data and giving particular emphasis to the case of molecular crystal structures. The current scope and future potential of powder X-ray diffraction as a strategy for crystal structure determination are discussed, and examples of applications across several disciplines of materials chemistry are presented.

Keywords Powder diffraction · Molecular solids · Organic crystals · Crystal structure · Direct space · Structure solution · Structure determination

Contents

K.D.M. Harris (✉)
School of Chemistry, Cardiff University, Park Place, Cardiff, Wales CF10 3AT, UK
e-mail: HarrisKDM@cardiff.ac.uk

1 Introduction

Single-crystal X-ray diffraction (XRD) [1] is without question the most important and powerful technique for determining crystal and molecular structures, and applications of this technique led to many of the most important scientific advances that emerged during the twentieth century. There is every reason to expect that the central importance of single-crystal XRD, both in the physical and biological sciences, will continue to be consolidated in the years to come. The wide-ranging applications of single-crystal XRD in the modern day have arisen both through advances in instrumentation as well as through the development of tremendously powerful strategies for data analysis, such that crystal structures can be determined almost routinely in all but the most challenging cases. Thus, provided a single crystal of sufficient size and quality is available for the material of interest, successful structure determination by analysis of single-crystal XRD data is nowadays very routine. However, the requirement to prepare a suitable single crystal specimen of appropriate size and quality for single-crystal XRD experiments can often represent a limitation of this technique, and many important crystalline materials have eluded structure determination simply because they can be prepared only as microcrystalline powders.

Under such circumstances, the most direct approach for investigating the structural properties of the material of interest is to use powder XRD, although it is important to emphasize that the process of carrying out structure determination from powder XRD data is substantially more challenging than from single-crystal XRD data. There are therefore considerable opportunities for the development of

new strategies and methodologies for carrying out structure determination directly from powder XRD data, and as many important materials can be prepared only as microcrystalline powders, progress in advancing the scope and power of methodologies in this field has the potential to make considerable impact in several areas of structural sciences.

Although single-crystal XRD and powder XRD patterns contain essentially the same information, the diffraction data are distributed in three-dimensional space in the single-crystal XRD pattern, whereas the diffraction data are "compressed" into one dimension in the powder XRD pattern (Fig. 1). As a consequence, there is usually considerable overlap of peaks in the powder XRD pattern. Such peak overlap obscures information on the positions and intensities of the diffraction maxima, and the intrinsic difficulty of obtaining reliable information of this type from the powder XRD pattern can impede (or in some cases prohibit) the process of carrying out crystal structure determination. Molecular solids typically have large unit cells and low symmetry, which result in a high density of peaks in the powder XRD pattern. Thus, the problem of peak overlap is often particularly severe for such materials, and the task of carrying out structure determination from powder XRD data is rendered more challenging. Nevertheless, in the case of organic

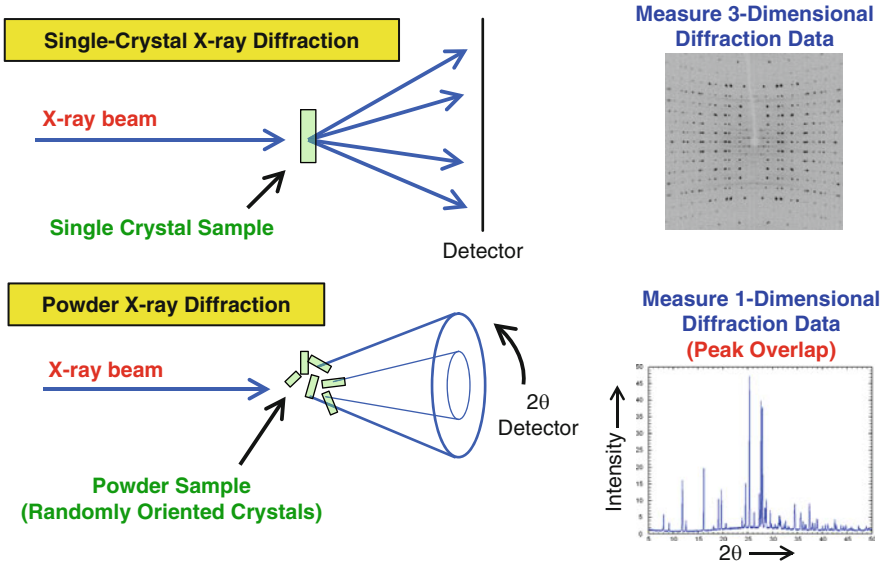

Fig. 1 Comparison of single-crystal and powder XRD measurements. In powder XRD, the diffraction phenomenon for each individual crystallite in the powder is the same as the diffraction phenomenon in single-crystal XRD. However, the powder comprises a large collection of crystallites with (in principle) a random distribution of crystallite orientations, and as a consequence, the three-dimensional diffraction data are effectively compressed into one dimension (intensity vs diffraction angle 2θ) in the powder XRD measurement

molecular materials, recent advances in techniques for structure determination from powder XRD data [2–20] are such that the structural properties of organic molecular materials of moderate complexity can now be established relatively routinely by this approach (in particular by exploiting the direct-space strategy for structure solution [2]), creating the opportunity to elucidate the structural properties of a wide range of materials that are unsuitable for investigation by single-crystal XRD.

This chapter highlights the current state-of-the-art in structure determination from powder XRD data, giving particular emphasis to the case of *molecular* solids. Fundamental aspects of the techniques used to carry out structure determination from powder XRD data are described (Sect. 2), and examples illustrating the application of these techniques for determining the crystal structures of molecular materials are presented (Sect. 6). While the examples highlighted in Sect. 6 are taken primarily from the work of the author's own research group, these examples are illustrative of the types of structural problem that are nowadays being tackled successfully by a number of research groups dedicated to this field. Other topics covered include a discussion of the validation of results obtained by structure determination from powder XRD data (Sect. 3), emphasizing inter alia the benefits of utilizing evidence from other experimental techniques (particularly solid-state NMR) in conjunction with the powder XRD analysis, consideration of experimental aspects of powder XRD data (Sect. 4), particularly relating to issues of data quality and good practice that are conducive to successful structure determination, and a discussion of certain issues relating to the use of powder XRD for identification and "fingerprinting" of crystalline phases (Sect. 5). While the discussion of fundamentals and the highlighted examples focus on the case of powder XRD, it is relevant to note that the data analysis techniques discussed here are also generally applicable in the case of structure determination from powder neutron diffraction data. Nevertheless, to date these techniques have been applied much more extensively in the case of powder XRD data.

2 Structure Determination from Powder XRD Data

2.1 Relationship Between a Crystal Structure and Its Diffraction Pattern

In the diffraction pattern from a crystalline solid, the *positions* of the diffraction maxima depend on the periodicity of the structure (i.e. the dimensions of the unit cell), whereas the *relative intensities* of the diffraction maxima depend on the distribution of scattering matter (i.e. the atoms or molecules) within the unit cell. In the case of XRD, the scattering matter is the electron density within the unit cell. Each diffraction maximum is characterized by a unique set of integers h, k and l (Miller indices) and is defined by a scattering vector $\boldsymbol{H}$ in three-dimensional

"reciprocal space", given by $\boldsymbol{H} = h\boldsymbol{a}^* + k\boldsymbol{b}^* + l\boldsymbol{c}^*$. The basis vectors $\boldsymbol{a}^*$, $\boldsymbol{b}^*$ and $\boldsymbol{c}^*$ are called the reciprocal lattice vectors, and depend on the crystal structure. The three-dimensional space defining the crystal structure is called "direct space".

A given diffraction maximum $\boldsymbol{H}$ is completely defined by the structure factor $F(\boldsymbol{H})$, which has amplitude $|F(\boldsymbol{H})|$ and phase $\alpha(\boldsymbol{H})$. In XRD, the structure factor $F(\boldsymbol{H})$ is related to the electron density $\rho(\boldsymbol{r})$ within the unit cell by the following equation:

$$F(\boldsymbol{H}) = |F(\boldsymbol{H})|\exp(i\alpha(\boldsymbol{H})) = \int \rho(\boldsymbol{r})\exp[2\pi i\boldsymbol{H}\cdot\boldsymbol{r}]\,\mathrm{d}\boldsymbol{r}, \tag{1}$$

where $\boldsymbol{r}$ is the vector $\boldsymbol{r} = x\boldsymbol{a} + y\boldsymbol{b} + z\boldsymbol{c}$ in direct space ($\boldsymbol{a}$, $\boldsymbol{b}$ and $\boldsymbol{c}$ are the lattice vectors defining the periodicity of the crystal structure) and the integration is over all vectors $\boldsymbol{r}$ in the unit cell. It follows from (1) that

$$\rho(\boldsymbol{r}) = (1/V)\sum\nolimits_H |F(\boldsymbol{H})|\exp[i\alpha(\boldsymbol{H}) - 2\pi i\boldsymbol{H}\cdot\boldsymbol{r}], \tag{2}$$

where V is the volume of the unit cell and the summation is over all vectors $\boldsymbol{H}$ with integer coefficients h, k and l. If both the amplitude $|F(\boldsymbol{H})|$ and phase $\alpha(\boldsymbol{H})$ of the structure factor could be measured directly from the experimental XRD pattern, then $\rho(\boldsymbol{r})$ (i.e. the "crystal structure") could be determined directly from (2) by summing over the measured diffraction maxima $\boldsymbol{H}$. However, while the values of $|F(\boldsymbol{H})|$ can be obtained experimentally from the measured diffraction intensities $I(\boldsymbol{H})$, the values of the phases $\alpha(\boldsymbol{H})$ cannot be determined directly from the experimental diffraction pattern, which constitutes the so-called "phase problem" in crystallography. To determine a crystal structure from experimental XRD data by using (2), it is necessary to use techniques (e.g. direct methods or the Patterson method) that provide estimated values of the phases $\alpha(\boldsymbol{H})$. Using the estimated phases $\alpha(\boldsymbol{H})$ together with the experimentally determined $|F(\boldsymbol{H})|$ values in (2) allows the electron density $\rho(\boldsymbol{r})$ and hence the crystal structure to be elucidated (at least approximately). More details of the techniques for overcoming the "phase problem" are given elsewhere [1, 21].

Importantly, the reverse procedure of calculating the diffraction pattern for any given structure [using (1)] is an "automatic" calculation. Thus, the diffraction pattern ($|F(\boldsymbol{H})|$ data) can be calculated automatically for *any* crystal structure using the positions of the atoms in the crystal structure in (1), employing a form of (1) in which the electron density $\rho(\boldsymbol{r})$ is approximated by a function that depends on the positions of the atoms in the unit cell. This type of calculation is the basis of the *direct-space strategy* for structure solution. In the direct-space strategy, a large number of trial crystal structures are generated by computational procedures; the XRD pattern for each trial structure is then calculated automatically using (1), and these calculated XRD patterns are then compared with the experimental XRD pattern in order to assess the degree of "correctness" of each trial structure. More details of the direct-space strategy for structure solution are given in Sect. 2.6.2.

2.2 How to Compare Experimental and Calculated Powder XRD Patterns

The complete powder XRD profile (either for an experimental pattern or a calculated pattern) is described in terms of the following components: (1) the peak positions, (2) the background intensity distribution, (3) the peak widths, (4) the peak shapes, and (5) the peak intensities. The peak shape depends on characteristics of both the instrument and the sample, and different peak shape functions are appropriate under different circumstances. The most common peak shape for powder XRD is the pseudo-Voigt function, which represents a hybrid of Gaussian and Lorentzian character, although several other types of peak shape function may be applicable in different situations. These peak shape functions and the types of function commonly used to describe the 2θ-dependence of the peak width are described in detail elsewhere [22].

There are two general approaches for comparing experimental powder XRD data with powder XRD data calculated for a structural model during the process of structure determination: (1) comparison of the complete powder XRD profile and (2) comparison of integrated peak intensities. We now consider each of these approaches in turn.

Comparison of the complete powder XRD profile uses the entire digitized *experimental* powder XRD pattern directly "as measured", and requires a digitized powder XRD profile to be *calculated* from the structural model in order to compare it to the experimental pattern. To construct this calculated powder XRD pattern for a trial structure requires not only the intensities of all peaks in the powder XRD pattern, which are determined using (2), but also requires information on the peak positions, peak widths, peak shapes and the background intensity distribution. Clearly, reliable whole-profile comparison between calculated and experimental powder XRD patterns requires that the variables describing these aspects of the calculated pattern must accurately reflect those in the experimental pattern. The methodology for determining the values of the variables that describe these features of the experimental powder XRD profile is discussed in Sect. 2.5. After calculating the digitized powder XRD pattern for the structural model, it is compared directly with the experimental powder XRD pattern using an appropriate whole-profile figure-of-merit, the most common of which is the weighted profile R-factor R_{wp}, defined as

$$R_{\mathrm{wp}} = 100 \times \sqrt{\frac{\sum_i w_i (y_i - y_{\mathrm{c}i})^2}{\sum_i w_i y_i^2}}, \tag{3}$$

where y_i is the intensity of the ith point in the digitized experimental powder XRD pattern, $y_{\mathrm{c}i}$ is the intensity of the ith point in the calculated powder XRD pattern and w_i is a weighting factor for the ith point. A significant advantage of using a whole-profile figure-of-merit of this type is that it uses the experimental data (i.e. the

digitized data points $\{y_i\}$) directly "as measured", without further manipulation. This type of figure-of-merit is used in Rietveld refinement, as well as in several implementations of direct-space techniques for structure solution.

Consideration of integrated peak intensities, on the other hand, involves analysis of the experimental powder XRD pattern to extract a set of integrated peak intensities $I(\boldsymbol{H})$ [and hence $|F(\boldsymbol{H})|$ values] analogous to those obtained directly in single-crystal XRD. Because of the problem of peak overlap in powder XRD data, the task of extracting a reliable set of integrated peak intensities from a heavily overlapped powder XRD pattern is nontrivial. The basic techniques for achieving this task are discussed in Sect. 2.5. Methods have been developed for enhancing the reliability of the intensity extraction process, and using the extracted intensities in a manner that takes the reliability of the extraction process into account (by making use of the variance–covariance matrix [23]). After extracting a set of integrated peak intensities, the experimental and calculated $I(\boldsymbol{H})$ data can be compared using the types of figure-of-merit employed in the analysis of single-crystal XRD data. However, a disadvantage of this approach in the case of powder XRD data is that any errors or uncertainties associated with the process of extracting the integrated peak intensities from the experimental pattern (originating from ambiguities in handling the peak overlap) are inevitably propagated into the structure determination process, and may limit the reliability of the derived structural information or even prohibit successful structure determination. As discussed below, comparison of integrated peak intensities is central to the traditional approach for structure solution. In addition, some implementations of the direct-space approach are also based on comparison of integrated peak intensities, with the aim of maximizing speed (as such figures-of-merit are faster to calculate than those based on comparison of the complete powder XRD profile, such as R_{wp}) at the expense of reliability.

2.3 Overview of the Structure Determination Process

The three stages of structure determination from diffraction data are (1) unit cell determination and space group assignment, (2) structure solution, and (3) structure refinement. *Structure solution* aims to derive an approximately correct description of the structure, using the unit cell and space group determined in the first stage, but starting from no knowledge of the actual arrangement of atoms or molecules in the unit cell. If the structure solution represents a sufficiently good approximation to the true structure, a good quality description of the structure can then be obtained by *structure refinement*. For powder XRD data, unit cell determination is carried out using standard indexing procedures [24–26], and structure refinement is carried out routinely using the Rietveld profile refinement technique [22, 27, 28]. In the case of powder XRD data, an additional (and crucially important) stage of the structure determination process is the "profile refinement" stage, discussed in more detail in Sect. 2.5. The sequence of stages involved in structure determination from powder XRD data is summarized in Fig. 2.

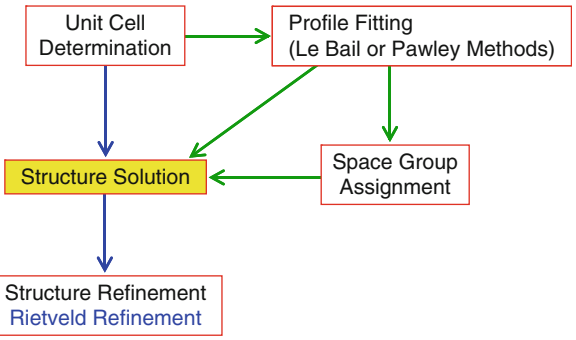

Fig. 2 Schematic diagram showing the sequence of stages involved in crystal structure determination from powder XRD data

2.4 *Unit Cell Determination (Indexing)*

The first stage of structure determination involves determination of the unit cell $\{a, b, c, \alpha, \beta, \gamma\}$ by analysis of the peak positions in the powder XRD pattern [this task is referred to as "indexing" the powder pattern, and involves assigning the Miller indices (h, k, l) to each observed peak in the experimental powder XRD pattern]. Clearly, the structure determination process can progress to the structure solution and structure refinement stages *only* if the correct unit cell is found at the indexing stage, and difficulties encountered in achieving reliable indexing of powder XRD patterns can sometimes be an insurmountable hurdle that prevents successful structure determination.

The different strategies that are available for indexing powder XRD data (which are incorporated into the widely used programs ITO [24], TREOR [25], DICVOL [26] and CRYSFIRE [29]) generally consider the measured positions of peak maxima for about 20 selected peaks at low diffraction angles. The existence of significant peak overlap can be particularly problematic in the indexing stage, as certain peaks that may be vital for correct indexing may be obscured or completely unresolved due to peak overlap. In this regard, successful indexing of powder XRD data in the case of molecular solids can sometimes be particularly challenging, as a consequence of the substantial peak overlap often observed for such materials, as noted above.

2.5 *Preparing the Intensity Data for Structure Solution: Profile Fitting*

After the unit cell has been determined, the next stage is to prepare the intensity data for space group determination and structure solution using an appropriate profile fitting technique such as the Pawley method [30] or the Le Bail method [31]. The aim of this stage of the structure determination process is to fit the complete experimental powder XRD profile by refinement of variables that describe:

(1) The peak positions (the variables that determine the peak positions include the unit cell parameters and the zero-point shift parameter)
(2) The background intensity distribution
(3) The peak widths
(4) The peak shapes
(5) The peak intensities

With regard to (1), the input values of the unit cell parameters used in the profile fitting procedure are those obtained in the indexing stage, and the refined values that result from the profile fitting procedure represent a more accurate set of unit cell parameters. It is important to emphasize that no structural model is used in the profile fitting procedure (except in so far as the unit cell parameters are used to determine the peak positions), and the intensities in (5) represent a set of intensity variables that are refined to give an optimal fit to the experimental powder XRD pattern without reference to any structural model. Thus, the aim of the profile fitting procedure is not to determine the crystal structure, but rather to obtain reliable values of the variables that describe different features of the powder XRD profile [i.e. (1)–(5) above] in preparation for the subsequent stages of the structure determination process. As now discussed, it is also important to note that different strategies for structure solution make use of different combinations of the variables in (1)–(5) as input information.

The traditional approach for structure solution requires, as input data, the integrated peak intensities extracted from the experimental powder XRD pattern – i.e. the fitted intensity values (5) obtained from the profile fitting procedure. In addition, some implementations of the direct-space strategy for structure solution are based on comparison of integrated peak intensities, and also make use of the intensity values (5) obtained at the profile fitting stage. After extracting the integrated peak intensities (5), these approaches do not make any further use of the experimental powder XRD profile during the structure solution stage (although the experimental powder XRD pattern is again used in the Rietveld refinement stage).

Alternatively, several other implementations of the direct-space structure solution strategy involve comparison between experimental and calculated data using a whole-profile figure-of-merit such as R_{wp}. In this case, the intensity data (5) extracted from the experimental powder XRD pattern in the profile fitting procedure are not used in the structure solution stage. Instead, the variables (1)–(4) determined in the profile fitting procedure are used (together with intensities calculated for trial structural models) to construct the calculated powder XRD pattern for each trial structure generated in the direct-space structure solution calculation.

Following the profile fitting procedure, the space group can be assigned by identifying the conditions for systematic absences in the intensity data (5). If the space group cannot be assigned uniquely, structure solution calculations should be carried out separately for each of the plausible space groups. Knowledge of unit cell volume and space group, together with density considerations, allows the contents of the asymmetric unit to be established. Information from other experimental techniques (particularly high-resolution solid-state NMR) may be particularly

helpful in confirming the number of independent molecules in the asymmetric unit and elucidating other structural aspects that may be useful in assisting the structure solution process (see Sect. 3).

2.6 Structure Solution

Techniques for structure solution from powder XRD data can be subdivided into two categories: the traditional and direct-space approaches.

2.6.1 The Traditional Approach for Structure Solution

The *traditional* approach for structure solution follows a close analogy to the analysis of single-crystal XRD data, in that the intensities $I(\boldsymbol{H})$ of individual reflections are extracted directly from the powder XRD pattern and are then used in the types of structure solution calculation (e.g. direct methods, Patterson methods or the recently developed charge-flipping methodology [32–34]) that are used for single-crystal XRD data. As discussed above, however, peak overlap in the powder XRD pattern can limit the reliability of the extracted intensities, and uncertainties in the intensities can lead to difficulties in subsequent attempts to solve the structure. As noted above, such problems may be particularly severe in cases of large unit cells and low symmetry, as encountered for most molecular solids. In spite of these intrinsic difficulties, however, there have been several reported successes in the application of traditional techniques for structure solution of molecular solids from powder XRD data.

2.6.2 The Direct-Space Approach for Structure Solution

In contrast to the traditional approach, the *direct-space* approach for structure solution [2] follows a close analogy to global optimization procedures. In the *direct-space* strategy, trial crystal structures are generated in direct space, independently of the experimental powder XRD data, and the suitability of each trial structure is assessed by direct comparison between the powder XRD pattern calculated for the trial structure and the experimental powder XRD pattern (see Sect. 2.2). This comparison is quantified using an appropriate figure-of-merit. Several implementations of the direct-space strategy have used the weighted powder profile R-factor R_{wp} (the R-factor normally employed in Rietveld refinement), which considers the entire digitized intensity profile point-by-point, rather than the integrated intensities of individual diffraction maxima. Thus, R_{wp} takes peak overlap implicitly into consideration. Furthermore, R_{wp} uses the digitized powder XRD data directly as measured, without further manipulation of the type required when individual peak intensities $I(\boldsymbol{H})$ are extracted from the experimental

powder XRD pattern. As discussed in Sect. 2.5, some implementations of the direct-space strategy (e.g. [35, 36]) have employed figures-of-merit based on integrated peak intensities $I(\boldsymbol{H})$ extracted from the experimental powder XRD pattern in the profile fitting procedure (i.e. the intensity data (5) discussed in Sect. 2.5), rather than comparison of the complete powder XRD profile by means of R_{wp}. Specific details are discussed in the papers cited.

The aim of the direct-space strategy is to find the trial crystal structure that corresponds to lowest R-factor, and is equivalent to exploring a hypersurface $R(\boldsymbol{\Gamma})$ to find the global minimum, where $\boldsymbol{\Gamma}$ represents the set of variables that define the structure (discussed in more detail below). In principle, any technique for global optimization may be used to find the lowest point on the $R(\boldsymbol{\Gamma})$ hypersurface, and much success has been achieved using Monte Carlo/simulated annealing [2, 35–57] and genetic algorithm [58–75] techniques in this field. In addition, grid search [76–80] and differential evolution [81, 82] techniques have also been employed.

We now consider the way in which trial structures are defined within the context of direct-space structure solution calculations for molecular solids. In principle, the set ($\boldsymbol{\Gamma}$) of structural variables could be taken to comprise the coordinates of each individual atom within the asymmetric unit, but this approach discards any prior knowledge of molecular geometry and corresponds to the maximal number of structural variables (3 N variables for N atoms in the asymmetric unit). Instead, it is advantageous to use directly all information on molecular geometry that is already known reliably [in the study of molecular materials, the identity of the molecule is generally known before starting the structure solution calculation, and if ambiguities remain concerning the atomic connectivity (e.g. tautomeric form), other techniques such as solid-state NMR may be useful to resolve these ambiguities before starting the structure solution calculation]. Thus, it is common to fix bond lengths and bond angles at standard values in direct-space structure solution calculations and to fix the geometries of well-defined structural units (e.g. aromatic rings). In general, the only aspects of intramolecular geometry that need to be determined are the values of some (or all) of the torsion angles that define the molecular conformation. Under these circumstances, each trial structure in a direct-space structure solution calculation is defined by a set ($\boldsymbol{\Gamma}$) of structural variables that represent, for each molecule in the asymmetric unit, the position of the molecule in the unit cell (defined by the coordinates $\{x, y, z\}$ of the centre of mass or a selected atom), the orientation of the molecule in the unit cell (defined by rotation angles $\{\theta, \phi, \psi\}$ relative to the unit cell axes) and the unknown torsion angles $\{\tau_1, \tau_2, \ldots, \tau_n\}$. Thus, in general, there are $6 + n$ variables, $\boldsymbol{\Gamma} = \{x, y, z, \theta, \phi, \psi, \tau_1, \tau_2, \ldots, \tau_n\}$, for each molecule in the asymmetric unit.

We emphasize that an important feature contributing to the success of the direct-space approach is that it makes maximal use of information on molecular geometry that is already known reliably, independently of the powder XRD data, prior to commencing the structure solution calculation. The traditional approach for structure solution, on the other hand, does not (in general) utilize prior knowledge of features of molecular geometry.

The significant advances that have been made in the last 17 years or so in the capability of determining crystal structures of organic molecular solids from powder XRD data have been catalyzed largely by the availability of direct-space techniques for structure solution, both because structure determination of molecular materials is particularly well suited to these techniques and because of improvements in computer power during this time. To date, most reported crystal structure determination of organic molecular solids from powder XRD data has used the direct-space strategy, although there have also been several reports of successful structure determination of such materials using the traditional approach (see examples discussed in [3, 7]). The first demonstration [83] of structure solution of a molecular crystal from powder XRD data was for the *previously known* structure of cimetidine using the traditional approach for structure solution (direct methods) and using data recorded at a synchrotron radiation source. The first *previously unknown* equal-atom molecular crystal structure to be solved from powder XRD data was formylurea, again using the traditional approach (direct methods) but from laboratory powder XRD data [84]. The first material of unknown crystal structure to be solved using a direct-space strategy was *p*-$BrC_6H_4CH_2CO_2H$ [2] using the Monte Carlo method, followed by other examples (including 3-chloro-*trans*-cinnamic acid [38] and 1-methylfluorene [85]) using the same technique.

For structure solution by the direct-space approach, the complexity of the structure solution problem is dictated largely by the dimensionality of the hypersurface to be explored (i.e. the total number of structural variables in the set $\mathbf{\Gamma}$) rather than the number of atoms in the asymmetric unit. Thus, the greatest challenges in the application of direct-space techniques arise when the number of structural variables is large; this situation occurs when there is considerable molecular flexibility (i.e. when the molecular geometry is defined by a large number of variable torsion angles) and/or when there are several independent molecules in the asymmetric unit.

We note that for molecular solids or other materials constructed from well-defined modular building units (such as metal-organic-framework materials), the direct-space strategy represents a particularly suitable approach for structure solution, given the wide availability of reliable information on the geometries of the molecular building units. For other types of materials, for which the peak overlap problem is less severe or for which there is insufficient prior knowledge of the geometry of a suitable structural fragment for use in direct-space calculations, the traditional approach would generally be the favoured approach for structure solution.

2.7 *Structure Refinement*

In Rietveld refinement [22, 27, 28], the variables that define the powder XRD profile (i.e. the variables (1)–(4) in Sect. 2.5) and the variables defining the structural model (which are used to determine the relative peak intensities in the calculated

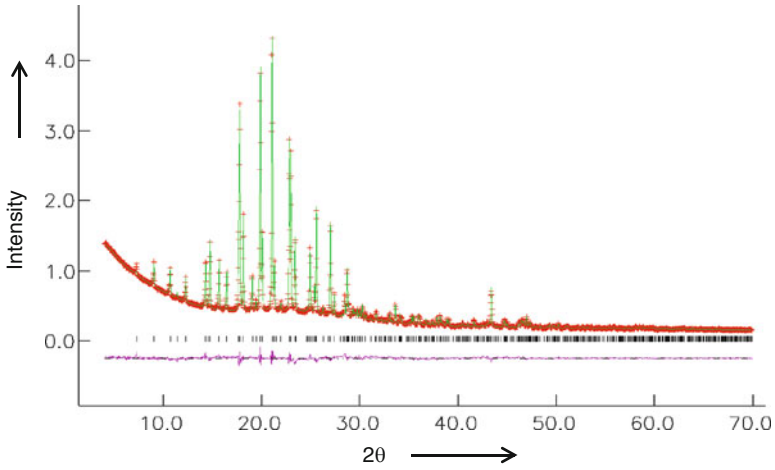

Fig. 3 A typical result from Rietveld refinement (specifically for the material **TDMM** discussed in Sect. 6.3). The experimental powder XRD pattern is shown as *red plus* marks and the calculated powder XRD pattern for the structural model is shown as the *green line*. The *tick marks* indicate peak positions. The difference between the experimental and calculated powder XRD profiles is shown as the *purple line* at the *bottom*. Clearly, for a good quality Rietveld refinement, this "difference profile" should be as flat as possible, and should ideally reflect only the noise level in the experimental data

powder XRD pattern) are adjusted by least squares methods in order to obtain an optimal fit between the experimental and calculated powder XRD patterns. In general, the weighted profile *R*-factor (R_{wp}) is used to assess the fit between experimental and calculated powder XRD patterns. An example of the fit obtained in a typical Rietveld refinement calculation is shown in Fig. 3. The structural variables in Rietveld refinement are analogous to those (e.g. atomic coordinates, atomic displacement parameters, site occupancies, etc.) used in refinement from single-crystal XRD data, and are thus different from the variables used in direct-space structure solution discussed in Sect. 2.6. Thus, while bond lengths and bond angles are usually fixed in direct-space structure solution calculations, such geometric constraints are generally relaxed in the Rietveld refinement stage.

For successful Rietveld refinement, the initial structural model (taken from the structure solution) must be a sufficiently good representation of the correct structure. As Rietveld refinement often suffers from problems of instability, the use of geometric restraints (soft constraints) based on standard molecular geometries generally need to be applied in order to ensure stable convergence of the refinement. Furthermore, it is common to use only isotropic displacement parameters in Rietveld refinement, rather than the anisotropic displacement parameters that are generally refined (except in the case of hydrogen atoms) for single-crystal XRD data. As in structure determination from single-crystal XRD data, the structural model obtained in the structure solution stage is sometimes an incomplete

representation of the true structure (particularly when structure solution is carried out using the traditional approach), and difference Fourier techniques can be used in conjunction with Rietveld refinement to complete the structural model.

Finally, it is relevant to comment on the quality of structural information that can be obtained by structure determination from powder vs single-crystal XRD data. In general, the final structural parameters obtained from powder XRD data are not as accurate or precise as those that could be determined from analysis of single-crystal XRD data for the same material (assuming that a suitable single crystal is available). Nevertheless, a carefully refined crystal structure from powder XRD data (for example, giving the quality of fit shown in Fig. 3) provides reliable information on the arrangement of atoms and molecules in the crystal structure, and allows an understanding of most aspects of the crystal structure that are of interest to chemists (such as details of the molecular packing arrangement and identification of the intermolecular interactions).

3 Validation of the Procedures and Results in Structure Determination from Powder XRD Data

Although computer programs for carrying out structure determination from powder XRD data are now readily accessible and relatively straightforward to use, it is essential that the structural results obtained from such calculations are subjected to adequate scrutiny before they can be assigned as definitely correct. In this regard, two aspects of validation must be considered: (1) validating the structural model used in direct-space structure solution (see Sect. 3.1) and (2) validating the final structure obtained from Rietveld refinement (see Sect. 3.2).

It is also important to emphasize the merit of exploiting information from other experimental and computational techniques within these validation processes. Such techniques include solid-state NMR spectroscopy, energy calculations (either on individual molecules or periodic crystal structures), vibrational spectroscopies and techniques of thermal analysis (e.g. DSC and TGA). Solid-state NMR, in particular, can play an important role, as it can provide insights on specific structural features independent of the diffraction data, including: the tautomeric form of the molecule, the number of independent molecules in the asymmetric unit, the question of whether molecules occupy general positions or special positions, direct evidence for the existence of specific interactions (e.g. hydrogen bonds), quantitative information on specific interatomic distances, and a priori insights on the existence of disorder within a crystal structure. Information on several of these structural aspects can be important in setting up the correct structural model for a direct-space structure solution calculation, or in validating the final structural results obtained from Rietveld refinement.

3.1 Validation Before Direct-Space Structure Solution

Aspects of validation prior to direct-space structure solution are focused on (1) establishing the correct representation of molecular geometry to be used in the direct-space structure solution calculation and (2) establishing independent evidence for the correct number of molecules in the asymmetric unit.

First we consider setting up a suitable structural model for direct-space structure solution. In general, the identity of the molecule(s) in the structure and the composition (e.g. in the case of a solvate or cocrystal phase) may be established readily by applying a range of analytical techniques, including high-resolution solid-state NMR. Another important issue concerns details of molecular geometry, recognizing that many molecules can adopt different tautomeric forms. The structure determination of red fluorescein [39] from powder XRD data provided an early example of the use of solid-state NMR data to inform the process of setting up a suitable structural model for direct-space structure solution. In this case, high-resolution solid-state ^{13}C NMR distinguished the correct tautomeric form of the molecule in the crystal structure. Clearly, in order to achieve successful structure solution in direct-space calculations, it is generally crucial to use a geometrically correct representation of the molecule (including correct assignment of the tautomeric form).

Second, we consider the number of molecules in the asymmetric unit. Following unit cell determination, the number of molecules in the unit cell is generally deduced straightforwardly from density considerations, but such information does not necessarily lead to a unique assignment of the number of molecules in the asymmetric unit, nor a unique assignment of the space group. In such cases, high-resolution solid-state NMR can often provide valuable independent information on the number of molecules in the asymmetric unit, based on the fact that, for example, the high-resolution solid-state ^{13}C NMR spectrum of an organic material should contain one peak for each crystallographically distinguishable carbon atom in the structure (although, in practice, the actual number of *observed* peaks may be less than this number due to accidental peak overlap). Thus, after assigning each peak in the solid-state ^{13}C NMR spectrum to a specific carbon environment within the molecule, it is generally straightforward to assess whether there are one, two or more molecules in the asymmetric unit, or only a fraction of the molecule (indicating that the molecule is located on a special position).

As an example [86], in structure determination of the 1:1 cocrystal formed between benzoic acid (**BA**) and pentafluorobenzoic acid (**PFBA**), the high-resolution solid-state ^{13}C NMR spectrum (Fig. 4) was found to contain two peaks for the carbon atom of the carboxylic acid group of **BA** and two peaks for the carbon atom of the carboxylic acid group of **PFBA**, leading to the conclusion that the asymmetric unit comprises two molecules of **BA** and two molecules of **PFBA**. In this case, systematic absences in the powder XRD pattern indicated that the structure is C-centred and has a *c*-glide plane, and density considerations suggested that there are eight molecules of **BA** and eight molecules of **PFBA** in the unit cell. The solid-state NMR data therefore point towards Cc as the correct space group

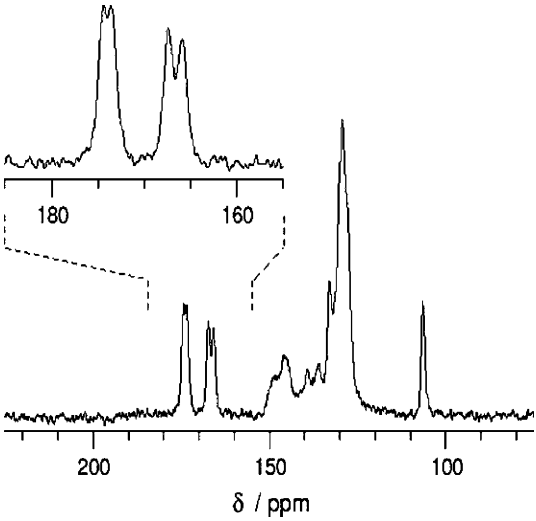

Fig. 4 High-resolution solid-state ^{13}C NMR spectrum of the 1:1 cocrystal containing benzoic acid (**BA**) and pentafluorobenzoic acid (**PFBA**). The two peaks at ca. 174 ppm represent the carboxylic acid group of **PFBA** and the two peaks at ca. 167 ppm represent the carboxylic acid group of **BA**

(with two molecules of **BA** and two molecules of **PFBA** in the asymmetric unit), rather than C2/c (with one molecule of **BA** and one molecule of **PFBA** in the asymmetric unit).

An example of high-resolution solid-state ^{13}C NMR yielding direct evidence that a molecule resides on a special position was encountered in structure determination of an early-generation dendrimeric material [87], with the solid-state ^{13}C NMR data supporting the assignment that the molecule is located on a crystallographic twofold rotation axis. Structure determination of a new polymorph (β phase) of the latent pigment DPP-Boc [88] from powder XRD data also relied on evidence from high-resolution solid-state ^{13}C NMR to confirm that the asymmetric unit comprises half the DPP-Boc molecule.

3.2 Aspects of Validation After Structure Refinement

Aspects of validation after Rietveld refinement are focused on (1) establishing whether the quality of agreement between experimental and calculated powder XRD patterns is sufficiently good to give confidence that the refined structure is correct, (2) assessing whether the refined structure is chemically and structurally sensible, (3) assessing whether there is evidence for disorder in the structure and (4) assessing whether the use of powder XRD data alone provides an adequate description of the structure or whether complementary techniques are required to resolve specific questions or ambiguities.

To assess the quality of the final structure obtained in structure determination, it is important to scrutinize carefully the difference profile obtained in the Rietveld refinement calculation (which represents the difference between the experimental

and calculated powder XRD patterns, as shown in Fig. 3). Clearly the difference profile should not contain any significant discrepancies, and any minor discrepancies that do exist (i.e. discrepancies that are higher than the noise level in the experimental data) must be properly understood before the Rietveld fit can be regarded as acceptable. In this regard, it is important to compare the difference profile obtained in the Rietveld refinement with the difference profile obtained *for the same experimental powder XRD pattern* in the profile-fitting stage of the structure determination process. The profile-fitting procedure establishes an upper limit to the quality of fit that could be obtained in a Rietveld refinement calculation for the same experimental powder XRD pattern (and for the same 2θ range). Thus, the Rietveld refinement should aspire to achieve a quality of fit (assessed from the difference profile) that is as close as possible to that obtained in the profile-fitting procedure. If the fit obtained in the Rietveld refinement is significantly worse than that obtained in the profile-fitting procedure, it is probably an indication that the refined structure is incorrect, or at least that some aspect of the true structure is not adequately described in the structural model.

An example of the importance of applying rigorous scrutiny before accepting the results from a Rietveld refinement calculation concerns the structure determination of 3,5-bis(3,4,5-trimethoxybenzyloxy)benzyl alcohol (**BTBA**) from powder XRD data [89]. Following structure solution by the direct-space genetic algorithm technique, Rietveld refinement gave the fit shown in Fig. 5a. For this Rietveld refinement ($R_{wp} = 8.25\%$), the difference profile might at first glance appear relatively flat, and could be quite readily misinterpreted as representing a correct, fully refined crystal structure. However, the discrepancies between experimental and calculated powder XRD patterns in the difference profile obtained in the Rietveld refinement are greater than those in the difference profile obtained in the profile fitting stage in which the Le Bail technique was used (Fig. 5b; $R_{wp} = 2.99\%$), suggesting that the refined structure, while probably substantially correct, is still not acceptable. Furthermore, it was found that the structure did not contain any O–H···O hydrogen bonding, which was somewhat surprising (although not impossible) for a molecule that has a single hydrogen bond donor (OH group) and several potential hydrogen bond acceptors (oxygen atoms of the $COCH_3$, $COCH_2$ and OH groups). Given these concerns, more detailed scrutiny involving difference Fourier analysis suggested that there was "missing" electron density in the structure. Following further experimental analysis (primarily by liquid state ^{1}H NMR and TGA), it was discovered that the material was actually a monohydrate of **BTBA**. Further Rietveld refinement was then carried out after adding the water molecule to the structural model, leading to a significant improvement in the quality of fit (Fig. 5c; $R_{wp} = 4.33\%$), which was considered to be acceptably close to the quality of fit obtained in the profile fitting procedure (Fig. 5b). Furthermore, the position of the water molecule in the crystal structure (Fig. 5d) gave rise to a structurally sensible hydrogen-bonding array (Fig. 5e) involving the water molecules and the OH groups of the **BTBA** molecules.

Next, we consider the use of other sources of information to provide additional support for specific structural features. In the structure determination of 1-formyl-2,4,6-trimethoxybenzene and 1-acetyl-2,4,6-trimethoxybenzene from

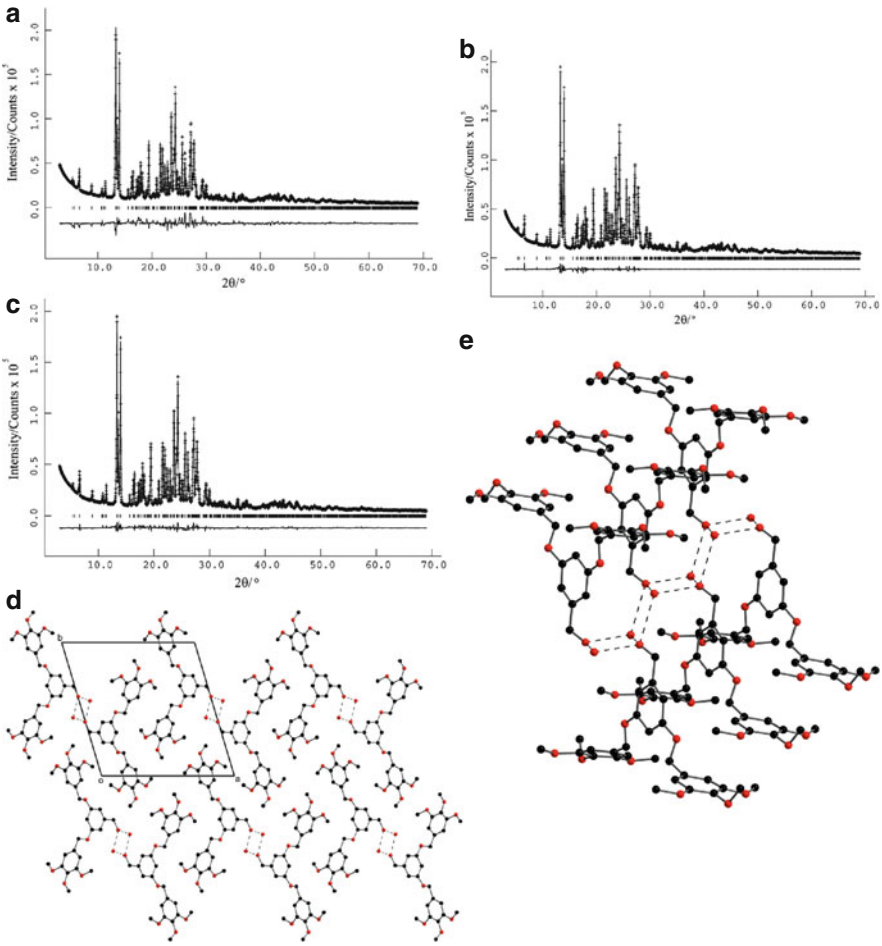

Fig. 5 (**a**) Rietveld fit for the structural model comprising **BTBA** only. (**b**) Fit obtained in the profile fitting procedure using the Le Bail technique. (**c**) Rietveld fit for the structural model comprising **BTBA** and water. (**d**) Final refined crystal structure of **BTBA** monohydrate (*dotted lines* indicate O–H···O interactions in the extended hydrogen-bonded array, which runs into the page). (**e**) Crystal structure of **BTBA** monohydrate viewed in a direction that shows the extended hydrogen-bonded array. Hydrogen atoms are omitted for clarity

powder XRD data [90], DFT calculations provided independent evidence to confirm that the structures correspond to energetically accessible conformations of the molecules. Another example [90] addressed the question of whether an OH group is involved in O–H···O hydrogen bonding by employing solid-state ^{2}H NMR spectroscopy (on the material in which the OH group is deuterated – i.e. OD), as the ^{2}H NMR quadrupole coupling constant (measured directly from the ^{2}H NMR spectrum) is sensitive to details of hydrogen-bonding geometry.

Another aspect of validation concerns the detection of disorder in the crystal structure, recalling that solid-state NMR can provide a means of directly detecting disorder (as well as distinguishing dynamic vs static disorder) in crystal structures. Cases of severe disorder generally require an appropriate description of the disorder to be incorporated in the structural model in both the structure solution and structure refinement stages. However, if the disorder concerns a sufficiently localized part of the structure, it may be possible to obtain a reasonable Rietveld fit using an ordered structural model, which can then be improved by incorporating a description of the disorder within the structural model. The latter situation was encountered in structure determination of the β polymorph of *p*-formyl-*trans*-cinnamic acid from powder XRD data [91] (Fig. 6). The structure was solved and refined as an ordered structure, leading to a good quality of fit in the Rietveld refinement ($R_{wp} = 3.27\%$). However, the high-resolution solid-state ^{13}C NMR spectrum showed evidence for

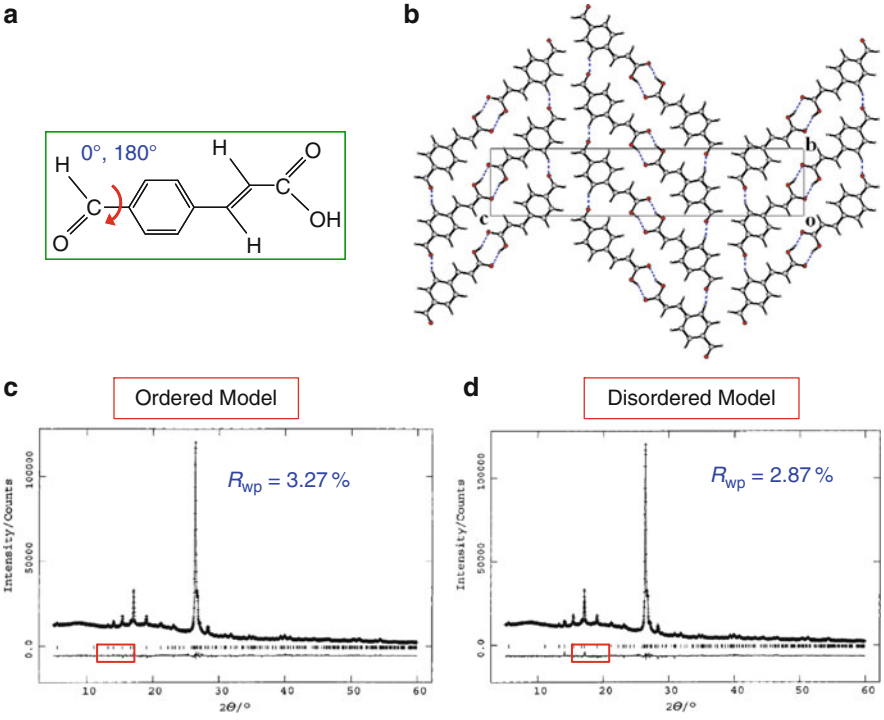

Fig. 6 Results from Rietveld refinement of the disordered crystal structure of the β polymorph of *p*-formyl-*trans*-cinnamic acid. The disorder concerns two orientations of the formyl group as shown in (**a**). The crystal structure in (**b**) shows only the disorder component of higher occupancy. The results from Rietveld refinement shown at the *bottom* are for (**c**) an ordered model comprising only the major orientation of the formyl group, and (**d**) the final disordered model (*right side*). Apart from the description of the order/disorder of the formyl group, all other aspects of these refinement calculations were the same. A slight improvement in the quality of the Rietveld fit for the disordered model is evident

disorder of the formyl group (with the remainder of the structure ordered). Thus, the ^{13}C NMR spectrum has two peaks for the ^{13}C site in the formyl group, whereas all other ^{13}C sites in the molecule give just a single peak. Integration of the two peaks for the formyl group indicated two components with relative populations ca. 69% and 31%. In subsequent Rietveld refinement, the disorder of the formyl group was modelled in terms of two orientations (with the plane of the formyl group in the same plane as the aromatic ring in each case, but differing by 180° rotation about the C–C bond that links the formyl group and the aromatic ring). Rietveld refinement of the disordered model gave an improved fit ($R_{wp} = 2.87\%$), with refined occupancies for the two orientations of the formyl group of 59% and 41%, in relatively close agreement with the relative populations established from the solid-state ^{13}C NMR data. In this case, if evidence of disorder had not been obtained from the solid-state ^{13}C NMR data, the Rietveld refinement obtained for the ordered model would probably have been considered to provide an acceptable fit to the experimental powder XRD data, and the existence of the disorder may not have been apparent from consideration of the powder XRD data alone.

Finally, we consider a case in which structure determination from powder XRD data alone could not elucidate all aspects of the crystal structure. In particular, for cases in which structural questions concern the details of hydrogen bonding arrangements, the advantages of employing powder neutron diffraction compared to powder XRD data must be emphasized. In spite of the historical importance of ammonium cyanate $NH_4^+OCN^-$ (first studied by Friedrich Wöhler over 180 years ago [92]), the crystal structure remained undetermined until recently [93, 94], as this material can be prepared only as a microcrystalline powder and is therefore unsuitable for structure determination by single-crystal XRD. Structure determination from powder XRD data established the positions of the nonhydrogen atoms [93], but could not reliably distinguish the correct orientation of the ammonium cation. In the crystal structure, the nitrogen atom of the ammonium cation resides at the centre of a nearly "cubic" arrangement of O and N atoms (from cyanate anions), which occupy alternate corners of the "cube". Two plausible orientations of the ammonium cation may be proposed, in one case forming four N–H···O hydrogen bonds and in the other forming four N–H···N hydrogen bonds. Early computational studies (periodic Hartree–Fock calculations) favoured the structure with N–H···O hydrogen bonding [93], although the results were later found to be very basis-set dependent, and subsequent computational studies based on periodic DFT calculations favoured the structure with N–H···N hydrogen bonding. To resolve this issue, neutron powder diffraction studies were carried out [94] on the deuterated material $ND_4^+OCN^-$ (actually ca. 81% D, 19% H). The neutron diffraction results definitively support the structure with N–D···N hydrogen bonding, with no detectable extent of disorder between the N–D···O and N–D···N hydrogen bonding arrangements. Results from solid-state ^{15}N NMR studies [94] are also consistent with this assignment of the hydrogen bonding arrangement. In particular, the temperature dependence of the ^{15}N NMR chemical shift of the cyanate anion is consistent with the changes that would be expected for the case in which the cyanate nitrogen atom is involved in N–H···N hydrogen bonding.

4 Experimental Considerations

4.1 Synchrotron vs Laboratory Powder XRD Data

We now consider the relative merits of using synchrotron powder XRD data vs conventional laboratory powder XRD data in structure determination from powder XRD data, recognizing that the use of synchrotron radiation generally gives rise to powder XRD data of higher resolution and improved signal/noise ratio. With high resolution, problems due to peak overlap can be alleviated, at least to some extent, thus increasing the reliability in determining accurate peak positions (which is particularly advantageous for unit cell determination) and increasing the reliability in extracting the intensities of individual diffraction maxima from the powder XRD pattern. In this regard, synchrotron radiation can be particularly advantageous when the traditional approach (or a direct-space technique that uses a figure-of-merit based on extracted peak intensities) is to be used for structure solution. Thus, the success of traditional techniques for structure solution is generally enhanced by using data recorded on an instrument with the highest possible resolution. However, for direct-space structure solution techniques that employ a figure-of-merit based on a profile R-factor (such as R_{wp}), the most important requirement is not high resolution itself, but rather that the peak profiles are well-defined and accurately described by the peak shape and peak width functions used in the structure solution calculation. In such cases, the use of laboratory powder XRD data can be just as effective as the use of synchrotron data, and many examples (including the majority of those presented in Sect. 6) demonstrate that the use of a good-quality, well-optimized laboratory powder X-ray diffractometer is usually perfectly adequate for research in this field. Within the context of Rietveld refinement, we note that the use of synchrotron data generally leads to structural results of greater accuracy, as a consequence of the fact that the data in the high 2θ region of the powder XRD pattern are usually of higher quality for synchrotron data than laboratory data.

4.2 Preferred Orientation

In general, structure solution from powder XRD data has a good chance of success only if the experimental powder XRD pattern contains reliable information on the intrinsic relative intensities of the diffraction maxima, which requires that there is no "preferred orientation" in the powder sample. Preferred orientation arises when the crystallites in the powder sample have a nonrandom distribution of orientations, and this effect can be particularly severe when the crystal morphology is strongly anisotropic (e.g. long needles or flat plates). When a powder sample exhibits preferred orientation, the measured relative peak intensities differ from the intrinsic relative diffraction intensities, limiting the prospects for determining reliable structural information from the powder XRD pattern. In order to circumvent this

difficulty, it is recommended that appropriate procedures [95] are carried out to screen powder samples for preferred orientation, and to take steps to ensure that the sample is free of preferred orientation *before* recording high-quality powder XRD data for use in structure determination calculations. If preferred orientation is detected, a variety of experimental approaches may be used to alleviate the effects of preferred orientation, such as using a capillary or end-loading sample holder, mixing the sample with an amorphous material, preparing the sample by spray-drying, or using an appropriate grinding procedure to induce a crystal morphology that is as isotropic as possible. Even if the effects of preferred orientation cannot be eliminated completely from the experimental powder XRD pattern, corrections for preferred orientation can be made retrospectively once a sufficiently good structural model is known, by refinement of parameters describing the preferred orientation during the Rietveld refinement stage. In general, attempted structure solution from powder XRD data affected *significantly* by preferred orientation has a high chance of being unsuccessful, and it is recommended that time should be devoted to checking the sample for preferred orientation and carrying out careful sample preparation to ensure, as far as possible, that the powder sample has a random distribution of crystallite orientations.

4.3 Phase Purity of the Powder Sample

Another issue that can have a profound bearing on the success of structure determination from powder XRD data is the phase purity of the powder sample. So far, the discussion in this chapter has assumed that the powder sample comprises only one crystalline phase. If the powder sample contains a second crystalline phase (e.g. a crystalline impurity or a second polymorph of the material of interest) and is *not known* to contain this second phase, then the structure determination process will almost certainly fail at the indexing stage (as it will be impossible to find a single unit cell that predicts the positions of all the peaks, arising from the two phases, in the powder XRD pattern). However, if the existence and identity of an impurity phase or second phase is known beforehand, the peaks due to this additional phase may be recognized and handled in an appropriate manner that allows the structure of the main phase of interest to be determined successfully. Clearly, the use of other experimental techniques (such as solid-state NMR) may be advantageous for providing independent evidence for the phase purity of a powder sample *before* starting the process of structure determination from powder XRD data (perhaps indicating that the sample preparation procedure needs to be optimized in order to obtain a phase-pure sample).

In favourable cases, however, careful inspection of the powder XRD data alone may allow the presence of more than one phase to be identified without utilizing information from other techniques, as illustrated in the structure determination of cyclopentadienyl rubidium [96] from the powder XRD pattern of a mixture of two polymorphs. Initial attempts to index the powder XRD pattern failed, but closer

inspection revealed that the data could be subdivided into two sets of peaks with appreciably different linewidths, which were attributed to the two polymorphs. Indexing and structure determination were then carried out successfully for both polymorphs.

5 Applying Powder XRD for "Fingerprinting" of Crystalline Phases

A basic, yet crucially important, application of powder XRD is in the identification ("fingerprinting") of crystalline phases, based on the fact that different crystal structures give rise to distinct powder XRD patterns. Qualitative characterization of materials in this manner finds applications in many scientific disciplines (both academic and industrial), including quality control, polymorph screening, and the characterization of products from rapid throughput crystallization experiments [97, 98].

This qualitative application of powder XRD is used extensively in all areas of materials preparation. The aim is to compare the experimental powder XRD pattern of a sample prepared by materials synthesis with the powder XRD patterns of known materials (either experimental powder XRD data recorded for materials prepared by other routes, or powder XRD patterns simulated from crystal structures determined previously). Sometimes these comparisons are carried out "by eye", based on visual assessment of the similarities and/or differences between the powder XRD patterns, rather than subjecting the powder XRD data to more rigorous quantitative analysis. In favourable cases, visual comparison may be unambiguous in confirming that the powder XRD pattern of the synthesized material either matches a known material or is clearly different from all potential candidate materials of known structure. However, much deeper scrutiny is often required, and cases in which unambiguous confirmation can be established simply by visual inspection are much less common. Unfortunately, comparisons based on visual inspection can allow considerable scope for misinterpretation, with the potential to lead to erroneous structural assignments. Ambiguity in comparing powder XRD patterns by visual inspection can arise either:

(1) When the prepared material is the same as a known material, but the powder XRD patterns may actually appear significantly different, such that the match to the known material is not easily identified by visual comparison.
(2) When the main features of the powder XRD patterns resemble each other significantly, but with some small differences. In such cases, visual comparison tends to focus on the main features of resemblance between the patterns and the small differences are often overlooked. However, small differences between powder XRD patterns can represent real and significant structural differences, and, if they are ignored, there is the risk that two materials that have genuinely different structures may be assigned wrongly as being the same material. In such cases, the two structures may indeed share some structural features in

common, but it is nevertheless crucial to determine the structural reasons for the small differences between the powder XRD patterns. Relevant issues in this regard include superstructures, subtle differences of symmetry, differences in the occupancy of a component (e.g. a solvent molecule) within the structure, or differing degrees of disorder. An illustrative example of this type of situation, taken in part from work described in [99], is illustrated in Fig. 7.

With regard to visual comparison, it is important to note that the appearance of an experimental powder XRD pattern can be influenced by several factors that are not related to the actual crystal structure of the material, but originate instead from

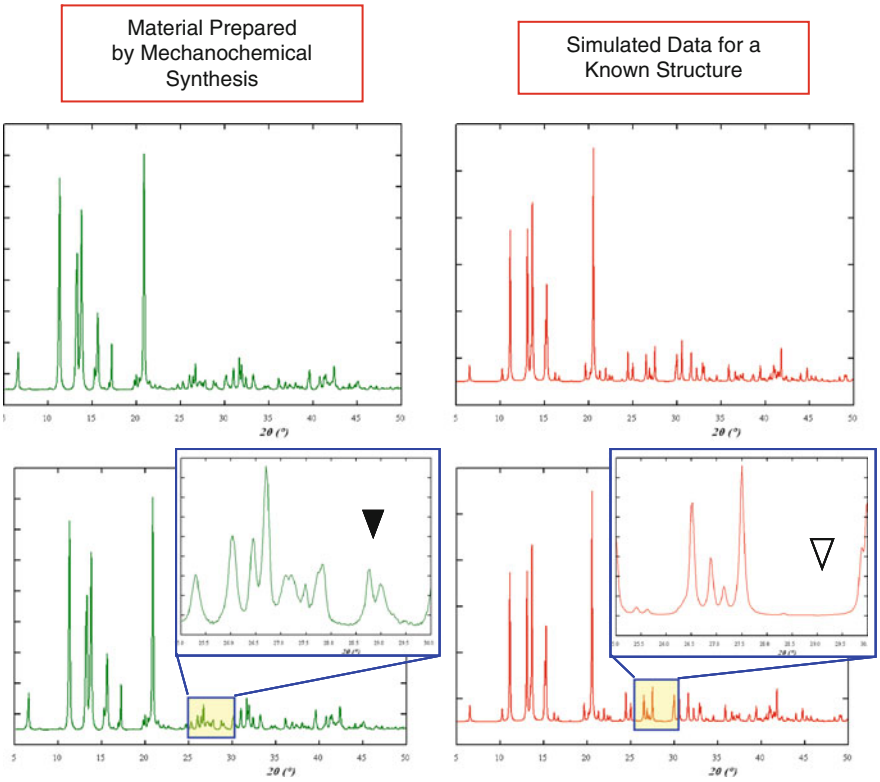

Fig. 7 Comparison between the experimental powder XRD pattern of a material prepared by mechanochemical synthesis and the simulated powder XRD pattern of a potential candidate known structure prepared previously by a solvothermal route. Visual comparison (*top part*) might tend to suggest that the two materials are very similar. However, detailed comparison (*bottom part*) reveals important differences between the powder XRD patterns. In particular, the peak at $2\theta \approx 29°$ is present for the material prepared by mechanochemical synthesis but is absent for the material prepared by solvothermal synthesis. This peak arises from a subtle structural difference and leads to the conclusion that the structures of the two materials cannot be identical. Structure determination of the material prepared by mechanochemical synthesis was carried out subsequently from powder XRD data. The actual structural differences are shown in Fig. 11

features of the instrumentation and/or the mode of data collection, as well as features relating to microstructural characteristics of the powder sample itself (e.g. the size, shape and orientational distribution of the crystallites in the powder). Thus, as identified in case (1) above, powder XRD patterns recorded for two materials with the same crystal structure might actually look quite different as a result of differences in some of these other factors, which include the following:

1. *Peak widths.* The lineshapes and linewidths of peaks in a powder XRD pattern depend on the crystallinity of the sample, as well as features of the instrumentation and the data collection procedure. In particular, peaks in the powder XRD pattern may be broadened as a consequence of small crystallite size. If the powder XRD patterns of two samples with the same crystal structure have significantly different linewidths, the visual appearance may differ substantially, especially in regions of significant peak overlap.
2. *Peak intensities.* If the material exhibits "preferred orientation" (i.e. a nonrandom distribution of orientations of the crystallites within a powder), the relative intensities of peaks in the powder XRD pattern will deviate from the intrinsic relative intensities that are characteristic of the crystal structure, and hence the powder XRD patterns recorded for two samples of the same material but exhibiting different degrees of preferred orientation may appear substantially different. This issue is particularly pertinent in comparing an experimental powder XRD pattern with a simulated powder XRD pattern for a known crystal structure, as there are implicitly no effects due to preferred orientation in the latter case.
3. *Peak positions.* Shifts in the positions of the peaks in an experimental powder XRD pattern may arise due to a number of instrumental factors. Furthermore, comparison of powder XRD patterns recorded at different temperatures may show differences in appearance (particularly in regions with significant peak overlap) as a result of anisotropic thermal expansion/contraction. This issue is particularly relevant when an experimental powder XRD pattern recorded at ambient temperature is compared with simulated powder XRD patterns for known crystal structures determined from single-crystal XRD data at low temperature.
4. *Phase purity of the sample*. Crystalline impurity phases present in a powder sample (e.g. residual amounts of starting materials from a synthetic procedure) contribute additional peaks to the experimental powder XRD pattern. As a result, the pattern may look substantially different from that of a pure sample of the main phase. Clearly, careful inspection should be carried out to assess the presence of impurity phases, particularly with regard to residual amounts of unreacted starting materials.

While the factors listed above can significantly undermine the ability to assess objectively the similarity between two powder XRD patterns on the basis of visual inspection, all of these factors can be taken directly into consideration via appropriate quantitative analysis of the powder XRD data. Thus, to verify whether a synthesized material matches a known material, the recommended protocol is to

carry out a Rietveld refinement calculation using the experimental powder XRD data recorded for the synthesized material and using the crystal structure of the known material as the initial structural model in the refinement. As discussed in Sect. 2.7, Rietveld refinement gives rigorous consideration to fitting the peak profiles, the peak positions, the peak intensities (including refinement of parameters describing the effects of preferred orientation), and the presence of any known impurity phases (by including such materials as a "second phase" in the refinement). This protocol allows the question of whether a synthesized material either matches or does not match the structure of a known material to be answered with confidence, and represents a substantially more rigorous approach than visual comparison of powder XRD patterns.

6 Examples of Structure Determination from Powder XRD Data

In this section we present illustrative applications of structure determination of molecular materials directly from powder XRD data, illustrating the current scope of methodologies in this field and highlighting some of the specific issues (and challenges) discussed above.

For many molecular materials, crystallization from solution does not yield single crystals of suitable size and quality for single-crystal XRD, and instead produces only microcrystalline powders. In such cases, structure determination from powder XRD data provides a viable route for establishing structural understanding of the resultant materials.

Certain solid phases, on the other hand, cannot be obtained (even as microcrystalline powders) by crystallization experiments, but instead can be generated only by other types of preparation procedure. Some types of preparation processes commonly (or in some cases inherently) yield microcrystalline products, including (1) preparation of materials directly from solid-state chemical reactions (see Sect. 6.6), (2) preparation of materials by solid-state desolvation processes (see Sect. 6.4), (3) preparation of materials by solid-state grinding (mechanochemical) processes (see Sect. 6.2), and (4) preparation of materials directly by rapid precipitation from solution (as opposed to crystallization) (see Sect. 6.7). Again, structure determination from powder XRD data may represent the only opportunity for determining the structural properties of new solid phases obtained by such processes.

6.1 Structure Determination of Oligopeptides

A number of oligopeptide structures have been determined from powder XRD data using the direct-space strategy for structure solution. The first example concerns Phe–Gly–Gly–Phe [100], for which the structure solution calculation (employing

the genetic algorithm technique) involved 11 variable torsion angles, with the peptide groups constrained to be planar units and the O–C–N–H torsion angle fixed at 180°. The structure (space group $P4_1$) comprises ribbons that run along the *c*-axis, with adjacent molecules in these ribbons interacting through three N–H···O hydrogen bonds in a manner directly analogous to an antiparallel β-sheet. Intermolecular N–H···O hydrogen bonds involving the end-groups of the oligopeptide chains give rise to two intertwined helical chains running along the 4_1 screw axis.

Structure determination of the peptides Piv–^{L}Pro–Gly–NHMe [101] and Piv–^{L}Pro–γ-Abu–NHMe [102] has also been carried out using the direct-space genetic algorithm technique for structure solution, with particular interest in the potential for these molecules to form β-turn conformations (structural features that allow polypeptide chain reversals in proteins). In the crystal structure of Piv–^{L}Pro–Gly–NHMe, a Type-II β-turn conformation is found, involving an intramolecular 4 → 1 hydrogen bond between the C=O group of the Piv residue and the methylamide N–H group. In the crystal structure of Piv–^{L}Pro–γ-Abu–NHMe (Fig. 8), a folded conformation is also observed (Fig. 8b), with a short C–H···O interaction [H···O, 2.51 Å; C···O, 3.59 Å; C–H···O, 172°; hydrogen atom position normalized according to standard geometries from neutron diffraction] between one of the methylene hydrogen atoms of γ-Abu and the C=O group of the Piv residue. This C–H···O interaction defines an intramolecular cyclic ten-atom motif, similar to that in the classical β-turn (which involves an intramolecular N–H···O=C hydrogen bond), as observed for Piv–^{L}Pro–Gly–NHMe.

Another example from the field of peptide research is the structure determination of the 5-residue peptide acetyl-YEQGL-amide [103]. The YEQGL motif has a known biological role as a trafficking motif in the C-terminus of mammalian P2X4 receptors. Comparison of the crystal structure of acetyl-YEQGL-amide (Fig. 9) determined directly from powder XRD data and that of a complex formed with the μ2 subunit of the clathrin adaptor protein complex AP2 reported previously from single-crystal XRD data [104] reveals differences in conformational properties, although, nevertheless, with certain similarities in aspects of the hydrogen-bonding arrangement and the hydrophobic environment of the leucine sidechain.

With regard to the wider development of powder XRD in structural biology, an ultimate future goal is clearly to achieve ab initio structure solution of small proteins, thus circumventing the need to grow single crystals of sufficient size for conventional protein crystallography. In this regard, considerable progress has been made in recent years in several aspects of the study of proteins by powder XRD [105], including the optimization of conditions for recording high-quality powder XRD data for such materials using synchrotron radiation sources. In favourable cases, the quality of data recorded has been shown to be adequate to allow successful indexing and structure refinement (the latter starting from a known structural model, including the application of "molecular replacement" strategies to define the starting model for structure refinement) [106–111]. Although complete ab initio structure solution of a protein structure from powder XRD data has not yet

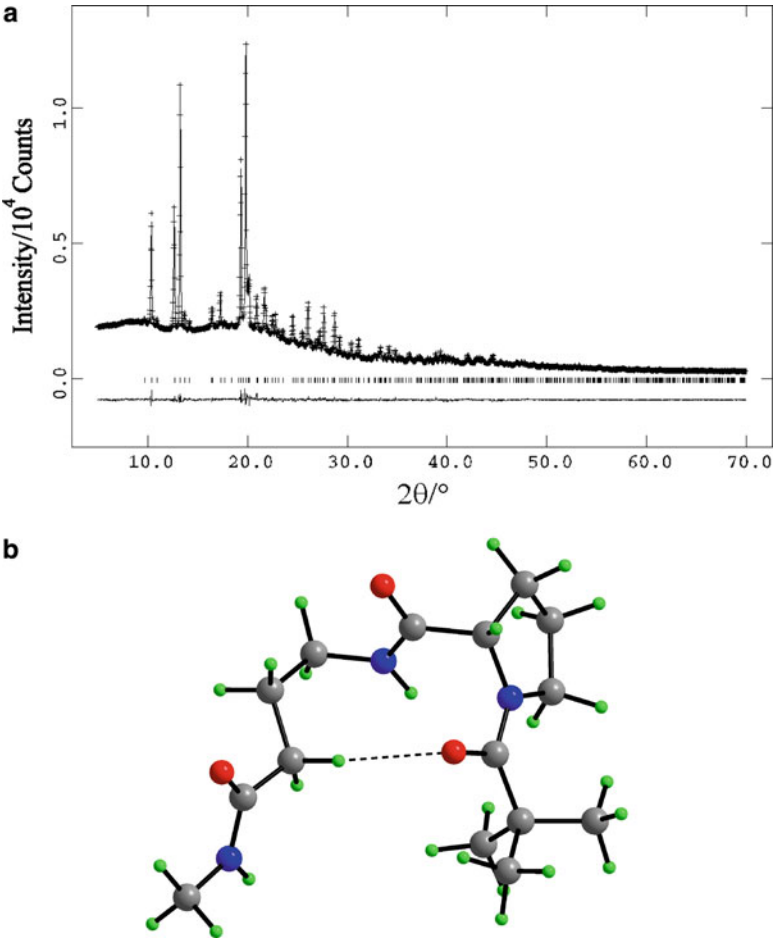

Fig. 8 (**a**) Final Rietveld refinement for Piv–^{L}Pro–γ-Abu–NHMe. (**b**) Conformation of Piv–^{L}Pro–γ-Abu–NHMe in the final refined crystal structure, showing the formation of an intramolecular C–H···O=C hydrogen bond

been reported, continued progress in the development of methodology in this field promises to pave the way for achieving this goal in the future.

6.2 Structure Determination of New Materials Produced by Solid-State Grinding

In addition to the preparation of molecular cocrystals by conventional solution phase crystallization, many materials (e.g. organic molecular cocrystals) can be prepared only by grinding together two (or more) solid phases to generate a single

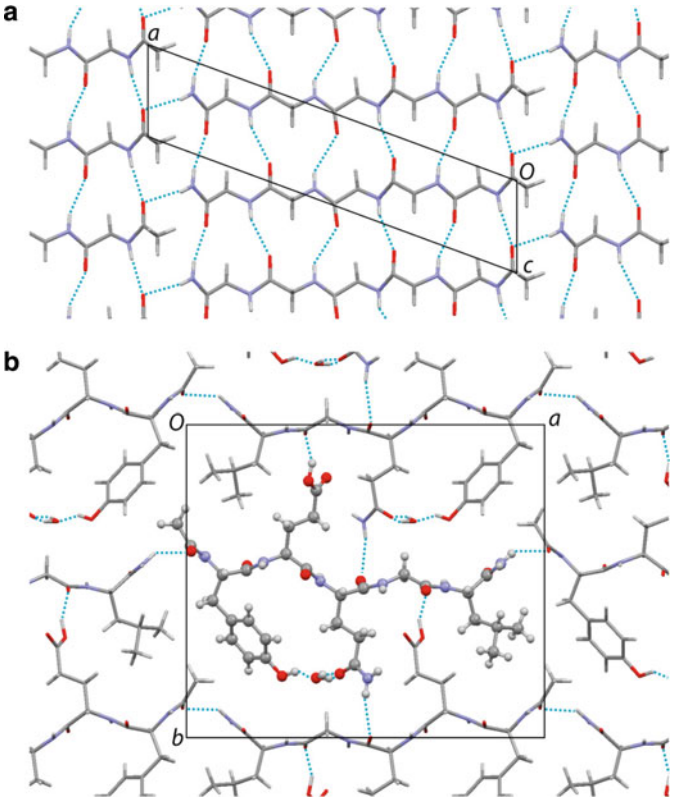

Fig. 9 Crystal structure of acetyl-YEQGL-amide viewed (**a**) along the *b*-axis, showing only the backbone of the peptide, and (**b**) along the *c*-axis. Hydrogen bonds are indicated by *blue dotted lines*

product phase. However, materials prepared by solid-state grinding ("mechano-chemical") procedures are virtually always microcrystalline powders and are thus not suitable for structural characterization by single-crystal XRD. The first report [112] of the use of powder XRD to determine the structure of a molecular cocrystal prepared by solid-state grinding concerned the three-component material prepared from racemic *bis*-β-naphthol (**BN**), benzoquinone (**BQ**) and anthracene (**AN**). Grinding together the pure crystalline phases of **BN**, **BQ** and **AN** produces a polycrystalline material with reddish purple colour (whereas crystallization of the same components from solution gives a different cocrystal with bluish black colour). The contents of the asymmetric unit (confirmed by high-resolution solid-state ^{13}C NMR) comprise one **BN** molecule, one **BQ** molecule and one half **AN** molecule (which resides on a twofold rotation axis). The direct-space structure solution calculation, employing the direct-space genetic algorithm technique, involved a total of 17 structural variables. The crystal structure (Fig. 10) is rationalized in terms of three different interaction motifs: edge-to-face interactions

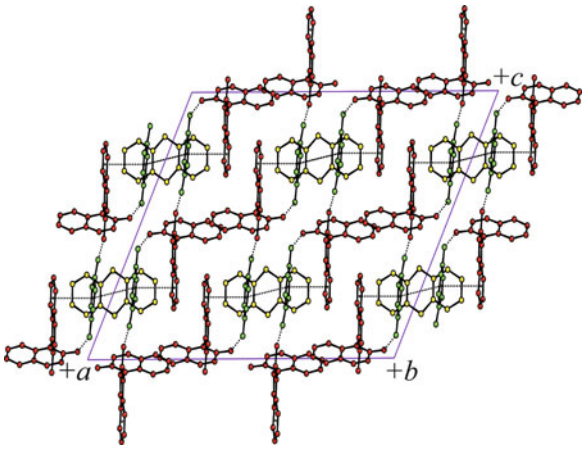

Fig. 10 Crystal structure of the **BN/BQ/AN** cocrystal material (**BN**, *red*; **BQ**, *green*; **AN**, *yellow*) prepared by solid-state grinding. *Dotted lines* indicate π-stacking interactions and hydrogen bonded chains

between **BQ** (edge) and **AN** (face) molecules, face-to-face interactions between **BQ** and **BN** molecules, and chains of O–H···O hydrogen bonds involving **BN** and **BQ** molecules. Hitherto, structural characterization of cocrystals prepared by solid-state grinding has been limited by the fact that the preparation procedure intrinsically yields microcrystalline powders. Structure determination from powder XRD data clearly has considerable potential in the structural characterization of new cocrystal phases prepared by such procedures.

Another example [99] of complete structure determination from powder XRD data of a material prepared by mechanochemical synthesis concerns a porous interpenetrated mixed-ligand metal-organic-framework material with composition $Zn_2(fma)_2(bipy)$. This material was prepared by a mechanochemical synthesis involving the reagents $Zn(OAc)_2.2H_2O$, fumaric acid (H_2fma) and 4,4′-bipyridine (bipy). The crystal structure of this material (Fig. 11a, b) has some similarity to that of a DMF solvate material $Zn_2(fma)_2(bipy)(DMF)_{0.5}$ [113] prepared by a solvothermal route, with the crystal structure (Fig. 11c, d) determined from single-crystal XRD data. Nevertheless, there are important structural differences between these materials, primarily concerning the fact that the bipy ligands in the DMF solvate structure are constrained to be planar (due to the mirror plane in the C2/m space group), whereas there is no such constraint in the structure of the mechanochemically prepared material (for which the space group is $P2_1/a$), and the dihedral angle between the two rings of the bipy ligand is 53.2°. Interestingly, desolvation of the DMF solvate material yields a material identical to that prepared by the mechanochemical synthesis.

There have been a number of other reports of the crystal structures of materials prepared under mechanochemical conditions being determined directly from powder XRD data. Examples include the structure determination of a metal-organic

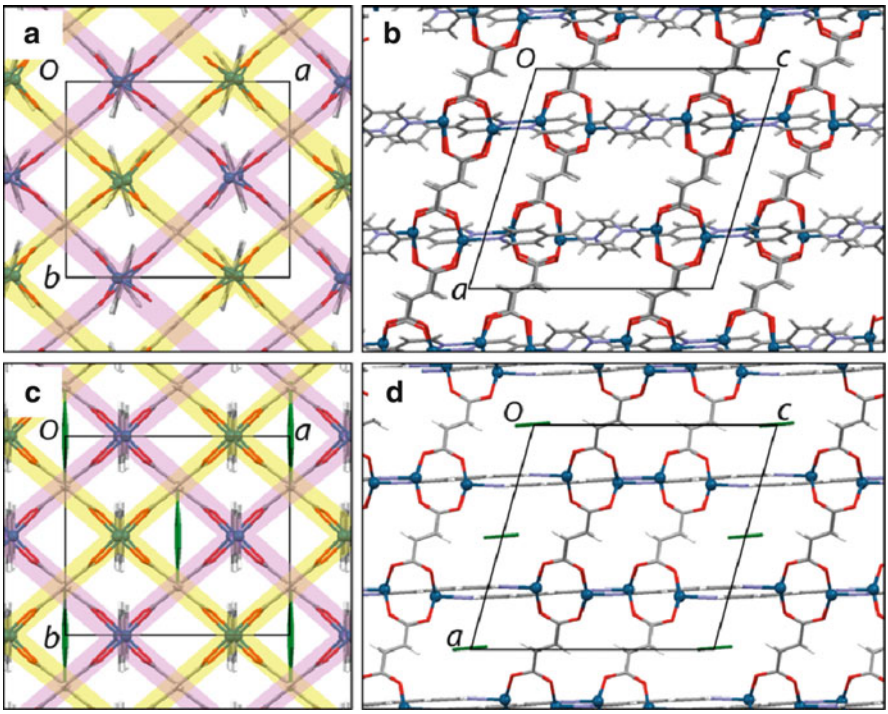

Fig. 11 Crystal structure of a metal-organic framework material $Zn_2(fma)_2(bipy)$ prepared by mechanochemical synthesis, with the structure determined directly from powder XRD data. The structure is viewed (**a**) along the *c*-axis and (**b**) along the *b*-axis. The two (identical) interpenetrated frameworks are indicated by *yellow* and *purple shading*. For comparison, (**c**) and (**d**) show the corresponding views of the structure of a DMF solvate material $Zn_2(fma)_2(bipy)(DMF)_{0.5}$ prepared by a solvothermal route. Although there is some similarity between these structures, there are nevertheless important structural differences between them

framework material with composition Co(dibenzoylmethanate)$_2$(nicotinamide)$_2$. This material was obtained by thermal desolvation of the corresponding acetone solvate, which was prepared under conditions of liquid-assisted grinding [114]. The structure determined from the powder XRD data comprises "wheel-and-axle" units of composition Co(dibenzoylmethanate)$_2$(nicotinamide)$_2$, which are assembled through hydrogen-bonded amide–amide interactions involving the nicotinamide molecules of neighbouring units, giving rise to antiparallel chains of amide functionalities in a ladder-type motif. The structure contains tunnels with approximately hexagonal cross-section running parallel to the direction of the hydrogen-bonded amide ladders.

Examples of other organic materials prepared by mechanochemical procedures, for which structure determination has been carried out directly from powder XRD data, include a hydrate cocrystal of 5-methyl-2-pyridone and trimesic acid, which was prepared by grinding a methanol solvate cocrystal of the same components

under ambient atmospheric conditions [115], and 1:1 cocrystals of theobromine with trifluoroacetic acid and theobromine with malonic acid, each of which was prepared by liquid assisted grinding [116].

6.3 Structure Determination of an Early-Generation Dendrimeric Material

Dendrimers are large, highly-branched molecules composed of a core moiety and radiating functionality. The highly branched architecture can lead to spatially well-defined voids within the dendrimer, and this structural feature is crucial for many of the wide-ranging applications of these materials. Many dendrimeric materials cannot be grown as suitable single crystals for single-crystal XRD, and structure determination from powder XRD data may represent the only viable opportunity for structural characterization. The first structure determination of a dendrimeric material directly from powder XRD data [87] concerned the early-generation dendrimer tetrakis[(3,5-dimethoxybenzyloxy)methyl]methane (**TDMM**). The space group was assigned as Fdd2, and density considerations together with results from high-resolution solid-state ^{13}C NMR suggested that the asymmetric unit comprises half the molecule (with the central carbon atom located on a twofold rotation axis). In the half-molecule, there are 12 variable torsion angles (Fig. 12a). Structure solution was carried out using the direct-space genetic algorithm technique followed by Rietveld refinement. In the crystal structure (Fig. 12b), the half-molecule that represents the asymmetric unit has two independent branches radiating from the core. Interestingly, the conformational properties of these two branches differ significantly, in terms of both the conformation of the C–CH_2–O–CH_2–Ph chain and the conformation of the two methoxy substituents on the benzyloxy ring.

6.4 Structure Determination of Materials Prepared by Solid-State Dehydration/Desolvation Processes

Although the chemical properties of benzene-1,2,3-tricarboxylic acid (**BTCA**) were first studied over 100 years ago, the crystal structure of **BTCA** was not reported until a recent powder XRD study [117]. In contrast, the crystal structures of several solvate phases of **BTCA** were determined previously, including a dihydrate structure and solvate structures containing different alcohols and other solvent molecules. The preparation of a "pure" (nonsolvate) crystalline phase of **BTCA** by crystal growth from solution is difficult due to the competitive formation of solvate phases. In such cases of materials that cannot be prepared as a "pure" (nonsolvate) phase by conventional crystal growth processes, a possible route to obtain the "pure" phase is to carry out desolvation of a solvate phase at elevated

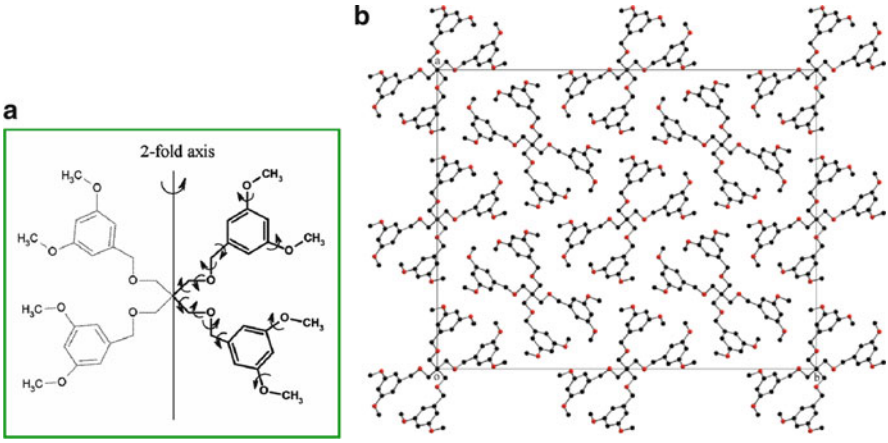

Fig. 12 (**a**) The molecular fragment (*thick lines*), comprising half the **TDMM** molecule, used in the direct-space genetic algorithm structure solution calculation from powder XRD data. The *arrows* indicate the variable torsion angles. The central carbon atom is located on a twofold rotation axis (as indicated), and the other half of the molecule (*faint lines*) is generated by this symmetry operation. (**b**) The final refined crystal structure of **TDMM**, with hydrogen atoms omitted for clarity

temperature and/or reduced pressure. However, such processes are often associated with loss of crystal integrity, and a single crystal of the parent (solvate) structure typically yields a polycrystalline product phase following desolvation (Fig. 13). In such cases, powder XRD is essential for structure determination of the product phase. In this regard, the direct-space genetic algorithm technique was used [117] to solve the structure of the "pure" phase of **BTCA** from powder XRD data.

A microcrystalline powder sample of the "pure" phase of **BTCA** was obtained by dehydration of the dihydrate phase of **BTCA** at elevated temperature. There are three independent **BTCA** molecules in the asymmetric unit, and trial structures in the genetic algorithm structure solution calculation were defined by a total of 27 structural variables (with nine variables required to define the position, orientation and conformation of each independent molecule). In the final refined structure of **BTCA** (Fig. 14), all carboxylic acid groups are engaged in intermolecular hydrogen bonding to other carboxylic acid groups via the double O–H···O hydrogen-bonded motif found in carboxylic acid "dimers". The three independent molecules have similar conformations (the "inner" carboxylic acid group is nearly perpendicular to the ring, whereas the two "outer" carboxylic acid groups lie closer to the plane of the ring). The structure of the "pure" phase of **BTCA** differs substantially from that of **BTCA** dihydrate, implying that the solid-state dehydration process is associated with substantial structural reorganization.

Another material that has a strong propensity to form solvate structures in crystallization experiments is trithiocyanuric acid (**TTCA**). Consequently, the "pure" crystalline phase of **TTCA** is difficult to obtain by crystallization from solution, but can be obtained instead by desolvation of these solvate phases. In this

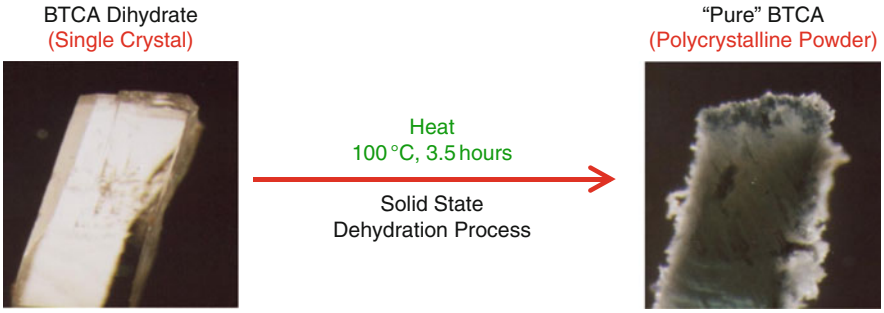

Fig. 13 Optical micrographs showing that a single crystal of **BTCA** dihydrate leads to a polycrystalline product ("pure" phase of **BTCA**) upon dehydration

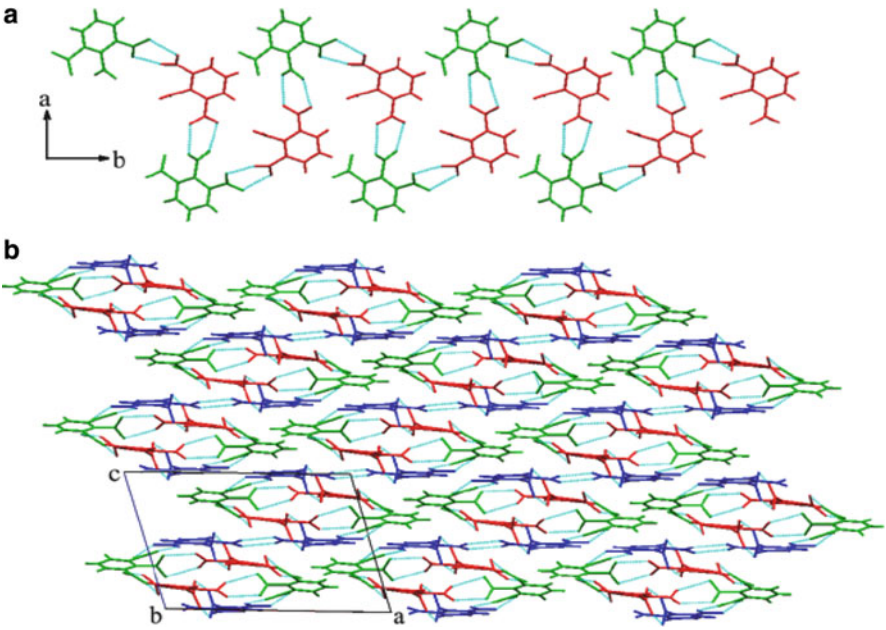

Fig. 14 Crystal structure of **BTCA**, with the three crystallographically independent molecules displayed in different colours (A, *green*; B, *blue*; C, *red*): (**a**) a hydrogen-bonded chain of A and C molecules viewed approximately along the *c*-axis, and (**b**) the complete crystal structure viewed along the *b*-axis (the AC chains run into the page, with adjacent AC chains cross-linked by hydrogen bonding to B molecules)

case, the structure of "pure" **TTCA** has again been determined [118] directly from powder XRD data, using the direct-space genetic algorithm technique for structure solution followed by Rietveld refinement. The structure of "pure" **TTCA**, shown in Fig. 15, presents interesting contrasts in comparison with the structure of the "pure" phase of the oxygen analogue cyanuric acid.

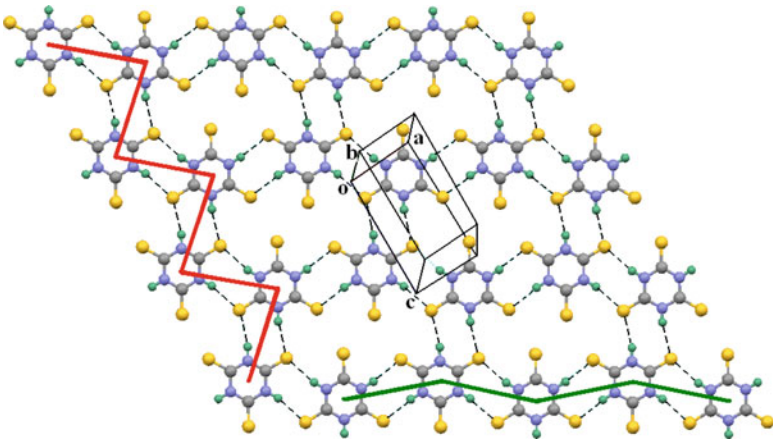

Fig. 15 Crystal structure of **TTCA** showing a single sheet viewed perpendicular to the plane of the sheet. *Dashed lines* indicate N–H···S hydrogen bonds, and different types of hydrogen bonded array are indicated by the *green* and *red lines*

Another example of structure determination of a material prepared by solid-state desolvation concerns dehydration of the hydrate crystalline phase of chloroquine bis-(dihydrogen phosphate) [denoted $CQ(DHP)_2$] to form an anhydrous phase of $CQ(DHP)_2$. In common with many processes of this type, the anhydrous product phase is obtained as a microcrystalline powder. The structure of the anhydrous phase has been determined [119] directly from powder XRD data using the direct-space genetic algorithm technique for structure solution followed by Rietveld refinement. The structure solution calculation involved three independent molecular fragments, representing a total of 26 structural variables (the CQ cation was defined by 14 variables $\{x, y, z, \theta, \varphi, \psi, \tau_1, \tau_2, \ldots, \tau_8\}$, including 8 variable torsion angles, and each DHP anion was defined by 6 variables $\{x, y, z, \theta, \varphi, \psi\}$). The structure of the anhydrous phase exhibits several interesting contrasts with the structure of the parent hydrate phase, most notably concerning the topology of the hydrogen-bonded chains of DHP anions that exist in both structures. Thus, while the hydrogen-bonded chains of DHP anions in the hydrate phase are linear, the corresponding chains in the anhydrous phase have a zigzag topology, resulting from changes in the mode of hydrogen bonding employed by the DHP anions within the chain. Given the substantial structural reorganization associated with the dehydration process, it is not at all surprising that this process is associated with the formation of a polycrystalline product phase.

6.5 *Structure Determination of a Multicomponent Cocrystal*

The structural properties of materials containing both aryl and perfluoroaryl groups have attracted attention in recent years because of the observed propensity for such

systems to form stacking arrangements of alternating aryl and perfluoroaryl rings, as observed in the prototypical example of the 1:1 cocrystal of benzene and hexafluorobenzene [120]. The structural properties of the 1:1 cocrystal containing benzoic acid ($C_6H_5CO_2H$; **BA**) and pentafluorobenzoic acid ($C_6F_5CO_2H$; **PFBA**) have been investigated, with structure determination carried out [86] directly from powder XRD data using the direct-space genetic algorithm technique for structure solution followed by Rietveld refinement. As highlighted in Sect. 3.1, high-resolution solid-state ^{13}C NMR provided direct evidence (prior to structure solution from the powder XRD data) that there are two crystallographically inequivalent molecules of **BA** and two crystallographically inequivalent molecules of **PFBA** in the asymmetric unit of this structure. In space group Cc, the values of x and z for one molecule may be fixed arbitrarily, and thus a total of 26 structural variables were required in the structure solution calculation (with 1 variable torsion angle for each of the 4 independent molecules in the asymmetric unit). As anticipated, the structure of the cocrystal (Fig. 16) comprises stacks of alternating **BA** and **PFBA** molecules, and there are two crystallographically independent stacks of this type in the structure. Molecules in the two types of stack engage in hydrogen bonding, involving the carboxylic acid group of a **BA** molecule in one stack and the carboxylic acid group of a **PFBA** molecule in the other stack. The two independent **BA** molecules and the two independent **PFBA** molecules differ appreciably in the torsion angle between the carboxylic acid and aryl units.

6.6 Structure Determination of the Product Phase from a Solid-State Photopolymerization Reaction

Many crystalline solids can undergo chemical transformations induced, for example, by incident radiation or by heat. An important aspect of such solid-state reactions is to understand the structural properties of the product phase obtained directly from the reaction, and in particular to rationalize the relationships between the structural properties of the product and reactant phases. In many cases, however, the product phase is amorphous, but for cases in which the product phase is crystalline, it is usually obtained as a microcrystalline powder that does not contain single crystals of suitable size and quality to allow structure determination by single-crystal XRD. In such cases, there is a clear opportunity to apply structure determination from powder XRD data in order to characterize the structural properties of product phases.

An example is the photopolymerization of 2,5-distyrylpyrazine (**DSP**) (Fig. 17), with polymerization occurring via intermolecular [2+2] photocyclization reactions at each end of the monomer molecule. Although this reaction is regarded as a classic solid-state reaction, having been studied extensively around 40 years ago [121, 122], structure determination of the polymeric product phase was only carried

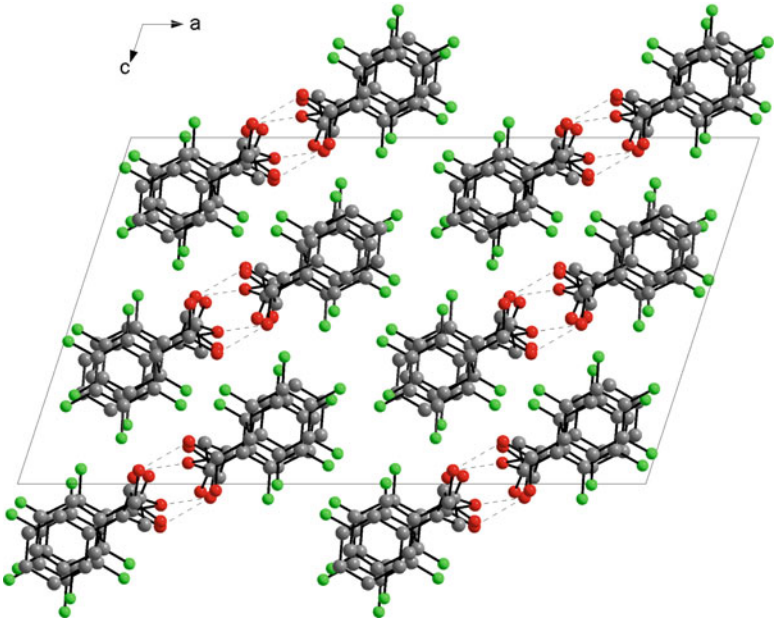

Fig. 16 Crystal structure of the **BA/PFBA** cocrystal viewed along the stacking axis. Interstack hydrogen bonding involving the carboxylic acid groups is shown as *dashed lines*. Hydrogen atoms are not shown, and the fluorine atoms of the **PFBA** molecules are shown in *green*

out very recently [123], with the structure determined directly from powder XRD data exploiting the direct-space strategy for structure solution. Under appropriate conditions, this reaction proceeds to 100% conversion and thus the powder XRD pattern does not contain residual amounts of the unreacted monomer phase (although, as the crystal structure of the monomer was already known, structure determination of the polymer product would still have been feasible if the powder had comprised a mixture of monomer and polymer phases).

In the crystal structure of the polymer phase (Fig. 17a), the polymer chains are aligned along the *c*-axis and the distance (3.71 Å) between the centres of adjacent cyclobutane and pyrazine rings corresponds to half the *c*-axis repeat of the unit cell. For comparison between the monomer and polymer structures, an overlay plot of these structures is shown in Fig. 17b. It is clear that the solid-state reaction is associated with only very small atomic displacements at the site of the [2+2] photocyclization reaction (the displacement of the carbon atoms of the C=C double bonds of monomer molecules on forming the cyclobutane ring of the polymer is only ca. 0.8 Å for one pair of carbon atoms and ca. 1.6 Å for the other pair). Such small displacements are completely in accord with the assignment of this solid-state reaction as a topochemical transformation [124–127] (in which the crystal structure of the reactant monomer phase imposes geometric control on the pathway of the

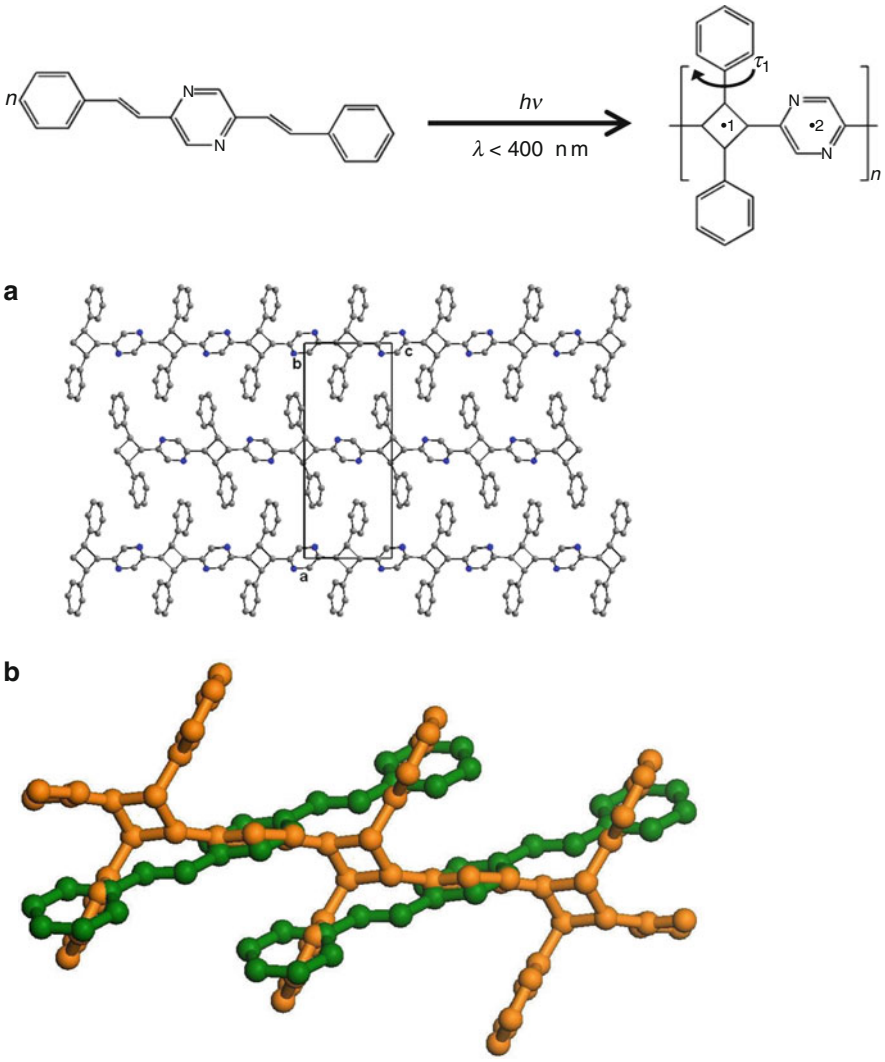

Fig. 17 The solid-state photopolymerization reaction of **DSP** (*shown at top*). (**a**) Crystal structure of the polymeric product phase obtained directly from the solid-state photopolymerization reaction of **DSP**, viewed along the *b*-axis (for clarity, only half the unit cell is shown along the direction of view), and (**b**) overlay of the monomer (*green*) and polymer (*orange*) in their crystal structures

polymerization reaction, thus controlling the structure and stereochemistry of the polymer product obtained in the reaction). As many other solid-state reactions (not only polymerization reactions) intrinsically generate polycrystalline product phases, there is considerable potential to exploit powder XRD techniques for structural rationalization of other reactions of this type.

6.7 Structure Determination of a Material Produced by Precipitation from Solution

A process that has been studied widely in relation to phenomena such as chiral symmetry breaking, spontaneous resolution and chiral amplification is the reaction (Fig. 18) of $[Co(H_2O)_2\{(OH)_2Co(en)_2\}_2](SO_4)_2$ (denoted **1**) with NH_4Br to give the chiral complex *cis*-$[CoBr(NH_3)(en)_2]Br_2$ (denoted **2**). This reaction is historically important, as **2** was one of the first octahedral metal complexes to be resolved into Δ and Λ stereoisomers, some years after Werner predicted that octahedral ions $M(en)_2XY$ should exist as enantiomeric pairs.

Two crystal structures containing **2**, determined by single-crystal XRD, were reported previously for single crystals prepared by recrystallization of **2**. In one case [128], the single crystal was grown from a homochiral sample [$(+)_{589}$-enantiomer], and the crystal structure has the chiral space group $P2_12_12_1$ with one molecule in the asymmetric unit. In the other case [129], the single crystal was a dihydrate of **2**, prepared by crystallization using a racemic mixture of **2**, and the crystal structure is racemic with nonchiral space group C2/c.

Clearly, these structures do not necessarily correspond to the solid product formed directly in the reaction – as rapid precipitation of **2** occurs from the solution in which the reaction is carried out, the material obtained directly from the reaction is a microcrystalline powder. Indeed, powder XRD indicates [130] that the product obtained directly from the reaction is a new solid phase of **2**, which differs from the structures of **2** reported previously. Structure determination of this new phase of **2** was carried out [130] directly from powder XRD data using the direct-space genetic algorithm technique for structure solution followed by Rietveld refinement. In the crystal structure (Fig. 18b), the *cis*-$[CoBr(NH_3)(en)_2]^{2+}$ complexes are arranged in two different types of chain, propagated along the *a*-axis and *b*-axis respectively, with neighbouring complexes in each type of chain linked by N–H···Br^-···H–N interactions. Along the *a*-axis, neighbouring repeat units are related by translation and the chain is relatively straight, whereas along the *b*-axis, neighbouring repeat units are related by the 2_1 symmetry operation and the chain is helical. With regard to chirality, the most important feature of this result is the fact that the structure is racemic (nonchiral space group $P2_1/n$, with one formula unit in the asymmetric unit). Studies of this reaction under a wide range of experimental conditions led consistently to this new racemic phase of **2**, and conglomerate phases of **2** were never obtained. The implications of this result in relation to previous reports of spontaneous induction of chirality in this system are discussed in detail elsewhere [130].

6.8 Exploiting Anisotropic Thermal Expansion in Structure Solution

As discussed in Sect. 2.6, structure solution from powder XRD data by the traditional approach relies upon the availability of accurate values of the extracted

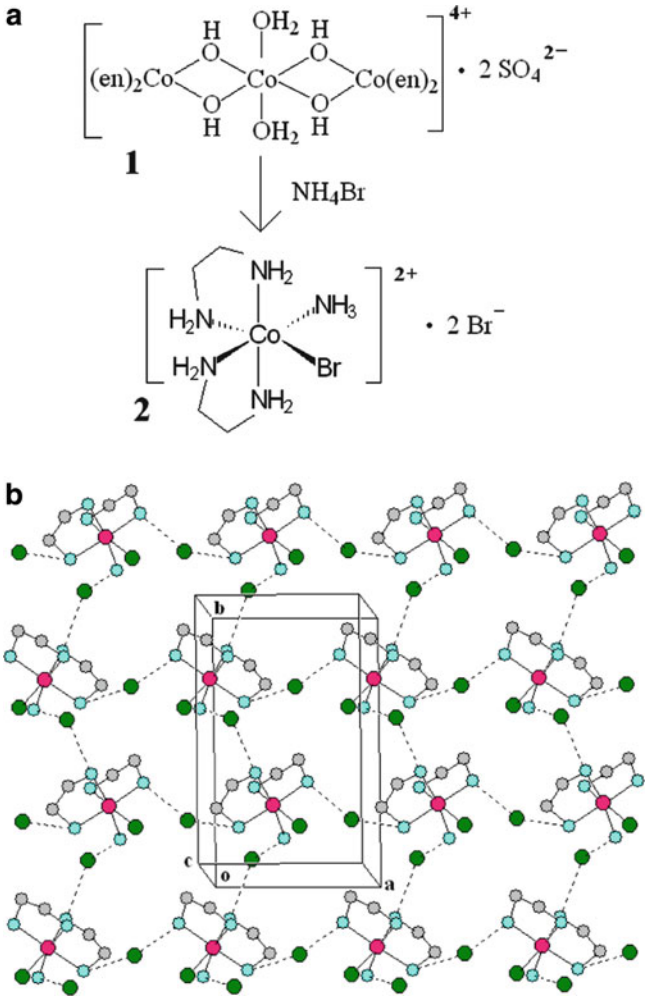

Fig. 18 (**a**) The solution-state reaction to produce *cis*-[CoBr(NH_3)$(en)_2$]Br_2 (denoted **2**). (**b**) Crystal structure of the new racemic phase of **2** viewed nearly along the *c*-axis, showing the straight and helical chains that run along the *a*-axis and *b*-axis respectively (Co, *red*; Br, *green*; N, *blue*; C, *grey*). Hydrogen atoms are omitted for clarity

intensities of individual reflections in the powder XRD pattern. The difficulty in obtaining reliable intensities in this way was one of the primary factors that motivated the development of direct-space strategies, which, as discussed above, do not require the use of extracted peak intensities. However, it is important to emphasize that structure solution by the traditional approach can still be successful when the powder XRD pattern suffers from substantial peak overlap, as illustrated by the case of 9-ethylbicyclo[3.3.1]nona-9-ol [131]. Powder XRD patterns were recorded for this material at several different temperatures. At each temperature, the

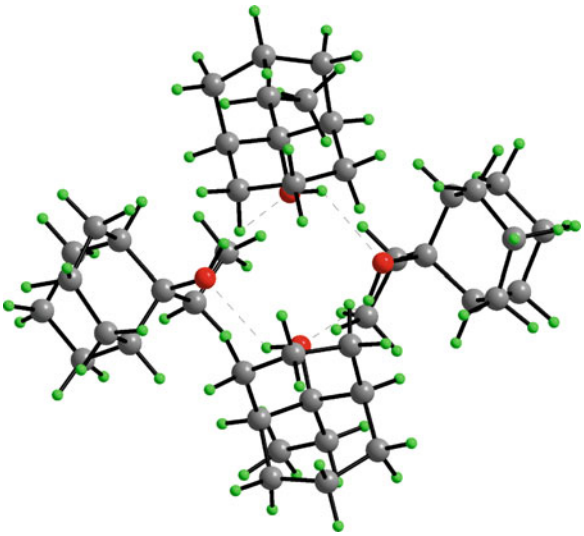

Fig. 19 The tetrameric association of 9-ethylbicyclo[3.3.1]nona-9-ol molecules in the crystal structure determined from powder XRD data

peaks in the powder XRD pattern are substantially overlapped, and the peak intensities extracted from the data recorded at any one of these temperatures did not allow the structure to be solved. To overcome this problem, anisotropic thermal expansion [132, 133] was exploited as a means of improving the intensity extraction process. As a consequence of anisotropic thermal expansion, different peaks in the powder XRD pattern shift to a different extent as temperature is varied, and hence the nature of the peak overlap changes with temperature. By carrying out a combined analysis of the data recorded at all temperatures studied, a more reliable extraction of the integrated peak intensities can be obtained. Using the accurate set of integrated peak intensities obtained from this multipattern peak extraction process, the crystal structure of 9-ethylbicyclo[3.3.1]nona-9-ol was solved successfully using direct methods (and analysis of difference Fourier maps). As shown in Fig. 19, this structure has four independent molecules in the asymmetric unit, assembled into a tetrameric unit held together by O–H···O hydrogen bonds.

7 Concluding Remarks

This chapter has aimed to demonstrate the feasibility of carrying out complete crystal structure determination from powder XRD data, particularly in the case of molecular materials, and has illustrated the scope of the methods currently available for this purpose, as well as discussing some of their current limitations. Although significant progress has been made in recent years in the development and

application of new techniques in this field, considerable scope still remains for the continued development of new strategies for further improving the opportunities to carry out successful structure determination of more complex and more challenging structures. In summary, recent developments in methodology for structure solution and other stages of the structure determination process, together with continuing developments in instrumentation for recording powder XRD data of higher quality, promise an optimistic outlook for the field of crystal structure determination from powder XRD data, and we confidently predict that the future will yield considerable new information on a wide range of important materials that have hitherto defied structural characterization.

Acknowledgments I am grateful to many members of my research group and research collaborators who have contributed to our research in this field over many years. I would also like to thank Gin Keat Lim, Gregory Edwards-Gau and Andrew Williams for assistance in checking this manuscript.

References

1. Dunitz JD (1995) X-ray analysis and the structures of organic molecules. Verlag Helvetica Chimica Acta, Basel
2. Harris KDM, Tremayne M, Lightfoot P, Bruce PG (1994) J Am Chem Soc 116:3543
3. Harris KDM, Tremayne M (1996) Chem Mater 8:2554
4. Langford JI, Louër D (1996) Rep Progr Phys 59:131
5. Poojary DM, Clearfield A (1997) Acc Chem Res 30:414
6. Meden A (1998) Croat Chem Acta 71:615
7. Harris KDM, Tremayne M, Kariuki BM (2001) Angew Chem Int Ed 40:1626
8. Chernyshev VV (2001) Russ Chem Bull 50:2273
9. David WIF, Shankland K, McCusker LB, Baerlocher C (eds) (2002) Structure determination from powder diffraction data. Oxford University Press (OUP/IUCr), Oxford
10. Huq A, Stephens PW (2003) J Pharm Sci 92:244
11. Harris KDM (2003) Cryst Growth Des 3:887
12. Harris KDM, Cheung EY (2004) Chem Soc Rev 33:526
13. Tremayne M (2004) Philos Trans R Soc 362:2691
14. Altomare A, Caliandro R, Camalli M, Cuocci C, Giacovazzo C, Moliterni AGG, Rizzi R, Spagna R, Gonzalez-Platas J (2004) Z Kristallogr 219:833
15. Favre-Nicolin V, Černý R (2004) Z Kristallogr 219:847
16. Shankland K, Markvardsen AJ, David WIF (2004) Z Kristallogr 219:857
17. Černý R (2006) Croat Chem Acta 79:319
18. Tsue H, Horiguchi M, Tamura R, Fujii K, Uekusa H (2007) J Synth Org Chem Jpn 65:1203
19. David WIF, Shankland K (2008) Acta Crystallogr Sect A 64:52
20. Harris KDM (2009) Mater Manufac Proc 24:293
21. Glusker JP, Trueblood KN (1985) Crystal structure analysis – a primer. Oxford University Press, Oxford
22. Young RA (ed) (1993) The Rietveld method. International Union of Crystallography, Oxford
23. David WIF (1999) J Appl Crystallogr 32:654
24. Visser JW (1969) J Appl Crystallogr 2:89
25. Werner P-E, Eriksson L, Westdahl M (1985) J Appl Crystallogr 18:367
26. Boultif A, Louër D (1991) J Appl Crystallogr 24:987

27. Rietveld HM (1969) J Appl Crystallogr 2:65
28. McCusker LB, Von Dreele RB, Cox DE, Louër D, Scardi P (1999) J Appl Crystallogr 32:36
29. Shirley R (2002) The *CRYSFIRE* 2002 system for automatic powder indexing: user's manual (Guildford: The Lattice Press)
30. Pawley GS (1981) J Appl Crystallogr 14:357
31. Le Bail A, Duroy H, Fourquet JL (1988) Mater Res Bull 23:447
32. Oszlányi G, Sütő A (2004) Acta Crystallogr Sect A 60:134
33. Oszlányi G, Sütő A (2005) Acta Crystallogr Sect A 61:147
34. Baerlocher C, McCusker LB, Palatinus L (2007) Z Kristallogr 222:47
35. David WIF, Shankland K, Shankland N (1998) Chem Commun 931
36. Pagola S, Stephens PW, Bohle DS, Kosar AD, Madsen SK (2000) Nature 404:307
37. Ramprasad D, Pez GB, Toby BH, Markley TJ, Pearlstein RM (1995) J Am Chem Soc 117:10694
38. Kariuki BM, Zin DMS, Tremayne M, Harris KDM (1996) Chem Mater 8:565
39. Tremayne M, Kariuki BM, Harris KDM (1997) Angew Chem Int Ed Engl 36:770
40. Freeman CM, Gorman AM, Newsam JM (1997) In: Catlow CRA (ed) Computer modelling in inorganic crystallography. Academic Press, San Diego
41. Elizabé L, Kariuki BM, Harris KDM, Tremayne M, Epple M, Thomas JM (1997) J Phys Chem B 101:8827
42. Andreev YG, Lightfoot P, Bruce PG (1997) J Appl Crystallogr 30:294
43. Engel GE, Wilke S, König O, Harris KDM, Leusen FJJ (1999) J Appl Crystallogr 32:1169
44. Miao P, Robinson AW, Palmer RE, Kariuki BM, Harris KDM (2000) J Phys Chem B 104:1285
45. Tanahashi Y, Nakamura H, Yamazaki S, Kojima Y, Saito H, Ida T, Toraya H (2001) Acta Crystallogr Sect B 57:184
46. Hsu H-P, Hansmann UHE, Lin SC (2001) Phys Rev E 64:056707
47. Andreev YG, Bruce PG (2001) J Phys Condens Matter 13:8245
48. Smith EDL, Hammond RB, Jones MJ, Roberts KJ, Mitchell JBO, Price SL, Harris RK, Apperley DC, Cherryman JC, Docherty R (2001) J Phys Chem B 105:5818
49. Shankland K, McBride L, David WIF, Shankland N, Steele G (2002) J Appl Crystallogr 35:443
50. Brodski V, Peschar R, Schenk H (2003) J Appl Crystallogr 36:239
51. Favre-Nicolin V, Černý R (2004) Mater Sci Forum 443:35
52. Brodski V, Peschar R, Schenk H (2005) J Appl Crystallogr 38:688
53. David WIF, Shankland K, van de Streek J, Pidcock E, Motherwell WDS, Cole JC (2006) J Appl Crystallogr 39:910
54. Altomare A, Caliandro R, Cuocci R, Giacovazzo C, Moliterni AGG, Rizzi R, Platteau C (2008) J Appl Crystallogr 41:56
55. Pagola S, Stephens PW (2010) J Appl Crystallogr 43:370
56. Shankland K, Markvardsen AJ, Rowlatt C, Shankland N, David WIF (2010) J Appl Crystallogr 43:401
57. Deng XD, Dong C (2011) J Appl Crystallogr 44:230
58. Kariuki BM, Serrano-González H, Johnston RL, Harris KDM (1997) Chem Phys Lett 280:189
59. Shankland K, David WIF, Csoka T (1997) Z Kristallogr 212:550
60. Harris KDM, Johnston RL, Kariuki BM (1998) Acta Crystallogr Sect A 54:632
61. Kariuki BM, Calcagno P, Harris KDM, Philp D, Johnston RL (1999) Angew Chem Int Ed 38:831
62. Kariuki BM, Psallidas K, Harris KDM, Johnston RL, Lancaster RW, Staniforth SE, Cooper SM (1999) Chem Commun 1677
63. Turner GW, Tedesco E, Harris KDM, Johnston RL, Kariuki BM (2000) Chem Phys Lett 321:183
64. Habershon S, Harris KDM, Johnston RL (2003) J Comp Chem 24:1766

65. Harris KDM, Johnston RL, Habershon S (2004) Struct Bond 110:55
66. Dova E, Peschar R, Sakata M, Kato K, Stassen AF, Schenk H, Haasnoot JG (2004) Acta Crystallogr Sect B 60:528
67. Dova E, Peschar R, Sakata M, Kato K, Schenk H (2006) Chem Eur J 12:5043
68. Hirano A, Toyota S, Toda F, Fujii K, Uekusa H (2005) Angew Chem Int Ed 45:6013
69. Feng ZJ, Dong C (2007) J Appl Crystallogr 40:583
70. Hanson AJ, Cheung EY, Harris KDM (2007) J Phys Chem B 111:6349
71. Zhou Z, Siegler V, Cheung EY, Habershon S, Harris KDM, Johnston RL (2007) ChemPhysChem 8:650
72. Zhou Z, Harris KDM (2008) Phys Chem Chem Phys 10:7262
73. Fujii K, Ashida Y, Uekusa H, Guo F, Harris KDM (2010) Chem Commun 4264
74. Fujii K, Uekusa H, Itoda N, Hasegawa G, Yonemochi E, Terada K, Pan Z, Harris KDM (2010) J Phys Chem C 114:580
75. Lim GK, Zhou Z, Fujii K, Calcagno P, Tedesco E, Kitchin SJ, Kariuki BM, Philp D, Harris KDM (2010) Cryst Growth Des 10:3814
76. Reck G, Kretschmer R-G, Kutschabsky L, Pritzkow W (1988) Acta Crystallogr A44:417
77. Masciocchi N, Bianchi R, Cairati P, Mezza G, Pilati T, Sironi A (1994) J Appl Crystallogr 27:426
78. Dinnebier RE, Stephens PW, Carter JK, Lommen AN, Heiney PA, McGhie AR, Brard L, Smith AB III (1995) J Appl Crystallogr 28:327
79. Hammond RB, Roberts KJ, Docherty R, Edmondson M (1997) J Phys Chem B 101:6532
80. Chernyshev VV, Schenk H (1998) Z Kristallogr 213:1
81. Seaton CC, Tremayne M (2002) Chem Commun 880
82. Chong SY, Tremayne M (2006) Chem Commun 4078
83. Cernik RJ, Cheetham AK, Prout CK, Watkin DJ, Wilkinson AP, Willis BTM (1991) J Appl Crystallogr 24:222
84. Lightfoot P, Tremayne M, Harris KDM, Bruce PG (1992) J Chem Soc Chem Commun 14:1012
85. Tremayne M, Kariuki BM, Harris KDM (1996) J Mater Chem 6:1601
86. Albesa-Jové D, Kariuki BM, Kitchin SJ, Grice L, Cheung EY, Harris KDM (2004) ChemPhysChem 5:414
87. Pan Z, Xu M, Cheung EY, Harris KDM, Constable EC, Housecroft CE (2006) J Phys Chem B 110:11620
88. MacLean EJ, Tremayne M, Kariuki BM, Harris KDM, Iqbal AFM, Hao Z (2000) J Chem Soc Perkin Trans 2:1513
89. Pan Z, Cheung EY, Harris KDM, Constable EC, Housecroft CE (2005) Cryst Growth Des 5:2084
90. Pan Z, Xu M, Cheung EY, Platts JA, Harris KDM, Constable EC, Housecroft CE (2006) J Solid State Chem 179:3214
91. Meejoo S, Kariuki BM, Kitchin SJ, Cheung EY, Albesa-Jové D, Harris KDM (2003) Helv Chim Acta 86:1467
92. Wöhler F (1828) Pogg Ann 12:253
93. Dunitz JD, Harris KDM, Johnston RL, Kariuki BM, MacLean EJ, Psallidas K, Schweizer WB, Tykwinski RR (1998) J Am Chem Soc 120:13274
94. MacLean EJ, Harris KDM, Kariuki BM, Kitchin SJ, Tykwinski RR, Swainson IP, Dunitz JD (2003) J Am Chem Soc 125:14449
95. Cheung EY, Harris KDM, Foxman BM (2003) Cryst Growth Des 3:705
96. Dinnebier RE, Olbrich F, van Smaalen S, Stephens PW (1997) Acta Crystallogr Sect B 53:153
97. Peterson ML, Morissette SL, McNulty C, Goldsweig A, Shaw P, LeQuesne M, Monagle J, Encina N, Marchionna J, Johnson A, Gonzalez-Zugasti J, Lemmo AV, Ellis SJ, Cima MJ, Almarsson O (2002) J Am Chem Soc 124:10958

98. Florence AJ, Baumgartner B, Weston C, Shankland N, Kennedy AR, Shankland K, David WIF (2003) J Pharm Sci 92:1930
99. Fujii K, Lazuen Garay A, Hill J, Sbircea E, Pan Z, Xu M, Apperley DC, James SL, Harris KDM (2010) Chem Commun 46:7572
100. Tedesco E, Turner GW, Harris KDM, Johnston RL, Kariuki BM (2000) Angew Chem Int Ed 39:4488
101. Tedesco E, Harris KDM, Johnston RL, Turner GW, Raja KMP, Balaram P (2001) Chem Commun 1460
102. Cheung EY, McCabe EE, Harris KDM, Johnston RL, Tedesco E, Raja KMP, Balaram P (2002) Angew Chem Int Ed 41:494
103. Fujii K, Young MT, Harris KDM (2011) J Struct Biol 174:461
104. Royle SJ, Qureshi OS, Bobanovic LK, Evans PR, Owen DJ, Murrell-Lagnado RD (2005) J Cell Sci 118:3073
105. Margiolaki I, Wright JP (2008) Acta Crystallogr Sect A 64:169
106. Von Dreele RB (1999) J Appl Crystallogr 32:1084
107. Von Dreele RB (2001) Acta Crystallogr Sect D 57:1836
108. Basso S, Fitch AN, Fox GC, Margiolaki I, Wright JP (2005) Acta Crystallogr Sect D 61:1612
109. Margiolaki I, Wright JP, Fitch AN, Fox GC, Von Dreele RB (2005) Acta Crystallogr Sect D 61:423
110. Von Dreele RB, Lee PL, Zhang Y (2006) Z Kristallogr 23(Suppl):3
111. Margiolaki I, Wright JP, Wilmanns M, Fitch AN, Pinotsis N (2007) J Am Chem Soc 129:11865
112. Cheung EY, Kitchin SJ, Harris KDM, Imai Y, Tajima N, Kuroda R (2003) J Am Chem Soc 125:14658
113. Ma BQ, Mulfort KL, Hupp JT (2005) Inorg Chem 44:4912
114. Friščić T, Meštrović E, Škalec Šamec D, Kaitner B, Fábián L (2009) Chem Eur J 15:12644
115. Fujii K, Ashida Y, Uekusa H, Hirano S, Toyota S, Toda F, Pan Z, Harris KDM (2009) Cryst Growth Des 9:1201
116. Karki S, Fábián L, Friščić T, Jones W (2007) Org Lett 9:3133
117. Guo F, Harris KDM (2005) J Am Chem Soc 127:7314
118. Guo F, Cheung EY, Harris KDM, Pedireddi VR (2006) Cryst Growth Des 6:846
119. Albesa-Jové D, Pan Z, Harris KDM, Uekusa H (2008) Cryst Growth Des 8:3641
120. Williams JH (1993) Acc Chem Res 26:593
121. Nakanishi H, Nakano N, Hasegawa M (1970) J Polym Sci B Polym Lett 8:755
122. Sasada Y, Shimanouchi H, Nakanishi H, Hasegawa M (1971) Bull Chem Soc Jpn 44:1262
123. Guo F, Martí-Rujas J, Pan Z, Hughes CE, Harris KDM (2008) J Phys Chem C 112:19793
124. Schmidt GMJ (1971) Pure Appl Chem 27:647
125. Cohen MD, Schmidt GMJ (1964) J Chem Soc 1996
126. Thomas JM (1974) Philos Trans R Soc 277:251
127. Thomas JM (1981) Nature 289:633
128. Nakagawa H, Ohba S, Asakura K, Miura T, Tanaka A, Osanai S (1997) Acta Crystallogr Sect C 53:216
129. Bernal I, Cetrullo J, Jackson WG (1993) J Coord Chem 28:89
130. Guo F, Casadesus M, Cheung EY, Coogan MP, Harris KDM (2006) Chem Commun 1854
131. Brunelli M, Wright JP, Vaughan GBM, Nora AJ, Fitch AN (2003) Angew Chem Int Ed 42:2029
132. Zachariasen WH, Ellinger FH (1963) Acta Crystallogr 16:369
133. Shankland K, David WIF, Sivia DS (1997) J Mater Chem 7:569

Index